รายงานวิจัยฉบับสมบูรณ์

การยับยั้งเทโลเมอเรสและการกดการแสดงออกของอองโคยีน โดยสารอนุพันธ์
เพอรีลีน เพื่อใช้เป็นสารเคมีบำบัดต้านมะเร็งต่อมลูกหมาก

Telomerase inhibition and oncogene repression by perylene derivatives as
chemotherapeutic agents against prostate cancer

โดย รศ.ดร. วิโรจน์ ตันติเวชอภิกุล และคณะ

มีนาคม 2562

รายงานวิจัยฉบับสมบูรณ์

การยับยั้งเทโลเมอเรสและการกดการแสดงออกของอองโคยีน โดยสารอนุพันธ์เพอรีลีน เพื่อใช้เป็นสารเคมีบำบัดต้านมะเร็งต่อมลูกหมาก

Telomerase inhibition and oncogene repression by perylene derivatives as chemotherapeutic agents against prostate cancer

รศ.ดร. วิโรจน์ ตันติเวชอภิกุล

คณะแพทยศาสตร์

มหาวิทยาลัยเชียงใหม่

ACKNOWLEDGEMENT

ABSTRACT

Project Code: RSA5880007

Project Title: Telomerase inhibition and oncogene repression by perylene derivatives as chemotherapeutic agents against prostate cancer

Investigator: Assoc.Prof. Wirote Tuntiwechapikul

Department of Biochemistry, Faculty of Medicine, Chiang Mai University

E-mail Address: wirotetunti@yahoo.com

Project Period: 1 July 2015 - 30 June 2018

This report is divided into four chapters. Chapter 1 is the introduction to the background and significance of this project. Chapter 2 entitled "Telomerase Inhibition, Telomere Shortening, and Cellular Uptake of the Perylene Derivatives PM2 and PIPER in Prostate Cancer Cells", is the investigation of two perylene derivatives as telomerase inhibitors and their effects on prostate cancer cells. Chapter 3 entitled "Ginger Extract Promotes Telomere Shortening and Cellular Senescence in A549 Lung Cancer Cells", is our further investigation from the previously known that ginger extract has telomerase inhibitory effect. We investigated whether this telomerase inhibition would result in telomere shortening and cellular senescence or not. Chapter 4 entitled "Synthesis, DNA Binding Studies, and Telomerase Inhibition of New Perylene Derivatives" is the synthesis of some old and new perylene derivatives in order to improve binding affinity and specificity to G-quadruplex DNA from various G-quadruplex motif, and we also tested their telomerase inhibitory effect as G-quadruplex ligands.

Keywords : Telomerase, perylene, ginger, G-quadruplex

บทคัดย่อ

     รายงานวิจันนี้แบ่งออกเป็นสี่บท บทแรกจะเป็นบทนำเพื่อปูพื้นฐานความรู้และความ
สำคัญของงานวิจัย บทที่สองมีชื่อว่า "Telomerase Inhibition, Telomere Shortening, and
Cellular Uptake of the Perylene Derivatives PM2 and PIPER in Prostate Cancer Cells" เป็น
บทที่แสดงผลของสารอนุพันธ์เพอรีลีนสองตัวที่ยับยั้งการทำงานของเทโลเมอเรส และผลของนัน
ในเซลล์มะเร็งต่อมลูกหมาก บทที่สามมีชื่อว่า "Ginger Extract Promotes Telomere Shortening
and Cellular Senescence in A549 Lung Cancer Cells" เป็นผลงานต่อเนื่องจากที่เราเคยทราบ
แล้วว่า สารสกัดจากขิงมีฤทธิ์ต้านการแสดงออกของเทโลเมอเรสในเซลล์มะเร็งปอด ในงานวิจัยนี้
เราพบว่าสารสกัดจากขิงสามารถทำให้เทโลเมียร์หดสั้นและเซลล์มะเร็งเข้าสู่ภาวะแก่ ส่วนบทที่สี่
มีชื่อว่า "Synthesis, DNA Binding Studies, and Telomerase Inhibition of New Perylene
Derivatives" เป็นบทที่รวบรวมการสังเคราะห์สารอนุพันธ์เพอรีลีนทั้งเก่าและใหม่ เพื่อศึกษาและ
ปรับปรุงสารให้จับกับจี-ควาดรูเพล็กซ์ดีเอ็นเอได้ดีขึ้น หรือมีการเลือกจับกับจี-ควาดรูเพล็กซ์ดีเอ็น
เอแบบต่างๆ ตลอดจนศึกษาผลการยับยั้งเทโลเมอเรสของสารเหล่านี้

คำหลัก : เทโลเมอเรส เพอรีลีน มะเร็งต่อมลูกหมาก ขิง จี-ควาดรูเพล็กซ์

TABLE OF CONTENTS

CHAPTER 1

INTRODUCTION

1.1 Historical Background

Cancer cells exhibit unlimited replicative potential, in contrast to the limited lifespan of normal somatic cells. Most normal somatic cells are associated with two distinct barriers to proliferation: senescence, a typically irreversible entrance into a non-proliferative but the viable state, and crisis, which involves cell death. This limited lifespan has been found to be the consequence of telomere shortening, which is caused by the end replication problem [1]. With successive rounds of cell division, telomeres are shortened until they reach a critically short length, replication is halted, and cell enters senescence or cell death [2]. Cancer cells, on the other hand, escape cell senescence by maintaining their telomere lengths, which enables cancer cells to divide indefinitely. More than 85% of cancers maintain their telomeres by reactivating telomerase, the ribonucleoprotein enzyme that adds telomeric repeats onto 3' end of telomeric DNA [3]. Therefore, telomerase inhibition has emerged as a cancer-selective target, which will lead cancer cells to senescence or cell death.

Prostate cancer is the most common cancer in men in the world and the second most common cause of cancer-related death [4, 5]. Nearly all of the prostate cancer deaths are attributable to metastatic and castration-resistant prostate cancer (CRPC) that has progressed despite androgen deprivation therapy (ADT). It is the most common treatment for patients with recurrent or advanced prostate cancer [4]. Telomerase has been used as a reliable tumor marker in the diagnosis of prostatic intraepithelial neoplasia (PINs) and prostate cancer [6]. However, cancer eventually develops resistance and recurrence due to the small fraction of cancer cells, including cancer stem cells or tumor-initiating cells, survive the initial treatment and give rise to tumor recurrence.

Lung cancer has also been found to increase telomerase activity. Furthermore, several studies using animal models and human non-small cell lung cancer (NSCLC) tissues have reported that TERT mRNA and TERT protein are overexpressed in lung

cancer biopsies compared with normal lung tissues [7, 8]. Telomerase inhibition by MST312 activated DDR through induced telomere shortening in lung cancer stem cells (CSCs) [9]. Moreover, Imetelstat, another telomerase inhibitor, was found to efficiently inhibit telomerase, resulting in the shortening of telomeres in non-small cell lung cancer (NSCLCs), and in some cases, long-term treatment with Imetelstat increase sensitize to cytotoxic therapies in NSCLCs [10]. In addition, the clinical trial of Imetelstat in NSCLC showed that patients with short telomeres responded best to therapy [11]. These results support the hypothesis that telomerase inhibition could control tumor cell proliferation, and telomerase is an attractive option for treating lung cancer. Our data indicated more than 80 % of NSCLCs analyzed expressed telomerase activity and conferred the worst outcome [12], in agreement with previously reported [13], without significant differences in the mean telomere length values between telomerase positive and negative tumors. Although telomerase activation can be an early event in cancer, it is not necessary for cancer initiation.

G-quadruplex ligands are one of the most studied group of telomerase inhibitors. They inhibit telomerase by facilitating G-quadruplex DNA formation at the 3'-end of telomeric DNA, which prevent the access of telomerase to the telomeric end. Moreover, these compounds also promote G-quadruplex formation at the *hTERT* promoter, obstructing the transcription machinery to bind to the promoter and therefore suppressing hTERT expression. Since hTERT is the catalytic subunit of telomerase, hTERT suppression results in a reduction of telomerase activity in cancer cells. In our past investigation, we found that PM2 and PIPER, the synthetic G-quadruplex ligands, inhibit telomerase directly by interfering with its substrate binding, and indirectly via *hTERT* expression repression, which eventually leads to telomere shortening and cellular senescence in A549 lung cancer cells. Also, these compounds repress some oncogenic genes expression, such as *c-Myc* and *VEGF*, by inducing G-quadruplex formation at their promoters [14, 15]. However, the efficacy of these two compounds has never been studied in the prostate cancer cells.

Dietary phytochemicals are of considerable interest in cancer prevention. A literature search for plant-derived telomerase inhibitors found a few natural phytochemicals that inhibited telomerase in cancer cells; these include curcumin,

epigallocatechin-3-gallate (EGCG), resveratrol, genistein, sulforaphane, silibinin, and pristimerin, among others [16]. Previously, we reported that the crude extract of *Z. officinale* suppressed *hTERT* expression in A549 lung cancer cells, leading to the reduction of hTERT protein and telomerase activity [17]. However, the long-term effect of this crude ginger extract on telomere shortening and cellular senescence has never been investigated.

1.2 Objectives

The aim of this study is to investigate the short-term and long-term effects of our synthetic perylene derivatives on telomerase inhibition, telomere shortening, and cellular senescence in prostate cancer cells. Moreover, we further our investigation into examining the long-term effects of the crude ginger extract on telomere shortening and cellular senescence in lung cancer cells. Therefore, in this was divided into two parts.

Part I: Studies of perylene derivatives in prostate cancer cells

To investigate the effects of two perylene-derivatives (PM2 and PIPER) in 2 prostate cancer cell lines, including androgen sensitive carcinoma cell line (LNCaP) and androgen-independent tumor cell lines (PC-3) in term of:

1. Cell cytotoxicity

2. Oncogenic and androgen receptor (AR) genes expression

3. Telomerase inhibition

4. Telomere shortening and cellular senescence induction

5. Cellular uptake

Part II: Studies of crude ginger extract in A549 lung cancer cells

To study in long-term treatment effect of ginger extract in ethyl acetate fraction to telomere shortening and cellular senescence on A549 non-small lung carcinoma cells.

1.3 Literature reviews

1.3.1 Telomere structure and function

Telomeres are the specialized nucleoprotein structure located at both ends of the linear eukaryotic chromosomes. Telomeres have two main functions: to protect the end of the chromosome by preventing end-to-end fusion and degradation, and to avoid the loss of coding DNA during DNA replication [18, 19]. The human telomeric DNA composes of noncoding DNA sequence, long tracts of short repetitive double-stranded DNA $(TTAGGG)_n$ typically 2-15 kb in length, and the 150-200 nucleotides 3′ overhang with the same repetitive TTAGGG sequence [20]. The telomeric DNA is associated with telomere specific-proteins in term of shelterin complex [21, 22].

Shelterin proteins comprise of six proteins: telomeric repeat-binding factor 1 and 2 (TRF1 and TRF2), protection of telomere 1 (POT1), TRF1-interacting nuclear factor 2 (TIN2), TINF2-interacting protein 1 (TPP1), and the transcriptional repressor/activator protein 1 (Rap 1) [23-25]. TRF1 and TRF 2 bind with double-stranded telomeric DNA, while POT1 binds directly with the 3' single-stranded telomeric DNA. The shelterin complex builds and stabilizes the telomere structure in the form of T-loop, in which the 3' single-stranded DNA overhang folds back and invades into the double-stranded telomeric DNA, creating a displacement d-loop structure at the invasion site (Figure 1.1). The telomere-shelterin complex protects the chromosome end from being recognized as DNA double-strand break [26-28].
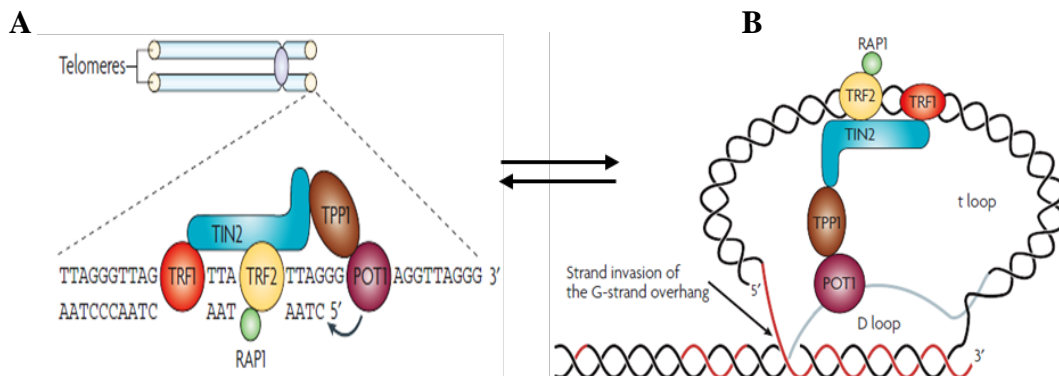
Figure 1.1: Telomere structure (A) and shelterin protein complex (B)

1.3.2 Telomere shortening

Telomere shortening occurs at every round of cell division, as a result of the incomplete replication referred to as the "end replication problem". Telomeres are shortened by about 50-200 bp in each cell division [26]. In DNA replication, the double stranded-DNA template is separated, and the replication of each strand is done individually. In the leading strand, the DNA synthesis is continuous; while in lagging strand, DNA replication must be done in segments called Okazaki fragments. Each fragment is initiated using an RNA-DNA primer synthesized by DNA polymerase α. Eventually, these primers are removed, and the Okazaki fragments are ligated together to create a continuous strand [30]. However, DNA polymerase α cannot initiate primer synthesis at the very end of the telomeric DNA, along with the removal of the last primer, resulting in the incomplete DNA replication at the end of telomeres. Therefore, the end of the chromosome is not fully replicated, and telomeres become progressively shortened with each cell division [31, 32].

The end replication problem occurs in almost normal somatic cells. This event is limited by the telomere length. When the telomere becomes too short, it no longer forms the regular telomere structure and exposes its DNA end which appears as if it were DNA double-strand break. The DNA damage response then triggers an irreversible growth arrest called replicative senescence, or mortality stage 1 (M1). Thus, telomere is the biological molecular clock that defines a number of cell division and provides a tumor-suppression mechanism [34]. However, in cells that have abrogation of cell cycle checkpoint; for instance TP53, p16INK4a, and pRB, they escape replicative senescence and continue to divide with further telomere loss until telomere becomes critically short, the cells are driven to "crisis", or mortality stage 2 (M2) [35, 36]. Between the M1 and M2 stages, the occurrence of chromosomal end fusion can lead to the chromosome bridge-breakage-fusion (BFB) cycle which increases the chromosomal instability and abnormalities [35]. The chromosomal abnormality may result in the reactivation of telomerase, an enzyme that extends the telomeric DNA. The cells become immortalized, which is an essential step during cancer progression (Figure 1.2) [37].
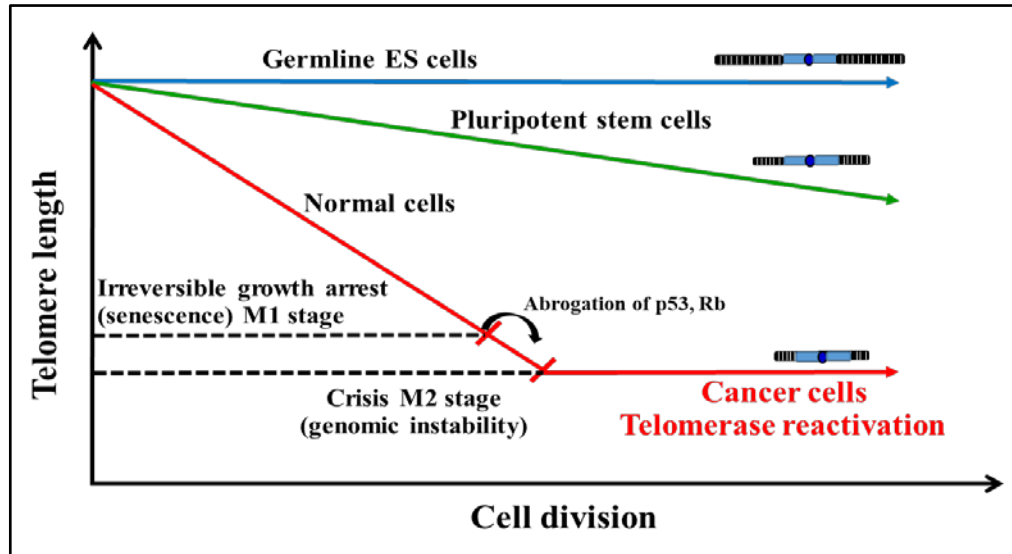
Figure 1.2: Telomere shortening in cell division progression

1.3.3 Cellular senescence

The limitation in the divided capacity of normal human fibroblast cells was discovered by Hayflick and Moorhead in 1961. They found that fibroblast cells could undergo about 50-60 rounds of cell division, after which they stopped dividing, and their phenotype was changed characterized by cell enlargement, flat shape, and the presence of senescence-associated β-galactosidase (SA-β gal) activity. The limit proliferation capacity has been known in term of replicative senescence, which is a form of cellular senescence [38, 39]

Cellular senescence is an irreversible cell cycle arrest. It is considered one of the tumor-suppressing mechanisms to suppress tumor initiation and tumor progression. There are two major pathways that regulated the senescence induction. The first one is the p16^{INK4a}/pRb pathway, and the second one is the p53/p21 pathway. Cellular senescence is triggered by many cellular factors as follows:

- **Telomere shortening**. In each round of cells division, telomere progressively shorten. When telomeres become too short to form the T-loop structure, they appear as if they were double-stranded DNA breaks that consequently activate DNA damage response pathway by first arresting the cell cycle by the p53/p21 pathway, resulting in telomere-induced senescence or apoptosis activation [41, 42].

7

- **INK4a/ARF derepression**. The INK4a/ARF locus encodes two critical tumor suppressors, p16INK4 and ARF, are important inducers of cellular senescence. Whereas p16INK4a is an inhibitor of the cyclin-dependent kinases CDK4 and CDK6 and acts by imposing a G1 cell cycle arrest, ARF regulates p53 stability through inactivation of the p53-degrading ubiquitin ligase MDM2 [43, 44]. Normally, the INK4a/ARF express at very low levels in most tissues in young organisms but become derepressed with aging [45]. The factors that induce cellular senescence via INK4a/ARF dependent pathway include the stimulation of mitogenic factors [46, 47] and oxidative damage [48]. The molecular mechanisms responsible for the increased expression of p16INK4a and ARF are mostly involved in the transcriptional level. In particular, the increase of transcriptional activator Ets1 correlates with the upregulation of p16INK4a during mouse aging [49, 50]. Whereas, the decrease in p16INK4a repressor expression (Bmi1) is observed with aging in human skin [51].

- **DNA damage**. The accumulation of various forms of DNA damage such as DNA mutation [52], DNA oxidation [53], chromosome losses [54, 55], and telomere-dependent γH2AX foci [56] was found to trigger cellular senescence. These observations have led to the conclusion that DNA damages and DNA damage signals as possible factors conducing to cellular senescence and to organismal aging. The accumulation of senescent cells in aged tissues arise from the accumulation of DNA damages. Senescence induction is the protective mechanism to prevent these damaged cells to progress to cancer [57].

Senescent cells are viable, but stop dividing. The senescent cells exhibit many changes in both cell appearance and cell metabolism. The hallmarks of cell senescence include: increase in size, irreversible growth arrest, the expansion of the lysosomal compartment leading to high expression and increase activity levels of the lysosomal senescence-associated β-galactosidase enzyme, at pH 6.0 in human and p16INK4a, secretion of numerous growth factors, cytokines, proteases, and other proteins collectively called as senescence-associated secretory phenotype (SASP), and presence of nuclear foci containing DDR proteins (DNA-SCARS) or heterochromatin (SAHF).

1.3.4 Telomerase

Telomerase is a ribonucleoprotein whose catalytic function depends minimally on two components: the telomerase reverse transcriptase (TERT) protein and telomerase RNA (TR) (figure 1.7). In human, the isolated catalytically active enzyme consists of two molecules each of human telomeric RNA (hTR), human telomerase reverse transcriptase (hTERT), and dyskerin [59, 60]. Dyskerin binds with hTR and hTERT to increase the stabilization of the complex [61]. Human telomerase uses its internal RNA as a template to catalyze the addition of 6-base pairs repeats $(TTAGGG)_n$ to the 3' telomere ends, and thereby prevents the telomeres from becoming critically short [54]. It adds multiple telomeric sequences through repeated cycles of extension and translocation reactions. The length of newly synthesized telomeric DNA is controlled by some telomeric proteins.

The hTERT protein is the catalytic component of the enzyme. This DNA polymerase belongs to the reverse transcriptase family [62]. The corresponding gene is a 37-kb long gene located at the end of chromosome 5 (5p15.33) [63-65]. It consists of 16 exons [66] and encodes a protein of 1132 amino acids (127 kDa). The hTR is the RNA component of telomerase. It is a 451-nucleotide RNA which contains an 11-nucleotide long template sequence for telomeric repeat synthesis [67]. The gene encoding hTR is a single copy gene localized to chromosome 3 at 3q26.3 [68]. The half-life of this RNA varies from 4 to 32 days and is the longest ever reported for a eukaryotic RNA [69]. Processing and stability of hTR require binding of nucleolar RNA binding proteins such as dyskerin, NHP2, NOP10, and GAR1 to the H/ACA motif [70]. Its interaction with hTERT determines catalytic activity, processivity, telomere binding and has a role in proper ribonucleoprotein folding and assembly. Like other snoRNP complexes, telomerase assembly occurs in the nucleolus. Telomerase assembly also requires Hsp90 and p23 [71].

1.3.5 Telomerase regulation

Telomerase is generally expressed in cells with high proliferative potential, and absent in quiescent cells [73]. In mammals, telomerase is strongly expressed in germinal cells but is extinguished in the oocyte of adults and the mature spermatozoa. It is active

during embryonic development starting from the blastula stage, then, gradually repressed during differentiation in the majority of somatic cells [74-76]. In adult, it is detected only in certain stem cells in bone marrow, skin and intestine. The reason why telomerase is repressed during terminal differentiation is not yet elucidated. However, it is suggested that this repression acts as a tumor suppressor mechanism.

Telomerase is regulated at different levels, including transcription, mRNA splicing and maturation, and modification of hTERT protein and hTR. Studies have shown that hTR is widely expressed in most cells types, even in telomerase-negative cells such as differentiated somatic cells [77, 78]. The hTERT is tightly regulated during differentiation and is not expressed or expressed at a very low level in most somatic cells. These observations suggested that hTERT is the most important determinant and the rate-limiting factor in the regulation of telomerase activity. The cloning of hTERT promoter facilitated the identification of possible mechanisms of hTERT regulation [66, 79-81]. The analysis of its sequence reveals that it is deprived of TATA and CAAT boxes but rich in CpG islands. Many potential binding sites for various transcription factors were identified. The capacity of these factors to activate or repress hTERT expression was then tested using gel shift experiments, chromatin immunoprecipitation assay or reporter gene systems. Positive regulators of hTERT transcription include c-Myc oncogene, Sp1 transcription factor, E6 human papillomavirus protein (HPV), and steroid hormones. In addition to these inducers of telomerase activity, negative regulators of hTERT transcription have also been described, including Mad1 transcription factor, Menin tumor suppressor, SIP1 (Smad-interacting protein, a TGF-b regulated transcription factor), p53, pRB, E2F, Wilms' tumor suppressor 1 protein (WT1), myeloid-specific zinc finger protein 2 (MZF-2), T-cell leukemia virus type I oncoprotein HPV E2 and a number of antiproliferative cytokines such as interferon-g , and TGF-β [82]. Taken together, these studies highlight the complexity of hTERT transcriptional regulation not only in human cancer cells but also during development. However, the participation of many of these transcription factors in hTERT regulation has been shown from studies utilizing *in vitro* cell cultures and analyses of overexpressed and/or recombinant proteins rather than endogenous ones. The physiological target genes of a transcription factor can, in fact, be different from genes affected when it is overexpressed.

The presence of CpG islands on the hTERT promoter [73] suggested that methylation can play an important role in the regulation of hTERT transcription in normal and cancer cells. However, no coherent correlation between hTERT promoter methylation and telomerase activity could be found [83, 84]. Some findings demonstrate that hypermethylation of hTERT promoter negatively controls hTERT in some telomerase-negative cells and treatment with 5-Azacytidine, a DNA methylation inhibitor, leads to the re-expression of hTERT. In contrast, other works report a positive correlation between hypermethylation of the hTERT promoter, hTERT mRNA expression and telomerase activity. Treatment with 5-azacytidine leads to hTERT repression, a decrease of telomerase activity, and telomere shortening [85]. In conclusion, hTERT regulation by methylation of its promoter is possible and cell-type dependent.

Emerging evidence suggests that reversible acetylation/deacetylation of nucleosomal histones and the resulting changes in the chromatin structure are important processes in gene transcription regulation [86]. Acetylation of lysine residues of histones leads to chromatin decondensation, increasing the accessibility for RNA polymerase complexes. Chromatin remodeling is a dynamic process catalyzed by histone acetyltransferase (HAT) and histone deacetylase (HDAC). Transcription factors, such as Mad, can repress gene expression by recruiting HDACs to specific sites in gene promoters. Since hTERT promoter contains Mad-binding sites, histone acetylation may be involved in the transcriptional regulation of hTERT [87, 88]. However, as for DNA methylation, the role of histone acetylation in the regulation of hTERT expression is controversial.

Post-transcriptional and post-translational modifications of hTERT can also regulate telomerase activity. Pre-mRNA splicing is a fundamental biological process involved in the expression of genes. Alternative splice variants of hTERT, leading to distinct hTERT isoforms have been identified [65, 89]. The variants with α and β deletions are the best characterized. The α-deletion lacks 36 nucleotides from exon 6 including motif A, and the β-deletion lacks 182 nucleotides from exon 7 and 8, including motif B' [89]. Besides the deletion-type splice variants, a number of insertion-type mutations have also been reported likely participating in the regulation of telomerase [66,

89]. The insertion-types are the 38-nucleotide insertion of intron 14 (INS1), the partial insertion of intron 11 (INS2), the 159-nucleotide insertion of intron 14 (INS3), and replacement of the complete exon 15 and the 5' part of exon 16 with the first 600 nucleotides of intron 14. There is a tissue-specific pattern of splicing of hTERT during human development and in specific adult tissues. The function of hTERT alternative splicing is still unclear. The expression of some of these hTERT isoforms may have a role in telomerase regulation [76], and it seems possible that modulation of this splicing pattern has a role in the regulation of the amount of the active protein.

Chaperone proteins allow the appropriate folding of the proteins with which they interact. The assembly of the telomerase holoenzyme is controlled by chaperone proteins helping the formation of the active enzyme [90]. While the interaction with Hsp70 protein is transitory, Hsp90 and p23 proteins remain permanently associated with the telomerase complex affecting its activity. Recently, overexpression of MKRN1 in telomerase-positive cells promotes the degradation of hTERT, suggesting that it can play an important role in modulating telomere length homeostasis [91].

Phosphorylation of proteins is a major post-translational mechanism, very often used to regulate protein activity. Phosphorylation of hTERT protein at specific serine/threonine or tyrosine residues is one of the mechanisms of hTERT activation. Telomerase activity can be controlled by proteins kinases, including protein kinase C (PKC) and B (PKB/Akt) and also by protein phosphatase A (PP2A).

1.3.6 Telomerase inhibition

Telomerase is an attractive target for cancer therapy and cancer prevention due to its essential role in the immortal characteristic of most cancer cells. The absence of its activity in most normal somatic cells means that telomerase inhibition does not affect these cells; therefore, there are fewer side effects to normal tissues and organs. With telomerase inhibition, telomeres of cancer cells expressed telomerase are shortened in every cell division just like most normal somatic cells, and once one or more telomeres are shortened to a critical length, the cancer cells are triggered to cellular senescence [92]. Because telomerase inhibition does not immediately kill cancer cells, it might be suitable

for cancer prevention or as an adjunct therapy to prevent cancer relapse from cancer-initiating cells [93].

The strategies for telomerase inhibition is based on all aspects of telomere/telomerase biology. Numerous approaches are divided into two parts. The first one is the interference in telomerase expression and activity, while in the other direction, interfering with telomerase substrate (telomeric DNA) (figure 1.9) [94]. These strategies include:

- Inhibiting telomerase activity

- Inhibiting the hTR template

- Inhibiting *hTERT* or *hTR* expression

- Inhibiting telomerase assembly protein (telomerase holoenzyme)

- Inhibiting the access of telomerase to the substrate (telomere)

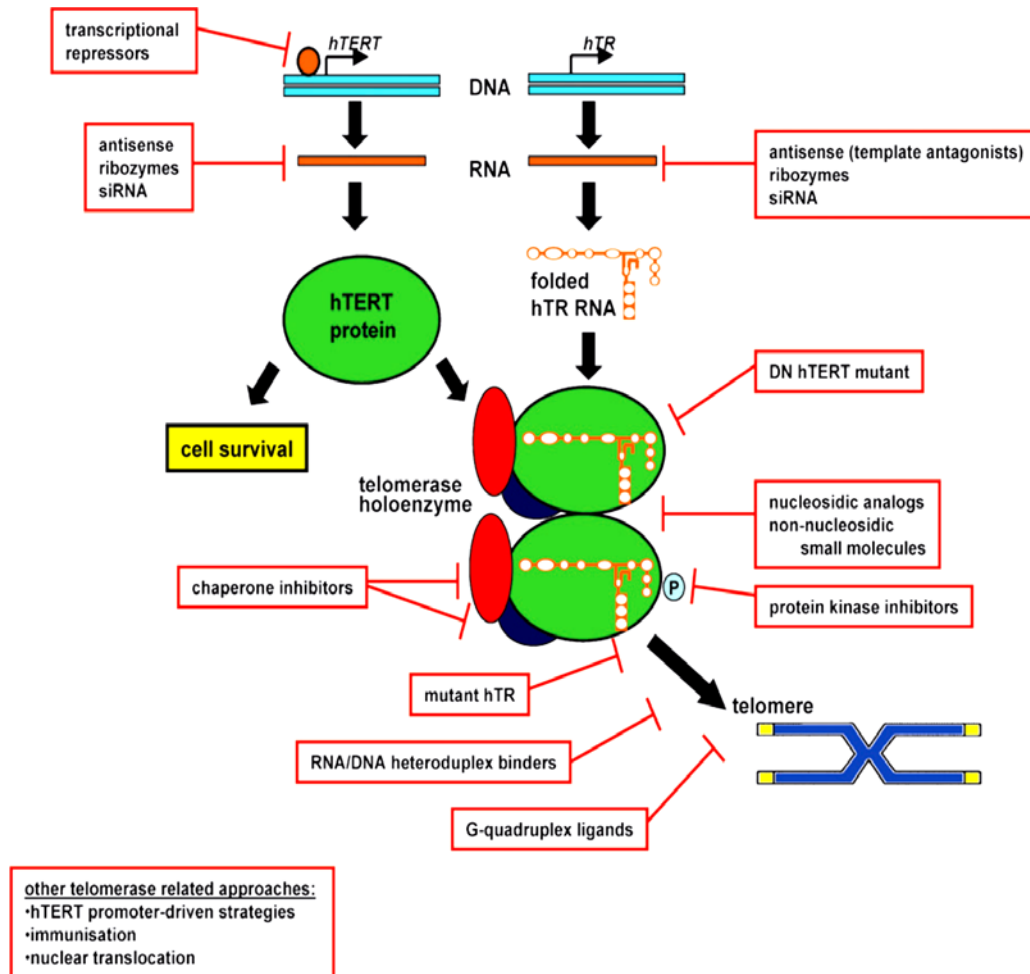- Inhibiting recruitment of telomerase to telomere

Figure 1.3: The molecular target of telomerase inhibition

1.3.7 G-quadruplex DNA structure

DNA is often found in the form of a duplex, in which one strand anneals with its complementary strand. Nevertheless, certain nucleic acid sequences containing tandem repeats of short runs of guanines (G) nucleotides can form four-stranded DNA secondary structures in termed G-quadruplex structure (G4 structure) [96]. The four-guanine residues connected by cyclic Hoogsteen hydrogen bonding to generate a square-planar platform called G-tetrads. The G4 structures comprise a core of two or more of stacked G-tetrads [97]. Monovalent cations (e.g., Na^+, K^+) stabilize these structures by coordinating with eight carbonyl oxygen atoms between the stacked tetrads [98], neutralizing the electrostatic repulsion of inwardly pointing guanine oxygens [99] (Figure 1.4). The G4 structure has a variety of forms; these structures can be categorized in terms of their G-strand-directional (which can be mutually parallel or anti-parallel) and molecularity [100]. Moreover, they can form within one strand (intramolecular G-quadruplex) or from multiple strands (intermolecular G-quadruplex), and multiple loop structures as well [96, 100]
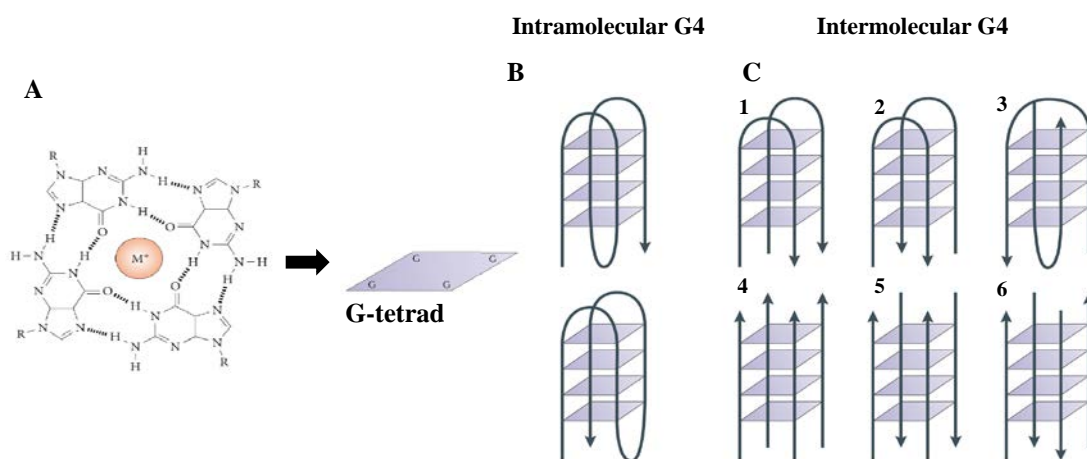

Figure 1.4: The G-tetrad (A) and the form of G-quadruplex formation (B-C)]

15

1.3.8 Biological roles of G-quadruplex DNA

The bioinformatics study has disclosed more than 375,000 putative G4 forming sequences (PQS) presenting in the human genome. These sequences consist of at least four runs of guanines (G-tracts), in which each G-tract contain at least three guanine residues [99, 101]. Especially, many PQS was observed in the biological significance regions such as telomeric DNA and transcriptional regulatory region in several important oncogenes [102].

Maintaining the integrity of the single strand G-rich 3′ overhang is essential for cell survival [102]. As mentioned earlier, the 3'-overhang of telomeric DNA forms a T-loop structure by invading into the duplex region to form a displacement loop. However, the G-quadruplex formation can also provide an alternative G-rich 3′-overhang protection, which likely involves an alignment of sister chromatins, as shown in Figure 1.5A. The 3′G-rich overhang can fold back to form a hairpin structure through G–G base pairing. Such hairpins from different chromosomes can then dimerize to form a G-quadruplex structure and help the alignment of sister chromatins [103]. Alternatively, the G-rich overhang can fold over to form an intramolecular G-quadruplex, which poses a physical blockade for the access of telomerase to the chromosomes ends, as a display in Figure 1.5B [104].
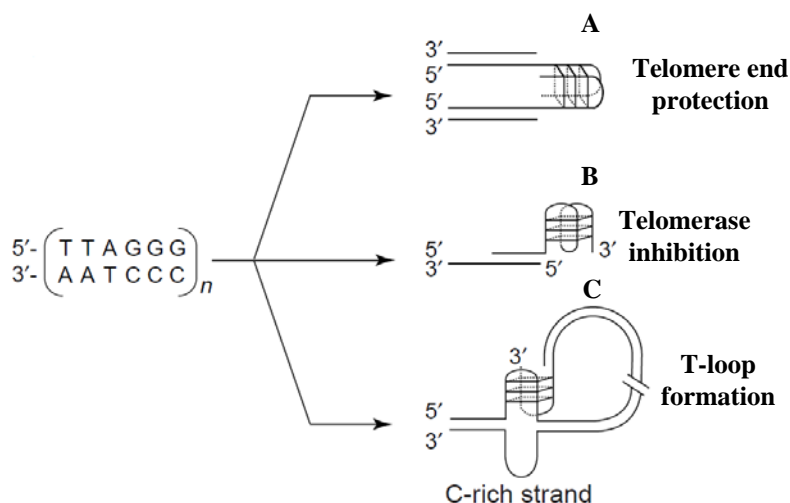

Figure 1.5: Putative functional roles of G-quadruplex structures at telomeres

The formation of G-quadruplex, instead of the duplex, at the promoter gene region is associated with an altered state of transcription. The G-quadruplex motifs are particularly widespread near promoter regions and found within 1kb upstream of the transcriptional start site (TSS) of 50% of human genes, suggesting a potential role in the regulation of gene transcription [105]. Computational studies show that the promoter-associated G4 motifs of human oncogenes are found more often than average, whereas G4 motifs are found less in the promoters of housekeeping and tumor suppressor genes [106, 107], (Figure 1.6). These findings may have an application in cancer treatment.
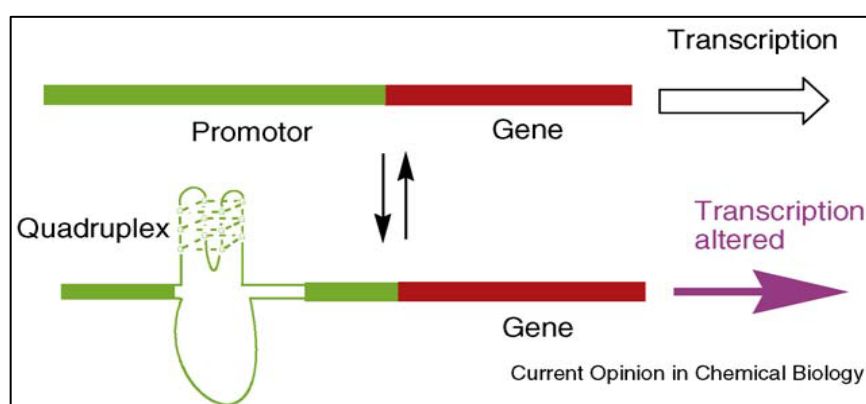

Figure 1.6: G-quadruplex formation in the promoter region

The formation of G4 structure in or near promoter region may affect gene expression in both positive and negative ways. First, it depends on where the G4 motif is. If the G4 formation is on the template strand, it can block the transcription machinery via inhibiting the RNA polymerase (Figure 1.7A). However, if the G4 structure formation is on the non-template strand, it can enhance transcriptional activity by keeping the transcribed strand in the single-stranded conformation (Figure 1.7B). Second, it depends on the regulatory proteins, whether these proteins are enhancers or repressors. The G-quadruplex formation will impede the binding of these proteins and therefore could impact the transcription of the gene (Figure 1.7 C and D) [108].
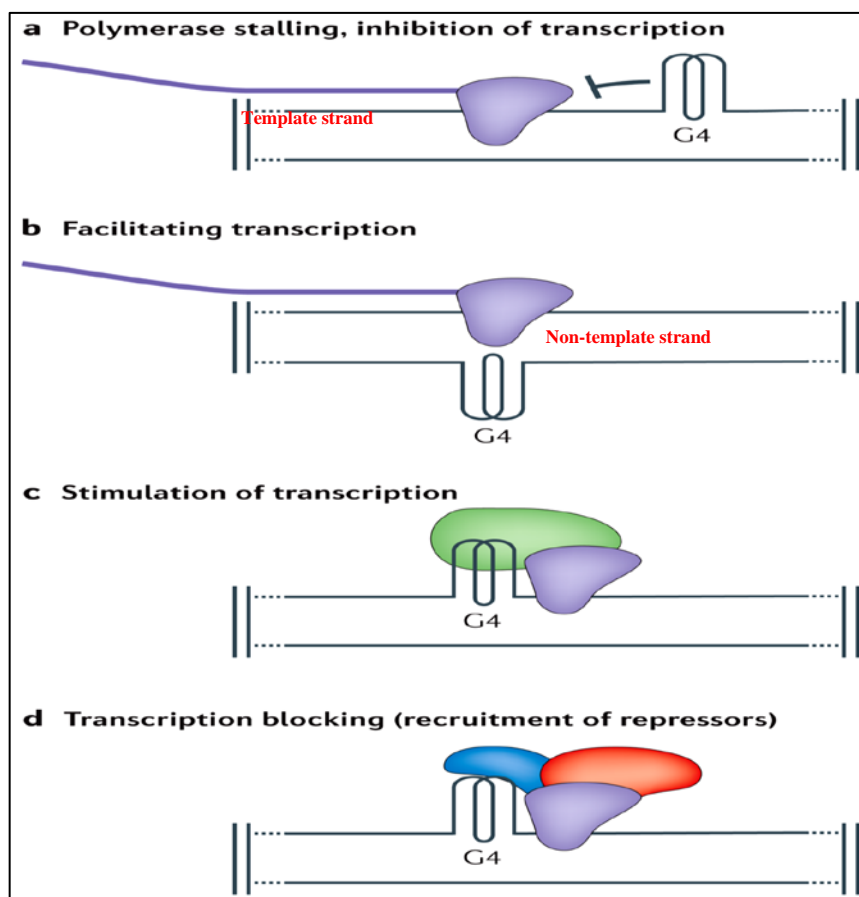
Figure 1.7: Functional roles of G-quadruplex structures during transcription

G-quadruplex motif is found within the promoter of a number of cancer-related gene, such as *c-MYC* [109], VEGF [110], HIF1ɒ [111], RET [112], bcl-2 [113, 114], as well as PDGF-A [115]. It has been reported that the G-rich DNA sequences of these gene promoters (*c-MYC*, *VEGF*, *HIF-1α*, Ret, *Bcl-2*) can form three-tetrad G4 structures [110-114, 116-125], while PDGF-A and c-Myb form different types of G4 structures [126, 127]. In general, the G-quadruplex motif loop regions have been displayed, $G_3N_1G_3N_2-9G_3N_1G_3$ (except for the BCL-2 sequence and where N represents the nucleotides), which a common indicator for the capability to form a three-tetrad intramolecular G-quadruplex of G-rich DNA oligomer [128]

Figure 1.8A shows the hTERT core promoter, located at −180 to +1 relative to the transcriptional start site. It contains a c-Myc binding site (E-box), and five Sp1 binding sites [130]; these binding sites are important for the promoter activity. The Sp1 binding sites locate between −22 to −90 nucleotides; this section contains 12 consecutive

G-tracts of three or more guanine residues, which can form G4 structure comprise two parallel intramolecular G4 and a hybrid-type G4 structure separated by 26-nucleotide long middle loop (figure 1.8B). This G4 structure formation blocks the binding of Sp1 in TERT core promoter and leads to the inhibition of the promoter transcriptional activity. Therefore, G-rich sequence within TERT promoter may provide the binding site of G4-interacting agents [131].
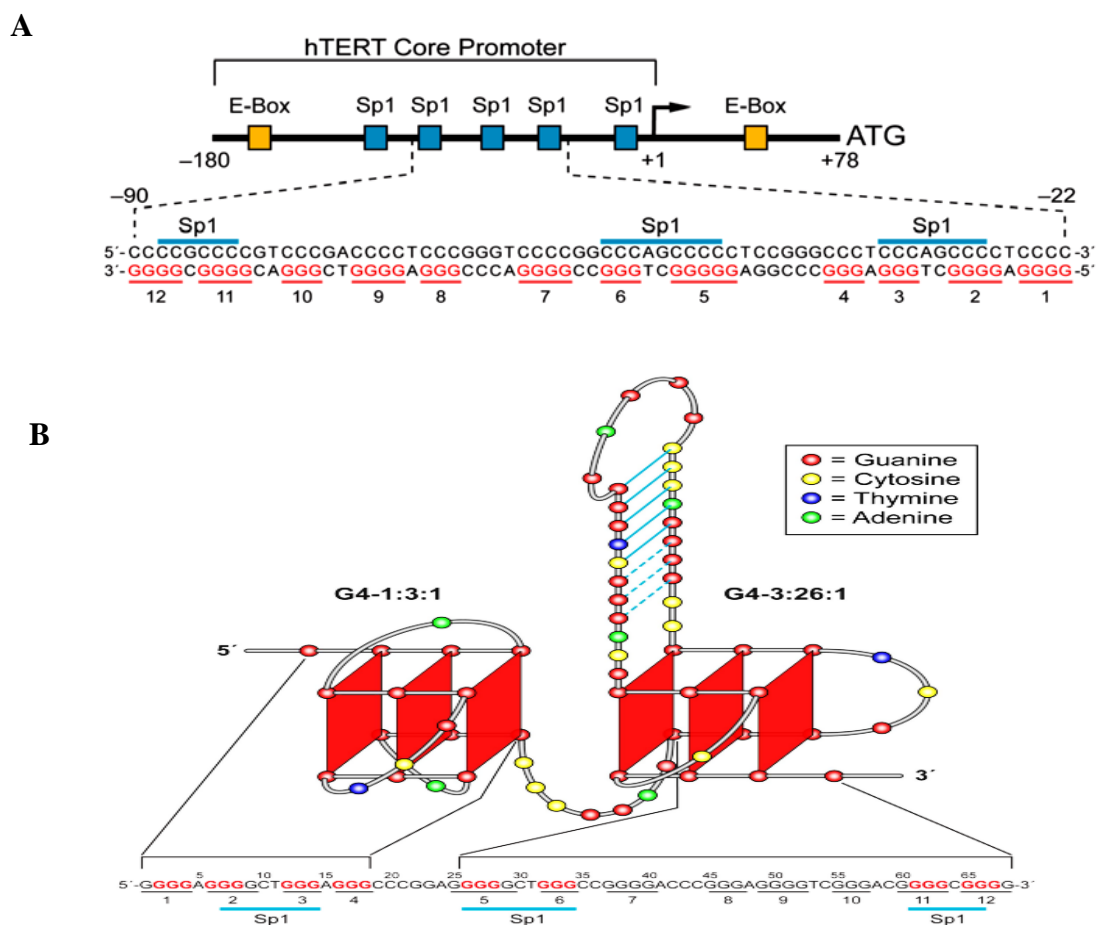

Figure 1.8: The hTERT core promoter (A) and the model of the G-quadruplex structure formed in the hTERT core promoter (B)

1.3.9 G-quadruplex interactive agents

G4 structures are unique from the duplex nucleic acid, providing the potential of a small molecule to bind with high specificity and affinity when compared with duplex DNA. Thus, one strategy for telomerase inhibition through telomere maintaining mechanism is the development and design of G-quadruplex stabilizing ligands [132, 133].

The G4 binding ligands mostly contain a planar polycyclic aromatic moiety, and at least one substituent is terminating in a cationic group. The planar moiety is essential for stacking effectively onto a terminal G-quartet or intercalation into the targeted G4 structure [101, 132-134]. The cationic group such as diethylamine, pyrrolidine or piperidine can form an electrostatic interaction with the phosphate backbone of the G-quadruplex DNA. The groove and loop regions within G4 structures can also offer considerable potential for selective recognition [135]. Below shows some of the G-quadruplex ligands that inhibit telomerase via G-quadruplex formation. These agents belong to a category of chemical groups such as anthraquinones, cationic porphyrins as well as perylenes, etc, as shown in Figure 1.9.

- Anthraquinones: A series of 1,4-diamido anthracene-9,10-diones was found to inhibit telomerase activity via binding and stabilizing of telomeric G-quadruplex structures [135]. For example, BSU1051 (2,6-diamido anthraquinone analog) can bind and stabilize G4 structure via interaction with the intramolecular G4 structure formed by four repeats of telomeric DNA. It was found to inhibit telomerase in a cell-free system.
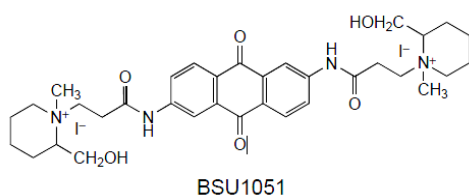
- Cationic porphyrins: Porphyrins have been interested in photodynamic cancer therapy because of their ability to accumulate more in tumor than normal tissue. Moreover, the porphyrin analog such as TMPyP4 can bind and stabilize with both parallel and antiparallel G4 structures [136, 137]. TMPyP4 inhibits telomerase by interacting with G4 DNA, but not its isomer TMPyP2. In addition, TMPyP4 inhibited cell growth in various cancer cell line [138, 139] and induced significant telomere shortening in osteosarcoma cell lines [139].

- **Perylenes:** Perylene derivatives are well studied as telomerase inhibitors. PM2 and PIPER were found to inhibit telomerase through the G-quadruplex formation at both

telomeric sequence and hTERT promoter. Moreover, PM1, PM2, and PIPER also induced G-quadruplex formation from the VEGF gene promoter sequence and resulted in the down-regulation of VEGF expression [15].

     - Another group: BRACO-19 (acridine derivative) appears to directly target telomeres, and it can interact with three grooves of G-quadruplexes in addition to stacking on the terminal G-quartet [140,141]. Treatment with BRACO19 in DU145 prostate cancer xenograft resulted in tumor regression within 7-10 days of the initiation [142]. BRACO19 can inhibit telomerase activity paralleled with telomere shortening in long-term treatment, resulting in cell growth arrest in numerous cancer cell lines [143-145]. Telomestatin is a natural compound isolated from *Streptomyces anulatus* 3533-SV4 [146]. The experiment revealed that telomestatin was 70 folds more preferential binding with intramolecular G-quadruplex structures than duplex DNA, and interacted preferentially with intramolecular versus intermolecular G-quadruplex structures [147]. Telomestatin induced dissociation of the TRF2 shelterin protein and downregulated telomerase expression in glioblastoma cancer stem cells [148]. Telomestatin treatment resulted in a decrease in telomerase activity, telomere shortening, growth inhibition, and eventually induced apoptosis both in *vitro* and in *vivo* studies [149, 150].
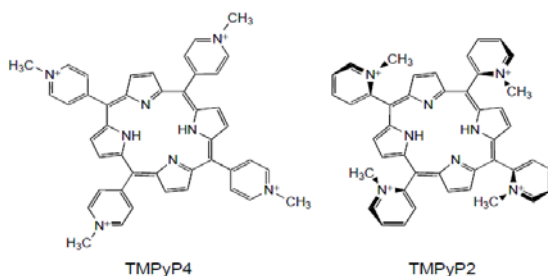
Anthraquinone

BSU1051

Perylenes

PIPER

Cationic porphyrins

TMPyP4
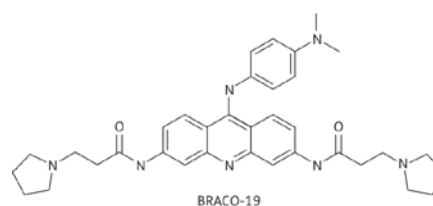
TMPyP2

Other groups

BRACO-19
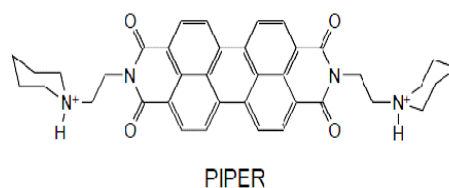
Figure 1.9: G-quadruplex interactive compounds

1.3.10 Prostate Cancer and Therapeutic problem

Prostate cancer is the second most commonly diagnosed cancer and remains the third leading cause of cancer-related mortality in men [151, 11]. The molecular events of prostate cancer progression include chronic inflammation, oxidative stress, oncogene overexpression, tumor suppressor mutation, and telomere shortening. Telomerase reactivation helps prostate cancer cells to escape replicative senescence and promotes cell proliferation [152], leading to metastasis and castration-resistant.

In addition, androgen receptor (AR) is important in the development, as well as the progression, of prostate cancer, because the activated AR has an important role in the proliferation of prostate cancer cells [153, 154]. The mechanisms of the development of prostate cancer are divided into two pathways; those are androgen-dependent and androgen-independent pathways [155].

The AR gene is regularly up-regulated during prostate cancer progression [156]. During androgen-independent progression this pathway involving AR-mediated the survival of prostate cancer including [155];

1. AR gene amplification: this amplification leads to an increase in the expression of the AR gene and enhanced activation by the low level of androgens.

2. AR gene mutation: these mutations increase the number of ligands that can activate the receptor. Normally AR binds and activated by androgens, but in these mutations, AR can bind with other steroids and antiandrogen as well.

3. Alteration in growth factor and cytokines for AR activation: these pathways involves the function and the expression of AR coactivators.

4. Bypass the AR pathway; For example: [157]

- Neuroendocrine cells secrete neuropeptide which can increase the proliferation of neighboring cancer cells, thus allowing the progression of prostate cancer cells.

- Deregulation of apoptosis genes: loss of tumor suppressor genes is the regular event occur in cancer including prostate cancer. The loss of PTEN expression leads to the PI3K/Akt activation and blocks apoptosis.

Most prostate cancers are androgen-dependent, meaning that they respond to androgen ablation therapy [155]. In localized prostate cancer, the treatment of choice is surgery and radiation. While the hormonal therapy using androgen deprivation therapy (ADT) is the mainstay of metastatic prostate cancer, the combination with chemotherapy appears to extend survival rate in prostate cancer patients. For such, abiraterone and enzalutamide was challenged commonly held beliefs in metastatic prostate cancer specifically, both are hormonal therapies that have shown activity in what has been termed castration resistant disease [158]. Abiraterone works through selective inhibition of CYP17 lyase. The mechanism of enzalutamide differs significantly from abiraterone. Specifically, enzalutamide is a potent antiandrogen that inhibits nuclear translocation of the androgen receptor [158]. However, most cancers often develop recurrence and resistant to this treatment and develop the so-called "castration-resistant prostate cancer" (CRPC). This form of prostate cancer is the leading cause of death in prostate cancer patients [159]. Thus, the new therapeutic approach to prostate cancer treatment is urgent to treat this form of cancer.

1.3.11 Telomerase in Prostate Cancer

In normal human prostate cells, AR represses hTERT expression via transrepression of AR binding to the hTERT promoter, in cooperation with the tumor suppressor p53, resulting in a decrease in telomerase activity [159]. Hence, the downregulated *hTERT* expression in the AR-positive cell lines might result from the reduced AR occupancy at the hTERT promoter [160]. By contrast, in the human prostate cancer cell line LNCaP, which has a point mutation in the AR gene, androgen promotes the transcription of hTERT [159, 161]. Furthermore, treatment with AR antagonist (bicalutamide or enzalutamide) resulted in telomere dysfunction in LNCaP (AR-positive) but not observed in PC-3 (AR-negative) cells [162].

During an early event in prostate cancer tumorigenesis, abnormally telomere shortening is detectable in prostate intraepithelial neoplasia (PIN), resulting in the chromosomal abnormality, the crucial feature in prostate cancer [163]. The telomere shortening apparently occurs before telomerase activation [164]. Moreover, the telomere length in PINs is found to be shorter than adjacent normal cells [163]. Malignant prostate cancer cells originate from a subset of transit amplifying cells (intermediate cells) in the

situation of sustained telomere shortening and chronic inflammation. These cells may be the subset of PIN cells in which telomerase is reactivated, resulting in the escape of the critical replicative senescence induction, following by the cellular immortalization. Ultimately, this leads to progression of prostate cancer [165, 166]. Therefore, telomerase activation is considered one critical step in prostate cancer progression, as displayed in Figure 1.10.

Another point of concern in cancer therapy is that cancer cells are resistant to conventional treatments (irradiation, chemotherapy) and become relapse, which is the leading cause of mortality in cancer patients. Most anticancer drugs target rapid proliferating cells. However, a small population of dormant cancer cells called tumor-initiating cells (TICs) or cancer stem cells is usually resistant to these drugs, leading to cancer relapse. Since most TICs have telomerase activity, telomerase inhibition might be a good way to prevent these cells from developing into prostate cancer cells.
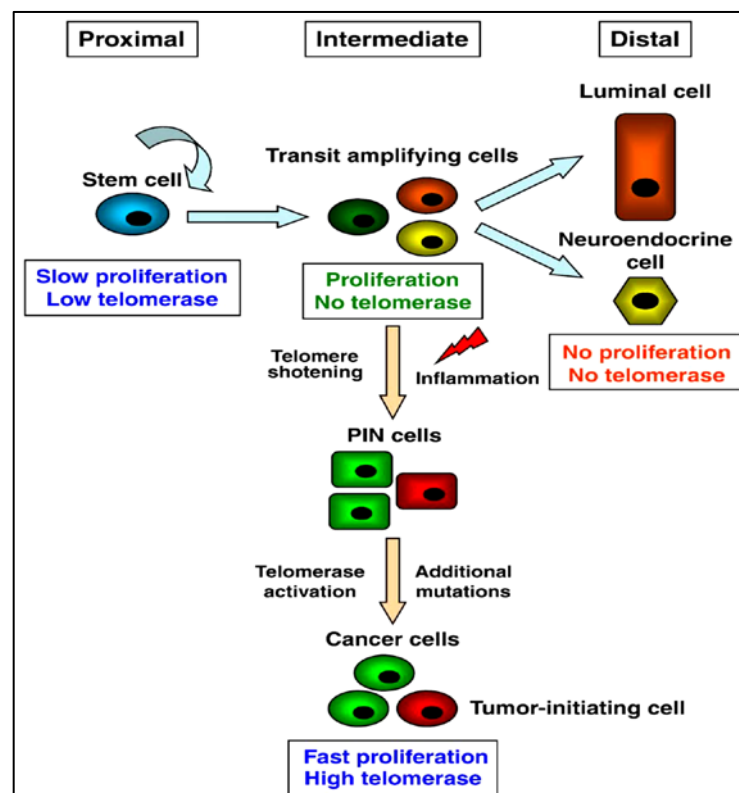
Figure 1.10: Telomere dysfunction and telomerase activation in prostate carcinogenesis

1.3.12 Prostate cancer and therapeutic strategies

As mentioned earlier, telomerase reactivation is a key process in prostate tumorigenesis. Telomerase reactivation might occur in two distinct events: (i) telomerase reactivation before senescence checkpoint and oncogenic transformation, and (ii) telomerase reactivation after crisis state, in which the cell eventually progresses into invasive carcinoma. In earlier activation of telomerase may have a role in prostate cancer chemoprevention by attenuating oncogenic transformation due to genetic instability caused by critical telomere shortening [168, 169]. According to the model presented in Figure 1.11, malignant prostate cancer cells originate from intermediate cells that lost key genome-protective mechanisms, including telomerase. These cells undergo telomere loss dictated by the end-replication problem and normally cease to divide at the senescence checkpoint. However, if the cells undergo oncogenic transformation before senescence, they can bypass the checkpoint and continue to proliferate. These cells may be the telomerase-negative prostatic intraepithelial neoplasia (PIN) [166], in absence of telomerase, attain secondary genetic changes owing to chromosome instability contributed in part by telomere shortening. Eventually, these cells activate telomerase and progress into invasive carcinoma. If telomerase activates before oncogenic transformation, genomes of these cells are protected from telomere shortening–induced genetic instability, and the resulting cells progress into less malignant tumors or premalignant lesions such as the telomerase-positive PIN specimens described

In the model of benign prostatic hyperplasia (BPH). BPH may derive directly from the stem cell pool that somehow inactivates telomerase expression, or may derive from telomerase-negative intermediate cells that are locked out of the normal differentiation pathway. In both cases, even in the absence of telomerase, BPH cells retained other genome-protective mechanisms [166], thus preventing further genetic alterations that could lead to oncogenic transformation. This knowledge is essential for the therapeutic approach of targeting telomerase in prostate cancer. The first approach is the prevention step by inhibiting telomerase reactivation before senescence checkpoint and oncogenic transformation, thus preventing further genomic abnormality and

oncogenic transformation. The second approach is telomerase-inhibition treatment in crisis stage, resulting in telomere shortening and cellular senescence, or cell death.
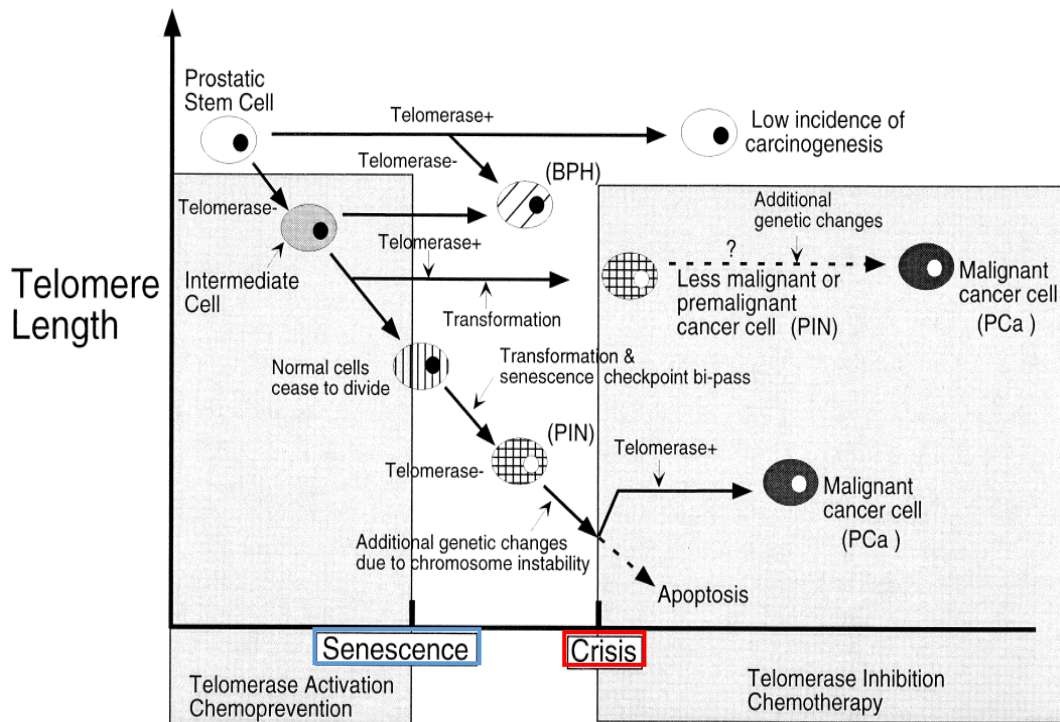

Figure 1.11: The therapeutic intervention base on targeting telomerase in prostate cancer

Treatment with a single telomerase inhibitor will take a long period of time to see the effect, depending on the initial telomere length and proliferating rate of the cancer cells. Whereas, conventional therapies (surgery, irradiation, chemotherapy) contribute to significantly decrease in tumor growth in relatively fast, but may not be effective in advance cancer due to the inherent resistance of TICs [171-173]. This is the essential reason for the combination treatment between conventional therapeutic approaches with telomerase inhibitors in prostate cancer therapy.

In the combination treatment, conventional approaches are initiated to target the burden tumor, after a duration of time telomerase inhibitor is given to culminate in telomere shortening in tumor cells and TICs to a critical level, resulting in apoptosis and death in TICs. Thus, there might be a good therapeutic approach that would contribute to cancer cell death without irreversibly impact with the normal cells and prevent cancer

cells resistant to treatment, and potentially lead to the great durable response as well [174].

1.3.13 Telomerase in lung cancer cells

In lung cancer telomere length diminishes throughout the multistep human lung carcinogenesis progression until a point when a stable short length is reached and telomerase is activated [177]. Telomere length is decreased in atypical adenomatous hyperplasias and bronchioalveolar carcinomas concomitant with positive expression of hTERT mRNA, indicating telomere dysfunction in the earliest phase of pulmonary carcinogenesis [178]. Several studies have been published on the expression of telomerase in preneoplastic lesions in lung cancer and in other tumors. In general, these reports show an increase in telomerase expression at the late dysplastic lesions. These immunocytochemical studies have been carried out by means of commercially available antibodies, the specificity of which has been recently challenged [177, 179]. Validation studies with new highly specific antibodies are needed to confirm the reported data on expression of telomerase and other related proteins.

Mechanisms for telomerase activation in lung cancer cells are not known yet. Comparative genomic hybridization studies in samples from early stages of NSCLC have shown that the genomic region that harbors hTERT gene, 5p15.33, is frequently amplified when compared with normal tissues [180]. Mutations in TERT or TERC that result in telomere shortening confer increase in susceptibility to adult-onset idiopathic pulmonary fibrosis [181]. However, none of these mutations have been associated to lung cancer. The expression of other telomere-associated proteins has been also reported as altered in lung cancer. Quantitative polymerase chain reaction studies showed that TRF1 expression is lower in NSCLC tissues when compared with the adjacent normal tissues [182].

Different compounds with telomerase activity inhibition properties have been studied in vitro and in animal models. Three of them, BIBR1532, GRN163, and GRN163L have been proven to have anticancer properties in several animal models [183]. Other small-molecule modulators of telomerase/ telomere biology, notably G-quadruplex ligands such as RHPS4, are in preclinical development [184]. GRN163L is the only one being tested in humans. Four trials with this oligonucleotide-based compound targeting the telomerase RNA template are in phase I for different cancer types. Specifically, study NCT00510445 was designed to determine the safety and the

maximum tolerated dose of GRN163L when administered in combination with a standard paclitaxel/carboplatin regimen to patients with advanced or metastatic NSCLC. This lung cancer trial is the first to study GRN163L in combination with standard chemotherapy. Recruitment for this study is due to be completed in December 2008 [185]. Cancer immunotherapies use selfantigens up-regulated in cancer cells, to overcome self-recognition by normal cells. Currently, there are some products which use synthetic TERT peptides to induce antigen-presenting cells to produce an immune response against cancer cells expressing TERT antigens. The most advanced ones are GV1001 and GRNVAC1. Trial NCT00509457 was designed to examine the safety and efficacy of GV1001 telomerase peptide vaccination in patients with NSCLC after having been treated with conventional therapy with radiotherapy and docetaxel as a radiosensitizer. The trial started in November 2006 and is still recruiting patients [185]. The vaccine Vx-001 using a hTERT cryptic peptide has completed a "proof of principle" Phase I/II clinical trial presented at ASCO 2008. Vx-001 has also obtained an orphan drug designation for NSCLC from EMEA [186].

The results of the mentioned clinical trials, and new trials designed to test new antitelomerase drugs need to be followed carefully as they may provide new avenues for isolated or combined targeted therapies for lung cancer. It could be of interest to see if there is a gene signature linked to the molecular status of telomere-related proteins that could predict the response to telomerase inhibitors. The question about the relevance of telomeres and telomerase pathway for lung cancer therapy will hopefully be solved in the very next future.

1.3.14 *Zingiber officinale Roscoe, Zingiberaceae*

Zingiber officinale Roscoe, or ginger, is one of the most natural dietary agents used for seasoning in foods and beverages. Ginger rhizome has been used in traditional medicine for relieving of various human illness, for instance, colds, fever, rheumatic disorders, motion sickness, gastrointestinal discomforts. Ginger rhizome contains numerous biologically active compounds such as gingerol, paradol, shogoal, and zingerone (Figure 1.12), which are pungent ingredients that have been shown to possess antioxidant anti-inflammatory, analgesic, anti-carcinogenic, anti-atherosclerotic anti-cancer properties [186, 187].
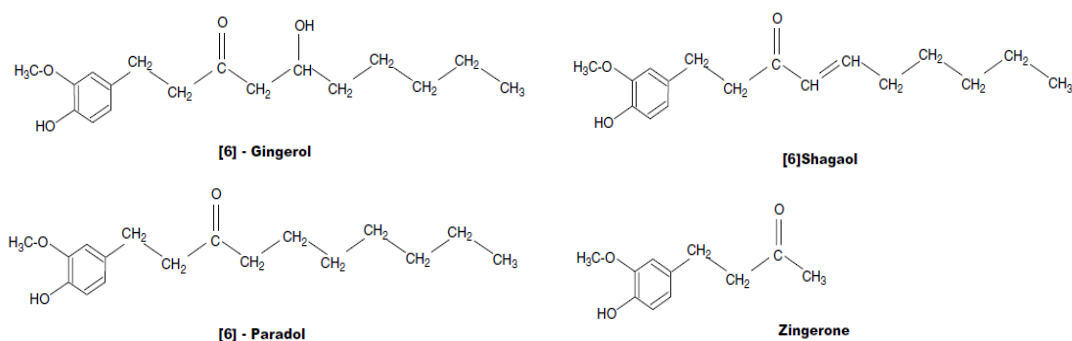
Figure 1.12: Non-volatile pungent components of ginger

Compounds in ginger have been found to suppress tumor progression. For examples, 6-Paradol inhibited tumor transformation induced by EGF in JB6 cells through apoptosis induction and inhibition of AP-1 transcription factor [188]. 6-Gingerol inhibited LPS-induced transformation cells in JB6 cells via nitric oxide synthase suppression [189]. 6-gingerol and 6-paradol inhibited tumor promotion in mouse skin promoted by TPA-induced ornithine decarboxylase [190, 191]. 6-Shogaol prevented 7,12-dimethylbenz[a]anthracene (DMBA) induced inflammation and cell proliferation in hamster buccal pouch mediated by inhibiting NF-κB and AP-1, the nuclear transcription factor translocation [192].

Previously, we reported that the crude extract of *Z. officinale* suppressed *hTERT* expression in A549 lung cancer cells, leading to the reduction of hTERT protein and telomerase activity [17]. However, we wonder whether this telomerase suppression by ginger extract would lead to telomere shortening and cellular senescence using a subcytotoxic dose. This will have an application in cancer treatment and cancer prevention.

REFERENCES

1. Shay JW, Wright WE. Role of telomeres and telomerase in cancer. *Semin Cancer Biol.* 2011; 21(6): 349-53.
2. Artandi SE, DePinho RA. Telomeres and telomerase in cancer. *Carcinogenesis.* 2010; 31: 9-18.
3. Hahn WC, Stewart SA, Brooks MW, York SG, et al. Inhibition of telomerase limits the growth of human cancer cells. *Nat Med.* 1999; 5: 1164-70.
4. Gao L, Schwartzman J, Gibbs A, Lisac R et al. Androgen receptor promotes ligandindependent prostate cancer progression through c-Myc upregulation. *PLoS One.* 2013; 8(5): e63563.
5. Kahn B, Collazo J, Kyprianou N. Androgen receptor as a driver of therapeutic resistance in advanced prostate cancer. *Int J Biol Sci.* 2014; 10: 588-95.
6. Glybochko PV, Zezerov EG, Glukhov AI, Alyaev YG, et al. Telomerase as a tumor marker in diagnosis of prostatic intraepithelial neoplasia and prostate cancer. *Prostate.* 2014; 74: 1043-51.
7. Serrano D, Bleau AM, Fernandez-Garcia I, Fernandez-Marcelo T et al. Inhibition of telomerase activity preferentially targets aldehyde dehydrogenase-positive cancer stem-like cells in lung cancer. *Mol Cancer.* 2011; 10: 96.
8. Frink RE, Peyton M, Schiller JH, Gazdar AF er al. Telomerase inhibitor imetelstat has preclinical activity across the spectrum of non-small cell lung cancer oncogene types in a telomere length dependent manner. *Oncotarget.* 2016; 7: 31639-51.
9. Chiappori AA, Kolevska T, Spigel DR, Hager S, Rarick M, Gadgeel S, Blais N, Von Pawel J, Hart L, Reck M, Bassett E, Burington B and Schiller JH. A randomized phase II study of the telomerase inhibitor imetelstat as maintenance therapy for advanced non-small-cell lung cancer. *Annals of oncology.* 2015; 26: 354-362.
10. Taka T, Huang L, Wongnoppavich A, Tam-Chang SW et al. Telomere shortening and cell senescence induced by perylene derivatives in A549 human lung cancer cells. *Bioorg Med Chem.* 2013; 21(4): 883-90.
11. Taka T, Joonlasak K, Huang L, Randall Lee T et al. Down-regulation of the human VEGF gene expression by perylene monoimide derivatives. *Bioorg Med Chem Lett.* 2012; 22(1): 518-22.
12. Alibakhshi, A.; Ranjbari, J.; Pilehvar-Soltanahmadi, Y.; Nasiri, M.; Mollazade, M.; Zarghami, N. An update on phytochemicals in molecular target therapy of cancer: Potential inhibitory effect on telomerase activity. *Curr. Med. Chem.* 2016, *23*, 2380-2393.
13. Tuntiwechapikul, W.; Taka, T.; Songsomboon, C.; Kaewtunjai, N.; Imsumran, A.; Makonkawkeyoon, L.; Pompimon, W.; Lee, TR. Ginger extract inhibits human telomerase reverse transcriptase and c-Myc expression in A549 lung cancer cells. *J. Med. Food.* 2010; 13(6): 1347-1354.
14. Blasco MA. Telomeres and human disease: ageing, cancer and beyond. *Nat Rev Genet.* 2005; 6(8):611-22.

15. Blackburn EH. Telomeres and telomerase: the means to the end (Nobel lecture). *Angew Chem Int Ed Engl*. 2010; 49(41): 7405-21.

16. de Lange T. Protection of mammalian telomeres. *Oncogene*. 2002; 21(4): 532-40.

17. de Lange T. Shelterin: the protein complex that shapes and safeguards human telomeres. *Genes Dev*. 2005; 19(18): 2100-10.

18. Liu D, O'Connor MS, Qin J, Songyang Z. Telosome, a mammalian telomere-associated complex formed by multiple telomeric proteins. *Biol Chem*. 2004; 279(49): 51338-42.

19. d'Adda di Fagagna F, Reaper PM, Clay-Farrace L, Fiegler H et al. A DNA damage checkpoint response in telomere-initiated senescence. *Nature*. 2003; 426(6963): 194-8.

20. Blasco MA. Telomere length, stem cells and aging. *Nat Chem Biol*. 2007; 3(10): 640-9.

21. Blasco MA. Telomeres and human disease: ageing, cancer and beyond. *Nat Rev Genet*. 2005; 6(8): 611-22.

22. Griffith JD, Comeau L, Rosenfield S, Stansel RM et al. Mammalian telomeres end in a large duplex loop. *Cell*. 1999; 97(4): 503-14.

23. Deng Y, Chan SS, Chang S. Telomere dysfunction and tumour suppression: the senescence connection. *Nat Rev Cancer*. 2008; 8(6): 450-8.

24. Granger M P, Wright W E, Shay J W. Telomerase in cancer and aging. Critical Reviews in Oncology/Hematology. 2002; 41:29–40.

25. Olovnikov AM. A theory of marginotomy. The incomplete copying of template margin in enzymic synthesis of polynucleotides and biological significance of the phenomenon. *J Theor Biol*. 1973; 41(1): 181-90

26. Watson JD. Origin of concatemeric T7 DNA. *Nat New Biol*. 1972; 239(94): 197-201.

27. Jayakrishnan (JK) Nandakumar. Chromosome end protection [internet]. 2018 October. [Cited 2018 October 10]. Available from: https://sites.lsa.umich.edu/nandakumar-lab/research/.

28. Shay JW, Wright WE. Telomeres in dyskeratosis congenita. *Nat Genet*. 2004; 36(5): 437-8.

29. Wright WE, Pereira-Smith OM, Shay JW. Reversible cellular senescence: implications for immortalization of normal human diploid fibroblasts. *Mol Cell Biol*. 1989; 9(7): 3088-92.

30. Zou, Y., Sfeir, A., Shay, J. W. & Wright, W. E. Does a sentinel or groups of short telomeres determine replicative senescence? *Mol. Biol. Cell.* 2004: 15: 3709–3718.

31. Shay JW. Aging and cancer: are telomeres and telomerase the connection?. *Mol Med Today*. 1995; 1(8): 378-84.

32. Hayflica L, Moorhead PS. The serial cultivation of human diploid cell strains. *Exp Cell Res*. 1961; 25: 585-621.

33. Dimri GP, Lee X, Basile G, Acosta M, Scott G et al. Abiomarker that identifies senescent human cells in culture and in aging skin in vivo. *Proc Natl Acad Sci U S A*. 1995; 92(20): 9363-7.

34. Collado M, Blasco MA, Serrano M. Cellular senescence in cancer and aging. *Cell*. 2007; 130(2): 223-33.

35. De Lange T. Telomere-related genome instability in cancer. *Cold Spring Harb Symp Quant Biol*. 2005; 70: 197-204

36. d'Adda di Fagagna F, Reaper PM, Clay-Farrace L, Fiegler H et al. A DNA damage checkpoint response in telomere-initiated senescence. *Nature*. 2003; 426(6963):194-8.

37. Gil J, Peters G. Regulation of the INK4b-ARF-INK4a tumour suppressor locus: all for one or one for all. *Nat Rev Mol Cell Biol*. 2006; 7(9): 667-77.

38. Kim WY, Sharpless NE. The regulation of INK4/ARF in cancer and aging. *Cell*. 2006; 127(2): 265-75.

39. Krishnamurthy J, Torrice C, Ramsey MR, Kovalev GI et al. Ink4a/Arf expression is a biomarker of aging. *J Clin Invest*. 2004; 114(9): 1299-307.

40. Ramirez RD, Morales CP, Herbert BS, Rohde JM et al. Putative telomere-independent mechanisms of replicative aging reflect inadequate growth conditions. *Genes Dev*. 2001; 15(4): 398-403.

41. Woo RA, Poon RY. Activated oncogenes promote and cooperate with chromosomal instability for neoplastic transformation. *Genes Dev*. 2004; 18(11): 1317-30.

42. Iwasa H, Han J, Ishikawa F. Mitogen-activated protein kinase p38 defines the common senescence-signalling pathway. *Genes Cells*. 2003; 8(2): 131-44.

43. Ohtani N, Zebedee Z, Huot TJ, Stinson JA et al. Opposing effects of Ets and Id proteins on p16INK4a expression during cellular senescence. *Nature*. 2001; 409(6823): 1067-70.

44. Krishnamurthy J, Torrice C, Ramsey MR, Kovalev GI et al. Ink4a/Arf expression is a biomarker of aging. *J Clin Invest*. 2004; 114(9): 1299-307.

45. Ressler S, Bartkova J, Niederegger H, Bartek J et al. p16INK4A is a robust *in vivo* biomarker of cellular aging in human skin. *Aging Cell*. 2006; 5(5): 379-89.

46. Vijg J. Somatic mutations and aging: a re-evaluation. *Mutat Res*. 2000; 447(1): 117-35.

47. Hamilton ML, Van Remmen H, Drake JA, Yang H *et al*. Does oxidative damage to DNA increase with age?. *Proc Natl Acad Sci U S A*. 2001; 98(18): 10469-74.

48. Rehen SK, Yung YC, McCreight MP, Kaushal D et al. Constitutional aneuploidy in the normal human brain. *J Neurosci*. 2005; 25(9): 2176-80.

49. Weaver BA, Silk AD, Montagna C, Verdier-Pinard P, Cleveland DW. Aneuploidy acts both oncogenically and as a tumor suppressor. *Cancer Cell*. 2007; 11(1): 25-36.

50. Sedelnikova OA, Horikawa I, Zimonjic DB, Popescu NC et al. Senescing human cells and ageing mice accumulate DNA lesions with unrepairable double-strand breaks. *Nat Cell Biol*. 2004; 6(2): 168-70.

51. Lombard DB, Chua KF, Mostoslavsky R, Franco S et al. DNA repair, genome stability, and aging. *Cell*. 2005; 120(4): 497-512.

52. Schmitt CA. Cellular senescence and cancer treatment. *Biochim Biophys Acta*. 2007; 1775(1):5-20.

53. Feng J, Funk WD, Wang SS, Weinrich SL et ytga ET et al. The RNA component of human telomerase. *Science*. 1995; 269(5228): 1236-41.

54. Autexier C, Lue NF. The structure and function of telomerase reverse transcriptase. *Annu Rev Biochem*. 2006; 75: 493-517.

55. Cohen SB, Graham ME, Lovrecz GO, Bache N et al. Protein composition of catalytically active human telomerase from immortal cells. *Science*. 2007; 315(5820): 1850-3.

56. Cech, T. R., Nakamura, T. M. & Lingner, J. Telomerase is a true reverse transcriptase. A review, *Biochemistry (Mosc)*. 1997; 62: 1202-5.

57. Meyerson M, Counter CM, Eaton EN, Ellisen LW et al. hEST2, the putative human telomerase catalytic subunit gene, is up-regulated in tumor cells and during immortalization. *Cell*. 1997; 90: 785-95.

58. Nakamura TM, Morin GB, Chapman KB, Weinrich SL et al. Telomerase catalytic subunit homologs from fission yeast and human. *Science*. 1997; 277(5328): 955-9

59. Kilian A, Bowtell DD, Abud HE, Hime GR et al. Isolation of a candidate human telomerase catalytic subunit gene, which reveals complex splicing patterns in different cell types. *Hum Mol Genet*. 1997; 6(12): 2011-9.

60. Wick M, Zubov D, Hagen G. Genomic organization and promoter characterization of the gene encoding the human telomerase reverse transcriptase (hTERT). Gene. 1999; 232(1): 97-106.

61. Feng J, Funk WD, Wang SS, Weinrich SL et al. The RNA component of human telomerase. *Science*. 1995; 269(5228): 1236-41.

62. Soder AI, Hoare SF, Muire S, Balmain A et al. Mapping of the gene for the mouse telomerase RNA component, Terc, to chromosome 3 by fluorescence in situ hybridization and mouse chromosome painting. *Genomics*. 1997; 41(2): 293-4.

63. Yi X, Tesmer VM, Savre-Train I et al. Both transcriptional and posttranscriptional mechanisms regulate human telomerase template RNA levels. *Mol Cell Biol*. 1999; 19(6): 3989-97.

64. Pogacić V, Dragon F, Filipowicz W. Human H/ACA small nucleolar RNPs and telomerase share evolutionarily conserved proteins NHP2 and NOP10. *Mol Cell Biol*. 2000; 20(23): 9028-40.

65. Kim JH, Park SM, Kang MR et al. Ubiquitin ligase MKRN1 modulates telomere length homeostasis through a proteolysis of hTERT. Genes Dev.2005 Apr 1;19(7):776-81.

66. Shay JW, Wright WE. Telomerase therapeutics for cancer: challenges and new directions. *Nat Rev Drug Discov*. 2006; 5(7): 577-84.

67. Belair CD, Yeager TR, Lopez PM et al. Telomerase activity: a biomarker of cell proliferation, not malignant transformation. *Proc Natl Acad Sci U S A*. 1997; 94(25): 13677-82.

68. Lee HW, Blasco MA, Gottlieb GJ et al. Essential role of mouse telomerase in highly proliferative organs. *Nature*. 1998; 392(6676): 569-74.

69. Martín-Rivera L, Herrera E, Albar JP et al. Expression of mouse telomerase catalytic subunit in embryos and adult tissues. *Proc Natl Acad Sci U S A*. 1998; 95(18): 10471-6.

70. Ulaner GA, Hu JF, Vu TH et al. Telomerase activity in human development is regulated by human telomerase reverse transcriptase (hTERT) transcription and by alternate splicing of hTERT transcripts. *Cancer Res*. 1998; 58(18): 4168-72.

71. Yi X, Tesmer VM, Savre-Train I et al. Both transcriptional and posttranscriptional mechanisms regulate human telomerase template RNA levels. *Mol Cell Biol*. 1999; 19(6): 3989-97.

72. Soder AI Going JJ, Kaye SB et al. Tumour specific regulation of telomerase RNA gene expression visualized by in situ hybridization. *Oncogene*. 1998; 16(8): 979-83.

73. Horikawa I, Cable PL, Afshari C et al. Cloning and characterization of the promoter region of human telomerase reverse transcriptasegene. *Cancer Res*. 1999; 59(4): 826-30.

74. Takakura M, Kyo S, Kanaya T et al. Cloning of human telomerase catalytic subunit (hTERT) gene promoter and identification of proximal core promoter sequences essential for transcriptional activation in immortalized and cancer cells. *Cancer Res*. 1999; 59(3): 551-7.

75. Cong YS, Wright WE, Shay JW. Human telomerase and its regulation. *Microbiol Mol Biol Rev*. 2002; 66(3): 407-25.

76. Pendino F, Tarkanyi I, Dudognon C et al. Telomeres and telomerase: Pharmacological targets for new anticancer strategies? *Curr Cancer Drug Targets*. 2006; 6(2): 147-80.

77. Devereux TR, Horikawa I, Anna CH et al. DNA methylation analysis of the promoter region of the human telomerase reverse transcriptase (hTERT) gene. Cancer Res. 1999; 59(24): 6087-90.

78. Dessain SK, Yu H, Reddel RR et al. Methylation of the human telomerase gene CpG island. Cancer Res. 2000; 60(3): 537-41.

79. Grandjenette C, Schnekenburger M, Karius T et al. 5-aza-2'-deoxycytidine-mediated c-myc Down-regulation triggers telomere-dependent senescence by regulating human telomerase reverse transcriptase in chronic myeloid leukemia. *Neoplasia*. 2014; 16(6): 511-28

80. Liu C, Xu D. Inhibition of histone deacetylases. *Methods Mol Biol*. 2004; 287: 87-97.

81. Cong YS, Bacchetti S. Histone deacetylation is involved in the transcriptional repression of hTERT in normal human cells. *J Biol Chem*. 2000; 275(46): 35665-8.

82. Hou M, Wang X, Popov N et al. The histone deacetylase inhibitor trichostatin A derepresses the telomerase reverse transcriptase (hTERT) gene in human cells. *Exp Cell Res*. 2002; 274(1): 25-34.

83. Hisatomi H, Ohyashiki K, Ohyashiki JH et al. Expression profile of a gamma-deletion variant of the human telomerase reverse transcriptasegene. Neoplasia. 2003; 5(3): 193-7.

84. Holt SE, Aisner DL, Baur J et al. Functional requirement of p23 and Hsp90 in telomerase complexes. Genes Dev. 1999; 13(7): 817-26.

85. Hahn WC, Counter CM, Lundberg AS et al. Creation of human tumour cells with defined genetic elements. Nature. 1999; 400(6743): 464-8.

86. Allen ND, Baird DM. Telomere length maintenance in stem cell populations. *Biochim Biophys Acta*. 2009; 1792(4): 324-8.

87. Rousseau P, Autexier C. Telomere biology: Rationale for diagnostics and therapeutics in cancer. *RNA Biol*. 2015; 12(10): 1078-82.

88. Ginelle C.Gellert , Shalmica R.Jackson Z, GunnurDikmen, Woodring E.Wright et al. Telomerase as a therapeutic target in cancer. *Drug Discovery Today: Disease Mechanisms*. 2005; 2(2): 159-164

89. Zimmermann S, Martens UM. Telomeres and telomerase as targets for cancer therapy. *Cell Mol Life Sci*. 2007; 64(7-8): 906-21.

90. Han H, Hurley LH. G-quadruplex DNA: a potential target for anti-cancer drug design. *Trends Pharmacol Sci*. 2000; 21(4): 136-42.

91. Xu T, He K, Wang L, Goldkorn A. Prostate tumor cells with cancer progenitor properties have high telomerase activity and are rapidly killed by telomerase interference. *Prostate*. 2011; 71: 1390-400.

92. Williamson JR, Raghuraman MK, Cech TR. Monovalent cation-induced structure of telomeric DNA: the G-quartet model. Cell. 1989; 59(5): 871-80.

93. Bochman ML, Paeschke K, Zakian VA. DNA secondary structures: stability and function of G-quadruplex structures. *Nat Rev Genet*. 2012; 13(11): 770-80.

94. Balasubramanian S, Neidle S. G-quadruplex nucleic acids as therapeutic targets. *Curr Opin Chem Biol*. 2009; 13(3): 345-53.

95. Du Y, Zhou X. Targeting non-B-form DNA in living cells. *Chem Rec*. 2013; 13(4): 371-84.

96. Sandell LL, Zakian VA. Loss of a yeast telomere: arrest, recovery, and chromosome loss. *Cell*. 1993; 75(4): 729-39.

97. Sundquist WI, Klug A. Telomeric DNA dimerizes by formation of guanine tetrads between hairpin loops. *Nature*. 1989; 342(6251): 825-9.

98. Bryan TM, Baumann P. G-quadruplexes: from guanine gels to chemotherapeutics. *Mol Biotechnol*. 2011; 49(2): 198-208.

99. Huppert JL, Balasubramanian S. G-quadruplexes in promoters throughout the human genome. *Nucleic Acids Res*. 2007; 35(2): 406-13.

100. Eddy J, Maizels N. Gene function correlates with potential for G4 DNA formation in the human genome. *Nucleic Acids Res*. 2006; 34(14): 3887-96.

101. Eddy J, Maizels N. Gene function correlates with potential for G4 DNA formation in the human genome. *Nucleic Acids Res*. 2006; 34(14): 3887-96.

102. Qin Y, Hurley LH. Structures, folding patterns, and functions of intramolecular DNA G-quadruplexes found in eukaryotic promoter regions. *Biochimie*. 2008; 90(8):1149-71.

103. Simonsson T, Pecinka P, Kubista M. DNA tetraplex formation in the control region of c-myc. *Nucleic Acids Res*. 1998; 26(5): 1167-72.

104. Sun D, Guo K, Rusche JJ, Hurley LH. Facilitation of a structural transition in the polypurine/polypyrimidine tract within the proximal promoter region of the human VEGF gene by the presence of potassium and G-quadruplex-interactive agents. *Nucleic Acids Res*. 2005; 33(18):6070-80.

105. De Armond R, Wood S, Sun D, Hurley LH, Ebbinghaus SW. Evidence for the presence of a guanine quadruplex forming region within a polypurine tract of the hypoxia inducible factor 1alpha promoter. *Biochemistry*. 2005; 44(49): 16341-50.

106. Guo K, Pourpak A,Beetz-Rogers K, Gokhale V et al. Formation of pseudosymmetrical G-quadruplex and i-motif structures in the proximal promoter region of the RET oncogene. *J Am Chem Soc*.2007; 129(33): 10220-8.

107. Cogoi S, Xodo LE. G-quadruplex formation within the promoter of the KRAS proto-oncogene and its effect on transcription. *Nucleic Acids Res*. 2006; 34(9): 2536-49.

108. Dai J, Chen D, Jones RA, Hurley LH, Yang D. NMR solution structure of the major G-quadruplex structure formed in the human BCL2 promoter region. *Nucleic Acids Res*. 2006; 34(18): 5133-44.

109. Qin Y, Rezler EM, Gokhale V, Sun D, Hurley LH. Characterization of the G-quadruplexes in the duplex nuclease hypersensitive element of the PDGF-A promoter and modulation of PDGF-A promoter activity by TMPyP4. *Nucleic Acids Res*. 2007; 35(22): 7698-713.

110. Siddiqui-Jain A, Grand CL, Bearss DJ, Hurley LH. Direct evidence for a G-quadruplex in a promoter region and its targeting with a small molecule to repress c-MYC transcription. *Proc Natl Acad Sci U S A*. 2002; 99(18): 11593-8

111. Hurley LH, Von Hoff DD, Siddiqui-Jain A, Yang D. Drug targeting of the c-MYC promoter to repress gene expression via a G-quadruplex silencer element. *Semin Oncol*. 2006; 33(4): 498-512.

112. Yang D, Hurley LH. Structure of the biologically relevant G-quadruplex in the c-MYC promoter. *Nucleosides Nucleotides Nucleic Acids*. 2006; 25(8): 951-68.

113. Seenisamy J, Rezler EM, Powell TJ, Tye D et al. The dynamic character of the G-quadruplex element in the c-MYC promoter and modification by TMPyP4. *J Am Chem Soc*. 2004; 126(28): 8702-9.

114. Dexheimer TS, Sun D, Hurley LH. Deconvoluting the structural and drug-recognition complexity of the G-quadruplex-formingregion upstream of the bcl-2 P1 promoter. *J Am Chem Soc*. 2006; 128(16): 5404-15.

115. Rankin S, Reszka AP, Huppert J, Zloh M et al. Putative DNA quadruplex formation within the human c-kit oncogene. *J Am Chem Soc*. 2005; 127(30): 10584-9.

116. Fernando H, Reszka AP, Huppert J, Ladame S et al. A conserved quadruplex motif located in a transcription activation site of the human c-kit oncogene. Biochemistry. *Biochemistry*. 2006; 45(25): 7854-60.

117. Phan AT, Kuryavyi V, Burge S, Neidle S, Patel DJ. Structure of an unprecedented G-quadruplex scaffold in the human c-kit promoter. *J Am Chem Soc*. 2007; 129(14): 4386-92.

118. Shirude PS, Okumus B, Ying L, Ha T, Balasubramanian S. Single-molecule conformational analysis of G-quadruplex formation in the promoter DNA duplex of the proto-oncogene c-kit. *J Am Chem Soc*. 2007; 129(24): 7484-5.

119. Todd AK, Haider SM, Parkinson GN, Neidle S.Sequence occurrence and structural uniqueness of a G-quadruplex in the human c-kit promoter. *Nucleic Acids Res*. 2007; 35(17): 5799-808.

120. Qin Y, Rezler EM, Gokhale V, Sun D, Hurley LH. Characterization of the G-quadruplexes in the duplex nuclease hypersensitive element of the PDGF-A promoter and modulation of PDGF-A promoter activity by TMPyP4. *Nucleic Acids Res*. 2007; 35(22): 7698-713.

121. Palumbo SL Memmott RM, Uribe DJ, Krotova-Khan Y et al. A novel G-quadruplex-forming GGA repeat region in the c-myb promoter is a critical regulator of promoter activity. *Nucleic Acids Res*. 2008; 36(6): 1755-69.

122. Eddy J, Maizels N. Gene function correlates with potential for G4 DNA formation in the human genome. *Nucleic Acids Res*. 2006; 34(14): 3887-96.

123. Brooks TA, Kendrick S, Hurley L. Making sense of G-quadruplex and i-motif functions in oncogene promoters. *FEBS J*. 2010; 277: 3459-69.

124. Takakura M, Kyo S, Kanaya T, Hirano H et al. Cloning of human telomerase catalytic subunit (hTERT) gene promoter and identification of proximal core promoter sequences essential for transcriptional activation in immortalized and cancer cells. *Cancer Res*. 1999; 59(3): 551-7.

125. Palumbo SL, Ebbinghaus SW, Hurley LH. Formation of a unique end-to-end stacked pair of G-quadruplexes in the hTERT core promoter with implications for inhibition of telomerase by G-quadruplex-interactive ligands. *J Am Chem Soc*. 2009; 131(31): 10878-91.

126. Monchaud D, Teulade-Fichou MP. A hitchhiker's guide to G-quadruplex ligands. *Org Biomol Chem*. 2008; 6(4): 627-36.

127. De Cian A, Lacroix L, Douarre C, Temime-Smaali N et al. Targeting telomeres and telomerase. *Biochimie*. 2008; 90(1): 131-55.

128. Sun D, Thompson B, Cathers BE, Salazar M et al. Inhibition of human telomerase by a G-quadruplex-interactive compound. *J Med Chem*. 1997; 40(14): 2113-6.

129. Perry PJ, Gowan SM, Reszka AP, Polucci P et al. 1,4- and 2,6-disubstituted amidoanthracene-9,10-dione derivatives as inhibitors of human telomerase. *J Med Chem*. 1998; 41(17): 3253-60.

130. Anantha NV, Azam M, Sheardy RD. Porphyrin binding to quadrupled T4G4. *Biochemistry*. 1998; 37(9): 2709-14.

131. Shi DF, Wheelhouse RT, Sun D, Hurley LH. Quadruplex-interactive agents as telomerase inhibitors: synthesis of porphyrins and structure-activity relationship for the inhibition of telomerase. *J Med Chem*. 2001; 44(26): 4509-23.

132. Izbicka E, Wheelhouse RT, Raymond E, Davidson KK et al. Effects of cationic porphyrins as G-quadruplex interactive agents in human tumor cells. *Cancer Res*. 1999; 59(3): 639-44.

133. Fujimori J, Matsuo T, Shimose S, Kubo T et al. Antitumor effects of telomerase inhibitor TMPyP4 in osteosarcoma cell lines. *J Orthop Res*. 2011; 29(11):1707-11.

134. Read M, Cuesta J, Basra I, et al. Rational design approaches to increase the potency of G-quadruplex mediated telomerase inhibitors. *Clin Cancer Res*. 2001; 7(11): 3797S–3797S.

135. Read M, Harrison RJ, Romagnoli B, Tanious FA et al. Structure-based design of selective and potent G quadruplex-mediated telomerase inhibitors. *Proc Natl Acad Sci U S A*. 2001;98(9): 4844-9

136. Kelland LR. Overcoming the immortality of tumour cells by telomere and telomerase based cancer therapeutics—current status and future prospects. *Eur J Cancer* .2005; 41(7): 971-9.

137. Zhou G, Liu X, Li Y, Xu S et al. Telomere targeting with a novel G-quadruplex-interactive ligand BRACO-19 induces T loop disassembly and telomerase displacement in human glioblastoma cells. *Oncotarget*. 2016; 7(12): 14925-39.

138. Gunaratnam M, Greciano O, Martins C, Reszka AP et al. Mechanism of acridine-based telomerase inhibition and telomere shortening. *Biochem Pharmacol*. 2007; 74(5): 679-89.

139. Burger AM, Dai F, Schultes CM, Reszka AP et al. The G-quadruplex-interactive molecule BRACO-19 inhibits tumor growth, consistent with telomere targeting and interference with telomerase function. *Cancer Res*. 2005; 65(4): 1489-96.

140. Shin-ya K, Wierzba K, Matsuo K, Ohtani T et al. Telomestatin, a novel telomerase inhibitor from Streptomyces anulatus. *J Am Chem Soc*. 2001; 123(6): 1262-3.

141. Kim MY, Duan W, Gleason-Guzman M, Hurley LH. Design, synthesis, and biological evaluation of a series of fluoroquinoanthroxazines with contrasting dual mechanisms of action against topoisomerase II and G-quadruplexes. *J Med Chem*. 2003; 46(4): 571-83.

142. Hasegawa D, Okabe S, Okamoto K, Nakano I et al. G-quadruplex ligand-induced DNA damage response coupled with telomere dysfunction and replication stress in glioma stem cells. *Biochem Biophys Res Commun*. 2016; 471(1): 75-81.

143. Tauchi T, Shin-ya K, Sashida G, Sumi M et al. Telomerase inhibition with a novel G-quadruplex-interactive agent, telomestatin: in vitro and in vivo studies in acute leukemia. *Oncogene*. 2006; 25(42): 5719-25.

144. Long S, Argyle DJ, Gault EA, Nasir L. Inhibition of telomerase in canine cancer cells following telomestatin treatment. *Vet Comp Oncol*. 2007; 5(2): 99-107.

145. Jemal A, Siegel R, Ward E, Hao Y, et al. Cancer statistics, 2008. *CA Cancer J Clin*. 2008; 58(2): 71-96.

146. Shen MM, Abate-Shen C. Molecular genetics of prostate cancer: new prospects for old challenges. *Genes Dev*. 2010; 24(18): 1967-2000.

147. Balk SP, Knudsen KE. AR, the cell cycle, and prostate cancer. *Nucl Recept Signal*. 2008; 6: 1-12.

148. Dehm SM, Tindall DJ. Androgen receptor structural and functional elements: role and regulation in prostate cancer. *Mol Endocrinol*. 2007; 21(12): 2855-63.

149. Debes JD, Tindall DJ. Mechanisms of androgen-refractory prostate cancer. *N Engl J Med*. 2004; 351: 1488-90.

150. Chen CD, Welsbie DS, Tran C et al. Molecular determinants of resistance to antiandrogen therapy. *Nat Med*. 2004; 10(1): 33-9.

151. Grossmann ME, Huang H, Tindall DJ. Androgen receptor signaling in androgen-refractory prostate cancer. *J Natl Cancer Inst*. 2001; 93(22): 1687-97.

152. Filson CP, Marks LS, Litwin MS. Expectant management for men with early stage prostate cancer. *CA Cancer J Clin*. 2015; 65(4): 265-82.

153. Moehren U, Papaioannou M, Reeb CA, Grasselli A. et al. Wild-type but not mutant androgen receptor inhibits expression of the hTERT telomerase subunit: a novel role of AR mutation for prostate cancer development. *FASEB J*. 2008; 22: 1258-67.

154. Graham MK, Meeker A. Telomeres and telomerase in prostate cancer development and therapy. *Nat Rev Urol*. 2017; 14: 607-619.

155. Guo C, Armbruster BN, Price DT, Counter CM et al. *In vivo* regulation of hTERT and telomerase activity by androgen. *J Urol*. 2003; 170: 615-8**.**

156. Kim SH, Richardson M, Chinnakannu K, Bai VU et al. Androgen receptor Interacts with telomeric proteins in prostate cancer cells. *J Biol Chem*. 2010; 285(14): 10472-6.

157. Meeker AK, Hicks JL, Platz EA, March GE et al. Telomere shortening is an early somatic DNA alteration in human prostate tumorigenesis. *Cancer Res*. 2002; 62(22): 6405-9.

158. Gurel B, Iwata T, Koh CM, Jenkins RB et al. Nuclear MYC protein overexpression isan early alteration in human prostate carcinogenesis. *Mod Pathol*. 2008; 21(9): 1156-67.

159. Meeker AK, Gage WR, Hicks JL, Simon I et al. Telomere length assessment in human archival tissues: combined telomere fluorescence in situ hybridization and immunostaining. *Am J Pathol*. 2002; 160(4): 1259-68.

160. Koeneman KS, Pan CX, Jin JK, Pyle JM 3rd et al. Telomerase activity, telomere length, and DNA ploidy in prostatic intraepithelial neoplasia (PIN). *J Urol*. 1998; 160(4): 1533-9.

161. Marian CO, Shay JW. Prostate tumor-initiating cells: a new target for telomerase inhibition therapy?. *Biochim Biophys Acta*. 2009; 1792(4): 289-96.

162. Kim NW, Hruszkewycz AM. Telomerase activity modulation in the prevention of prostate cancer. *Urology*. 2001; 57(4 Suppl 1): 148-53.

163. Bao S, Wu Q, McLendon RE, Hao Y et al. Glioma stem cells promote radioresistance by preferential activation of the DNA damage response. *Nature*. 2006; 444(7120): 756-60.

164. Liu G, Yuan X, Zeng Z, Tunici P et al. Analysis of gene expression and chemoresistance of CD133+ cancer stem cells in glioblastoma. *Mol Cancer*. 2006; 5: 67.

165. Kang MK, Kang SK. Tumorigenesis of chemotherapeutic drug-resistant cancer stem-like cells in brain glioma. *Stem Cells Dev*. 2007; 16(5): 837-47.

166. Zahler AM, Williamson JR, Cech TR, Prescott DM. Inhibition of telomerase by G-quartet DNA structures. *Nature*. 1991; 350(6320):718-20.

167. Lantuejoul S, Raynaud C, Salameire D, Gazzeri S et al. Telomere maintenance and DNA damage responses during lung carcinogenesis. *Clin Cancer Res*. 2010; 16: 2979-88.

168. Marian CO, Wright WE, Shay JW. The effects of telomerase inhibition on prostate tumor-initiating cells. *Int J Cancer*. 2010; 127(2): 321-31.

169. Shukla Y, Singh M. Cancer preventive properties of ginger: a brief review. *Food Chem Toxicol*. 2007; 45(5): 683-90.

170. Surh YJ, Park KK, Chun KS, Lee LJ et al. Anti-tumor-promoting activities of selected pungent phenolic substances present in ginger. *J Environ Pathol Toxicol Oncol.* 1999; 18(2): 131-9.

171. Bode AM, Ma WY, Surh YJ, Dong Z. Inhibition of epidermal growth factor-induced cell transformation and activator protein 1activation by [6]-gingerol. Cancer Res. 2001; 61(3): 850-3.

172. Ippoushi K, Azuma K, Ito H, Horie H, Higashio H. [6]-Gingerol inhibits nitric oxide synthesis in activated J774.1 mouse macrophages and preventsperoxynitrite-induced oxidation and nitration reactions. *Life Sci*. 2003; 73(26): 3427-37.

173. Chung WY, Jung YJ, Surh YJ, Lee SS, Park KK. Antioxidative and antitumor promoting effects of [6]-paradol and its homologs. *Mutat Res*. 2001; 496(1-2):199-206.

174. Park KK, Chun KS, Lee JM, Lee SS, Surh YJ. Inhibitory effects of [6]-gingerol, a major pungent principle of ginger, on phorbol ester-induced inflammation, epidermal ornithine decarboxylase activity and skin tumor promotion in ICR mice. *Cancer Lett. 1998*; 129(2): 139-44.

175. Annamalai G, Suresh K. [6]-Shogaol attenuates inflammation, cell proliferation via modulate NF-κB and AP-1 oncogenic signaling in 7,12-dimethylbenz[a]anthracene induced oral carcinogenesis. *Biomed Pharmacother*. 2018; 98: 484-490.

176. Kundu JK, Na HK, Surh YJ. Ginger-derived phenolic substances with cancer preventive and therapeutic potential. *Forum Nutr*. 2009; 61: 182-92.

177. Tuntiwechapikul W, Taka T, Bethencourt M, Makonkawkeyoon L, Lee TR. The influence of pH on the G-quadruplex binding selectivity of perylene derivatives. *Bioorg Med Chem Lett*. 2006; 16: 4120-6.

178. Huang L, Tam-Chang SW. 9-Piperazine substituted perylene-3,4-dicarboximide as a fluorescent probe in ratiometric analysis. *Chem Commun*. 2011; 47: 2291-3.

179. Liang Xue, Nihar Ranjan, and Dev P. Arya. Synthesis and Spectroscopic Studies of the Aminoglycoside (Neomycin)-Perylene Conjugate Binding to Human Telomeric DNA. *Biochemistry*. 2011; 50: 2838-49.

180. Vichai V, Kirtikara K. Sulforhodamine B colorimetric assay for cytotoxicity screening. *Nat Proc*. 2006; 1: 1112-6.

181. Szatmari I, Aradi J. Telomeric repeat amplification, without shortening or lengthening of the telomerase products: a method to analyze the processivity of telomerase enzyme. Nucleic Acids Res. 2001; 29: E3.

182. Shawi M, Autexier C. Telomerase, senescence and ageing. *Mech Ageing Dev*. 2008; 129: 3-10.

183. A Simple Method Based on One Phase Measurement for Determination of the Octanol-Water Partition Coefficient of Drugs Partition coefficient *n*-octanol/water. *Chiang Mai J. Sci*. 2015; 42.

184. Wattanasin P, Saetear P, Wilairat P et al. Zone fluidics for measurement of Octanol/water partition coefficient of drugs. *Anal Chim Acta*. 2015; 860: 1-7.

185. Balasubramanian S, Hurley LH, Neidle S. Targeting G-quadruplexes in gene promoters: a novel anticancer strategy?. *Nat Rev Drug Discov*. 2011; 10: 261-75.

186. Mancini J, Rousseau P, Castor KJ, Sleiman HF, Autexier C. Platinum(II) Phenanthro-imidazole G-quadruplex ligand induces selective telomere shorteningin A549 cancer cells. *Biochimie*. 2016; 121: 287-97.

187. Solís-Calero C, Augusto TM, Carvalho HF. Human-specific features of the G-quadruplex in the androgen receptor gene promoter: A comparative structural and dynamics study. *J Steroid Biochem Mol Biol*. 2018; pii: S0960-0760: 30198.

188. Braig, M., Lee, S., et al. Oncogene-induced senescence as an initial barrier in lymphoma development. *Nature*. 2005: 436; 660–665.

189. Ohtani, N.; Mann, D. J.; Hara, E. Cellular senescence: Its role in tumor suppression and aging. *Cancer Sci.* 2009; 100: 792-797.

190. Hemann, M. T.; Strong, M. A.; Hao, L. Y.; Greider, C. W. The shortest telomere, not average telomere length, is critical for cell viability and chromosome stability. *Cell* 2001; 107: 67-77.

191. Kim NW, Piatyszek MA, Prowse KR, Harley CB et al. Specific association of human telomerase activity with immortal cells and cancer. *Science.* 1994, 266, 2011-2015.

192. Chen RC, Rumble RB, Loblaw DA, Finelli A. et al. Active surveillance for the management of localized prostate cancer (Cancer Care Ontario Guideline): American society of clinical oncology clinical practice guideline endorsement. *J. Clin. Oncol.* 2016; 34: 2182–2190.

CHAPTER 2

Telomerase Inhibition, Telomere Shortening, and Cellular Uptake of the Perylene Derivatives PM2 and PIPER in Prostate Cancer Cells

SUMMARY

Prostate cancer is the second most common cancer among men worldwide, and it is ranked first in the United States and Europe. Since prostate cancer is slow-growing, active surveillance for low-risk cancer has been increasingly supported by various guidelines. Most prostate cancers reactivate telomerase to circumvent the replicative senescence caused by the end replication problem; therefore, telomerase inhibition is potentially useful for the suppression of prostate cancer progression during this active surveillance or for the prevention of cancer recurrence after conventional therapies. In this study, we demonstrated that the perylene derivatives, PM2 and PIPER, could suppress *hTERT* expression and telomerase activity in the short-term treatment of LNCaP and PC3 prostate cancer cells. Long-term treatment with subcytotoxic doses of these compounds in both prostate cancer cells showed telomere shortening and a significant increase in senescent cells. Although the acute cytotoxicity of PM2 was about 30 times higher than that of PIPER in both prostate cancer cells, the cellular uptake of both compounds was comparable as determined by flow cytometry and fluorescent microscopy.

Keywords: prostate cancer; telomerase; telomere; perylene; cellular senescence

INTRODUCTION

Prostate cancer is the second most common cancer among men worldwide, and it is ranked first in the United States and Europe [1-3]. In Asia, the incidence of prostate cancer is relatively low, but there has been a rapid rise of prostate cancer incidence due to the introduction of prostate-specific antigen (PSA) testing [3]. Although the PSA-based screening was found to correlate with mortality reduction, it also coincided with high proportions of unnecessary biopsies, overdiagnosis, and overtreatment [3]. Compared with other types of cancers, prostate cancer grows relatively slowly and sometimes causes no problems for years [4,5]. Treatment with surgery or radiation is a standard local therapy, but about one-third of patients will develop biochemical recurrence [6], and many are living with urinary or sexual function problems afterward [7]. As a result, active surveillance is now recognized as a preferred strategy in patients with low-risk localized prostate cancer as an alternative to the immediate radical treatment [6,8]. For patients with metastatic prostate cancer, androgen deprivation therapy (ADT) is the standard of care. However, most patients progress to castration-resistant prostate cancer (CRPC) [6,9]. Considering the advanced age of most patients, the current chemotherapeutic drugs have done little to improve the survival rate of these CRPC patients [10]. Therefore, new targeted therapies with fewer side effects are urgently needed for the management of prostate cancer, both in the active surveillance state and in the metastatic CRPC. One such strategy, telomerase inhibition after conventional therapeutic approaches (surgery and chemotherapy/radiotherapy), was suggested to be an ideal strategy for prostate cancer therapy [11].

Progressive telomere shortening from cell division provides a barrier for cancer progression [12]. With each round of cell division, telomeric DNA is shortened by 50-200 base pairs due to the end replication problem [13]. The cells are allowed to replicate for a number of cell divisions until a few telomeres are shortened to a critical length, at which the shortening triggers an irreversible cell cycle arrest called replicative senescence [14]. Most cancer cells, including prostate cancers, reactivate telomerase to maintain their telomeres [3,15]. Human telomerase is a multi-subunit ribonucleoprotein complex in which the isolated catalytically active enzyme consists of two molecules each of human telomeric RNA (hTR), human telomerase reverse transcriptase (hTERT), and dyskerin [16]. Human telomerase uses its internal RNA as a template to catalyze the

addition of 6-base pairs repeats $(TTAGGG)_n$ to the 3' telomere ends, and thereby prevents the telomeres from becoming critically short [17]. Although hTR and hTERT are both essential components for telomerase activity and telomere maintenance, transcriptional regulation of *hTERT* is the predominant mechanism for controlling telomerase activity [18].

Among several strategies to inhibit telomerase, those based on G-quadruplex ligands are perhaps the most widely studied [19]. G-quadruplex ligands prevent the access of telomerase to the 3' telomeric ends by facilitating and/or stabilizing G-quadruplex formation of G-rich telomeric DNA [18]. They are also found to down-regulate *hTERT* expression by facilitating the formation of G-quadruplex at the *hTERT* promoter, preventing the transcriptional machinery from accessing its promoter [20]. In the same manner, G-quadruplex ligands have been shown to stabilize the G-quadruplex structure on the G-quadruplex motif from the promoters of several genes controlling cellular proliferation, such as *c-MYC*, *c-KIT*, *k-RAS*, and *VEGF*, among others, leading to the down-regulation of these genes and antiproliferative activity in cancer cell lines [21].

Previously, we reported that certain G-quadruplex ligands, specifically the perylene derivatives PM2 and PIPER shown in Figure 2.1, facilitated the G-quadruplex formation of the telomeric DNA sequence and the *hTERT* promoter DNA sequence, leading to the inhibition of telomerase activity and suppression of *hTERT* expression in A549 lung cancer cells, respectively [22]. The long-term treatment of A549 cells with a subcytotoxic dose of both perylene derivatives led to telomere shortening, decreased cell proliferation and tumorigenicity, and cellular senescence. However, the potential anticarcinogenic effects of these perylenes on prostate cancer cells has not been established. Therefore, in this study, we investigated the efficacy of PM2 and PIPER by examining their impact on the two most commonly studied prostate cancer cell lines, the androgen-dependent prostate cancer cell line LNCaP and the androgen-independent prostate cancer cell line PC3. Since PM2 and PIPER differ in their states of acute cytotoxicity, we also investigated their partition coefficients and cellular uptake in these two prostate cancer cell lines.
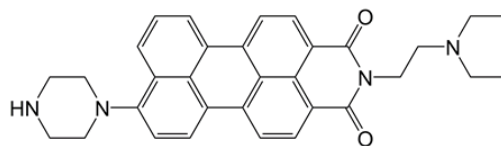
PM2
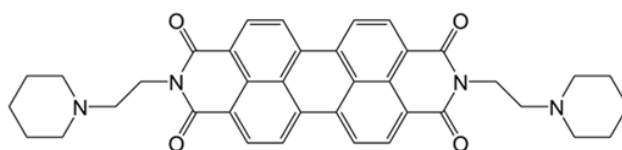
PIPER

Figure 2.1: Structure of PM2 and PIPER

MATERIALS AND METHODS

Chemicals and Reagents

Samples of PM2 and PIPER were synthesized using previously published protocols [23,24]. The characterization data for both compounds are consistent with the literature and are provided in the Supplementary Materials S1. All other chemicals were of molecular biology grade and purchased from commercial suppliers. All oligonucleotides and fluorescence-tagged oligonucleotides were purchased from Ward Medic (Thailand).

Cell Culture

Human prostate cancer cell lines LNCaP and PC3 were obtained from the American Type Culture Collection (Rockville, MD). The cells were cultured in Roswell Park Memorial Institute medium 1640 (RPMI 1640) with 10% fetal bovine serum (FBS) and 1% antibiotics (50 units/ml penicillin, 50 µg/ml streptomycin) at 37 ˚C in a humidified atmosphere of 5% CO_2 and 95% air. The peripheral blood mononuclear cells (PBMC) were collected from healthy volunteers and cultured in the same medium and conditions.

Cell Growth Inhibition Assay

The cell growth inhibition of the perylene derivatives was determined using the sulforhodamine B (SRB) assay according to the published protocol [25]. The indicated cancer cells (1.0×10^4 cells) or PBMC cells (1.0×10^5 cells) were incubated with various concentrations of either PM2 or PIPER at 37 ˚C for 72 h in a humidified incubator with 5% CO_2. The 50% growth inhibitory concentration (IC_{50}) was calculated from the dose-response relationship curve between the drug concentration and the percentage of cell viability using the software CurveExpert 1.4. The reported results represent the mean values of three independent experiments.

Semi-Quantitative RT-PCR Analysis

Prostate cancer cells (LNCaP or PC3, 5.0×10^5 cells) were grown on a 6-well tissue culture plate for 24 h before being treated with various concentrations of PM2 or PIPER for 24 h at 37 °C in a humidified CO_2 (5%) incubator. The total RNA was collected, and the mRNA was converted into cDNA using oligo-$(dT)_{18}$ primer and RevertAid reverse transcriptase (Thermo Scientific) according to the manufacturer's instructions. The cDNAs were then amplified by PCR using specific primers for each gene. Each PCR cycle was carefully chosen so that the intensity of the detected PCR product was proportional to the initial amount of cDNA in the reaction (see Supplementary Materials Figure S2.1). PCR products were then separated by agarose gel electrophoresis and visualized under UV light using Nucleic Acid Staining solution (RedSafe™, Intron Biotechnology). The primer sequences, annealing temperatures, and PCR cycles are summarized in the Supplementary Materials Table S2.1.

Modified Fluorescent Telomeric Repeat Amplification Protocol (TRAP) Assay

Prostate cancer cells (LNCaP or PC3, 5.0×10^5 cells) were grown on a 6-well tissue culture plate for 24 h before being treated with various concentrations of PM2 or PIPER for 48 h at 37 °C in a humidified CO_2 (5%) incubator. The cells were lysed with 50 μL of CHAPS lysis buffer [10 mM Tris-HCl (pH 7.5), 1 mM $MgCl_2$, 0.1 mM EGTA, 5 mM β-mercaptoethanol, 0.5 % CHAPS, 10% glycerol, protease inhibitor cocktail, and 200 units/mL RNase inhibitor] and centrifuged at 12,000 g for 10 min. The supernatant was collected and quantified for protein concentration by Bradford assay (BioRad). A 40 μg sample of protein from this supernatant served as a source of telomerase for the

TRAP assay. A modified fluorescent TRAP assay was performed according to a published protocol; this assay uses a specific primer to prevent the shortening and lengthening of the original telomerase products as normally seen from a standard TRAP assay [26]. Briefly, the 40 μg sample of crude telomerase from the cells treated with the test sample were incubated with 35 μL of telomerase reaction buffer [20 mM Tris HCl (pH 8.3), 1.5 mM MgCl$_2$, 63 mM KCl, 1 mM EGTA, 0.1 mg/mL bovine serum albumin, 0.005% Tween 20, 200 μM dNTPs, and 15 pmol MTS primer] at 30 °C for 30 min. The telomerase-extended products were then amplified by adding 15 μL of amplification reaction mixture (2.5 units Taq DNA polymerase, 15 pmol RP-FAM primer, 0.25 pmol RPc3g, 0.01 amol IC, and 7.5 pmol NT primer in 20 mM Tris-HCl, pH 8.3), and PCR was performed in a thermocycler with the following conditions: 3 cycles of (95 °C for 30 s; 58 °C for 60 s; and 72 °C for 90 s) and 28 cycles of (95 °C for 30 s; 65 °C for 30 s; and 72 °C for 30 s). The amplification products were separated by non-denaturing acrylamide gel electrophoresis and visualized with a phosphoimaging system (Typhoon; Molecular Dynamics). The oligonucleotides used in this assay are summarized in Supplementary Materials Table S2.2.

Long-Term Proliferation Assay

For the long-term proliferation assay, three sets of cell cultures were compared: the control group and the two experimental groups with the subcytotoxic doses of a test compound added to the culture media. The LNCaP cells (8×10^5 cells) or PC3 cells (2×10^5 cells) were first seeded onto a 75 cm^2 tissue culture flask in RPMI 1640 medium supplemented with 10% fetal bovine serum, with or without the indicated concentration of PM2 or PIPER. The culture media in each set was then changed after 3 days. After the cells reached confluence on Day 6, the cells were trypsinized and counted. The same number of cells for each prostate cancer were then subcultured onto a new 75 cm^2 tissue culture flask, and the process was repeated for up to 90 days. The remaining cells in each passage were collected and used for telomere length assay and senescence-associated β-galactosidase activity assay. The number of population doubling was calculated by the equation: $n = (\log P_n - \log P_0)/\log 2$, where P_n is the number of cells after n doublings and P_0 is the initial seeding density. The cumulative number of population doubling was then plotted against time.

Telomere Length Assay

The average telomere length of LNCaP and PC3 cells, collected at the indicated passages from the long-term proliferation assay, were assayed using the *TeloTAGGG* Telomere Length Assay kit (Roche Applied Science) according to the manufacturer's instructions. In brief, total DNA was isolated from the prostate cancer cells using DNAzol® (Invitrogen). Then, 8 µg of purified genomic DNA was digested by two restriction enzymes (*Hinf* I and *Rsa* I), before the digested DNA fragments were separated by 0.8% agarose gel electrophoresis and blotted onto a nylon membrane (Immobilon™-Ny$^+$, Millipore). The telomeric DNA fragments were then hybridized with a DIG-labeled telomeric probe, followed by DIG-specific antibody coupled with alkaline phosphatase, and visualized on X-ray film using a chemiluminescent system. The average telomere restriction fragment (TRF) length was calculated according to the formula $\sum(ODi)/\sum(ODi/Li)$, where ODi indicates the chemiluminescent signal at the position i, and Li is the molecular weight marker at the same position.

Senescence-Associated β-Galactosidase Activity Assay

LNCaP and PC3 cells (1×10^3 cells), collected at the indicated passages from the long-term proliferation assay, were seeded on glass cover slides and grown under 500 µL of culture media for 24 h. The cells were washed twice with PBS and fixed with 2% formaldehyde and 0.2% glutaraldehyde solution for 5 min at room temperature. The cells were then washed twice with PBS and incubated with the senescence-associated β-galactosidase (SA-β gal) solution (1 mg/ml X-gal, 40 mM citric acid/sodium phosphate (pH 6), 5 mM potassium ferrocyanide, 5 mM potassium ferricyanide, 150 mM NaCl, and 2 mM MgCl$_2$) for 24 h at 37 °C. The X-gal solution was removed, and the cells were rinsed once with PBS. The β-galactosidase positive cells were monitored under a phase contrast microscope with a blue stain, and were usually accompanied with cell morphological changes. The percentage of β-galactosidase positive cells was calculated and plotted against time.

Octanol/H$_2$O Partition Coefficient (P$_{ow}$) by Shake Flask Method

The general procedure of this experiment was based on OECD Test Guideline 107 [27]. The calculation of P$_{ow}$ was based on absorbance measurements of a single liquid phase previously described by Wattanasin *et al* [28]. Measurements of P$_{ow}$ for

PM2 and PIPER were performed using 1-octanol (Fluka, Switzerland) and 10 mM Tris buffer (pH 10) as solvents. Measurements of P_{ow} for caffeine and riboflavin as reference compounds were also performed using 1-octanol and 10 mM PBS buffer (pH 7.4) as solvents.

Cellular Uptake of PM2 and PIPER by Flow Cytometry

LNCaP and PC3 cells (5 x 10^5 cells) were seeded on 6 wells plate for 24 h before they were treated with the indicated concentrations of PM2 or PIPER for 24 h at 37 °C in a humidified 5% CO_2 incubator. The cells were then washed, and the trypsinized cells were collected by centrifuging at 500× g for 5 min. The cells were resuspended in 500 ml PBS before they were analyzed using CyAn ADP flow cytometer equipped with Kaluza, Flow Cytometry Analysis Software (Beckman Coulter, USA). The data were collected from 50,000 gated events with λ_{Ex} of 488 nm and λ_{Em} of 680 nm.

Fluorescence Microscopy

LNCaP or PC3 cells (1 x 10^5 cells) were seeded on a glass cover slide under 500 μL of culture media for 24 h. The cells were then washed twice with PBS and treated with 2 mL of the indicated concentration of a perylene derivative in culture media for 48 h before the cell nuclei were stained with 500 μL of 100 nM DAPI for 45 min. The excess dye was then washed before the intracellular localization of DAPI (using DAPI filter) and the perylene derivative (using a Red filter) were accessed using an Olympus AX70 fluorescence microscope.

Statistical Analysis

All values are given as mean ± standard derivation (Mean ± SD) from triplicate samples of three independent experiments. The Student *t*-test and two-way analysis of variance (ANOVA) with SPSS 11.5 software package were used to compare the treated and control cells. Differences are considered statistically significant when $p < 0.05$ or < 0.01.

RESULTS

Acute Cytotoxicity of PM2 and PIPER in Prostate Cancer Cell Lines and PBMC Cells

The sulforhodamine B (SRB) assay was employed to evaluate the acute cytotoxicity of PM2 and PIPER in prostate cancer cell lines (LNCaP and PC3) and peripheral blood mononuclear cells (PBMC). The prostate cancer cells and PBMC were incubated with various concentrations of either PM2 or PIPER for three days. The 50% growth inhibitory concentration (IC_{50}) was calculated from the dose-response relationship curve between the drug concentration and the percentage of cell viability using the software CurveExpert 1.4 (see Supplementary Materials Figure S2.2). The IC_{50} values for PM2 in LNCaP and PC3 cells were 3.0 ± 0.3 and 3.2 ± 1.0 μM, respectively, while the IC_{50} values for PIPER in LNCaP and PC3 were 89.6 ± 16.3 and 92.7 ± 8.5 μM, respectively. The cytotoxicity of PM2 and PIPER is similar to our published results in A549 lung cancer cells, in which the IC_{50} of PM2 and PIPER were 4.0 ± 0.1 μM and 52.4 ± 0.2 μM, respectively [29]. As indicated by these results, PM2 is much more toxic in cancer cells than PIPER. Both PM2 and PIPER appear to have little effect on peripheral blood mononuclear cells, in which the percentage of cell viability remained relatively constant in the presence of 0-160 μM of either PM2 or PIPER (see Figure S2.2C).

Suppression of *hTERT* Expression and Telomerase Activity by PM2 and PIPER in LNCaP and PC3 Prostate Cancer Cells

Previously, PM2 was found to be more effective than PIPER in terms of G-quadruplex formation, down-regulation of *hTERT* expression, and suppression of telomerase activity in A549 lung cancer cells [21]. To evaluate these abilities in LNCaP and PC3 prostate cancer cells, we employed the same semi-quantitative RT-PCR to assess mRNA gene expression and modified TRAP assay to assess telomerase activity. For the RT-PCR assay, the prostate cancer cells were incubated with 0-4 μM of PM2 or 0-20 μM of PIPER for 24 h before the total mRNAs were converted to cDNAs and amplified using gene-specific primers. As illustrated in Figure 2.2A, both PM2 and PIPER suppressed *hTERT* gene expression in a concentration-dependent manner in both LNCaP and PC3 cells, while the GAPDH housekeeping gene was not affected. For the TRAP assay, the

prostate cancer cells were incubated with 0-4 μM of PM2 or 0-20 μM of PIPER for 48 h before crude protein extract was used as the source of telomerase in the TRAP assay. As illustrated in Figure 2.2B, both PM2 and PIPER suppressed telomerase activity in a concentration-dependent manner in both LNCaP and PC3 cells. Telomerase activity was markedly reduced at the lowest concentration of PM2 and PIPER used, and PM2 appeared to suppress telomerase better than PIPER for both types of prostate cancer cells.
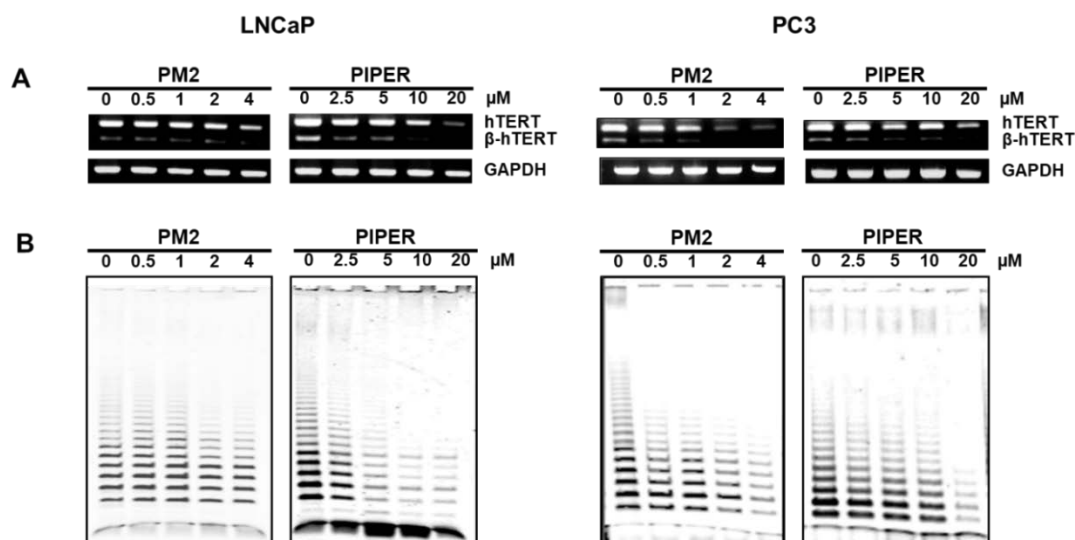
Figure 2.2: PM2 and PIPER suppressed *hTERT* expression and telomerase activity in LNCaP and PC3 prostate cancer cells. (A) To assay for gene expression, the indicated prostate cancer cells were incubated with the indicated concentrations of either PM2 or PIPER for 24 h before their RNAs were extracted and assayed by semiquantitative RT-PCR analysis. (B) To assay for telomerase activity, the cells were incubated with the indicated concentrations of either PM2 or PIPER for 48 h before the crude protein extract was used as the source of telomerase in a modified TRAP assay.

As mentioned above, G-quadruplex ligands have been found to facilitate G-quadruplex formation at the promoter sequences from several cancer-related genes. Our previous publications have also demonstrated that PM2 and PIPER induced G-quadruplex formation using short DNA sequences from the *hTERT* and *VEGF* promoters, and the expression of these genes in A549 lung cancer cells was suppressed.[21,28] In this study, the gene expressions of *hTERT*, *c-Myc*, and *VEGF* from both LNCaP and PC3 cells treated with either PM2 or PIPER were found to be down-regulated, while the gene expressions of other telomerase-related genes: *hTR*, *TRF1*, *TRF2*, and *hTEP1*, which have no G-quadruplex motif on their promoters, were not affected (see Supplementary Materials Figure S2.3). Therefore, the suppression of *hTERT* gene expression in these prostate cancer cells is likely due to the obstruction of

the transcription machinery by G-quadruplex formation at its promoter.

Effects of Long-Term Treatment with Subcytotoxic Doses of PM2 And PIPER in LNCaP and PC3 Cells

Most prostate cancer cells, including LNCaP and PC3 cells, maintain their telomere length by reactivating telomerase [30]. Therefore, treatment with a telomerase suppressor should allow these cancer cells to exhibit telomere shortening after successive rounds of cell division in the same manner as normal somatic cells, albeit faster due to the rapid cell division in cancer cells. When one or more telomeres are shortened to a critical length, the cell is triggered to enter an irreversible cell cycle arrest called cellular senescence [13]. Ideally, a specific telomerase inhibitor should cause telomere shortening in cancer cells without interfering with other cellular mechanisms, which might otherwise affect normal somatic cells and thereby cause side effects. Our previous study showed that PM2 and PIPER could directly inhibit telomerase in an *in vitro* TRAP assay [21], and in the present study, we showed that they could suppress hTERT gene expression and telomerase activity in both LNCaP and PC3 prostate cancer cells. As such, our next step was to investigate whether subcytotoxic doses of these two compounds would allow the LNCaP and PC3 cells to proliferate for several generations and display telomere shortening and subsequent cellular senescence.

LNCaP and PC3 cells were treated with 0.4 and 0.8 μM of PM2, or 1.0 and 2.0 μM of PIPER, supplemented in the culture media, with the change of fresh media every three days and subculturing every six days. The cells were counted, and the numbers of population doublings were calculated. The graph plotted between the cumulative number of population doublings and incubation time is shown in Figure 2.3. The plots were linear in the control set for both LNCaP cells and PC3 cells. Based on the graph, the population doubling time (PDT) of the LNCaP cells in the control set was 3.8 days, while the PDT of the PC3 cells was 2.4 days. The PDT of the PC3 cells, the more aggressive form of prostate cancer cells, was about 1.6-fold faster than that of the LNCaP cells. The presence of subcytotoxic doses of PM2 or PIPER decreased the population doubling slightly in a concentration-dependent manner (Figure 2.3A-D). The effect on the population doubling of both compounds was minimal in the early rounds of cell passage, but it declined at a higher rate during the latter rounds of cell passage. In particular, the LNCaP cells treated with 0.8 μM of PM2 or 2.0 μM of PIPER proliferated so much

slower after day 60 that we were unable to harvest sufficient cells to perform our subsequent experiments.
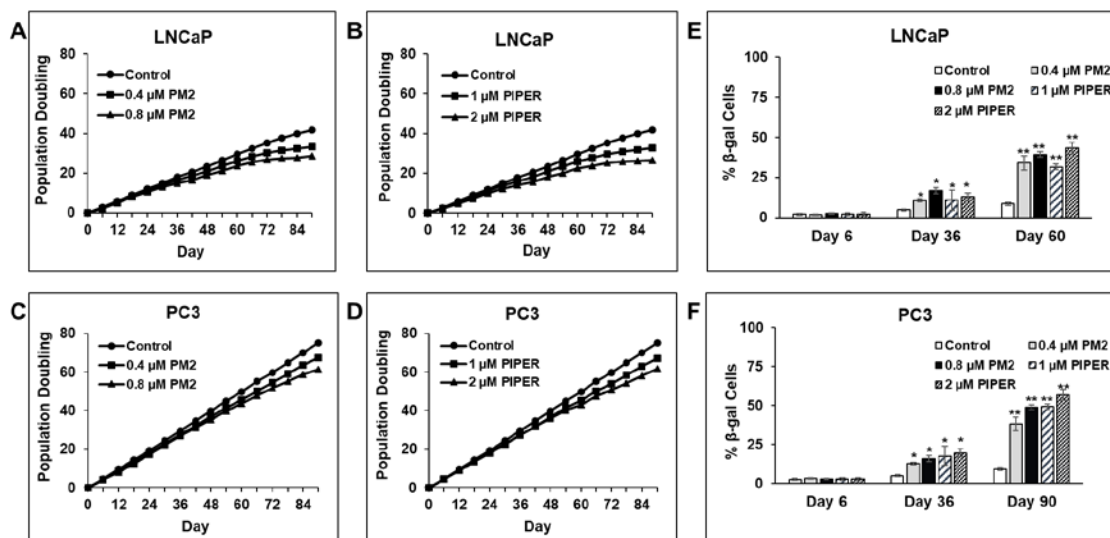
Figure 2.3: Effects of long-term treatment with PM2 and PIPER on population doubling and cellular senescence in LNCaP and PC3 prostate cancer cells. The cells were treated with the indicated concentrations of PM2 or PIPER for the indicated days, with a change of fresh media every three days and subculturing of the cells every six days. (A-D) The indicated prostate cells from each passage were counted, and the growth curves between the cumulative numbers of population doublings were plotted against time. (E-F) The indicated cells were collected on the indicated day and recultured in a 6-well plate. The cells were allowed to grow for 24 h, fixed, stained with X-gal solution, and photographed under a phase contrast microscope. The percentage of β‑galactosidase positive cells (% β-gal cells) was then calculated and plotted against time.

To investigate whether this decline in population doubling by PM2 and PIPER was due to cellular senescence, we collected LNCaP and PC3 cells on the indicated day to test for β-galactosidase activity, a common senescence marker. The β-galactosidase positive cells were monitored under a phase-contrast microscope with a blue stain, usually accompanied with cell morphological changes. The percentage of β-galactosidase positive cells (% β-gal cells) was then calculated and plotted against time. Figures 2.3E and 2.3F show that on day 6, the % β-gal cells of both LNCaP and PC3 treated with PM2 or PIPER were not substantially different from the controls, suggesting that neither compound induced cellular senescence during this short-term treatment. However, the fraction of % β-gal cells increased significantly in a time- and concentration-dependent manner. The % β-gal cells in LNCaP and PC3 cells treated with

PM2 or PIPER collected at day 36 were under 20%. In contrast, at day 60, the % β-gal cells in LNCaP treated with 0.4 μM and 0.8 μM of PM2, 1.0 μM and 2.0 μM of PIPER, were up to 34%, 35%, 32%, and 38%, respectively; while the % β-gal cells of PC3 cells collected at day 90 were 38%, 48%, 49%, and 56%, respectively. From these data, we conclude that the decline in population doubling in both LNCaP and PC3 cells in the long-term treatment with PM2 and PIPER is likely caused by cellular senescence in these cells.

Next, we investigated whether the increase in cellular senescence in the long-term treatment of LNCaP and PC3 cells with PM2 and PIPER correlated with telomere shortening in these cells. The LNCaP cells collected on days 6, 36, and 60, and the PC3 cells harvested on day 6, 36, and 90, were subjected to the telomere length analysis. The genomic DNAs extracted from the cells were first digested with *Hinf* I and *Rsa* I before the telomere restriction fragments (TRF) were analyzed by Southern blotting using a *TeloTAGGG* Telomere Length Assay kit. As illustrated in Figure 2.4A, the mean TRF lengths of LNCaP cells in the control set remained relatively constant at around 2.6 kb over a course of 60 days. In the cells treated with 0.4 and 0.8 μM of PM2, the mean TRF length decreased slightly with time, while the difference between the two doses was insubstantial. The mean TRF lengths in the LNCaP cells treated with 1.0 and 2.0 μM of PIPER also decreased progressively with time, but the decrease was more discernible in the cells treated with 2.0 μM of PIPER.

In the experiments with PC3 cells, as demonstrated in Figure 2.4B, the mean TRF lengths of PC3 cells in the control set were in the range of 8.5-8.7 kb during the course of 90 days. However, the mean TRF lengths in the cells treated with either PM2 or PIPER noticeably decreased progressively with time. The mean TRF lengths decreased from 8.6 kb on day 6, to 7.9 kb on day 36, and to 6.8 kb on day 90 in the PC3 cells treated with 0.4 μM of PM2; while in the cells treated with 0.8 μM of PM2, the mean TRF lengths decreased from 8.7 kb on day 6, to 7.7 kb on day 36, and to 6.2 kb on day 90. In the PC3 cells treated with PIPER, the mean TRF lengths decreased from 8.7 kb on day 6, to 7.7 kb on day 36, and to 6.5 kb on day 90 at the dose of 1.0 μM PIPER, while the mean TRF lengths decreased from 8.7 kb on day 6, to 7.7 kb on day 36, and to 6.4 kb on day 90 at the dose of 2.0 μM PIPER.
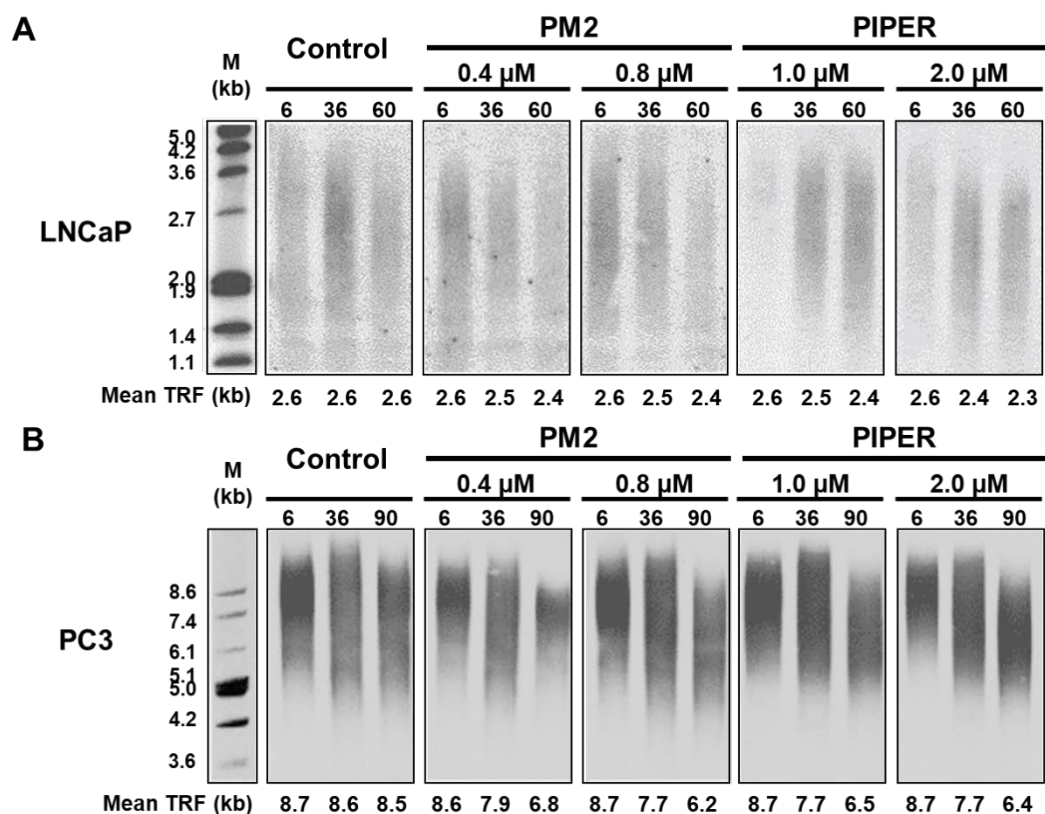
Figure 2.4: Effect of PM2 and PIPER on telomere shortening in LNCaP (A) and PC3 (B) prostate cancer cells. The prostate cells were treated with the indicated concentrations of either PM2 or PIPER for the indicated days, with a change of fresh media every three days and subculturing of the cells every six days. Genomic DNA was extracted, and telomere restriction fragments (TRF) were analyzed using the *TeloTAGGG* Telomere Length Assay kit. M represents a molecular weight marker.

From the results above, the decrease in telomere length caused by both PM2 and PIPER in PC3 cells was much greater than that in LNCaP cells, probably because telomere lengths in PC3 cells are long (mean TRF length of 8.7 kb), while those in LNCaP cells are shorter (mean TRF length of 2.6 kb, for which some telomeres were already close to the critically short stage). With telomerase being inhibited, the long telomeres in the PC3 cells allowed most cells to proliferate, and telomere lengths were shortened accordingly. In contrast, more LNCaP cells were prone to become senescent in each cell passage, but the cells that proliferated were from cells with longer telomeres; therefore, the mean TRF length did not change much from the previous passages.

Another point of discussion would be why there were senescent cells in the PC3

culture, of which the average telomere length was much longer than that found in LNCaP cells. This observation can probably be explained by the heterogeneity of telomere lengths in PC3 cells. It was found that variable telomere lengths in prostate cancer cells and telomere shortening in cancer-associated stromal cells correlates with lethal disease [31]. Since the shortest telomere, not the average telomere length, is critical for cell viability and the onset of replicative senescence [31,32], telomerase inhibition in PC3 cells could possibly inhibit the elongation of these few short telomeres and trigger these cells toward cellular senescence.

Partition Coefficient and Cellular Uptake of PM2 and PIPER in Prostate Cancer Cells

From the experiments above, PM2 and PIPER induces telomere shortening and cellular senescence in both LNCaP and PC3 cells at a comparable concentration. However, the acute cytotoxicity test by SRB assay showed that PM2 is about 30 times more toxic than PIPER. We wondered whether cellular uptake of these two compounds might be different. First, we determined the octanol/H_2O partition coefficient (P_{ow}) of both compounds by the shake flask method. The P_{ow} of PM2 and PIPER were found to be 1.5 ± 0.2 and 2.6 ± 0.1, respectively. Both compounds are lipophilic, but the P_{ow} of PIPER is about one order of magnitude higher than that of PM2. We then measured the cellular uptake of PM2 and PIPER in LNCaP and PC3 cells using flow cytometry. As shown in Figure 2.5A, both PM2 and PIPER appear to be absorbed into both LNCaP and PC3 cells in a concentration-dependent manner within the 24 h incubation time. Figure 2.5B shows pictures from fluorescence microscopy, of which LNCaP and PC3 cells were incubated with 4 μM of either PM2 or PIPER for 24 h before the cell nuclei were stained with DAPI. Both PM2 and PIPER appear to enter LNCaP and PC3 cells and distribute throughout the cells including the nucleus, where the fluorescent light merged with that of DAPI. The data from both flow cytometry and fluorescence microscopy suggest that both compounds are absorbed into the LNCaP and PC3 cells to a comparable extent, considering that they both have the same perylene chromophore. Therefore, the higher degree of cytotoxicity of PM2 over PIPER likely arises from mechanisms other than the cellular uptake of these compounds.
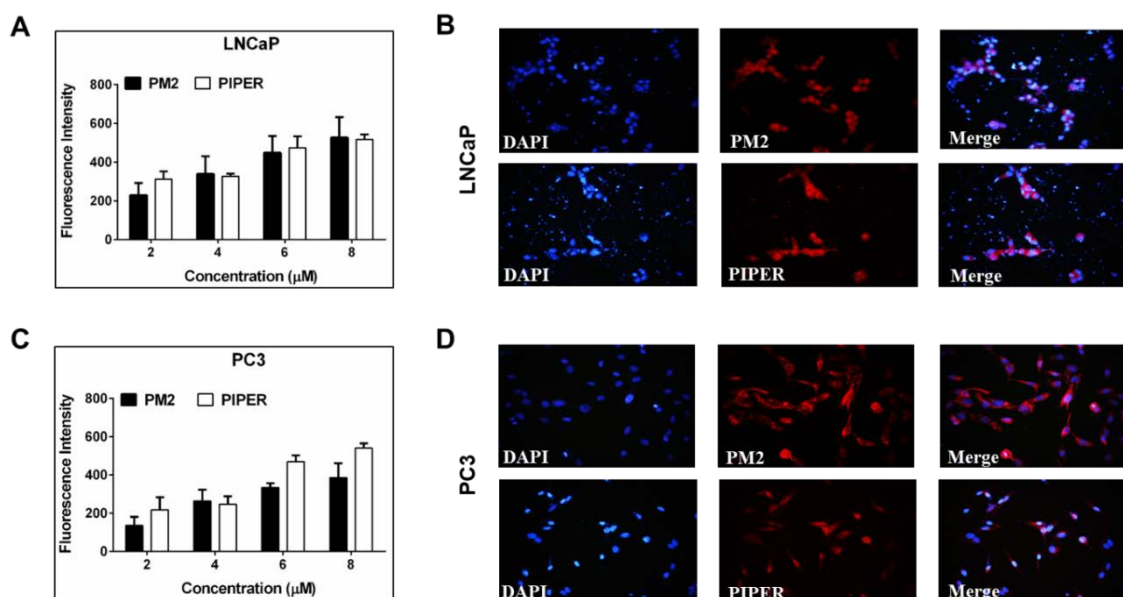
Figure 2.5: The cellular uptake of PM2 and PIPER by LNCaP and PC3 cells. (A,C) The prostate cells were treated with the indicated concentrations of either PM2 or PIPER for 24 h before they were analyzed using a flow cytometer. The fluorescence intensity represents the geometric mean value from data collected from 50,000 gated events. (B,D) The prostate cells were plated on a cover slide for 24 h before they were treated with 4 µM of PM2 or PIPER for 48 h. After treatment, cells were washed and stained with 100 nM DAPI for 45 min for nuclei staining. Intracellular localization of PM2 or PIPER were access by fluorescence microscopic imaging.

DISCUSSION

Prostate cancer is a slow-growing cancer, with a 5-year relative survival rate of 99% [2]. Active surveillance for low-risk cancer has been increasingly adopted in the United States and internationally, and it is supported by various guidelines [34,35]. Since most prostate cancers reactivate telomerase to circumvent the replicative senescence caused by end replication problem, telomerase inhibition could be useful for the suppression of prostate cancer during this active surveillance. For a detectable solid tumor, a therapy regimen that combines telomerase inhibitors after conventional therapies such as surgery, radiotherapy, and chemotherapy, was suggested to be effective and durable responses for prostate cancer therapy [36]. Sustained telomerase inhibition would lead the small population of dormant cancer cells, including cancer stem cells, to critical telomere attrition and ultimately cell senescence or cell death, with minimal impact on other normal somatic cells [36]. However, this approach would be successful only if the telomerase inhibitor is safe to use for an extended period of time.

In the present study, we investigated two perylene derivatives, PM2 and PIPER, as effective telomerase inhibitors in two types of prostate cancer cells, LNCaP and PC3 cells. Both compounds were previously found to be G-quadruplex ligands that facilitate G-quadruplex formation of both telomeric DNA and the promoters of *hTERT*, leading to the inhibition of telomerase in an *in vitro* TRAP assay, and the suppression of *hTERT* gene expression and telomerase activity in A549 lung cancer cells [22]. To investigate the effects of PM2 and PIPER during the early and late stages of prostate cancer, we chose LNCaP and PC3 prostate cancer cell lines to represent these stages. LNCaP cells represent an early stage of prostate cancer based on their source of origin (lymph node metastatic lesion of human prostate adenocarcinoma), androgen-sensitive cell growth, and the progression to AR-independent growth [37]. PC3 cells represent an advanced stage of prostate cancer based on their source of origin (prostatic adenocarcinoma metastatic to bone), androgen-insensitive characteristics, and a more aggressive phenotype that is highly angiogenic [37]. Our results showed that both PM2 and PIPER suppressed *hTERT* expression and telomerase activity in both types of cells. Long-term treatment with subcytotoxic doses of these two compounds led to telomere shortening and cellular senescence in both types of cells. However, the telomere shortening in LNCaP was not as noticeable as it was in PC3 due to the much shorter telomeres in LNCaP, which are probably close to the critical stage of triggering cellular senescence. Cellular senescence increased significantly in both cells during long-term treatment with either PM2 or PIPER, correlating well with the telomere shortening found in these cells. It is worth mentioning that in the controls set of both LNCaP and PC3 cells, there was a small increase in cellular senescence upon passages, which might reflect the insufficient telomerase-based elongation of telomeres or other senescence stimuli presence during cell passages. The short telomeres in LNCaP cells might be responsible for the genomic instability often observed in these cells, which leads to their androgen-independent progression upon passages [38].

An ideal telomerase inhibitor should exert its activity on telomerase with minimal effect on cell viability, which reflects certain mechanisms other than telomerase inhibition. PM2 is an asymmetrical perylene monoimide, while PIPER is a symmetrical perylene diimide. In the acute cytotoxicity test, PM2 was about 30 times more toxic than PIPER in both LNCaP and PC3 prostate cancer cells. In short-term treatments, PM2 appeared to be more effective than PIPER in the suppression of *hTERT* expression and

telomerase activity in both types of prostate cancer cells. These results are similar to the results we previously found in A549 lung cancer cells [22]. In long-term treatments, both PM2 and PIPER induced telomere shortening and cellular senescence at doses much closer in concentration to each other (0.4-0.8 μM of PM2 versus 1.0-2.0 μM of PIPER). The differences between PM2 and PIPER in the acute cytotoxicity and the short-term results from *hTERT* expression assay and telomerase activity assay prompted us to suspect whether these discrepancies were due to differences in the cellular uptake of these two compounds. PM2 is more water-soluble than PIPER; consequently, there might be more free molecules of PM2 available in solution at equivalent concentrations. PIPER is also well-known to aggregate in aqueous solution, especially at basic pH.[23] In this study, we found that the partition coefficient (P_{ow}) of PM2 and PIPER were 1.5 ± 0.2 and 2.6 ± 0.1, respectively. Therefore, both compounds are lipophilic, but the P_{ow} for PIPER was about a magnitude of order higher than that for PM2. However, the difference in lipophilicity does not seem to affect the cellular uptake of both compounds into both LNCaP and PC3 cells. Using flow cytometry, we found that the uptake of both compounds into both both types cancer cells occurred with similar intensity in a concentration-dependent manner, suggesting a passive absorption through the lipid bilayer of the cells. Fluorescence microscopy revealed that both compounds distributed throughout the whole cells, including in the nucleus. Although these two methods could not directly quantify the cellular uptake of the compounds, at least they imply a similar uptake of both compounds into both types of prostate cells in a similar manner (i.e., not with a 30-fold difference in cellular uptake). Therefore, the more acute cytotoxicity of PM2 is likely due to other cellular mechanisms, and PIPER might have a wider window of safety than PM2 when used as a telomerase inhibitor. It is also worth mentioning that both compounds were found to have little effect on peripheral blood mononuclear cells in the presence of 0-160 μM of either PM2 or PIPER.

When taken as a whole, these preliminary results in cell culture are encouraging, but it would be premature to extrapolate these results into clinical settings where many more factors need to be considered. The future animal and clinical trials will determine whether either of these compounds can safely prevent prostate cancer progression.

Acknowledgements

References

1. Torre LA, Bray F, Siegel RL, Ferlay J, Lortet-Tieulent J, Jemal A. Global cancer statistics, 2012. *CA. Cancer J. Clin.*, **65**, 87-108 (2015).

2. Siegel RL, Miller KD, Jemal A. Cancer statistics, 2018. *CA. Cancer J. Clin.*, **68**, 7-30 (2018).

3. Zhang K, Bangma CH, Roobol MJ. Prostate cancer screening in Europe and Asia. *Asian J. Urol.*, **4**, 86-95 (2017).

4. Graham MK, Meeker A. Telomeres and telomerase in prostate cancer development and therapy. *Nat. Rev. Urol.*, **14**, 607-619 (2017).

5. Lee DJ, Mallin K, Graves AJ, Chang SS, Penson DF, Resnick MJ, Barocas DA. Recent changes in prostate cancer screening practices and epidemiology. *J. Urol.*, **198**, 1230-1240 (2017).

6. Fakhrejahani F, Madan RA, Dahut WL. Management options for biochemically recurrent prostate cancer. *Curr. Treat. Options Oncol.*, **18**, 26 (2017).

7. Litwin MS, Tan HJ. The diagnosis and treatment of prostate cancer: a review. *JAMA*, **317**, 2532-2542 (2017).

8. Cooperberg MR, Brooks JD, Faino AV, Newcomb LF, Kearns JT, Carroll PR, Dash A, Etzioni R, Fabrizio MD, Gleave ME, Morgan TM, Nelson PS, Thompson IM, Wagner AA, Lin DW, Zheng Y. Refined analysis of prostate-specific antigen kinetics to predict prostate cancer active surveillance outcomes. *Eur. Urol.*, **74**, 211-217 (2018).

9. Saad F, Fizazi K. Androgen deprivation therapy and secondary hormone therapy in the management of hormone-sensitive and castration-resistant prostate cancer. *Urology*, **86**, 852-861 (2015).

10. Aragon-Ching JB, Dahut WL. Chemotherapy in androgen-independent prostate cancer (AIPC): what's next after taxane progression? *Cancer Therapy*, **5**, 151–160 (2007).

11. Marian CO, Wright WE, Shay JW. The effects of telomerase inhibition on prostate tumor-initiating cells. *Int. J. Cancer*, **127**, 321-331 (2010).

12. Shay JW, Wright WE. Role of telomeres and telomerase in cancer. *Semin. Cancer Biol.*, **21**, 349-353 (2011).

13. Shay JW, Wright WE. Hayflick, his limit, and cellular ageing. *Nat. Rev. Mol. Cell Biol.*, **1**, 72-76 (2000).

14. Victorelli S, Passos JF. Telomeres and cell senescence - Size matters not. *EBioMedicine*, **21**, 14-20 (2017).

15. Kim NW, Piatyszek MA, Prowse KR, Harley CB, West MD, Ho PL, Coviello GM, Wright

WE, Weinrich SL, Shay JW. Specific association of human telomerase activity with immortal cells and cancer. *Science*, **266**, 2011-2015 (1994).

16. Cohen SB, Graham ME, Lovrecz GO, Bache N, Robinson PJ, Reddel RR. Protein composition of catalytically active human telomerase from immortal cells. *Science*, **315**, 1850-1853 (2007).

17. Cong YS, Wright WE, Shay JW. Human telomerase and its regulation. *Microbiol. Mol. Biol. Rev.*, **66**, 407-425 (2002).

18. Ramlee MK, Wang J, Toh WX, Li S. Transcription regulation of the human telomerase reverse transcriptase (hTERT) gene. *Genes* (Basel), **7**, E50 (2016).

19. Neidle S. Human telomeric G-quadruplex: the current status of telomeric G-quadruplexes as therapeutic targets in human cancer. *FEBS J.*, **277**, 1118-1125 (2010).

20. Palumbo SL, Ebbinghaus SW, Hurley LH. Formation of a unique end-to-end stacked pair of G-quadruplexes in the hTERT core promoter with implications for inhibition of telomerase by G-quadruplex-interactive ligands. *J. Am. Chem. Soc.*, **131**, 10878-10891 (2009).

21. Francisco AP, Paulo A. Oncogene expression modulation in cancer cell lines by DNA G-quadruplex-interactive small molecules. *Curr. Med. Chem.*, **24**, 4873-4904 (2017).

22. Taka T, Huang L, Wongnoppavich A, Tam-Chang SW, Lee TR, Tuntiwechapikul W. Telomere shortening and cell senescence induced by perylene derivatives in A549 human lung cancer cells. *Bioorg. Med. Chem.*, **21**, 883-890 (2013).

23. Tuntiwechapikul W, Taka T, Bethencourt M, Makonkawkeyoon L, Lee TR. The influence of pH on the G-quadruplex binding selectivity of perylene derivatives. *Bioorg. Med. Chem. Lett.*, **16**, 4120-4126 (2006).

24. Huang L, Tam-Chang SW. 9-Piperazine substituted perylene-3,4-dicarboximide as a fluorescent probe in ratiometric analysis. *Chem. Commun.*, **47**, 2291-2293 (2011).

25. Vichai V, and Kirtikara K: Sulforhodamine B colorimetric assay for cytotoxicity screening. *Nat. Protoc.,* **1**, 1112-1116 (2006).

26. Szatmari I, Aradi J. Telomeric repeat amplification, without shortening or lengthening of the telomerase products: a method to analyze the processivity of telomerase enzyme. *Nucleic Acids Res.*, **29**, E3 (2001).

27. OECD guideline for the testing of chemicals. No. 107: Partition coefficient (n-octanol/water): shake flask method, OECD Publishing, Paris. (1995).

28. Wattanasin P, Saetear P, Wilairat P, Nacapricha D, Teerasong S. Zone fluidics for measurement of octanol-water partition coefficient of drugs. *Anal. Chim. Acta.*, **860**, 1-7 (2015).

29. Taka T, Joonlasak K, Huang L, Randall Lee T, Chang SW, Tuntiwechapikul W. Down-regulation of the human VEGF gene expression by perylene monoimide derivatives. *Bioorg. Med. Chem. Lett.*, **22**, 518-522 (2012).

30. Sommerfeld HJ, Meeker AK, Piatyszek MA, Bova GS, Shay JW, Coffey DS. Telomerase activity: a prevalent marker of malignant human prostate tissue. *Cancer Res.*, **56**, 218-222 (1996).

31. Graham MK, Meeker A. Telomeres and telomerase in prostate cancer development and therapy. *Nat. Rev. Urol.*, **14**, 607-619 (2017).

32. Hemann MT, Strong MA, Hao LY, Greider CW. The shortest telomere, not average telomere length, is critical for cell viability and chromosome stability. *Cell*, **107**, 67-77 (2001).

33. Xu Z, Duc KD, Holcman D, Teixeira MT. The length of the shortest telomere as the major

determinant of the onset of replicative senescence. *Genetics*, **194**, 847-857 (2013).

34. Chen RC, Rumble RB, Loblaw DA, Finelli A, Ehdaie B, Cooperberg MR, Morgan SC, Tyldesley S, Haluschak JJ, Tan W, Justman S, Jain S. Active surveillance for the management of localized prostate cancer (Cancer Care Ontario Guideline): American society of clinical oncology clinical practice guideline endorsement. *J. Clin. Oncol.*, **34**, 2182–2190 (2016).

35. Loeb S. Active surveillance for prostate cancer. *Rev. Urol.*, **20**, 101-103 (2018).

36. Marian CO, Shay JW. Prostate tumor-initiating cells: a new target for telomerase inhibition therapy? *Biochim. Biophys. Acta.*, **1792**, 289-296 (2009).

37. Dozmorov MG, Hurst RE, Culkin DJ, Kropp BP, Frank MB, Osban J, Penning TM, Lin HK. Unique patterns of molecular profiling between human prostate cancer LNCaP and PC-3 cells. *Prostate*, 69, 1077-1090 (2009).

38. Langeler EG, van Uffelen CJ, Blankenstein MA, van Steenbrugge GJ, Mulder E. Effect of culture conditions on androgen sensitivity of the human prostatic cancer cell line LNCaP. *The Prostate*, **23**, 213–223 (1993).

S1: Synthesis Scheme and Characterization of PIPER and PM2

(a) PIPER, N,N'-Bis[2-(1-piperidino)ethyl]-3,4,9,10-perylenetetracarboxylic diimide, was synthesized using a procedure adapted from the literature [Fedoroff OY, *et al.* *Biochemistry*, **37**, 12367 (1998)].
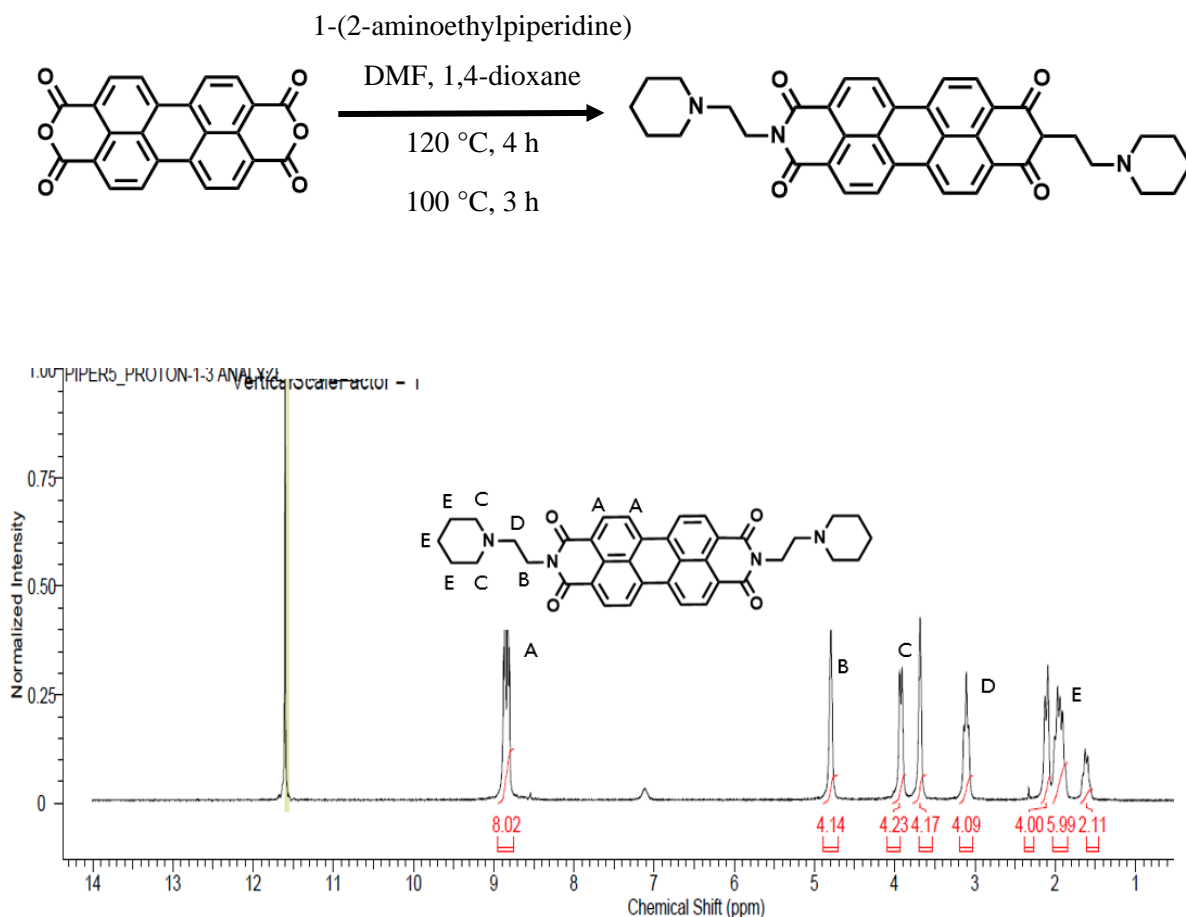
Figure S2.1: ^{1}H NMR Spectrum of PIPER in CF$_3$COOD at 400 MHz

^{1}H NMR (400 MHz, dTFA): δ 1.55 (m, 2H), 1.84-1.89 (bm, 6 H), 2.11-2.30 (m, 4 H), 3.11 (m, 4 H), 3.61 (m, 4 H), 3.95 (m, 4 H), 4.86 (m, 4 H), 8.71-8.98 (m, 8 H). Exact mass calcd for C$_{38}$H$_{36}$N$_4$O$_4$ (M+H): 613.2737. Found: 613.2714.

(b) PM2, *N*-(2-(*N'*,*N'*-diethylamino)ethyl)-9-piperazinylperylene-3,4-dicarboximide, was synthesized using a procedure adapted from the literatures (Tam-Chang SW, *et al., J. Org. Chem.* **69**, 2719 (2004) and Huang L, *et al.*, *Chem. Commun.*, **47**, 2291 (2011)].
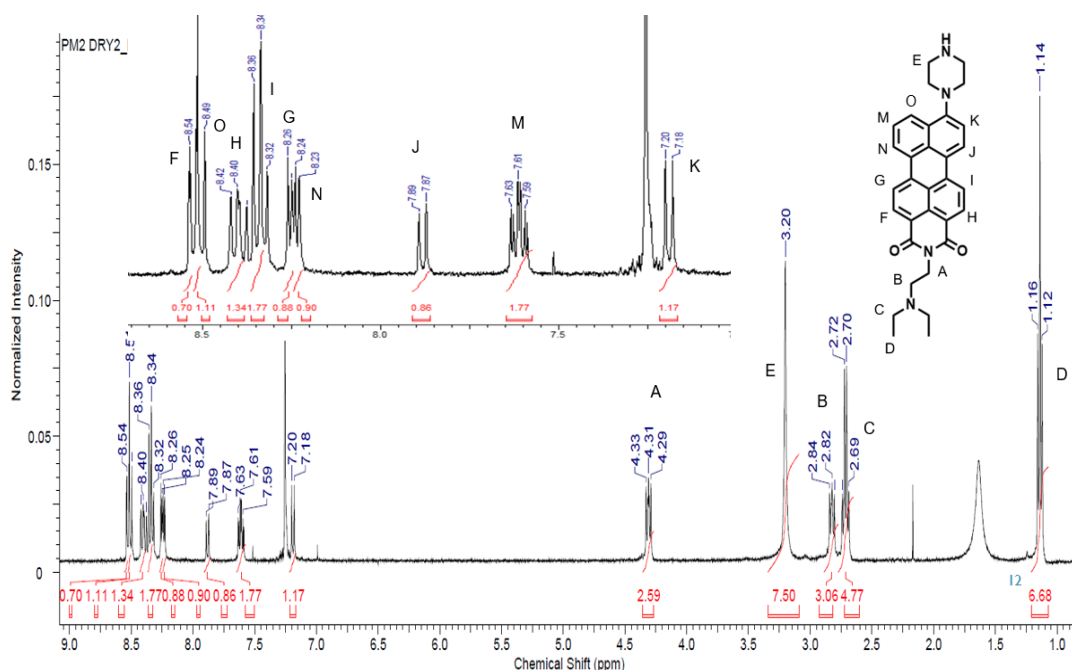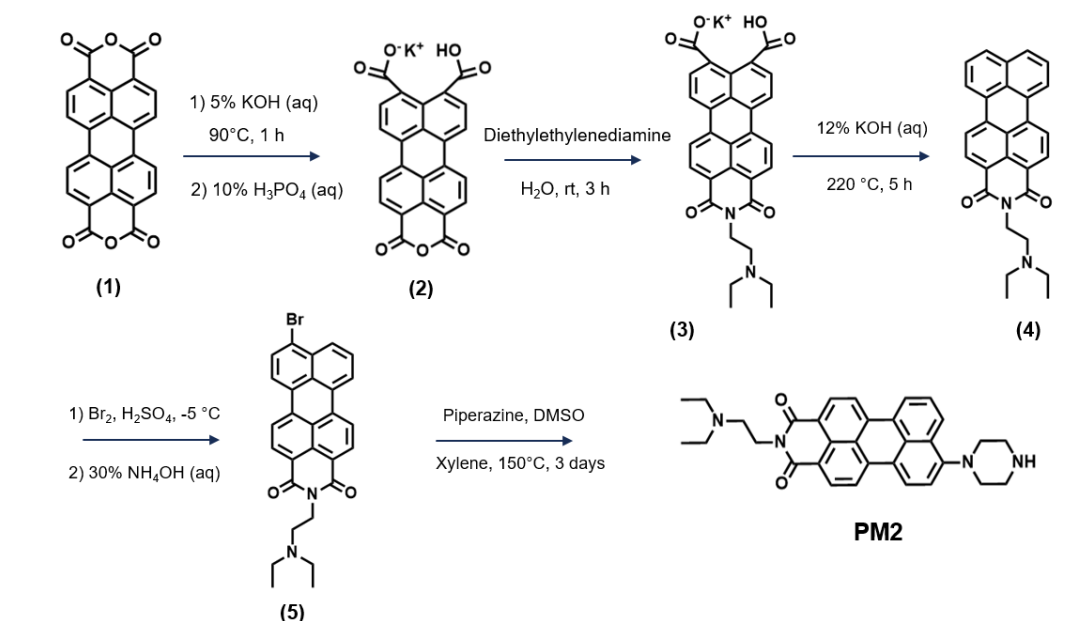
Figure S2.2: ¹H NMR Spectrum of PM2 in CDCl₃ at 400 MHz

¹H NMR (400 MHz, CDCl₃): δ 1.15 (t, 6 H), 2.70 (m, 4 H), 2.84 (m, 2 H), 3.11-3.45 (bm, 8 H), 4.31 (t, 2 H), 7.20 (d, 1 H), 7.61 (t, 1 H), 7.89 (d, 1 H), 8.24 (d, 1 H), 8.26 (d, 1 H), 8.32 (s, 1 H), 8.40 (s, 1 H), 8.50 (s, 1 H), 8.54 (s, 1 H).
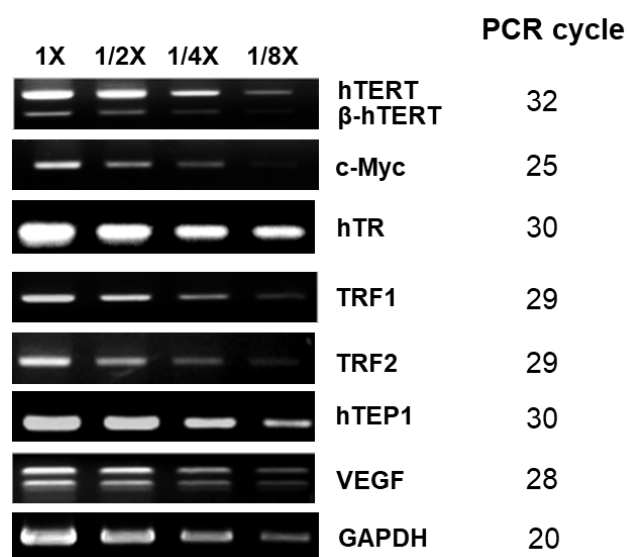
Figure S2.3: The Chosen PCR Cycle for Semiquantitative RT-PCR Analysis. The PCR cycle for each gene was carefully chosen so that it represents the amount of the cDNA in the sample. The cDNA from A549 cells was diluted two-fold serially and was amplified using gene-specific primers.

Table S2.1:   Primer Sequence, Product Size, Annealing Temperature, and PCR Cycle Used in Semiquantitative RT-PCR

Name	Primer Sequence	Product Size (bp)	Annealing Temp. (°C)	PCR Cycle
c-Myc (F) c-Myc (R)	TAATTCCAGCGAGAGGCAGA GTCCCCAAATGGGCAGAATA	290	60	25
GAPDH (F) GAPDH (R)	CCACAGTCCATGCCATCAC CCACCACCCTGTTGCTGTA	450	60	20
hTEP1 (F) hTEP1 (R)	TCAAGCCAAACCTGAATCTGAG CCCCGAGTGAATCTTTCTACGC	264	60	30
hTERT (F) hTERT (R)	GCCTGAGCTGTACTTTGTCAA CGCAAACAGCTTGTTCTCCATGTC	275, 457	62	32
hTR (F) hTR (R)	GAAGGGCGTAGGCGCCGTGCTTTTGC GTTTGCTCTAGAATGAACGGTGGAAG G	111	62	30
TRF1 (F) TRF1 (R)	TGTGCGGATGGTAGGGATGC GGGCTGATTCCAAGGGTGTA	421	62	29
TRF2 (F) TRF2 (R)	AGTCAATCGCTGGGTGCTCA CCTGGTGCTGGCTGTTTATC	636	62	29
VEGF (F) VEGF (R)	TGCATTGGAGCCTTGCCTTG CGGCTCACCGCCTCGGCTTG	410, 540	62	28

* F = Forward primer, R = Reverse primer

Table S2.2: Oligonucleotides Used in the Modified Fluorescent TRAP Assay

Name	Sequence
MTS	5'-AGCATCCGTCGAGCAGAGTT-3'
RPc3g	5'-TAGAGCACAGCCTGTCCGTG(CTAACC)$_3$GG-3'
RP-FAM	FAM-5'-TAGAGCACAGCCTGTCCGTG-3'
IC	5'-TAGAGCACAGCCTGTCCGTGAAAAGGCCGAGAAGCGATCG-3'
NT	5'-CGATCGCTTCTCGGCCTTTT-3'
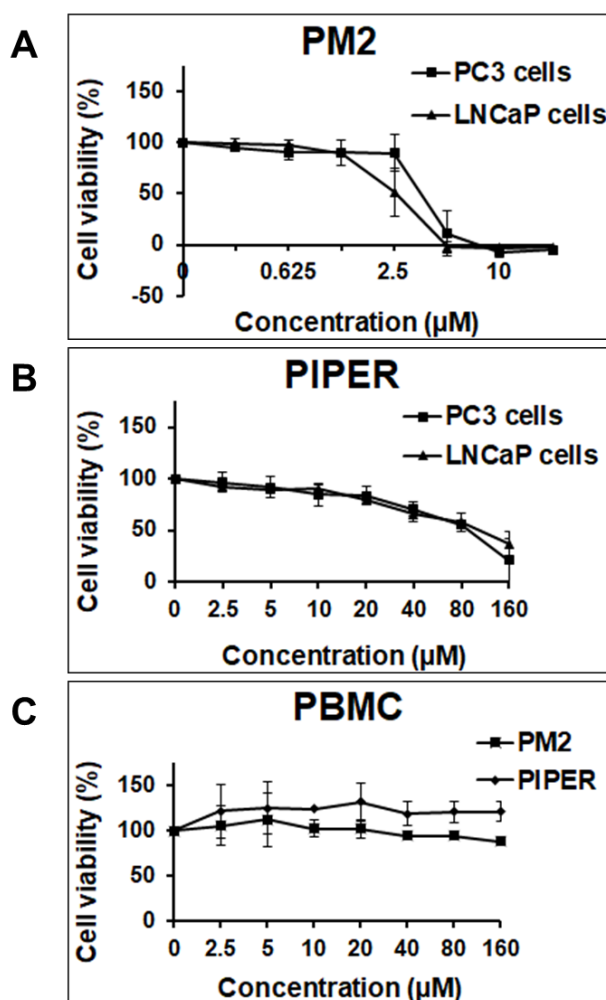
Figure S2.4: Dose-Response Relationship between the Percentage of Cell Viability and the Concentration of PM2 or PIPER from SRB Assays. (A) SRB assay of PM2 in PC3 and LNCaP prostate cancer cells. (B) SRB assay of PIPER in PC3 and LNCaP prostate cancer cell lines. (C) SRB assay of PM2 and PIPER in peripheral blood mononuclear cells (PBMC).
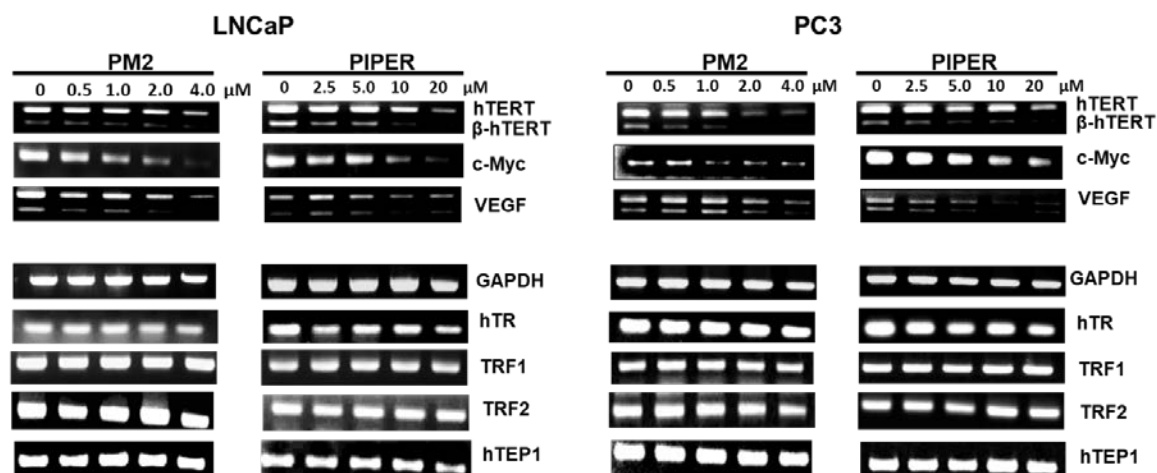
Figure S2.5: Effect of PM2 and PIPER on Gene Expression in LNCaP and PC3 Prostate Cancer Cells. The indicated prostate cancer cells were incubated with the indicated concentrations of either PM2 or PIPER for 24 h before their RNAs were extracted and assayed by semiquantitative RT-PCR analysis using gene-s

CHAPTER 3

Ginger Extract Promotes Telomere Shortening and Cellular Senescence in A549 Lung Cancer Cells

SUMMARY

Replicative senescence, which is caused by telomere shortening from the end replication problem, is considered one of the tumor-suppressor mechanisms in eukaryotes. However, most cancers escape this replicative senescence by reactivating telomerase, an enzyme that extends the 3′-ends of the telomeres. Previously, we reported the telomerase inhibitory effect of a crude *Zingiber officinale* extract (ZOE), which suppressed *hTERT* expression, leading to a reduction in hTERT protein and telomerase activity in A549 lung cancer cells. In the present study, we found that ZOE induced telomere shortening and cellular senescence during the period of 60 days when these A549 cells were treated with the subcytotoxic doses of ZOE. Using assay-guided fractionation and GC/MS analysis, we found that the major compounds in the active subfractions were paradols and shogaols of various chain length. The results from studies of pure 6-paradol and 6-shogaol confirmed that these two compounds could suppress *hTERT* expression as well as telomerase activity in A549 cells. These results suggest that these paradols and shogaols are likely the active compounds in ZOE that suppress *hTERT* expression and telomerase activity in these cells.

Keywords: *Zingiber officinale*, Telomerase inhibition, Telomere shortening, Paradol, Shogaol

INTRODUCTION

Telomeres are specialized nucleoprotein structures found at the ends of all eukaryotic chromosomes. Telomeres maintain chromosome stability by preventing nucleolytic degradation and end-to-end fusion [1], as well as facilitating chromosome segregation during meiosis [2]. The long repetitive telomeric DNA sequence and the specific telomeric protein complex called shelterin allow the telomere to form a loop structure called T-loop, which differentiates telomeric DNA from other double-stranded DNA breaks [3]. Telomeric DNA is shortened 50-200 base pairs during each round of DNA replication due to the end replication problem [4]. The long telomeric DNA allows somatic cells to replicate for a number of cell divisions until one of the cell's telomeric DNAs are shortened to a critical length when it triggers the irreversible cell cycle arrest called "replicative senescence" [5,6].

Replicative senescence is generally considered a tumor-suppressor mechanism [7]. To escape replicative senescence, the majority of human cancers maintain their telomere length by reactivating telomerase, the enzyme that normally adds telomeric DNA to the 3'-ends of chromosomes in germline cells [8,9]. The isolated active human telomerase consists of two sets of human telomerase reverse transcriptase (hTERT), human telomeric RNA (hTR), and dyskerin [10]. Although both hTERT and hTR are necessary for telomerase activity, the transcriptional regulation of *hTERT* expression is the principal mechanism for controlling telomerase activity [9,11].

Dietary phytochemicals have attracted considerable interest for cancer prevention due to at least three factors: (1) potential therapeutic effects, (2) low cost, (3) and good bioavailability [12,13]. However, applying plant chemicals for cancer prevention requires an in-depth knowledge of their mechanisms of action and their biosafety. One of the attractive targets for cancer prevention is telomerase, because telomerase-specific inhibition causes cancer cells and cancer-initiating cells to enter replicative senescence and apoptosis without any significant effect on normal somatic cells [14,15]. A literature search for plant-derived telomerase inhibitors found a few natural phytochemicals that inhibited telomerase in cancer cells; these include curcumin, epigallocatechin-3-gallate (EGCG), resveratrol, genistein, sulforaphane, silibinin, and pristimerin, among others [16]. However, only a few reports show the long-term effects of these phytochemicals on telomere shortening and cellular senescence because the cancer cells must grow and

normally divide for several generations in a nontoxic dose in order to attain a discernible telomere shortening. This aspect is crucially important because the viability of using dietary phytochemicals for cancer prevention depends on these agents being effective at nontoxic doses.

For millennia, the ginger (*Zingiber officinale* Roscoe) rhizome has been traditionally used for various ailments, including many gastrointestinal disorders such as nausea, vomiting, and abdominal spasm, as well as rheumatic disorders, arthritis, and muscular discomfort [17,18]. In recent years, scientists have revealed that various chemicals found in ginger rhizome--most notably gingerols, paradols, and shogaols--possess anti-cancer properties as shown in many experimental models [19-22]. Previously, we reported the telomerase inhibitory effect of the crude ethyl acetate fraction of *Zingiber officinale* extract (ZOE), which suppressed *hTERT* expression, leading to a reduction in hTERT protein and telomerase activity in A549 lung cancer cells [23]. However, there were two remaining important questions that we wanted to address; these are: (1) Would telomerase suppression by ginger extract lead to telomere shortening and cellular senescence at subcytotoxic doses? (2) What are the active compounds in the ginger extract that suppress hTERT expression? In this report, we demonstrate that ZOE induced telomere shortening and cellular senescence during the long-term treatment when these A549 cells were treated with the subcytotoxic doses of ZOE. We then identified the telomerase suppressors in the crude ginger extract using assay-guided fractionation and GC/MS analysis.

RESULTS

We previously reported that ZOE suppressed *hTERT* expression in A549 lung cancer cells, leading to the decrement of hTERT protein and telomerase activity.[23] In the present study, ZOE was extracted in the same manner, and the TLC fingerprint of ZOE was similar to what we previously reported [Supporting Information (SI) Figure S3.1]. The IC_{50} growth inhibitory effect of ZOE in A549 cells was 58 ± 2 µg/mL, compared to the 50 ± 4 µg/mL we previously reported.[23]

ZOE suppressed *hTERT* expression and telomerase activity in A549 lung cancer cells

We retested the new batch of ZOE for the suppression of *hTERT* expression and telomerase activity in A549 lung cancer cells. For the gene expression assay, we incubated the A549 cells with the indicated concentrations of ZOE for 24 h, before their RNAs were extracted and assayed by semiquantitative RT-PCR analysis. For each gene expression assay, we carefully chose the PCR cycle so that the detected amplified product could represent the initial amount of each cDNA in the reaction (SI Figure S3.2). As shown in Figure 3.1A, the *hTERT* and *c-Myc* mRNA expressions were suppressed after the A549 cells were treated with ZOE for 24 h in a concentration-dependent manner. On the other hand, the housekeeping gene *GAPDH* and other telomerase-related genes (*hTR*, *TRF1*, *TRF2*, and *hTEP1*) were not affected. For the telomerase activity assay, we incubated the A549 cells with the indicated concentrations of ZOE for 48 h. The crude protein was then extracted and used as the telomerase source in a modified TRAP assay. Figure 3.1B demonstrates that the telomerase activity of the A549 cells treated with ZOE for 48 h was also suppressed in a concentration-dependent manner. These results confirmed our initial contention that our new batch of ZOE could suppress *hTERT* expression and telomerase activity in A549 cells.
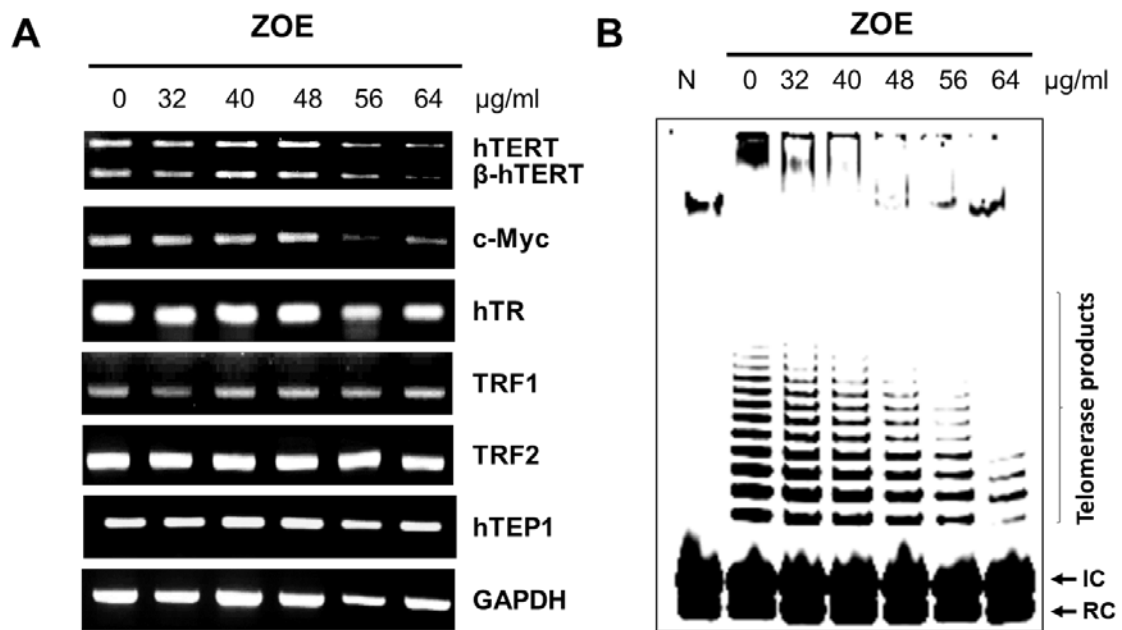
Figure 3.1: Short-term treatment of ZOE inhibits *hTERT* expression (A) and reduces telomerase activity in A549 lung cancer cells (B). (A) To assay for gene expression, the A549 cells were incubated with the indicated concentrations of ZOE for 24 h before their RNAs were extracted and assayed by semiquantitative RT-PCR analysis. (B) To assay the effect on telomerase activity, the A549 cells were incubated with the indicated concentrations of the ZOE for 48 h before the crude protein extract was used as the source of telomerase in a modified TRAP assay. Lane N represents the negative control experiment when telomerase was heat-denatured. IC and RC represent the internal control and recovery control.

Long-term treatment with ZOE led to telomere shortening in A549 cells

Most cancers treated with a telomerase suppressor should exhibit telomere shortening after successive rounds of cell replication, just like normal somatic cells. In order for this to happen and be observed, the dose of the agent must allow the cancer cells to proliferate normally for several passages. In this long-term treatment study, we treated the A549 cells with two subcytotoxic doses of ZOE (5 and 10 µg/mL) added in the culture media, with the changing of fresh media every three days and subculturing every six days for up to 60 days. Cells were collected and counted with each 6-day passage. We then plotted a graph between the cumulative number of population doublings and time (Figure 3.2A), which shows that the A549 cells in all three sets were steadily proliferating during the course of the 60-day experiment, although the population doublings in the experimental sets with ZOE (5 and 10 µg/mL) were a little less than those in the control set.

A number of A549 cells collected in Day 6, 30, and 60 were subjected to telomere length assay. We first digested the extracted genomic DNA with *Hinf* I and *Rsa* I, before the telomere restriction fragments (TRF) was analyzed by Southern blotting using a *TeloTAGGG* Telomere Length Assay kit. As shown in Figure 3.2B, the mean TRF lengths of the experimental sets (cells treated with ZOE) were less than that of the control set in a time- and concentration-dependent manner during the period of the 60-day study. In the control set, the mean TRF length remained relatively stable at 3.3 kb. However, it decreased from 3.3 to 3.1 kb on Day 30, and then to 3.0 kb on Day 60 in the cells treated with 5 µg/mL ZOE. With the treatment of 10 µg/mL ZOE, the decrease was much more noticeable, in which the mean TRF length decreased from 3.3 kb to 3.0 kb on Day 30, and to 2.6 kb on Day 60. Based on these results, we conclude that ZOE induces telomere shortening through the suppression of *hTERT* expression and telomerase activity in these cells.
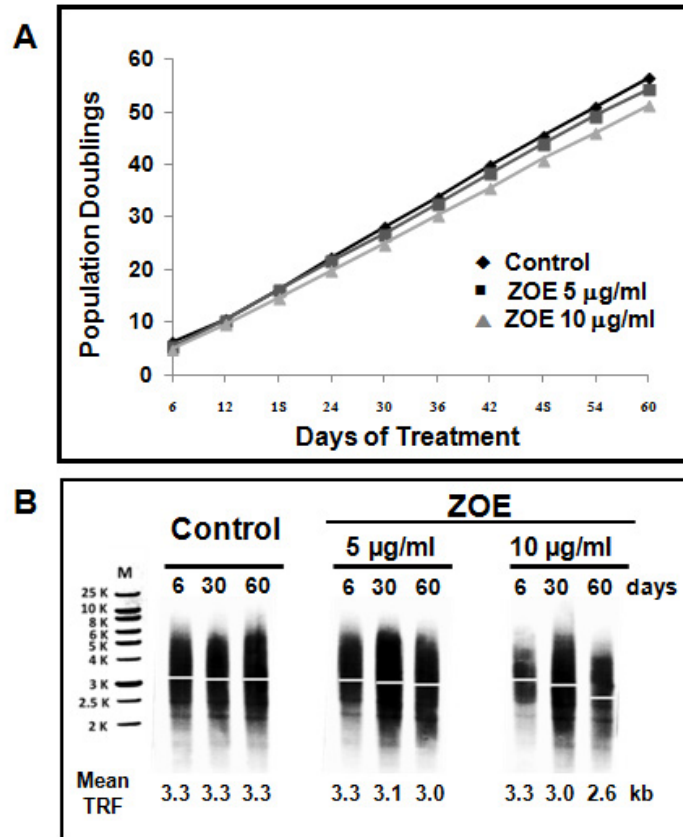
Figure 3.2: Population doublings (A) and telomere shortening (B) in long-term treatment of A549 cells with subcytotoxic doses of ZOE. A549 cells were incubated with or without (Control) the indicated concentration of ZOE supplemented in the culture media, with a change of fresh media every three days and subculturing of the cells every six days, up to 60 days. (A) Cells from each passage were counted, and the growth curves between the cumulative numbers of population doublings were plotted against time. (B) The A549 cells collected on Day 6, 30, and 60 were subjected to telomere length assay. The genomic DNA was extracted, and the mean telomere restriction fragments (TRF) were analyzed using the *TeloTAGGG* Telomere Length Assay kit. M represents a molecular weight marker.

The effect on cell senescence after long-term treatment with ZOE

One of the major causes of cellular senescence is telomere shortening. One or a few critically short telomeres can trigger DNA damage response pathways that eventually lead to cellular senescence [7,24]. From the experiments above, treating A549 cells with subcytotoxic doses of ZOE led to telomere shortening. Based on this finding, we further investigated whether this telomere shortening would accompany with the manifestation of cellular senescence. We conducted a senescence-associated β-galactosidase activity assay on the A549 cells collected from the long-term treatment study mentioned above. The A549 collected on Day 30 and 60 were recultured in a 6-well plate and allowed to grow for 24 h, before they were fixed, stained with X-gal solution, and photographed under a phase-contrast microscope. The blue-stained cells indicated the β-galactosidase positive cells, which often accompanied morphological changes. As shown in Figure 3.3A, there are more blue-stained cells in the experimental sets in which A549 cells were treated with ZOE than those found in the control set. The cells in each set were counted, and a graph between the percentage of the β-galactosidase positive cells and time was plotted (Figure 3.3B). In the control set, the percentage of the β-galactosidase positive cells remained around 10-15% of the cells collected on Day 30 and 60. However, after the A549 cells were treated with 5 µg/mL ZOE, the percentage of the β-galactosidase positive cells increased to 35% on Day 30, and then to 55% on Day 60, respectively. The percentage of the β-galactosidase positive cells was more profound after the A549 cells were treated with 10 µg/mL ZOE, with the percentage of the β-galactosidase positive cells rising to 43% on Day 30 and then to 69% on Day 60.
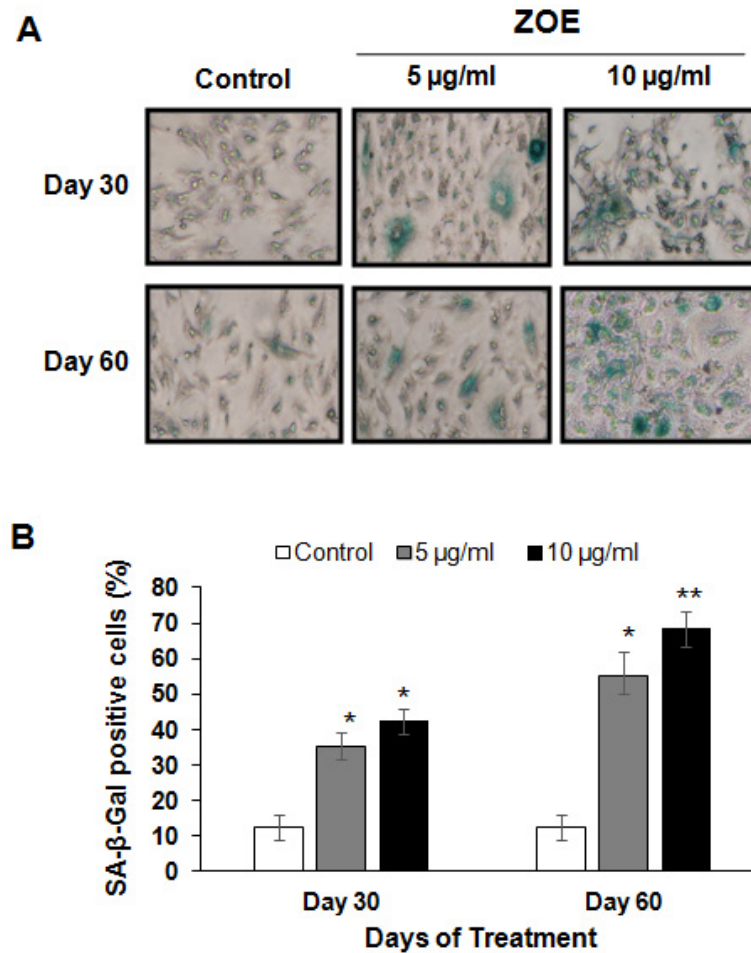
Figure 3.3: Senescence-associated β-galactosidase positive cells (A) and percentage of these cells (B) after long-term treatment with subcytotoxic doses of ZOE. The A549 cells from the long-term treatment with subcytotoxic doses experiment, collected on the indicated days, were subjected to senescence-associated β-galactosidase activity assay. The A549 cells (1×10^5 cells) were recultured in a 6-well plate and allowed to grow for 24 h. The cells were fixed, stained with X-gal solution, and photographed under a phase-contrast microscope. (A) The morphological changes and β-galactosidase positive cells (blue stained cells) are indicators of cell senescence. (B) The cells in each set were counted, and the percentage of the β-galactosidase positive cells were plotted against time. Differences are considered statistically significant when $* \, p < 0.05$ or $** \, p < 0.01$, compared to the control group.

The effect on clonogenicity after long-term treatment with ZOE

Cellular senescence is the state by which mitotic cells irreversibly stop dividing. This inability to divide can be tested using a simple colony-forming assay in which individual cells are spread on a tissue culture plate and allowed to form colonies. To evaluate the effect on clonogenicity of A549 cells after long-term treatment with ZOE, the A549 cells collected on Day 30 and 60 from the long-term treatment study were seeded at a low density (2×10^3 cells) in a 10-cm tissue culture dish and allowed to form colonies for a period of 14 days. The colonies were then stained with crystal violet and digitally scanned. The number of colonies was determined using the ImageQuant TL software. Figure 3.4A shows the pictures of the colony formation of the A549 cells collected from the untreated control set and the treated experimental sets (with 5 and 10 µg/mL of ZOE) on Day 30 and 60, respectively. The colonies from the untreated control set are densely populated, while the colonies from the treated experimental sets are less populous in a time- and concentration-dependent manner. The numbers of colonies were quantified, and the percentage of colony formations were compared to the control and plotted against time. The graph in Figure 3.4B shows that after the A549 cells were treated with 5 µg/mL ZOE, the percentage of colony formation decreased to 48% on Day 30, and to 42% on Day 60. After the A549 cells were treated with 10 µg/mL of ZOE, the percentage of colony formation decreased to 42% on Day 30, and to 35% on Day 60. From all of the experiments presented above, we conclude that ZOE suppresses *hTERT* expression and telomerase activity in A549 cells. The long-term treatment with subcytotoxic doses of ZOE in this cancer cell line leads to a gradual loss of telomere length, an induction of cellular senescence, and a reduction in clonogenicity.
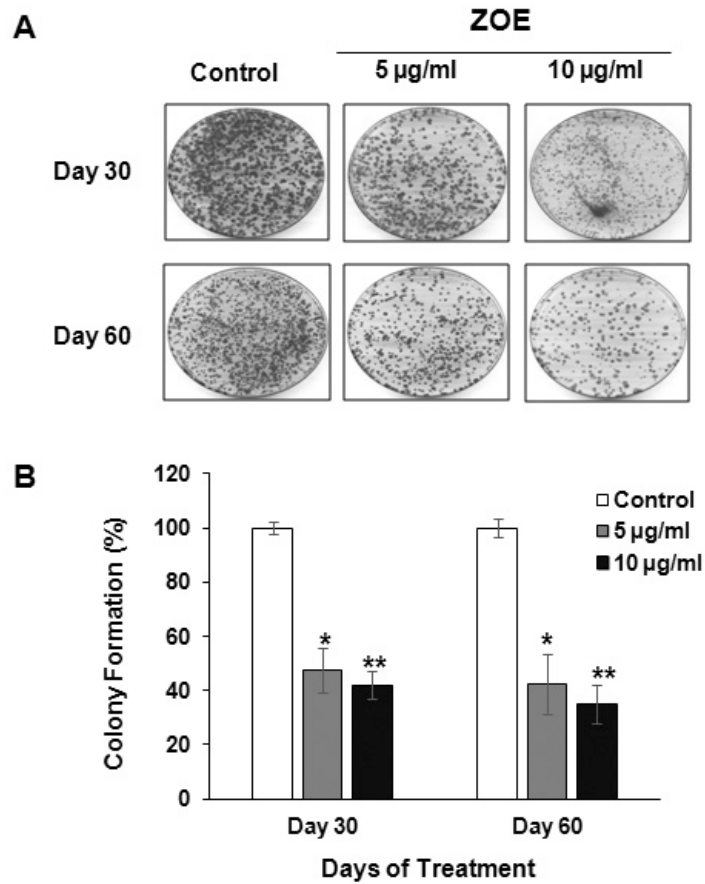
Figure 3.4: Clonogenicity of A549 cells (A) and percentage of colony formation (B) after long-term treatment with subcytotoxic doses of ZOE. The A549 cells collected on the indicated days were subjected to colony formation assay. The low number of cells $(2 \times 10^3$ cells) were recultured on a Petri dish. The cells were allowed to form colonies for 14 days and stained with crystal violet. Each plate was then scanned by a phosphoimager, and the colonies were counted using ImageQuant TL software. The percent colony formation was then plotted against time. Differences are considered statistically significant when $* \, p < 0.05$ or $** \, p < 0.01$, compared to the control group.

Identification of telomerase suppressors in ZOE

We employed assay-guided fractionation and GC/MS analysis to identify the active compounds in ZOE that suppress telomerase expression and activity in A549 cells. ZOE was purified by column chromatography to obtain 4 fractions: E1-E4. The ZOE and its fractions were fingerprinted by TLC and HPLC (SI Figure S3.1 and S3.2). The amount of 6-gingerol in these fractions was also quantified by HPLC. The E1 and E2 fractions contained an undetectable amount of 6-gingerol, while the E3 and E4 fractions contained about 30% and 40% of 6-gingerol, respectively. The semi-quantitative RT-PCR analysis found that only the E2 fraction significantly suppressed *hTERT* expression in a dose-dependent manner; while the E3 and E4 fractions, which contained a large amount of 6-gingerol, were not found to suppress *hTERT* expression (SI Figure S3.3A). These results confirm our previously published finding that 6-gingerol does not suppress *hTERT* expression [23].

We further fractionated the E2 fraction by column chromatography into four more subfractions: E2.1-E2.4. The results from RT-PCR studies showed that all of these subfractions could suppress the expression of *hTERT* in A549 cells (SI Figure S3.3B). These subfractions were then subjected to the same telomerase activity assay as previously described. All four subfractions were found to suppress telomerase activity in a concentration-dependent manner (SI Figure 3.4S).

We then employed GC/MS to identify the compounds within these subfractions. By using the fragment analysis of the ginger compounds reported by Tao *et al* [25] and Jolad *et al*.[26], we found that these active subfractions contained mostly paradols and shogaols of varying chain lengths (Table 3.1 and Figure 3.5). Therefore, we conclude that paradols and shogaols are likely to be the active compounds in ZOE that are responsible for the suppression of *hTERT* expression and telomerase activity. Although there are concerns about the thermal degradation and dehydration of compounds containing β-hydroxyketone group such as gingerols to aliphatic aldehyde, zingerone, and the corresponding shogaols under gas chromatography condition [26], we do not believe the paradols and shogaols we found in the E2.1-E2.4 subfractions were the products of thermal degradation or dehydration because gingerols were absent in the active E2 fraction, and were found only in E3 and E4 fractions.

Table 3.1: Major Compounds in the E2 Subfractions by GC/MS Analysis

E2.1	E2.2	E2.3	E2.4
11-paradol (75%)	11-paradol (26%)	7-paradol (42%)	6-shogaol (68%)
13-paradol (9%)	7-paradol (22%)	10-shogaol (33%)	8-shogaol (8%)
Bisabolene (7%)	6-paradol (22%)	11-paradol (9%)	10-shogaol (6%)
	9-paradol (16%)	6-paradol (6%)	7-paradol (5%)

*(%) represents percentage of peak area in GC chromatogram
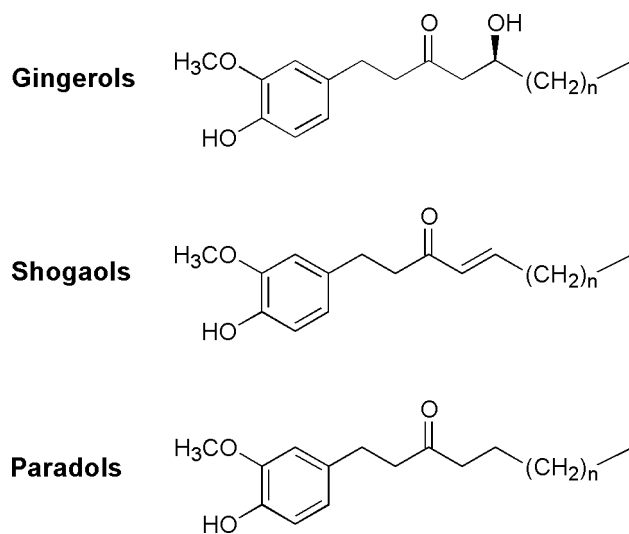
Figure 3.5: Chemical structures of gingerols, shogaols, and paradols.

Although the data and results above suggest that paradols and shogaols are likely the active compounds in ZOE and responsible for the suppression of *hTERT* expression and telomerase activity, we cannot rule out the possibility that some minor ingredients in the extract are responsible for the observed effects. To verify whether the activities arose specifically from paradols and shogaols, we obtained pure 6-paradol and pure 6-shogaol as representative compounds, and also pure 6-gingerol as a negative control. The same gene expression analysis by semiquantitative RT-PCR and telomerase activity assay were performed. The results are shown in Figure 3.6. The results showed that 6-paradol and 6-shogaol significantly suppressed *hTERT* expression in a dose-dependent manner, while 6-gingerol only slightly suppressed *hTERT* expression at a higher concentration. Telomerase activity in the cells treated with 6-paradol and 6-shogaol, but not 6-gingerol, was also suppressed in a concentration-dependent manner. These results confirmed that the suppression of *hTERT* expression and telomerase activity found in ZOE arose from the paradols and shogaols rather than the gingerols.

The chemical structures of gingerols, shogaols, and paradols (Figure 3.5) are similar in that they all contain the 4-hydroxy-3-methoxyphenyl nucleus linked to different side chains of various lengths at position 1. Gingerols contain a β-hydroxy ketone side chain, while shogaols contain an α,β-unsaturated ketone side chain, and paradols contain only one ketone group in their alkyl side chain. In term of chemistry, shogaols are the dehydrated form of gingerols, and paradols are the hydrogenated form of shogaols. The loss of activity to suppress *hTERT* expression and telomerase activity in gingerols might be due to the presence of the β-hydroxy group in the hydrocarbon side chain. The length of the side chain in paradols and shogaols might not affect the activity because all four subfractions (E2.1-E2.4), which have different compositions of paradols and shogaols (Table 3.1), had the capacity to suppress *hTERT* expression and telomerase activity.
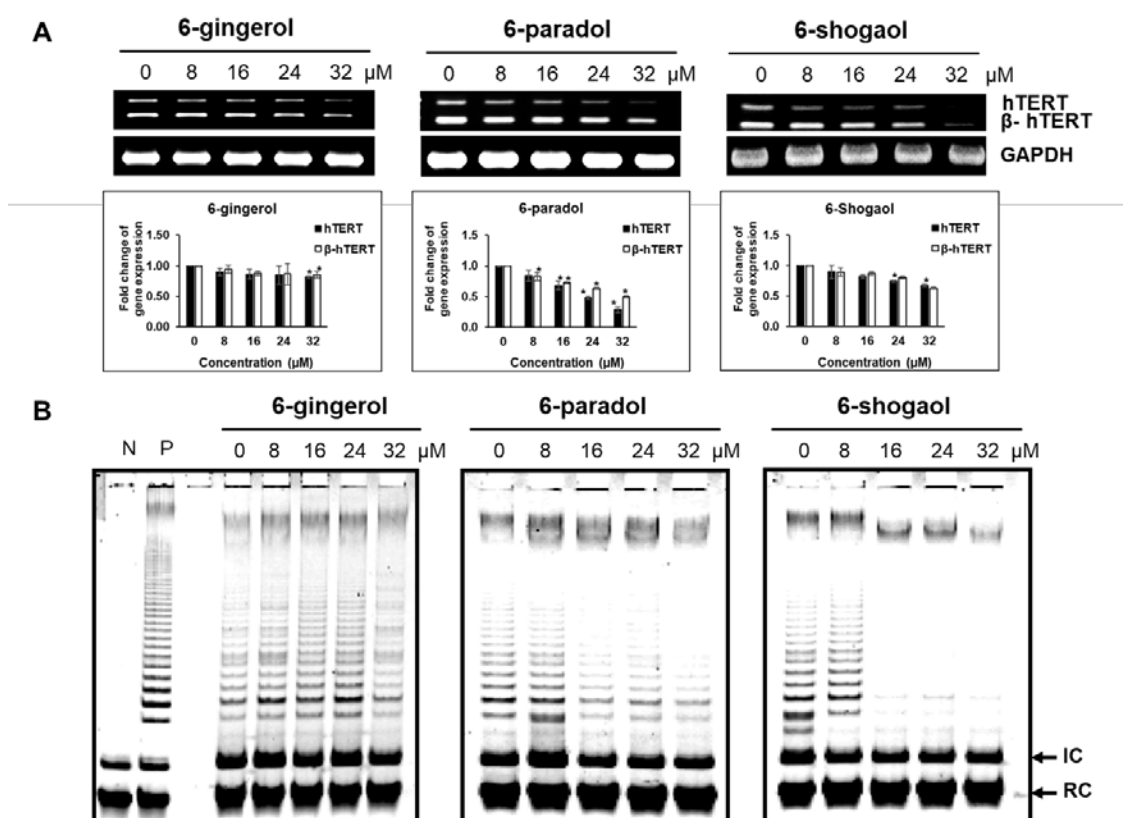
Figure 3.6: Effects of 6-gingerol, 6-paradol, and 6-shogaol on gene expression and telomerase activity in A549 lung cancer cells. (A) To assay for gene expression, the A549 cells were incubated with the indicated concentrations of the compound for 24 h before their RNAs were extracted and assayed by semiquantitative RT-PCR analysis. The hTERT and β-hTERT bands were quantified and normalized with those of GAPDH, and the graphs were plotted between fold change of gene expression and concentration. Differences are considered statistically significant when $* p < 0.05$ or $** p < 0.01$. (B) To assay the effect on telomerase activity, the A549 cells were incubated with the indicated concentrations of the compound for 48 h before the crude protein extract was used as the source of telomerase in a modified TRAP assay. Lane N represents the negative control experiment when telomerase was heat-denatured. Lane P represents the positive control.

DISCUSSION

Replicative senescence is a basic feature of normal somatic cells and is widely considered as a cancer prevention mechanism [7]. However, 85-90% of cancers escape this phenomenon by reactivating telomerase, which adds telomeric repeats to the 3′-end of telomeres [8]. Telomerase-specific inhibition should, therefore, not affect normal somatic cells. It would render cancer cells entering replicative senescence naturally, with the manifestation of telomere erosion occurring with each round of cell division similar to that of normal somatic cells. With this safe mode of action, telomerase-specific inhibition is an attractive strategy for cancer chemoprevention.

Dietary phytochemicals have attracted considerable interest for cancer prevention for some time due to their potential therapeutic effects and safety. In search of telomerase inhibitors from plants, a few natural phytochemicals were found to inhibit telomerase in cancer cells; these include curcumin, epigallocatechin-3-gallate (EGCG), resveratrol, genistein, sulforaphane, silibinin, and pristimerin, among others [30]. However, it is worth noting that only a few reports show the long-term effect of these phytochemicals on telomere shortening and cellular senescence after successive rounds of cell divisions using a nontoxic dose. This is probably due to their broad mechanism of actions and cytotoxicity. Among these few reports, EGCG is the only example that was found to induce telomere shortening and cellular senescence (in U937 leukemic cells and HT29 colon adenocarcinoma cells) with its nontoxic dose up to 55-60 population doublings.[31] Curcumin was also found to induce telomere shortening in several brain tumor cell lines after treating these cells with half the concentration of their IC_{50} for 15 days [32]. Similar to curcumin, thymoquinone (a compound from *Nigella sativa)* was found to induce telomere shortening in glioblastoma cell line M059K after treating these cells with approximately half the concentration of their IC_{50} for 15 days [33]. The *Inula viscosa* extracts, and its purified sesquiterpene lactone, tomentosin, were claimed to induce telomere shortening in cervical cancer cells [34,35]. However, these two reports only measured the length of the 3′ G-rich telomeric overhang after cells were treated with the test sample for 72 h.

In the present study, we add *Z. officinale* extract to this short list of plant-originated telomerase inhibitors that induce telomere shortening and cellular senescence in cancer cells using subcytotoxic doses. We first demonstrated that the *Z. officinale*

extract (ZOE) could suppress *hTERT* expression and telomerase activity in A549 lung cancer cells. The cells treated with the subcytotoxic doses of ZOE proliferated normally, but soon found to manifest telomere shortening and cellular senescence. Using assay-guided fractionation and GC/MS analysis, we found several paradols and/or shogaols as the major compounds in the active subfractions. The results from pure 6-paradol and 6-shogaol showed that these two compounds could suppress *hTERT* expression and telomerase activity in the A549 cells, although 6-gingerol could not. We have concluded that the active compounds in ZOE that are responsible for the suppression of *hTERT* expression and telomerase activity in A549 lung cancer cells are paradols and shogaols. Lastly, we also found that ZOE did not induce acute toxicity in rats and showed the anticlastogenic effect against liver micronucleus formation in rats.

Nowadays, much attention has been focused on products derived from food sources that provide extra health benefits. Cancer chemoprevention by dietary phytochemicals is of considerable interest due to their potential therapeutic effects and safety. Many dietary phytochemicals were found to possess chemopreventive properties in various epidemiological and pre-clinical studies [36]. Recently, clinical trials have added to the evidence supporting the efficacy of some selected compounds [37,38]. Ginger (*Zingiber officinale* Roscoe), an already established nutraceutical product, has been reputed to have anticancer properties in various experimental models. Experiments in A549 lung cancer cells reveal that gingerol, shogaol, and zerumbone exhibit anticancer activity through various mechanisms [39-43]. For example, gingerol was found to sensitize human lung cancer cells apoptosis.[39] 6-Shogaol was found to induce autophagy through the AKT/mTOR pathway and inhibit cancer via microsomal prostaglandin E2 synthase 1 (mPGES-1), β-catenin, and glycogen synthase kinase 3β (GSK-3β) pathways [40,41]. Moreover, 6-shogaol and its cysteine-conjugated metabolite induce lung cancer cell apoptosis through a p53 pathway in both *in vitro* and *in vivo* experiments [42]. Zerumbone was also found to suppress cell invasion through inhibiting the FAK/AKT/ROCK pathway [43]. Our present study shows that paradols and shogaols in the ginger extract (ZOE) suppressed telomerase, which led to telomere shortening and cellular senescence, with a significant reduction in clonogenicity of the A549 lung cancer, using only subcytotoxic doses. The extract was also found to be safe in rats, with an additional chemoprotective effect against DEN-induced liver micronucleus formation.

These results lead us to believe that ginger extract could potentially be a valuable tool in dietary cancer prevention against lung cancer.

METHODS

Chemicals

We purchased all materials from commercial suppliers. All oligonucleotides were supplied by Ward Medic (Thailand). The sulforhodamine B, 6-gingerol, and diethylnitrosamine were purchased from Sigma-Aldrich. Taq DNA polymerase was purchased from Vivantis. The collagenase type IV was purchased from Invitrogen (USA). Standard 6-shogaol and 6-paradol were provided by Prof. Apichart Suksamrarn (details of extraction, purification, and identification are shown in SI S1).

Plant collection and extraction

Ginger rhizome was collected in March 2012 from Lampang Province, Thailand, and was identified as *Zingiber officinale* Roscoe. A voucher specimen (BKF no. 118527) was deposited in the Forest Herbarium, Ministry of Natural Resources and Environment, Bangkok, Thailand. For the assay-guided fractionation study, ginger rhizomes (4.0 kg) were air-dried and finely pulverized. The ginger powder was then extracted into hexane, ethyl acetate, acetone, and methanol sequentially. After drying the solvents, we afforded 371.5 g, 235.8 g, 276.1 g, and 189.6 g of residues, respectively. The crude ethyl acetate extract (235.8 g) was purified by column chromatography using silica gel (Merck No. 7734, Mesh 70-230 ASTM) as the stationary phase. The first mobile phase was a gradient mixture of hexane (1 L) and ethyl acetate (1 L), followed by a gradient mixture of ethyl acetate (1 L) and methanol (1 L). The eluent was collected in a series of fractions, and the composition was visualized by thin layer chromatography (TLC), before the fractions with similar composition were collected into four main fractions, E1-E4. After evaporation, dry powders of E1 (85.7 g), E2 (16.5 g), E3 (23.1 g), and E4 (46.2 g) were obtained. The E2 fraction was found to suppress *hTERT* mRNA expression and telomerase activity, and 10 g of the E2 fraction was further purified by the same chromatography. The first mobile phase was a gradient mixture of hexane (100 mL) and ethyl acetate (100 mL), followed by a gradient mixture of ethyl acetate (100 mL) and methanol (100 mL). After evaporation, dry powders of E2.1 (2.2 g), E2.2 (1.7 g), E2.3 (3.1 g), and E2.4 (2.8 g) were obtained. These fractions and subfractions were dissolved

in dimethyl sulfoxide (DMSO) and stored at 4 °C. Prior to use, the stock solutions were diluted with distilled deionized water to working solutions with the same concentration of DMSO. The final concentration of DMSO was the same in all samples and was between 0.16-0.64% in the short-term cell culture experiments. For the long-term treatment of A549 cells, the crude ethyl acetate fraction of *Z. officinale* (ZOE) was obtained in a similar manner. The final concentration of DMSO in both experimental set and control set was 0.05%.

Thin layer chromatography (TLC) analysis

ZOE and its fractions and subfractions were TLC fingerprinted using silica gel GF254 (Fluka) as the stationary phase, and a mixture of hexane and ethyl acetate was used as the mobile phase. The TLC plate was then dipped in p-anisaldehyde/sulfuric acid reagent before color developing by heating at 100 °C.

High performance liquid chromatography (HPLC) analysis

We performed the HPLC analyses using an HPLC system (Agilent 1200 infinity series, Agilent, USA) and a C18 reverse phase column (4.6 mm x 150 mm, ZORBAX Eclipse Plus) as the stationary phase. A 50 μL sample of ZOE and its fractions (E1-E4) (10 mg/ml) were separated using a mixture of acetonitrile (A) and water (B) as the mobile phase at a flow rate of 2.0 mL/min. Within the total run time of 10 minutes, the solvent mixture profile of the mobile phase was as follows: 0-0.5 min, 35A:65B; 0.5-5 min, gradient mixture from 35A:65B to 95A:5B; and 5-10 min, 95A:5B. The compounds were detected using a UV-visible detector (Spec Monitor® 3200) at 280 nm. The mixture of standard 6-gingerol (0.4 mg/ml), 6-shogaol (0.2 mg/ml), and 6-paradol (0.2 mg/ml) was run separately using the same conditions.

Cell culture

The A549 human lung carcinoma cell line was obtained from American Type Culture Collection (Rockville, MD) and grown in RPMI 1640 culture media with 10% fetal bovine serum (FBS) and 1% antibiotics (50 μg/mL streptomycin, 50 units/mL penicillin) at 37 °C in a humidified incubator with 5% CO_2.

In vitro growth inhibition assays

We determined the growth inhibition of A549 cells by ginger extract and selected ginger compounds using sulforhodamine B (SRB) assay according to a published

protocol [44]. The A549 cells (1.0×10^4 cells) were incubated with various concentrations of the indicated ginger fraction or the pure compound at 37 ˚C for 72 h in a humidified incubator with 5% CO_2. The graphs between the concentration of the test sample and the percentage of cell viability, from three independent experiments, were plotted, and the 50% growth inhibitory concentrations (IC_{50}) were determined. The IC_{50} growth inhibitory concentrations of A549 lung cancer cells by ZOE, its subfractions, and some pure compounds are summarized in SI Table S3.1.

Semiquantitative RT-PCR analysis

We grew A549 cells (5.0×10^5 cells) on a 6-well tissue culture plate for 24 h at 37 °C, before they were treated with the indicated concentration of the test sample for another 24 h. The total RNA was collected, and the mRNA was converted into cDNA using RevertAid reverse transcriptase (Thermo Scientific). PCR amplification for each gene was carried out with the gene-specific primers. The primer sequences, annealing temperatures, and PCR cycles are summarized in SI Table S3.2.

Modified fluorescent telomeric repeat amplification protocol (TRAP) assay

We performed the TRAP assay according to a published protocol and our previous publication [23,45]. Briefly, the A549 cells (5.0×10^5 cells) were seeded on a 6-well tissue culture plate for 24 h before the test sample at the indicated concentration was added to the culture media. The cells were incubated for another 48 h before they were lysed with 200 μL of CHAPS lysis buffer. The 10 μg of crude cell extract was then used as the telomerase source in the telomerase reaction mixture, in which it extends a primer at 30 °C for 30 min. The DNA amplification mixture was added, and the telomerase-extended products were amplified by PCR. The amplified products were separated by non-denaturing acrylamide gel electrophoresis and results were recorded using a phosphoimaging system (Typhoon; Molecular Dynamics). The oligonucleotides used in this assay are summarized in SI Table S3.3.

Long-term proliferation assay

We compared three sets of A549 cell cultures for the long-term proliferation assay: the control group and the two experimental groups with the subcytotoxic doses (5 and 10 μg/mL) of ZOE added in the culture media. We subcultured A549 cells (1.5×10^5 cells) onto a 75 cm^2 tissue culture flask, with or without the indicated concentration

of ZOE, in RPMI 1640 medium supplemented with 10% fetal bovine serum. We changed the culture media after 3 days, and on Day 6, we trypsinized, collected, and counted the cells. Then, the process was repeated up to 60 days. The equation: $n = (\log P_n - \log P_0)/\log 2$, where P_n is the number of cells after n doublings, and P_0 is the initial seeding density, was then used to calculate the number of population doublings. The graph between cumulative number of population doublings and time was then plotted.

Telomere length assay

We performed a telomere length analysis using *TeloTAGGG* Telomere Length Assay kit (Roche Applied Science) according to the manufacturer's instruction and our published protocol [46]. The formula $\sum(ODi)/ \sum(ODi/Li)$, where ODi indicates the signal at the position i, and Li is the molecular weight marker at the same position was used to calculate the mean telomere restriction fragment (TRF) length.

Senescence-associated β-galactosidase activity assay

We performed β-galactosidase activity assay according to our published protocol [46]. We first grew the A549 cells (1×10^5 cells) collected from the long-term proliferation study in a 6-well plate for 24 h, before they were fixed with 2% formaldehyde and 0.2% glutaraldehyde solution. After that, the cells were washed and incubated in the 5-bromo-4-chloro-3-indolyl-β-D-galactopyranoside (X-gal) solution overnight at room temperature. Cells with β-galactosidase activity cleave X-gal and produce a blue stain. The β-galactosidase positive cells were monitored under a phase contrast microscope with a blue stain, usually accompanied by cell morphological changes. In each experiment, the blue-stained cells were counted in the field with more than 400 cells, for at least 10 fields. The graph between the percentage of β-galactosidase positive cells and time was then plotted.

Colony-forming assays

We performed a colony-forming assay according to our published protocol [46]. We first seeded the A549 cells collected from the long-term proliferation assay in a 10-cm dish at a low density (2×10^3 cells) and allowed the colonies to form for 2 weeks, with the change of fresh growth media every 3 days. Crystal violet was then used to stain the colonies. The number of colonies was obtained using the ImageQuant TL software (Nonlinear Dynamics).

Gas chromatography-mass spectrometry (GC-MS)

GC-MS data were collected with a GC7890 instrument from Agilent Technologies, with a DB-5MS column (30 m × 0.25 mm ID × 0.25 μm film thickness). The temperature programming was as follows: 50 °C, 5 min; to 200 °C at 10 °C/min; to 250 °C at 5 °C/min; and 250 °C, 35 min, and the ionizing voltage was 70 eV, with 1 μL split injection (split ratio 25:1). The flow rate of Helium gas was 1.5 mL/min. The identification of compounds was obtained using the Agilent Enhanced Chemstation MSD Data Analysis Tool with W8N08 mass spectrum library (John Wiley & Sons, Inc., USA).

For assays in cell culture, data were from triplicate samples of three independent experiments. Statistical significance between treatments and controls was analyzed using Student's t-test analysis. For assays in rats, data of each variable for each group are reported as means ± SD. The significance of differences between groups was analyzed using one-way analysis of variance (ANOVA) with the least significant difference (LSD) for post hoc tests. Values of $p < 0.05$ (*) were considered to be significant.

ACKNOWLEDGMENTS

REFERENCES

1. Meena, J.; Rudolph, K. L.; Günes, C. Telomere dysfunction, chromosomal instability and cancer. *Recent Results Cancer Res*. **2015**, *200*, 61-79.
2. Tomita, K.; Cooper J. P. The telomere bouquet controls the meiotic spindle. *Cell* **2007**, *130*, 113-126.
3. Martínez, P.; Blasco, M. A. Role of shelterin in cancer and aging. *Aging Cell* **2010**, *9*, 653-66.
4. Shay, J. W.; Wright, W. E. Hayflick, his limit, and cellular ageing. *Nat. Rev. Mol. Cell Biol.* **2000**, *1*, 72-6.
5. Victorelli, S.; Passos, J. F. Telomeres and cell senescence - Size matters not. *EBioMedicine* **2017**, *21*, 14-20.
6. Benarroch-Popivker, D.; Pisano, S.; Mendez-Bermudez, A.; Lototska, L.; Kaur, P.; Bauwens, S.; Djerbi, N.; Latrick, C. M.; Fraisier, V.; Pei, B.; Gay, A.; Jaune, E.; Foucher, K.; Cherfils-Vicini J.; Aeby, E.; Miron, S.; Londoño-Vallejo, A.; Ye, J.; Le Du, M. H.; Wang, H.; Gilson, E.; Giraud-Panis, M. J. TRF2-mediated control of telomere DNA topology as a mechanism for chromosome-end protection. *Mol. Cell* **2016**, *61*, 274-286.
7. Ohtani, N.; Mann, D. J.; Hara, E. Cellular senescence: Its role in tumor suppression and aging. *Cancer Sci.* **2009**, *100*, 792-797.
8. Kim, N. W.; Piatyszek, M. A.; Prowse, K. R.; Harley, C. B.; West, M. D.; Ho, P. L.; Coviello, G. M.; Wright W. E.; Weinrich, S. L.; Shay, J. W. Specific association of human telomerase activity with immortal cells and cancer. *Science* **1994**, *266*, 2011-2015.
9. Kumar, M.; Lechel, A.; Güneş, Ç. Telomerase: The Devil Inside. *Genes (Basel)* **2016**, *7*, E43.
10. Cohen, S. B.; Graham, M. E.; Lovrecz, G. O.; Bache, N.; Robinson, P. J.; Reddel, R. R. Protein composition of catalytically active human telomerase from immortal cells. *Science* **2007**, *315*, 1850-1853.
11. Ramlee, M. K.; Wang, J.; Toh, W. X.; Li, S. Transcription regulation of the human telomerase reverse transcriptase (hTERT) gene. *Genes (Basel)* **2016**, *7*, E50.
12. Scalbert, A.; Andres-Lacueva, C.; Arita, M.; Kroon, P.; Manach, C.; Urpi-Sarda, M.; Wishart, D. Databases on food phytochemicals and their health-promoting effects. *J. Agric. Food Chem.* **2011**, *59*, 4331-4348.
13. Gullett, N. P.; Ruhul Amin, A. R.; Bayraktar, S.; Pezzuto, J. M.; Shin, D. M.; Khuri, F. R.; Aggarwal, B. B.; Surh, Y. J.; Kucuk, O. Cancer prevention with natural compounds. *Semin. Oncol.* **2010**, *37*, 258-281.
14. Gomez, D. L.; Armando, R. G.; Cerrudo, C. S.; Ghiringhelli, P. D.; Gomez, D. E. Telomerase as a Cancer Target. Development of New Molecules. *Curr. Top. Med. Chem.* **2016**, *16*, 2432-2440.
15. Shay, J. W.; Keith, W. N. Targeting telomerase for cancer therapeutics. *Br. J. Cancer* **2008**, *98*, 677-683.
16. Alibakhshi, A.; Ranjbari, J.; Pilehvar-Soltanahmadi, Y.; Nasiri, M.; Mollazade, M.; Zarghami, N. An update on phytochemicals in molecular target therapy of cancer: Potential inhibitory effect on telomerase activity. *Curr. Med. Chem.* **2016**, *23*, 2380-2393.
17. Kundu, J. K.; Na, H. K.; Surh, Y. J. Ginger-derived phenolic substances with cancer preventive and therapeutic potential. *Forum. Nutr.* **2009**, *61*, 182-192.

18. Nigam, N.; George, J.; Shukla, Y. Ginger (6-gingerol). In *Molecular Targets and Therapeutic Uses of Spices: Modern Uses for Ancient Medicine*, Aggarwal B. B., Kunnumakkara A. B., eds.; World Scientific Publishing Co. Inc.: Hackensack, NJ., 2009, 225–256.

19. Kaur, I. P.; Deol, P. K.; Kondepudi, K. K.; Bishnoi, M. Anticancer potential of ginger: Mechanistic and pharmaceutical aspects. *Curr. Pharm. Des*. **2016**, *22*, 4160-4172.

20. Wang, C. Z.; Qi, L. W.; Yuan, C. S. Cancer chemoprevention effects of ginger and its active constituents: Potential for new drug discovery. *Am. J. Chin. Med*. **2015**, *43*, 1351-1363.

21. Zhang, F.; Thakur, K.; Hu, F.; Zhang, J. G.; Wei, Z. J. 10-Gingerol, a Phytochemical Derivative from "Tongling White Ginger", Inhibits Cervical Cancer: Insights into the Molecular Mechanism and Inhibitory Targets. *J. Agric. Food Chem.* **2017**, *65*, 2089-2099.

22. Hsu, Y. L.; Hung, J. Y.; Tsai, Y. M.; Tsai, E. M.; Huang, M. S.; Hou, M. F.; Kuo, P. L. 6-shogaol, an active constituent of dietary ginger, impairs cancer development and lung metastasis by inhibiting the secretion of CC-chemokine ligand 2 (CCL2) in tumor-associated dendritic cells. *J. Agric. Food Chem.* **2015**, *63*, 1730-1738.

23. Tuntiwechapikul, W.; Taka, T.; Songsomboon, C.; Kaewtunjai, N.; Imsumran, A.; Makonkawkeyoon, L.; Pompimon, W.; Lee, TR. Ginger extract inhibits human telomerase reverse transcriptase and c-Myc expression in A549 lung cancer cells. *J. Med. Food* **2010**, *13*, 1347-1354.

24. Hemann, M. T.; Strong, M. A.; Hao, L. Y.; Greider, C. W. The shortest telomere, not average telomere length, is critical for cell viability and chromosome stability. *Cell* **2001**, *107*, 67-77.

25. Tao, Y.; Li, W.; Liang, W.; Van Breemen, R. B. Identification and quantification of gingerols and related compounds in ginger dietary supplements using high-performance liquid chromatography-tandem mass spectrometry. *J. Agric. Food Chem.* **2009**, *57*, 10014-10021.

26. Jolad, S. D.; Lantz, R. C.; Solyom, A. M.; Chen, G. J.; Bates, R. B.; Timmermann, B. N. Fresh organically grown ginger (*Zingiber officinale*): Composition and effects on LPS-induced PGE2 production. *Phytochemistry* **2004**, *65*, 1937-1954.

27. Moghaddasi, M. S.; Kashani, H. H., Ginger (*Zingiber officinale*): a review. *J. Med. Plants Res.* **2012**, *6*, 4255-4258.

28. Mansour, M. A.; Bekheet, S. A.; Al-Rejaie, S. S.; Al-Shabanah, O. A.; Al-Howiriny, T. A.; Al-Rikabi, A. C.; Abdo, A. A. Ginger ingredients inhibit the development of diethylnitrosamine induced premalignant phenotype in rat chemical hepatocarcinogenesis model. *Biofactors* **2010**, *36*, 483-490.

29. Habib, S. H.; Makpol, S.; Abdul Hamid, N. A.; Das, S.; Ngah, W. Z.; Yusof, Y. A. Ginger extract (*Zingiber officinale*) has anti-cancer and anti-inflammatory effects on ethionine-induced hepatoma rats. *Clinics (Sao Paulo)* **2008**, *63*, 807-813.

30. Alibakhshi, A.; Ranjbari, J.; Pilehvar-Soltanahmadi, Y.; Nasiri, M.; Mollazade, M.; Zarghami, N. An update on phytochemicals in molecular target therapy of cancer: Potential inhibitory effect on telomerase activity. *Curr. Med. Chem.* **2016**, *23*, 2380-2393.

31. Naasani, I.; Seimiya, H.; Tsuruo, T. Telomerase inhibition, telomere shortening, and senescence of cancer cells by tea catechins. *Biochem. Biophys. Res. Commun.* **1998**, *249*, 391-396.

32. Khaw, A. K.; Hande, M. P.; Kalthur, G.; Hande M. P. Curcumin inhibits telomerase and induces telomere shortening and apoptosis in brain tumour cells. *J. Cell. Biochem.* **2013**, *114*, 1257-1270.

33. Gurung, R. L.; Lim, S. N.; Khaw, A. K.; Soon, J. F.; Shenoy, K.; Mohamed Ali, S.; Jayapal, M, Sethu, S.; Baskar R.; Hande, M. P. Thymoquinone induces telomere shortening, DNA damage and apoptosis in human glioblastoma cells. *PLoS. One* **2010**, *5*, e12124.

34. Merghoub, N.; El Btaouri, H.; Benbacer, L.; Gmouh, S.; Trentesaux, C.; Brassart, B.; Terryn, C.; Attaleb, M.; Madoulet, C.; Benjouad, A.; Amzazi, S.; El Mzibri, M.; Morjani, H. *Inula viscosa* extracts induces telomere shortening and apoptosis in cancer cells and overcome drug resistance. *Nutr. Cancer* **2016**, *68*, 131-143.

35. Merghoub, N.; El Btaouri, H.; Benbacer, L.; Gmouh, S.; Trentesaux, C.; Brassart, B, Attaleb, M.; Madoulet, C.; Wenner, T.; Amzazi, S.; Morjani, H.; El Mzibri, M. Tomentosin induces telomere shortening and caspase-dependent apoptosis in cervical cancer cells. *J. Cell. Biochem.* **2017**, *118*, 1689-1698.

36. Surh, Y.-J. Cancer chemoprevention with dietary phytochemicals. *Nature Rev. Cancer* **2013**, *3*: 768-780.

37. Kotecha, R.; Takami, A.; Espinoza, J. L. Dietary phytochemicals and cancer chemoprevention: a review of the clinical evidence. *Oncotarget* **2016**, *7*, 52517-52529.

38. Baena Ruiz, R.; Salinas Hernández, P. Cancer chemoprevention by dietary phytochemicals: Epidemiological evidence. *Maturitas* **2016**, *94*, 13-19.

39. Nazim, U, M.; Jeong, J, K.; Seol, J, W.; Hur, J.; Eo, S, K.; Lee, J, H.; Park, S, Y. Inhibition of the autophagy flux by gingerol enhances TRAIL-induced tumor cell death. *Oncol. Rep.* **2015**, *33*, 2331-2336.

40. Hung, J, Y.; Hsu, Y, L.; Li, C, T.; Ko, Y, C.; Ni, W, C.; Huang, M, S.; Kuo, P, L. 6-Shogaol, an active constituent of dietary ginger, induces autophagy by inhibiting the AKT/mTOR pathway in human non-small cell lung cancer A549 cells. *J. Agric. Food Chem.* **2009**, *57*, 9809-9816.

41. Eren, D.; Betul, Y, M. Revealing the effect of 6-gingerol, 6-shogaol and curcumin on mPGES-1, GSK-3β and β-catenin pathway in A549 cell line. *Chem. Biol. Interact.* **2016**, *258*, 257-265.

42. Warin, R, F.; Chen, H.; Soroka, D, N.; Zhu, Y.; Sang, S. Induction of lung cancer cell apoptosis through a p53 pathway by [6]-shogaol and its cysteine-conjugated metabolite M2. *J. Agric. Food Chem.* **2014**, *62*, 1352-1362.

43. Kang, C, G.; Lee, H, J.; Kim, S, H.; Lee, E, O. Zerumbone suppresses osteopontin-induced cell invasion through inhibiting the FAK/AKT/ROCK pathway in human non-small cell lung cancer A549 cells. *J. Nat. Prod.* **2016**, *79*, 156-160.

44. Vichai, V.; Kirtikara, K. Sulforhodamine B colorimetric assay for cytotoxicity screening. *Nat. Protoc.* **2006**, *1*, 1112-1116.

45. Szatmari, I.; Aradi, J. Telomeric repeat amplification, without shortening or lengthening of the telomerase products: a method to analyze the processivity of telomerase enzyme. *Nucleic Acids Res.* **2001**, *29*, E3.

46. Taka, T.; Huang, L.; Wongnoppavich, A.; Tam-Chang, S, W.; Lee, T, R.; Tuntiwechapikul, W. Telomere shortening and cell senescence induced by perylene derivatives in A549 human lung cancer cells. *Bioorg. Med. Chem.* **2013**, *21*, 883-890.
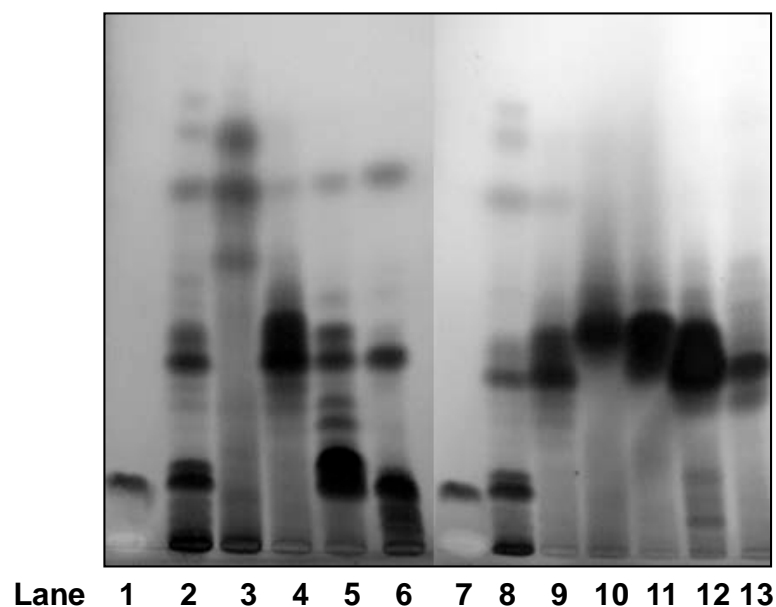
Figure S3.1: TLC fingerprinting of the *Z. officinale* extracts (E1-E4 fractions and E2.1-E2.4 subfractions). TLC fingerprinting of the *Z. officinale* extracts was performed using silica gel GF254 (Fluka) as the stationary phase and the solvent mixture of hexane and ethyl acetate (3:1) as the mobile phase. The TLC plate was then dipped in *p*-anisaldehyde/sulfuric acid reagent before color developing by heating at 100 °C. Lane 1, 7 = standard 6-gingerol; Lane 2, 8 = crude ethyl acetate extract; Lane 3-6 = E1-E4 fractions; Lane 9 = E2 fraction; Lane 10-13 = E2.1-E2.4 subfractions.
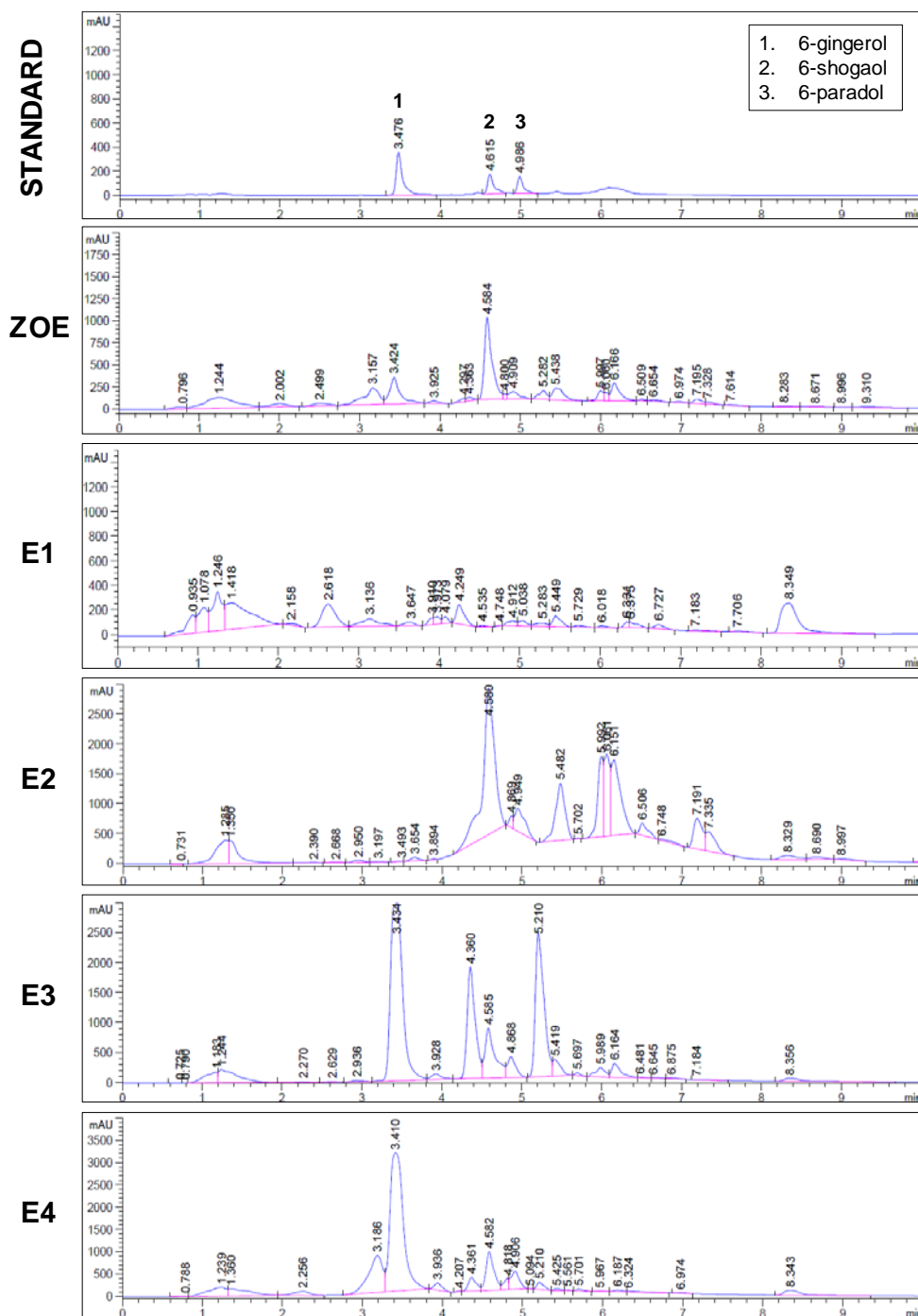
Figure S3.2: The HPLC chromatograms of the crude ethyl acetate extract of *Z. officinale* (ZOE) and its fractions (E1-E4). A 50 μL aliquot of each sample (10 mg/ml) was separated by HPLC (Agilent 1200 infinity series, Agilent, USA) using a C18 reverse phase column (4.6 mm x 150 mm, ZORBAX Eclipse Plus) as the stationary phase and a mixture of acetonitrile (A) and water (B) as the mobile phase at a flow rate of 2.0 mL/min. Within the total run time of 10 minutes, the solvent mixture profile of the mobile phase was as follows: 0-0.5 min, 35A:65B; 0.5-5 min, gradient mixture from 35A:65B to 95A:5B; and 5-10 min, 95A:5B. The compounds were detected using a UV-visible detector (Spec Monitor® 3200) at 280 nm. The mixture of standard 6-gingerol (0.4 mg/ml), 6-shogaol (0.2 mg/ml), and 6-paradol (0.2 mg/ml) was run separately using the same conditions.

Figure S3.3: Effects of ZOE fractions on *hTERT* expression by semiquantitative RT-PCR: (A) E1-E4 fractions and (B) E2.1-E2.4 subfractions. A549 cells (5.0×10^5 cells) were treated with various concentrations of each fraction for 24 h before the mRNAs were extracted from the cell lysate, converted to cDNAs, and amplified by PCR using gene-specific primers. The 457-bp RT-PCR products represent the full-length hTERT mRNA, and the 275-bp RT-PCR products represent the β-hTERT mRNA. The 450-bp RT-PCR products represent the GAPDH mRNA as the internal control gene.
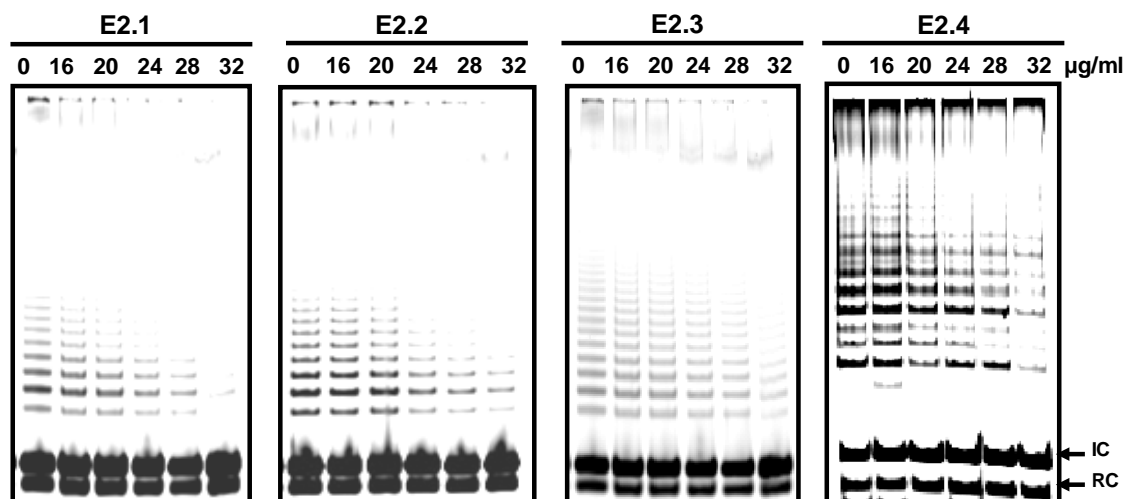
Figure S3.4: Effects of ZOE subfractions (E2.1-E2.4) on telomerase activity by modified TRAP assay. A549 cells (5.0 x 10^5 cells) were incubated with the indicated concentrations of each subfraction for 48 h before the crude protein extract was used as the source of telomerase in a modified TRAP assay. IC and RC represent internal control and recovery control, respectively.

Table S3.1: The IC$_{50}$ Growth Inhibitory Concentration of A549 Lung Cancer Cells by ZOE, Its Subfractions, and Selected Pure Compounds

Z. officinale Extracts	IC$_{50}$ (µg/ml)
ZOE	58.2 ± 2.1
E1	54.9 ± 3.5
E2	21.1 ± 1.6
E3	38.9 ± 0.7
E4	25.6 ± 4.3
E2.1	43.2 ± 4.5
E2.2	26.5 ± 1.6
E2.3	23.6 ± 1.2
E2.4	17.4 ± 3.9
6-gingerol	11.3 ± 0.8
	$(38.6 \pm 2.8 \ \mu M)$
6-paradol	10.1 ± 0.2
	$(36.2 \pm 0.7 \ \mu M)$
6-shogaol	8.0 ± 0.3
	$(28.9 \pm 1.3 \ \mu M)$

Table S3.2: Primer Sequences and Conditions Used in Semiquantitative RT-PCR

Name	Primer Sequence	Product Size (bp)	Annealing Temp. (°C)	PCR Cycle
GAPDH (F)	CCACAGTCCATGCCATCAC	450	60	20
GAPDH (R)	CCACCACCCTGTTGCTGTA			
c-Myc (F)	TAATTCCAGCGAGAGGCAGA	290	60	25
c-Myc (R)	GTCCCCAAATGGGCAGAATA			
hTEP1 (F)	TCAAGCCAAACCTGAATCTGAG	264	60	26
hTEP1 (R)	CCCCGAGTGAATCTTTCTACGC			
hTERT (F)	GCCTGAGCTGTACTTTGTCAA	275, 457	62	30
hTERT (R)	CGCAAACAGCTTGTTCTCCATGTC			
hTR (F)	GAAGGGCGTAGGCGCCGTGCTTTTGC	111	62	30
hTR (R)	GTTTGCTCTAGAATGAACGGTGGAAGG			
TRF1 (F)	TGTGCGGATGGTAGGGATGC	421	62	28
TRF1 (R)	GGGCTGATTCCAAGGGTGTA			
TRF2 (F)	AGTCAATCGCTGGGTGCTCA	636	62	25
TRF2 (R)	CCTGGTGCTGGCTGTTTATC			

* F = Forward primer, R = Reverse primer

Table S3.3: Oligonucleotides Used in the Modified Fluorescent TRAP Assay

Name	Sequence
MTS	5'-AGCATCCGTCGAGCAGAGTT-3'
RPc3g	5′-TAGAGCACAGCCTGTCCGTG(CTAACC)$_3$GG-3′
RP-FAM	FAM-5′-TAGAGCACAGCCTGTCCGTG-3′
IC	5'-TAGAGCACAGCCTGTCCGTGAAAAGGCCGAGAAGCGATCG-3'
NT	5'-CGATCGCTTCTCGGCCTTTT-3'

CHAPTER 4

Synthesis and DNA Binding Studies of New Perylene Derivatives

SUMMARY

New perylene derivatives, including symmetrical perylene diimide, asymmetrical perylene diimide, and asymmetrical monoimide derivatives, were synthesized and characterized. Their solubility, absorption spectra, and fluorescence spectra were studied. DNA binding selectivity of these compounds with various G-quadruplex motifs and duplex DNA was investigated using spectrophotometry, fluorescent intercalator displacement (FID) assay, and duplex-quadruplex competition. Results showed that aPDI-PHis, an asymmetrical perylene diimide derivative, had a broader range of solubility than PIPER, the prototypic perylene diimide derivative. It also bound better to G-quadruplex and had better telomerase inhibition than PIPER. These results suggest that having two different sidechains with selective properties might enhance the activity of perylene derivatives, which might lead to a better drug to use as a telomerase inhibitor.

4.1   Synthesis of PIPER, PM2, and new perylene monoimides

From our previous publication, we found that PIPER and PM2 could inhibit telomerase in an *in vitro* assay, and long-term treatment with a sub-cytotoxic dose of these compounds in A549 lung cancer cells led to telomere shortening and cellular senescence. PIPER is a symmetrical perylene diimide derivative, while PM2 is an asymmetrical perylenemonoimide derivative (Figure 4.1).

Figure 4.1: Chemical structures of PIPER and PM2

In order to be able to have an extensive study of these compounds, especially the research in an animal model which requires a large amount of compound to study, we set out to synthesis perylene derivatives in our laboratory. Besides from PIPER and PM2, we also decided to synthesize other perylene derivatives in three different groups: the symmetrical perylenediimide (PDI), the asymmetrical perylenediimide (aPDI), and the asymmetrical perylenemonoimide (aPMI), as shown as the general structures in Figure 4.2.
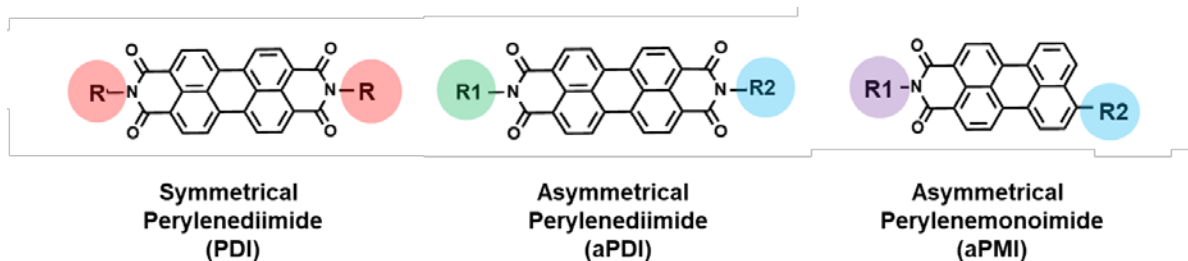
Figure 4.2: General structures of three groups of perylene derivatives

96

4.1.1 Synthesis of symmetrical perylenediimide (PDI) derivatives

The synthesis of the PDIs is a one-step reaction as illustrated in Scheme 4.1. The perylene-3,4,9,10-tetracarboxylic dianhydride (PTCD) was mixed with the selected amine to form the sidechains and refluxed for several hours. The final product was then purified from the reaction mixture. The PDIs synthesized in this project are summarized in Table 4.1.
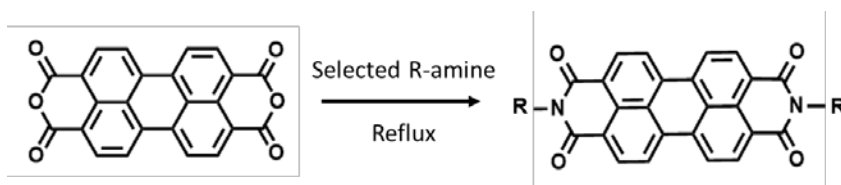
Scheme 4.1: Synthesis of PDIs

Table 4.1: List of symmetric perylene diimide derivatives

Name	Structure
PIPER	
PIPER3	
PDI-His	
PDI-Glu	
PDI-Ser	
PDI-Tris	

97

4.1.1.1 PIPER [N,N'-bis-(2-(1-piperidino)ethyl)-3,4,9,10-perylene tetracarboxylic acid diimide]

PTCD (1.0 g, 2.5 mmol) was mixed with 0.8 mL (0.72 g, 5.6 mmol) of 1-(2-aminoethyl) piperidine in 10 mL of DMF and 10 mL of 1,4-dioxane. The bright red mixture was heated under reflux for 4 hours until it became dark purple. The solvents were removed under reduced pressure. The resulting purple residue was dissolved in 1M HCl solution, and the solution was allowed to stand overnight in a refrigerator. Insoluble impurities were removed by suction filtration, and the resulting solution was adjusted to pH 12 with the addition of NaOH. A dark purple product precipitated and was isolated by suction filtration. The precipitate was washed with deionized water and dried under vacuum to afford 1.4 g (89% yield) of the desired product.
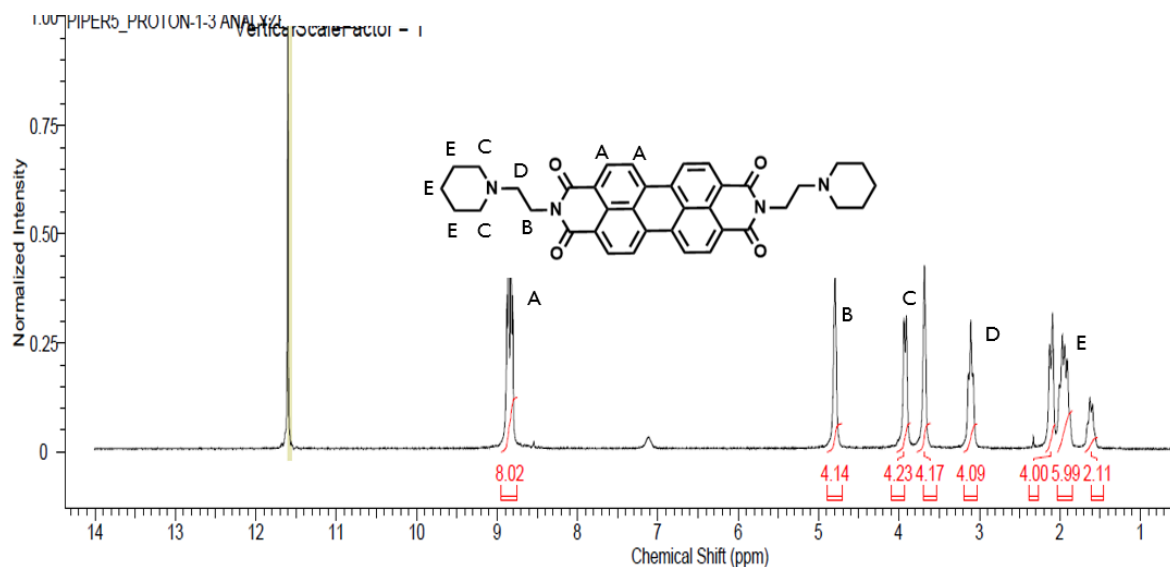
Figure 4.3:^{1}H NMR Spectrum of PIPER in CF$_3$COOD at 400 MHz

PIPER: ^{1}H NMR (400 MHz, dTFA): δ 1.55 (m, 2 H), 1.84-1.89 (bm, 6 H), 2.02-2.07 (m, 4 H), 3.04 (m, 4 H), 3.62 (m, 4 H), 3.85 (m, 4 H), 4.73 (m, 4 H), 8.77-8.86 (m, 8 H). Exact mass calcd for C$_{38}$H$_{36}$N$_4$O$_4$ (M+H): 612.27. Found: 612.73.

4.1.1.2 PDI-Tris [N,N'-Bis(tris-(2-aminoethyl)amine)-3,4,9,10 perylene tetracarboxylic diimide]

PTCD (0.54 g, 1.4 mmol) and tris-(2-aminoethyl) amine (10 mL, 67 mmol) were placed in a reflux apparatus. The mixture was stirred at 100 °C for 24 hours, and then the temperature was gradually increased to 170 °C over 2 hours. The mixture was then cooled to room temperature, and a mixture of 1-propanol and diethyl ether (1:4) was added. The resulting precipitate was collected by suction filtration, washed with benzene and diethyl ether, and dried under vacuum to afford 0.83 g (94% yield) of the desired product.
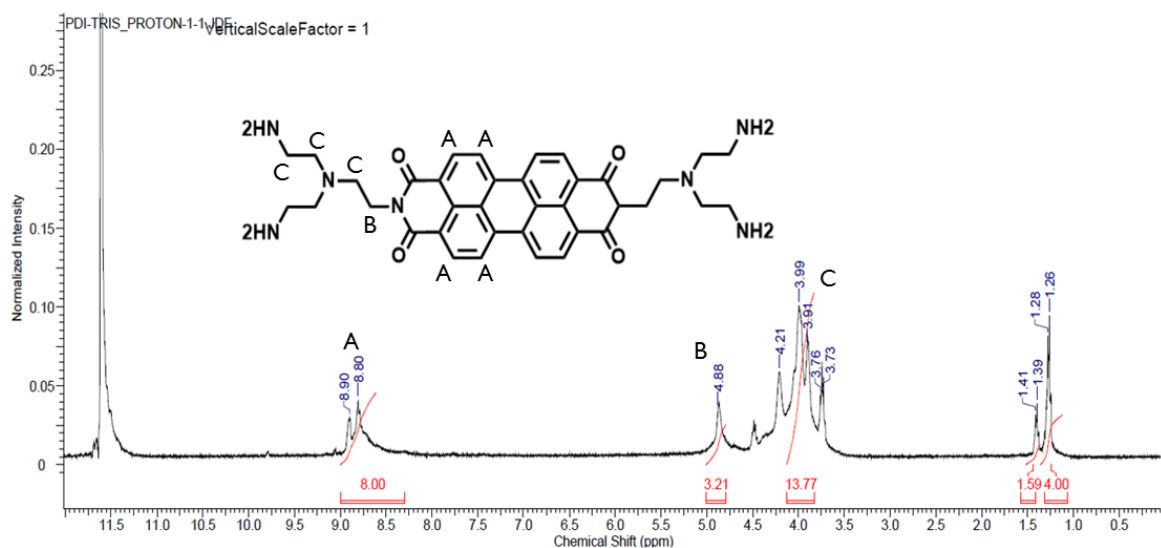
Figure 4.4: ^{1}H NMR Spectrum of PDI-Tris in CF$_3$COOD at 400 MHz

PDI-Tris: ^{1}H NMR (400 MHz, dTFA): δ 1.26-1.28 (m, 4 H), 1.39-1.41 (m, 2 H), 3.91-4.10 (m, 16 H), 4.88 (m, 4 H), 8.80-8.90 (m, 8 H).

4.1.1.3 PDI-His [N, N'-Bis[histidine]-3,4,9,10-perylenetetracarboxylic diimide]

Histidine (4.9 g, 32 mmol) was added to PTCD (0.50 g, 1.3 mmol) with imidazole (5 g) and the mixture was melted and stirred at 120 °C for 3 h. After cooling to room temperature, the mixture was dissolved in water and filtered. The filtrate was acidified (2 M HCl) and washed with EtOH (5–10 washes) to remove residual imidazole, as detected in 1H NMR spectra. The samples were dried vacuum to obtain 0.46 g (54% yield) of the red-pink product.
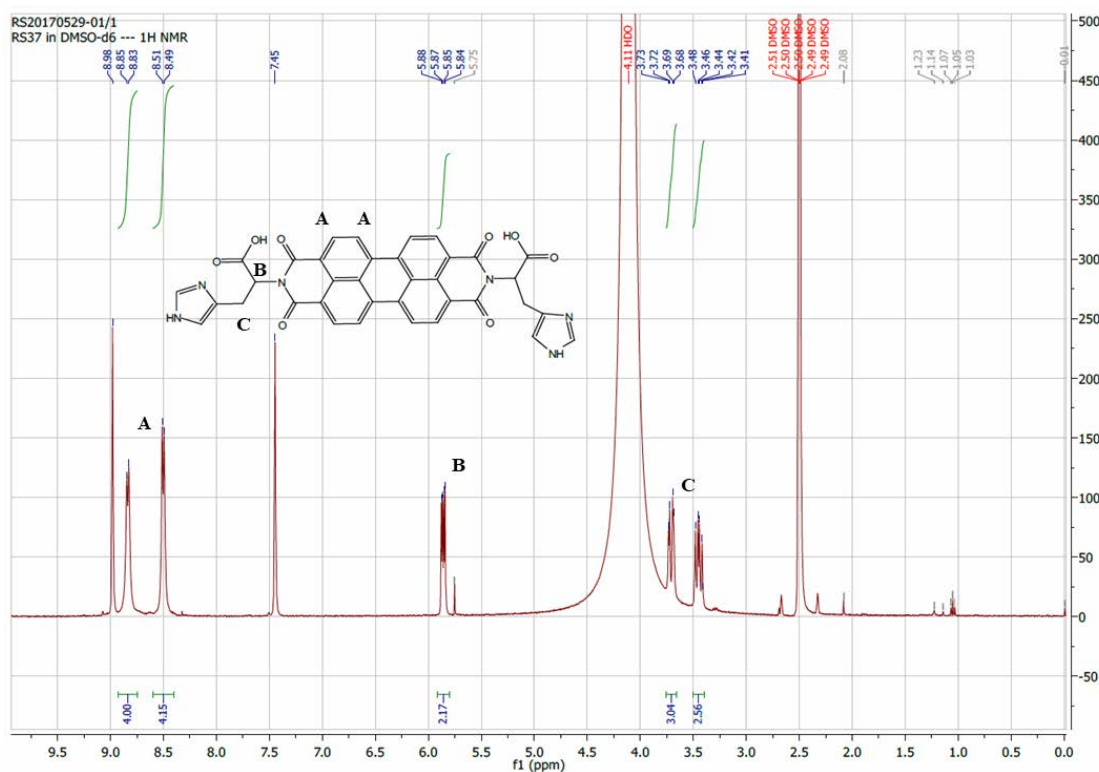
Figure 4.5: ^{1}H NMR Spectrum of PDI-His in DMSO-d6 at 400 MHz

PDI-His: ^{1}H NMR (400 MHz, DMSO-d6): δ 3.41-3.48 (m, 2 H), 3.68-3.73 (m, 2 H), 5.87 (m, 2 H), 8.50 (d, 4 H), 8.85 (d, 4 H). Exact mass calcd for $C_{36}H_{22}N_6O_8$ (M+H): 666.15. Found: 666.61.

4.1.1.4 PDI-Ser [N,N'-Bis[serine]-3,4,9,10-perylenetetracarboxylic diimide]

Serine (3.36 g, 32 mmol) was added to PTCD (0.50 g, 1.3 mmol) with imidazole (5 g) and the mixture was melted and stirred at 120 °C for 3 h. After cooling to room temperature, the mixture was dissolved in water and filtered. The filtrate was acidified (2 M HCl) and washed with EtOH (5–10 washes) to remove residual imidazole, as detected in 1H NMR spectra. The samples were dried vacuum to obtain 0.55 g (61 % yield) of the red-orange product.
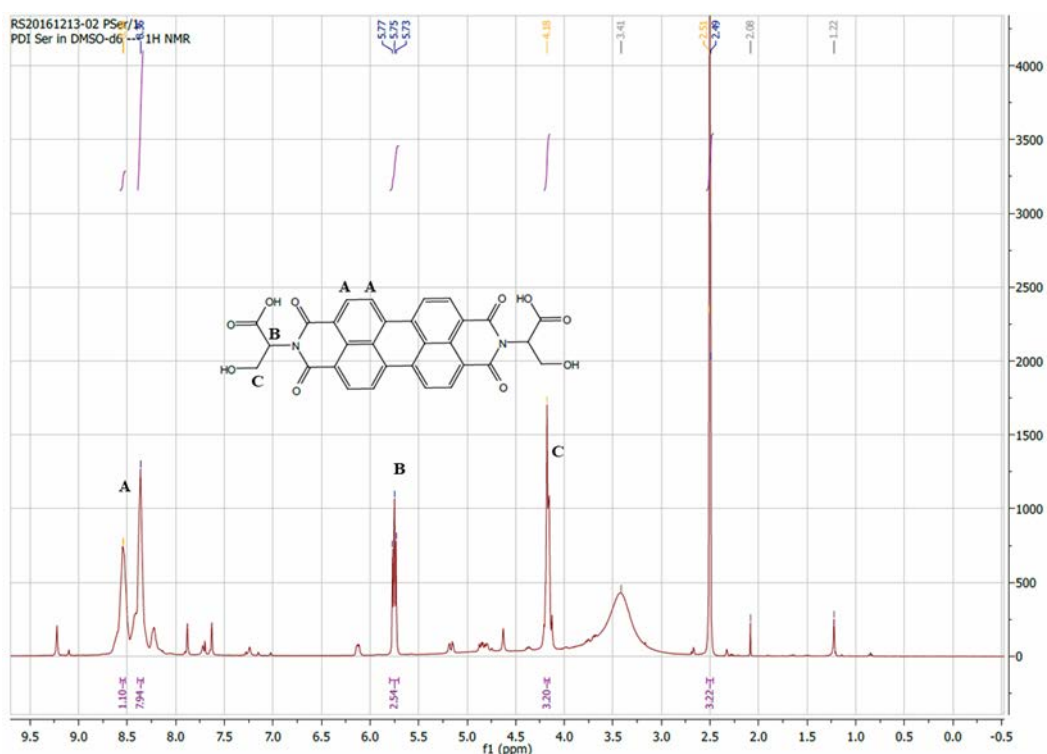
Figure 4.6: ^{1}H NMR Spectrum of PDI-Ser in DMSO-d6 at 400 MHz

PDI-Ser: ^{1}H NMR (400 MHz, dTFA): δ 2.77 (m, 6 H), 2.94 (m, 2 H), 6.14 (m, 2 H), 8.79-8.84 (m, 8 H).

4.1.1.5 PDI-Glu [N,N'-Bis[glutamine]-3,4,9,10-perylenetetracarboxylic diimide]

Glutamine (4.7 g, 32 mmol) was added to PTCD (0.50 g, 1.3 mmol) with imidazole (5 g) and the mixture was melted and stirred at 120 °C for 3 h. After cooling to room temperature, the mixture was dissolved in water and filtered. The product was precipitated by the addition of acetone. The solid material was then collected by filtration, washed twice with acetone, and dried under vacuum to afford 0.35 g (42% yield) of dark red product.
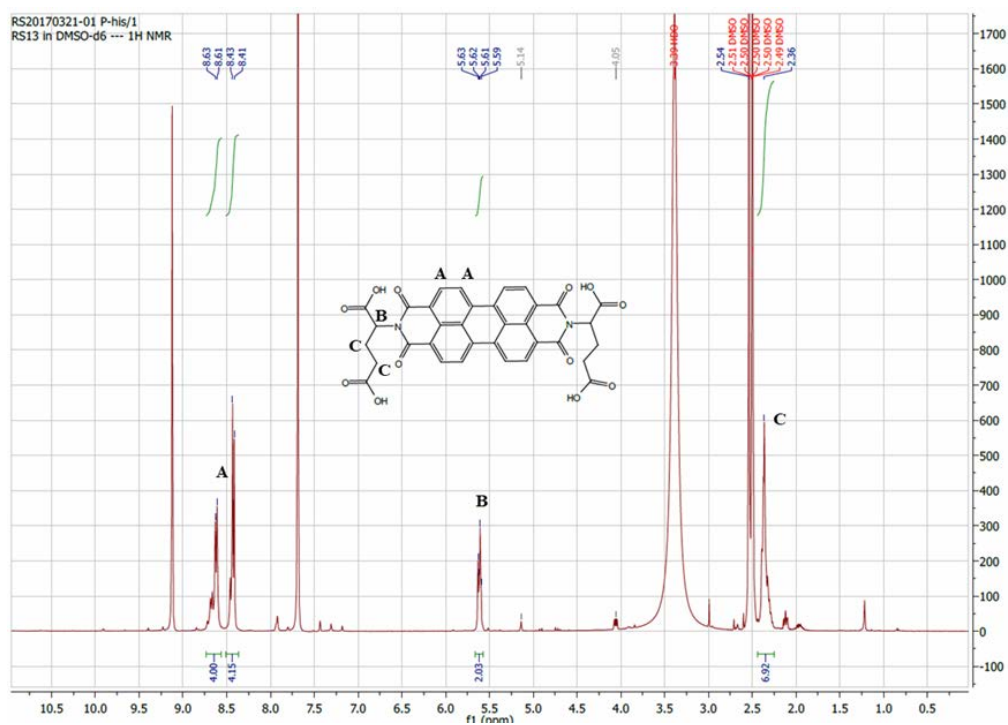
Figure 4.7: ¹H NMR Spectrum of PDI-Glu in DMSO-d6 at 400 MHz

PDI-Glu: ¹H NMR (400 MHz, dTFA): δ 2.77 (m, 6 H), 2.94 (m, 2 H), 6.14 (m, 2 H), 8.79-8.84 (m, 8 H).

4.1.1.6 PIPER3 [N,N'-bis-(2-(1-piperazino)ethyl)-3,4,9,10-perylene tetracarboxylic acid diimide]

PTCD (1.0 g, 2.5 mmol) was mixed with 0.8 mL (0.78 g, 6.03 mmol) of 1-(2- aminoethyl) piperazine in 10 mL of DMF and 10 mL of 1,4-dioxane. The bright red mixture was heated under reflux for 4 hours until it became dark red. The solvents were removed under reduced pressure. The resulting purple residue was dissolved in 1M HCl solution, and the solution was allowed to stand overnight in a refrigerator. Insoluble impurities were removed by suction filtration, and the resulting solution was adjusted to pH 12 with the addition of NaOH. A dark red product precipitated and was isolated by suction filtration. The precipitate was washed with deionized water and dried under vacuum to afford 1.3 g (86% yield) of the desired product.
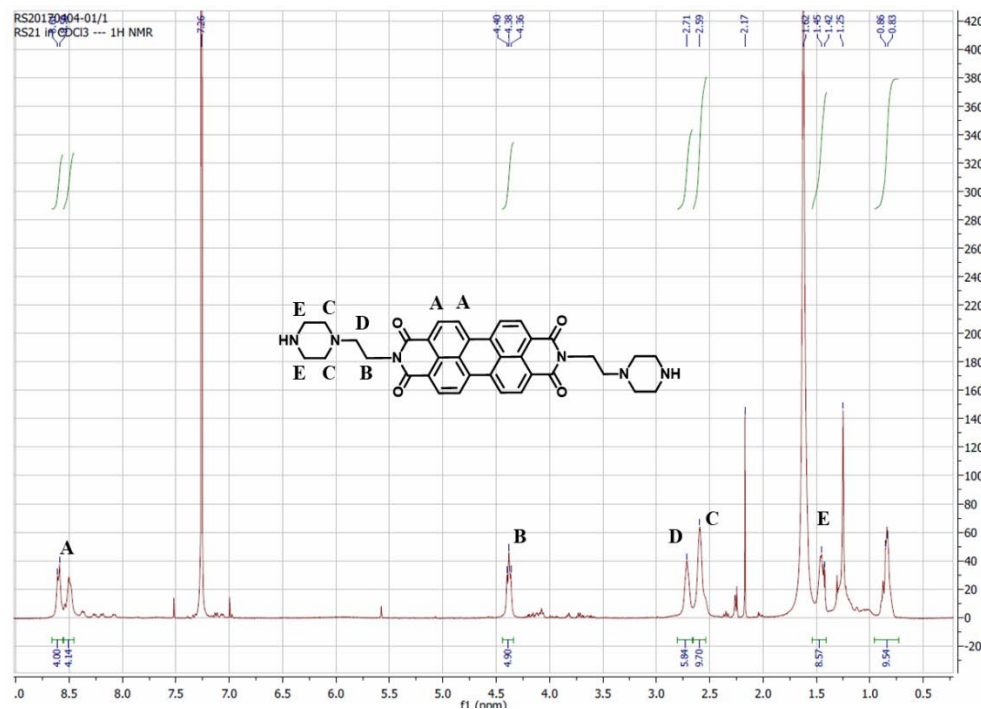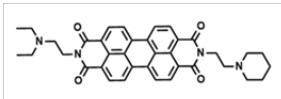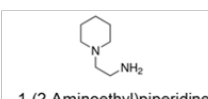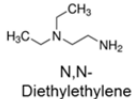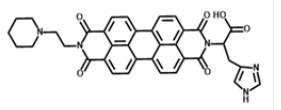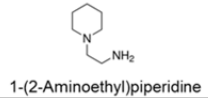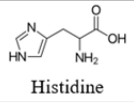
Figure 4.8: ^{1}H NMR Spectrum of PIPER3 in CDCl$_3$ at 400 MHz

PIPER3: ^{1}H NMR (400 MHz, CDCl$_3$): δ 1.42-1.45 (m, 8 H), 2.51-2.59 (m, 8 H), 2.71 (m, 4 H), 3.62 (m, 4 H), 4.38 (m, 4 H), 8.50-8.61 (m, 8 H).

103

4.1.2 Synthesis of asymmetrical perylenediimide (aPDI) derivatives

Synthesis of aPDIs involves more steps than PDIs. The synthesis starts by conditionally opening one side of the anhydride moieties of perylene-3,4,9,10-tetra-carboxylic dianhydride (PTCD), and the selected amine is attached at the remaining anhydride moiety. Then, the two carboxylic groups of the opened anhydride are closed with phosphoric acid, and another selected amine is attached. The final product was then purified from the reaction mixture. The sPDIs synthesized in this project are summarized in Table 4.2.

Table 4.2: List of asymmetric perylene diimide derivatives

Name	Structure	R1,R2
aPDI-PTea		1-(2-Aminoethyl)piperidine N,N-Diethylethylene diamine
aPDI-PHis		1-(2-Aminoethyl)piperidine Histidine

4.1.2.1 aPDI-PTea [N-diethylaminoethyl-N-2-(1-piperidino) ethyl]-3,4,9,10-perylenetetracarbo-xylic diimide]

The synthesis of aPDI-PTea was performed as shown in Scheme 4.2.
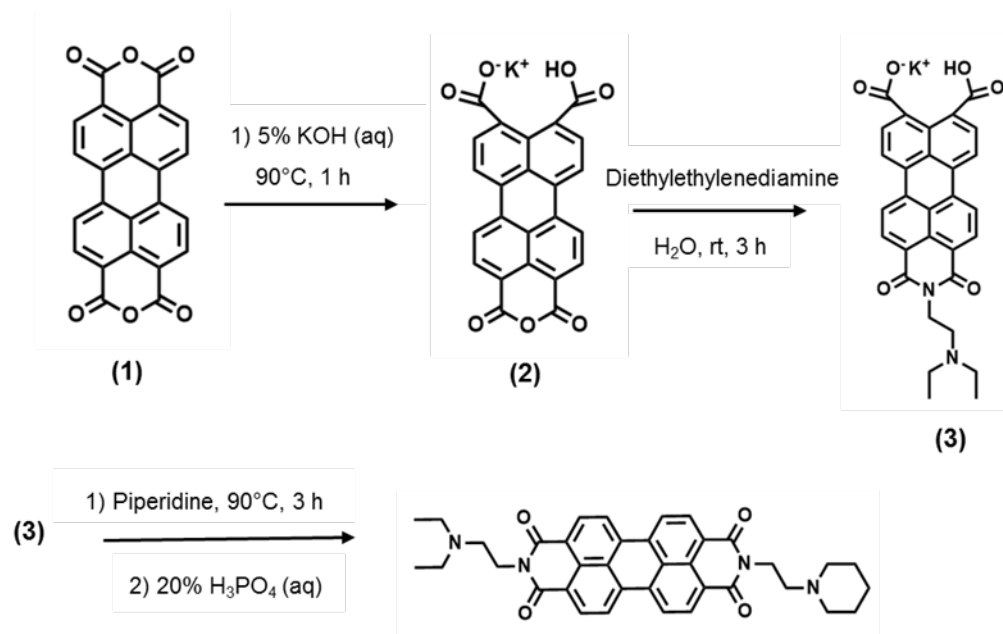
Scheme 4.2: Synthesis of aPDI-PTea

PTCD (1) (3 g, 7.6 mmol) was stirred in KOH solution (5%, 35 mL) for 4 h at 90 °C. After cooling to room temperature, 12.5 ml H_3PO_4 (10%) was added and stirred for 1 h at 90 °C. The precipitate formed was filtered, washed with water and dried in vacuum at 100 °C. Yield 89% (3.1 g, Bordeaux-red powder). (2)

Monopotassium salt of (2) (9.82 g, 21.9 mmol) was suspended in water (300 ml) at room temperature. N, N-Diethylethylenediamine (10.63 g, 89.60 mmol) dissolved in 50 mL of water was added slowly to the suspension. The mixture was stirred for 3 h at room temperature. Acetone (1 L) was added into the resulting red solution to induce precipitation. The mixture was allowed to stand overnight, and the resulting brick red precipitate was collected using suction filtration. The residue was resuspended in acetone, and the mixture was refluxed for 1 h. The brick-red

solid was then isolated by vacuum filtration, washed with acetone, and dried under vacuum at 120 °C overnight to yield 10.9 g (19.9 mmol, 91%) as a brick red solid. (3)

(3) was then mixed with 80 ml of water. Mixture was added with 0.8 mL (0.72 g, 5.6 mmol) of 1-(2- aminoethyl) piperidine. The mixture was heated to 90 °C for 3 hours. Then 11.5 mL of 20% phosphoric acid was added. After 2 h, the precipitated product was isolated on a frit filter and washed with water. to obtain 0.25 g (35 % yield) of the red-purple product.
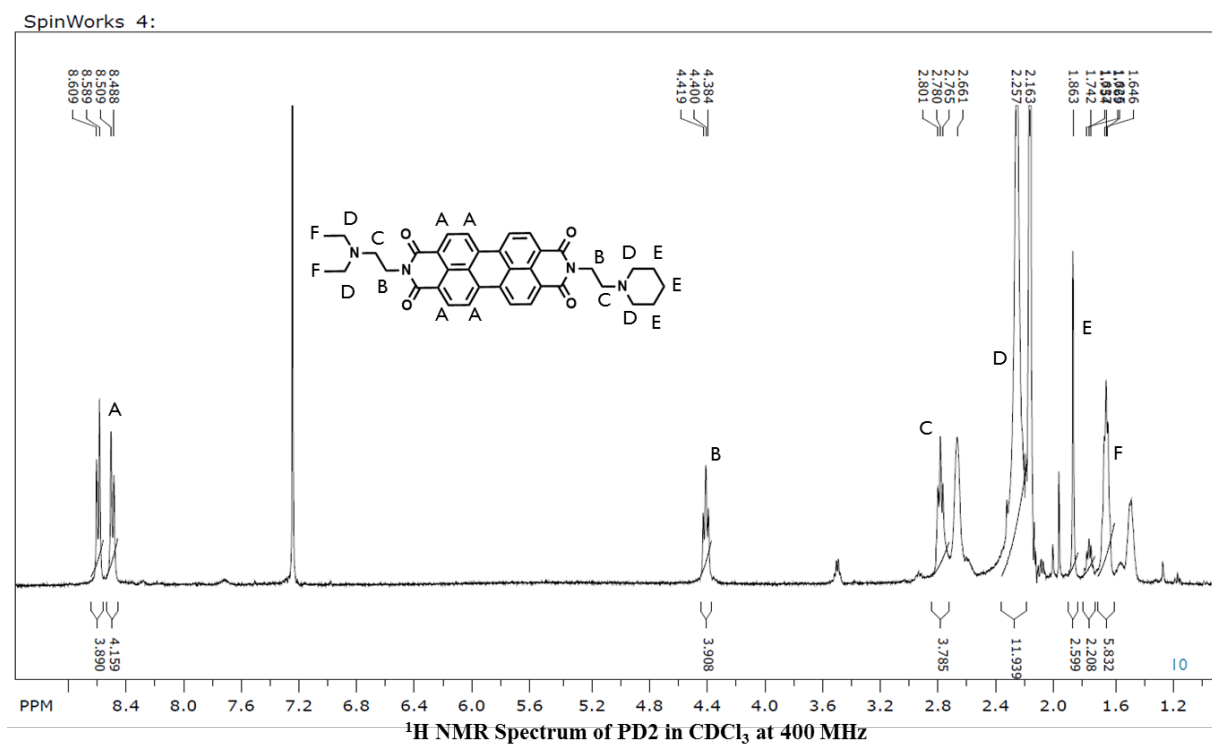
Figure 4.9: ^{1}H NMR Spectrum of aPDI-PTea in CDCl$_3$ at 400 MHz

aPDI-PTea: ^{1}H NMR (400 MHz, CDCl$_3$): δ 1.65 (m, 6 H), 1.69 (m, 2 H), 2.16-2.26 (m, 8 H), 2.80 (m, 4 H), 3.91 (m, 4 H), 8.48-8.61 (m, 8 H)

4.1.2.2 aPDI-PHis [N, N-histidine-N-2-(1- piperidino) ethyl]-3,4,9,10 perylene
tetracarboxylic diimide]

The synthesis of aPDI-PHis followed the general procedure shown in Scheme 4.2, with some modifications as follows. PTCD (1.0 g, 1.0 mmol), 10% potassium hydroxide (3.4 mmol) 20 ml were heated to 100 °C and maintained at this temperature for 50 min. After the solution was cooled, it was treated with 2 M aqueous HCl (20 mL). The mixture was then stirred at room temperature overnight. The precipitated product was isolated on a frit filter, washed with deionized water, and dried under vacuum to obtain red-purple products (0.3 g; 0.4 mmol; 40% yield).

To remove bisimide and dianhydride, the material was treated with 60 mL of 10% KOH for 2 h. The di-potassium salt of the monoimide precipitates. A drop on filter paper should migrate yellowish through the paper, not reddish. The precipitate is isolated on a frit filter after cooling and washed with 8 % KCl and 2 % K2CO3 until the filtrate is colorless (to remove the tetra-potassium salt of the bis-anhydride). The residue is dissolved in hot water and filtered to remove bisimide. From the filtrate, the monoimide-mono-anhydride was isolated at 90 ∘C by adding acid (HCl). The product was isolated and dried. PTCD PIPER monoanhydride Yield: 25 % 1H NMR (400 MHz, DMSO-d6): δ 1.44 (m, 1 H), 1.85 (bm, 3 H), 1.88 (m, 2 H), 3.03 (m, 2 H), 3.68 (m, 2 H), 3.85 (m, 2 H), 4.46(m, 2 H), 8.48-8.81 (m, 8 H).

5 g of imidazole and 300 mg (1.93 mmol) of histidine was added to 300 mg (0.196mmol) of mono-imidemono- anhydride, and the mixture was heated at 120 ℃ for 3 h. The cooled-down mixture was added 100 mL of ethanol and 300 mL of 2 M HCl. Precipitant was collected by filtration washed with ethanol and dried to obtain 100 mg (32 % yield) of reddish-pink material.
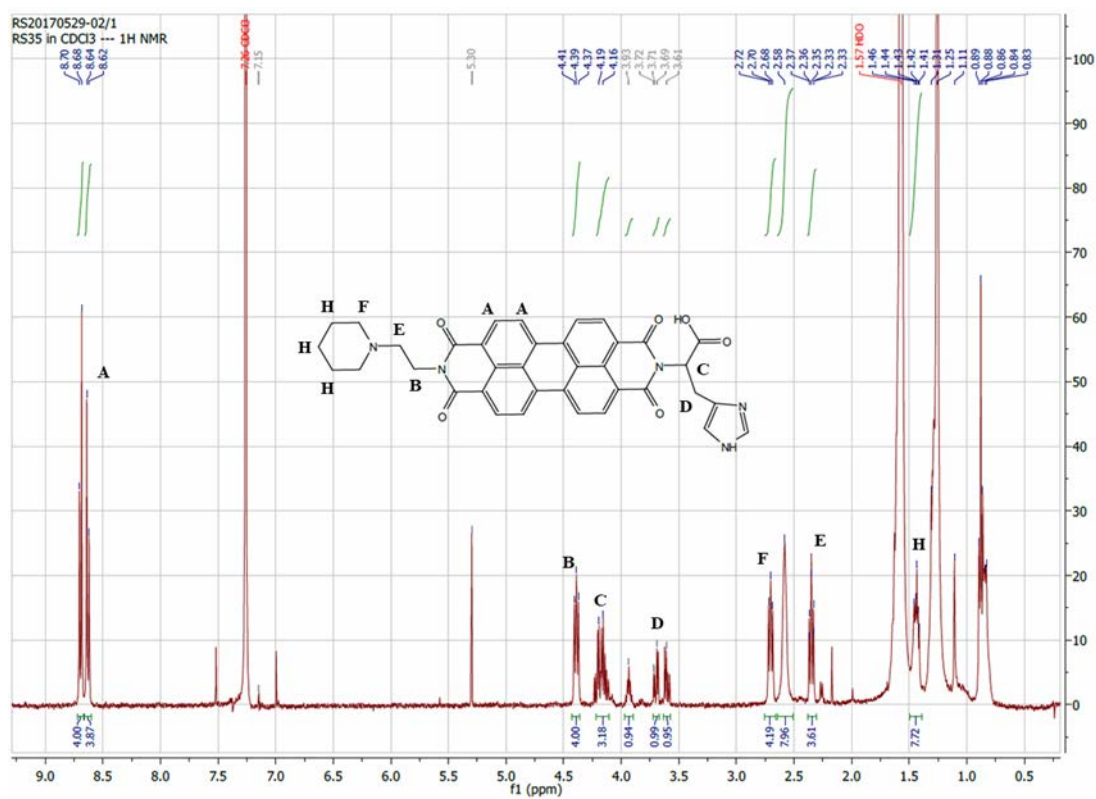
Figure 4.10: ¹H NMR Spectrum of aPDI-PHIS in CDCl₃ at 400 MHz

aPDI-PHis: ¹H NMR (400 MHz, CDCl₃): δ 1.41 (m, 6 H), 2.33-2.36 (m, 2 H), 2.68-2.72 (m, 4 H), 3.61-3.92 (m, 2 H), 4.16-4.19 (m, 1 H), 4.37-4.41 (m, 2 H), 8.62-8.70 (m, 8 H).

4.1.3   Synthesis of asymmetrical perylenemonoimide (aPMI) derivatives

4.1.3.1   PM2 [N-(2-(N′,N′- diethylamino) ethyl)-9-piperazinylperylene-3,4-
dicarboximide

The synthesis of PM2 was performed as shown in Scheme 4.3.
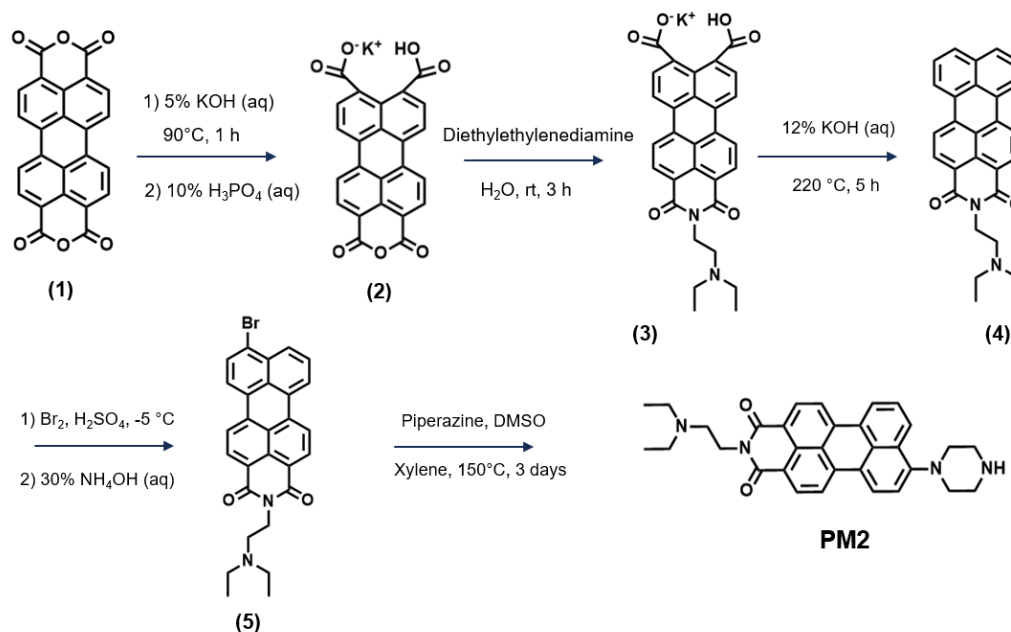
Scheme 4.3: Synthesis of PM2

Synthesis of (2) [Perylene-3,4,9,10-tetracarboxylic acid monoanhydride mono-
potassium carboxylate]

PTCD (1) (3 g, 7.6 mmol) was stirred in KOH solution (5%, 35 mL) for 4 h
at 90 °C. After cooling to room temperature, 12.5 ml H_3PO_4 (10%) was added and
stirred for 1 h at 90 °C. The precipitate formed was filtered, washed with water and
dried in vacuum at 100 °C. Yield 89% (3.1 g, Bordeaux-red powder).

Synthesis of (3) [(N, N-Diethylamino)ethylperylene- 9,10-dicarboximide-3,4-dicarboxylic Acid]

Monopotassium salt of (2) (9.82 g, 21.9 mmol) was suspended in water (300 ml) at room temperature. N,N-Diethylethylenediamine (10.63 g, 89.60 mmol) dissolved in 50 mL of water was added slowly to the suspension. The mixture was stirred for 3 h at room temperature. Acetone (1 L) was added into the resulting red solution to induce precipitation. The mixture was allowed to stand overnight, and the resulting brick red precipitate was collected using suction filtration. The residue was resuspended in acetone, and the mixture was refluxed for 1 h. The brick-red solid was then isolated by vacuum filtration, washed with acetone, and dried under vacuum at 120 °C overnight to yield 10.9 g (19.9 mmol, 91%) as a brick-red solid.

Synthesis of (4) [(N,N-Diethylamino) ethylperylene-3,4-dicarboximide]

Compound (3) (5.43 g, 9.93 mmol) and KOH (5.67 g, 86.8 mmol) were placed in a Teflon cup, and double-distilled water (80 g) was added. After sonication for 30 min, the Teflon cup was then placed inside a 325-ml stainless steel reactor vessel with a steel lid. The temperature was ramped to 190 °C and maintained for 5 h. The reactor was cooled to room temperature and opened. The resulting metallic brick-red suspension was washed out with an excess amount of water into a filter funnel and collected by suction filtration. The resulting residue was washed with water until the filtrate was colorless. After drying under vacuum, the residue was dissolved in CHCl$_3$ (200 mL), and the insoluble solid was removed by suction filtration. The solution in CHCl$_3$ was added to a basic alumina pad. The basic alumina was eluted with acetone/CHCl$_3$ (v/v) 2:8). The eluent was collected until the eluent became colorless. The solvent was then evaporated to give the compound as red needlelike crystals in 70% yield.

Synthesis of (5) [(N,N-Diethylamino)ethyl-9-bromoperylene-3,4-dicarboximide]

Compound (4) (1.20 g, 2.85 mmol) was mixed with 65 mL of concentrated sulfuric acid in a 250-mL round-bottom flask, and the mixture was cooled to -5 °C

before 0.19 mL of Br_2 was added dropwise with a syringe. The reaction mixture was stirred vigorously at -5 °C for 1 h. While still cold, the reaction mixture was poured into 250 mL of pre-chilled water in a 1000-mL recovery flask in an ice bath, and the pH of the resultant solution was adjusted to pH 8-9 by slowly adding about 170 mL of 30% NH_4OH(aq). A bright red precipitate formed, and the suspension was sonicated for 3 h to ensure complete deprotonation of the amine. The solid was filtered and washed with 300 mL of 5% NH_4OH(aq). The product was dried under vacuum to yield 1.41 g (2.81 mmol, 98%) of bright red solid. Compound (5) can be further purified by recrystallization in a 1% triethylamine/DMF solution. The filtered solid was washed with ether and dried under vacuum to recover 80% of the product.

Synthesis of PM2 [N-(2-(N′, N′-diethylamino) ethyl)-9-piperazinylperyl 3,4-dicarboximide]

The mixture of piperazine (6.40 g, 74.4 mmol), 3.1 mL of DMSO, and 4.7 mL of xylene was stirred at 80 °C for 1 h before the compound (5) (0.50 g, 1.0 mmol) was added into the flask. The mixture was heated at 140 °C-160 °C for 3 days under N_2. Then, the mixture was cooled to room temperature before CO_2-free double distilled water was added to the mixture. The precipitate formed was collected by suction filtration and washed with 5% KOH (aq) and double distilled water to remove excess solvent and piperazine. The solid residue was dried under vacuum overnight. The solid residue was suspended into a dilute KOH (3%) solution. The suspension was stirred at room temperature for 4 hours. Then a purple solid was collected by suction filtration and dried under vacuum overnight to afford PM2 (0.39 g, 0.78 mmol, 78%).
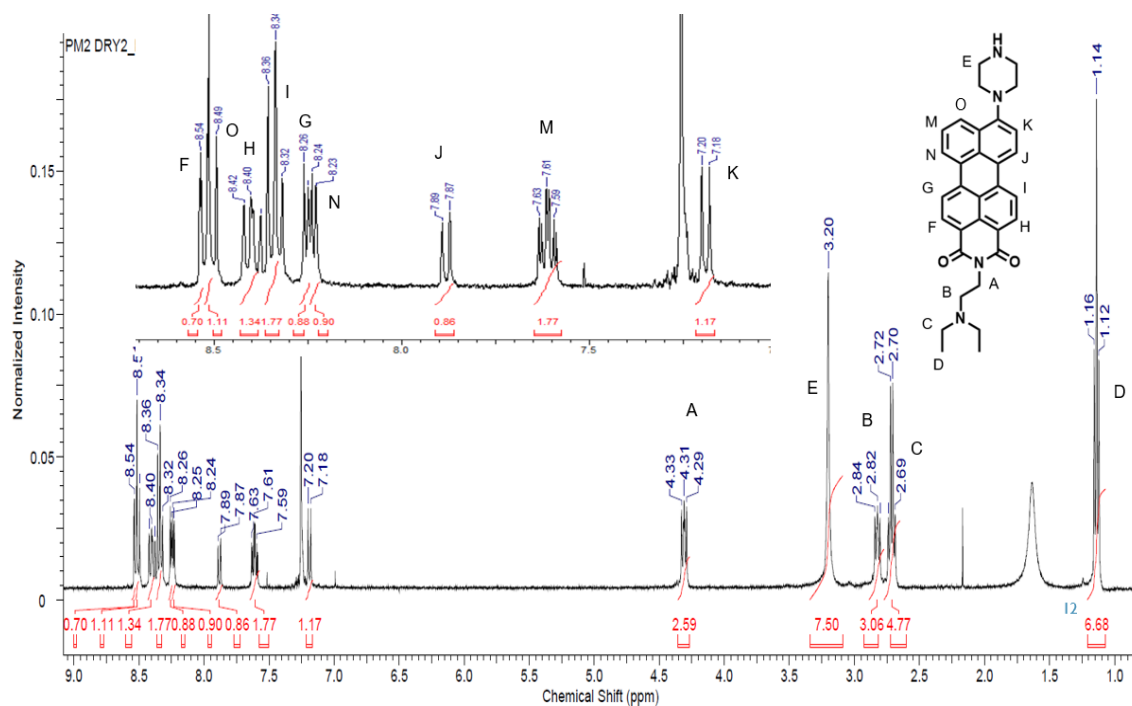
Figure 4.11: ^{1}H NMR Spectrum of PM2 in CDCl$_3$ at 400 MHz

PM2: ^{1}H NMR (400 MHz, CDCl$_3$): δ 1.15 (t, 6 H), 2.70 (m, 4 H), 2.84 (m, 2 H), 3.11-3.45 (bm, 8 H), 4.31 (t, 2 H), 7.20 (d, 1 H), 7.61 (t, 1 H), 7.89 (d, 1 H), 8.24 (d, 1 H), 8.26 (d, 1 H), 8.32 (s, 1 H), 8.40 (s, 1 H), 8.50 (s, 1 H), 8.54 (s, 1 H)

4.1.3.2 PM1 [(N,N-2-(1-piperidino)ethyl perylene-3,4-dicarboximide]

The synthesis of PM1 was performed as shown in Scheme 4.3, except for the last step.
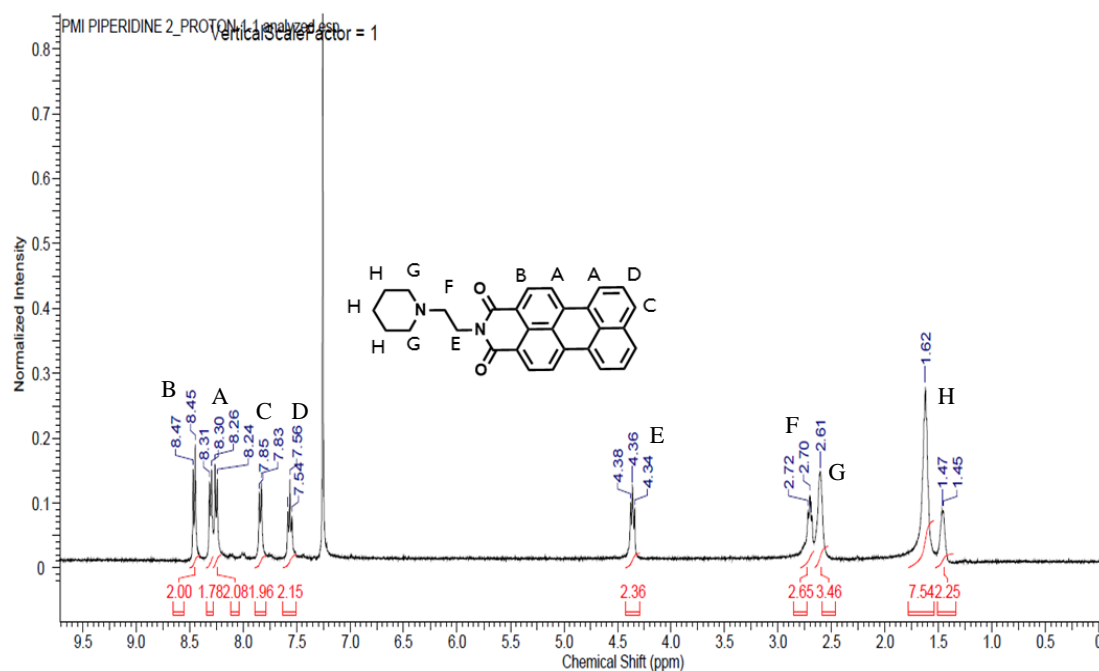
Figure 4.12: ^{1}H NMR Spectrum of PM1 in CDCl$_3$ at 400 MHz

PM1: ^{1}H NMR (400 MHz, CDCl$_3$): δ 1.32 (m, 6 H), 2.61 (m, 4 H), 2.72 (m, 2 H), 4.36 (m, 2 H), 7.54 (d, 2 H), 7.83 (t, 2 H), 8.24 (d, 2 H), 8.30 (d, 2 H), 8.47 (d, 2 H)

Table 4.3: List of perylene monoimide derivatives

Name	Structure	R1,R2
PM1		 1-(2-Aminoethyl)piperidine
PM2		

113

4.2   Molecular modeling.

Molecular modeling was performed using the G-quadruplex ligands database G4LDB and Autodock VINA. The G4LDB is a unique platform that contains an online ligand design module that can predict ligand binding affinity in real time. The results will be significantly improved the accuracy of the binding mode predictions by Autodock VINA.

In this experiment, the telomeric G-quadruplex structure was used as docking macromolecule.
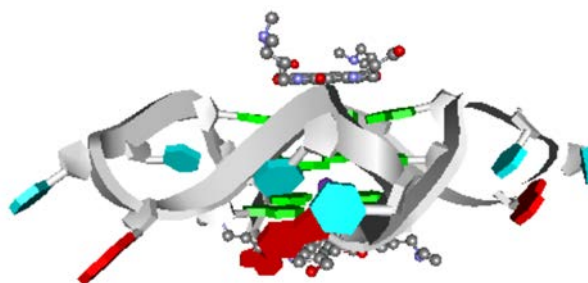
Source	J Mol Biol. 2008 Sep 19;381(5):1145-56. Epub 2008 Jun 17.
DOI	10.1016/j.jmb.2008.06.022
G4 Form	d(TAGGGTTAGGGTTAGGGTTAGGG)
Sequence	TAGGGTTAGGGTTAGGGTTAGGG
Site Center	2.705 -0.856 -14.119
Inter/Intra	intra
Description	Structural adaptation and conservation in quadruplex-drug recognition

Figure 4.13: Structure and source of telomeric G-quadruplex

4.2.1 Molecular modeling of telomeric G-quadruplex DNA with perylenediimide (PDI) derivatives

4.2.1.1 PIPER
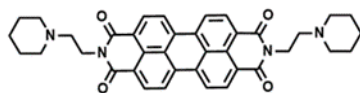
Binding affinity = -7.7 kcal/mol
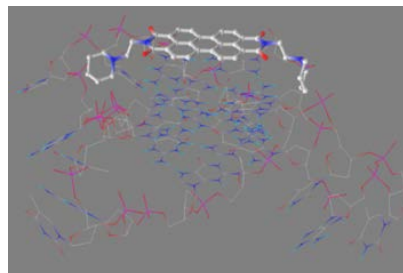
4.2.1.1 PDI-His
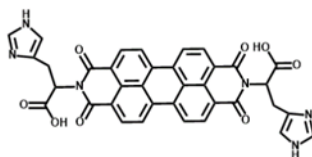
Binding affinity = -9.1 kcal/mol
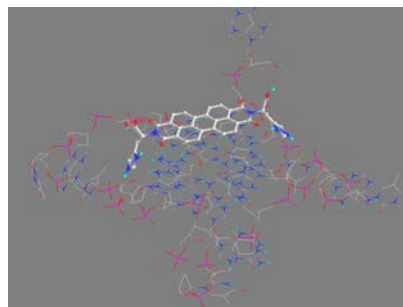
4.2.1.1 PDI-Ser
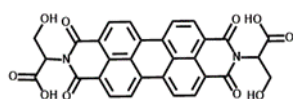
Binding affinity = -8.5 kcal/mol
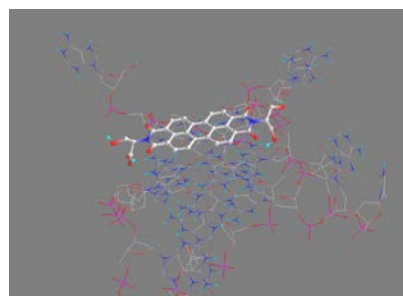
4.2.1.1 PDI-Lys
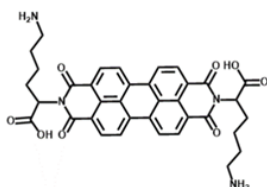
Binding affinity = -7.5 kcal/mol
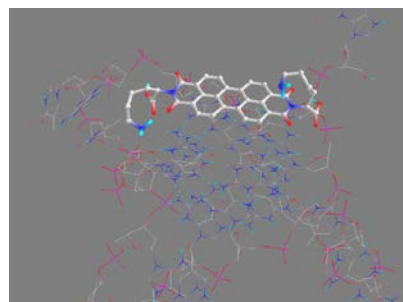
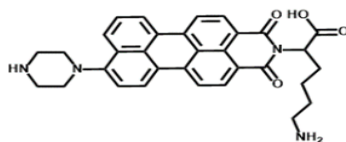**4.2.2 Molecular modeling of telomeric G-quadruplex DNA with asymmetric perylenediimide (aPDI) derivatives**

4.2.2.1 aPDI-PTea
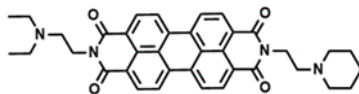
Binding affinity = -9.2 kcal/mol
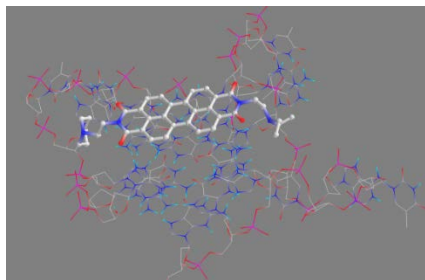
4.2.2.2 aPDI-PHis
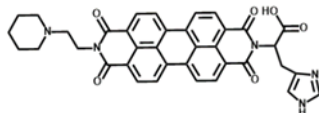
Binding affinity = -9.7 kcal/mol
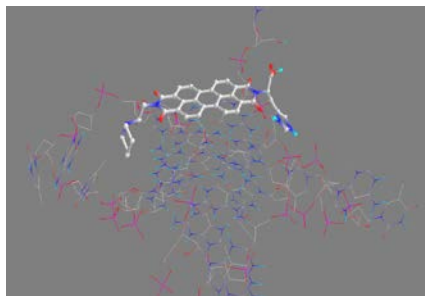
4.2.2.3 aPDI-PLys
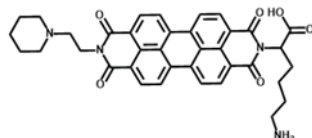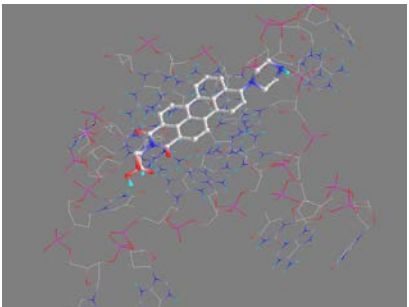

Binding affinity = -9.1 kcal/mol
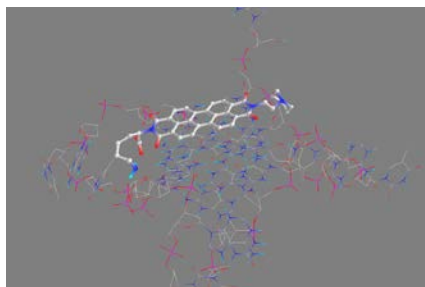
4.2.2.4 aPDI-PGlu
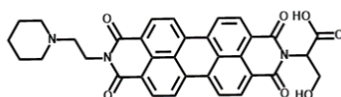
Binding affinity = -9.4 kcal/mol
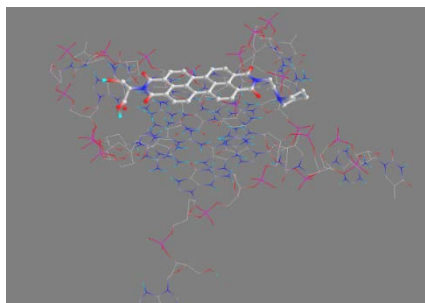
4.2.3 Molecular modeling of telomeric G-quadruplex DNA with perylenemonoimide (aPMI) derivatives
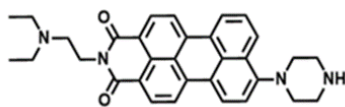
4.2.3.1 PM2	
Binding affinity = -9.0 kcal/mol	
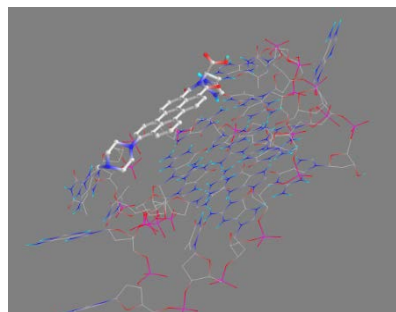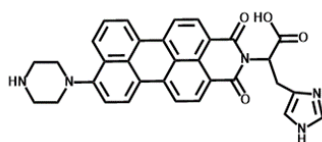
4.2.3.2 aPMI-PHis	
Binding affinity = -8.9 kcal/mol	
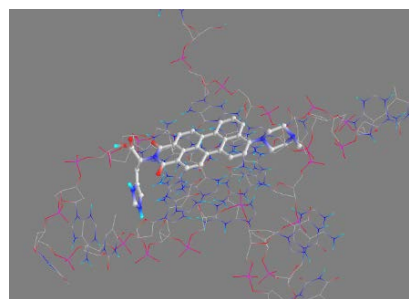
4.2.3.1 aPMI-PLys	
Binding affinity = -8.1 kcal/mol	
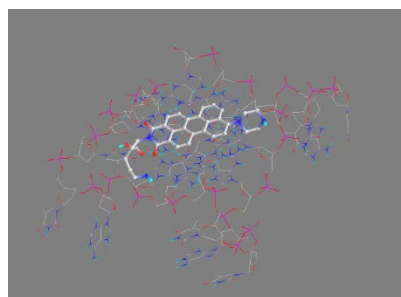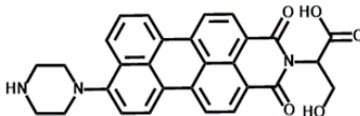
4.2.3.1 PM2	
Binding affinity = -8.3 kcal/mol	

Table 4.4: Comparison of calculated binding affinity among PDIs, aPDIs, aPMIs

Sidechain	Binding affinity (kcal/mol)		
	PDI	aPDI	aPMI
Piperidine	-7.7 (PIPER)	-9.2	-9.0 (PM2)
Histidine	-9.1	-9.7	-8.9
Lysine	-7.5	-9.1	-8.1
Serine	-8.5	-9.4	-8.3

Table 4.4 shows the binding affinity of perylene derivatives from simulating program. It can be found that asymmetric perylene diimide derivatives give binding affinity score higher than symmetric perylene diimide and slightly higher than perylene monoimide derivatives.

4.3 Absorption spectra and fluorescence emission spectra of perylene derivatives

The absorption spectra of perylene derivatives were obtained from the UV-1800 double-beam spectrophotometer (SHIMADZU, Japan). The fluorescence emission spectra were obtained from microplate reader (Synergy H4) using the λE_{xci} at 488 nm.
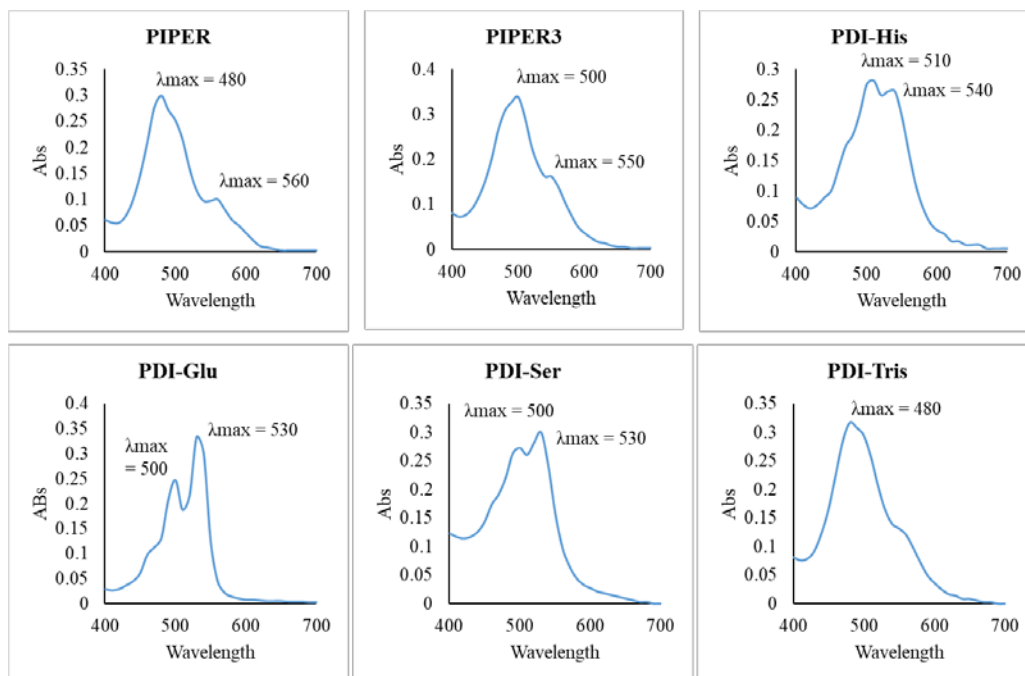

Figure 4.14: Absorption spectra of perylene diimide derivatives (PDIs). All compounds were measured at the concentration of 32 μM using UV-1800 double-beam spectrophotometer (SHIMADZU, Japan).
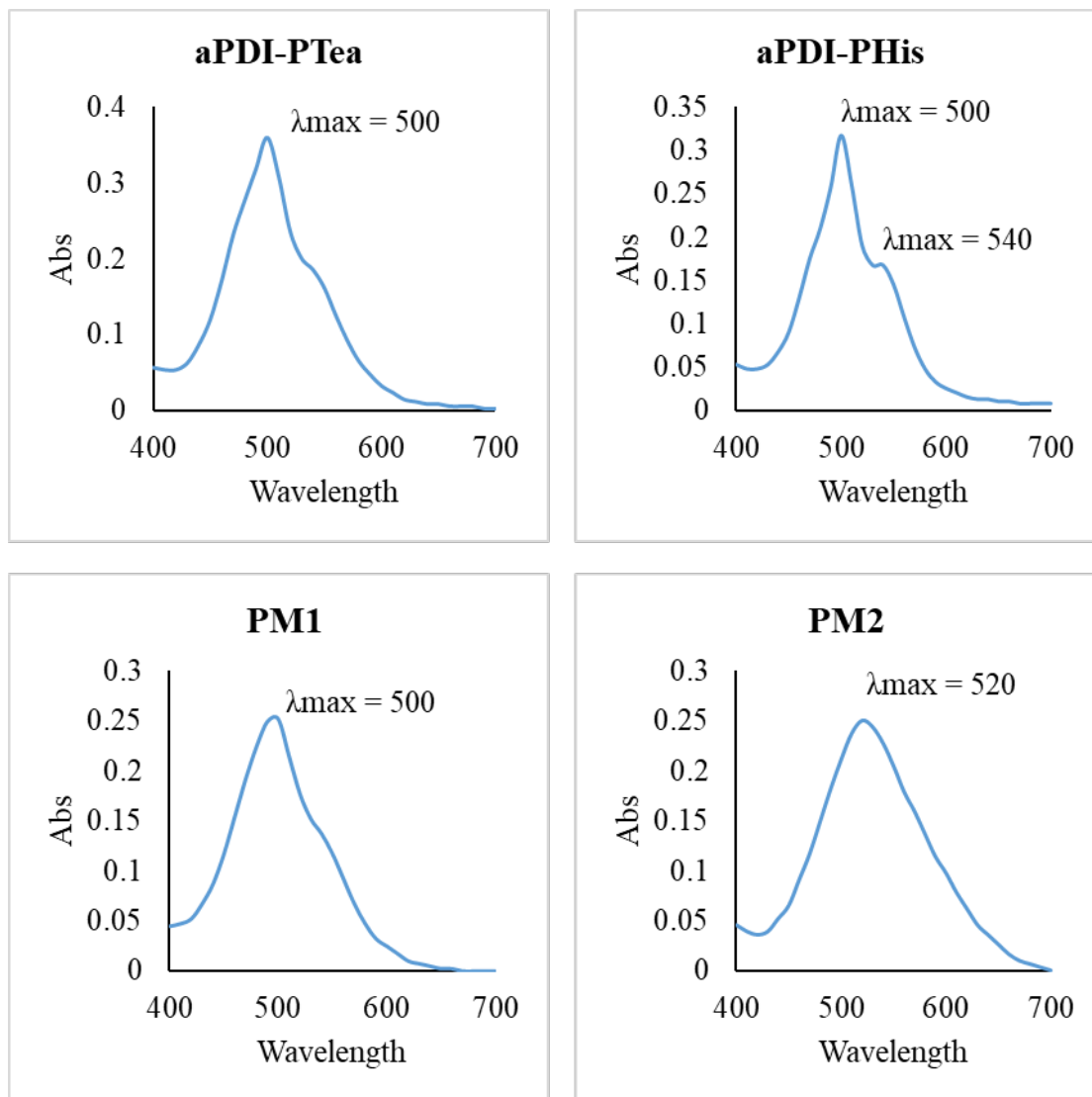
Figure 4.15: Absorption spectra of asymmetric perylene diimide derivatives (aPDIs) and asymmetric perylene monoimide derivatives (aPMIs). All compounds were measured at the concentration of 32 μM using UV-1800 double-beam spectrophotometer (SHIMADZU, Japan).
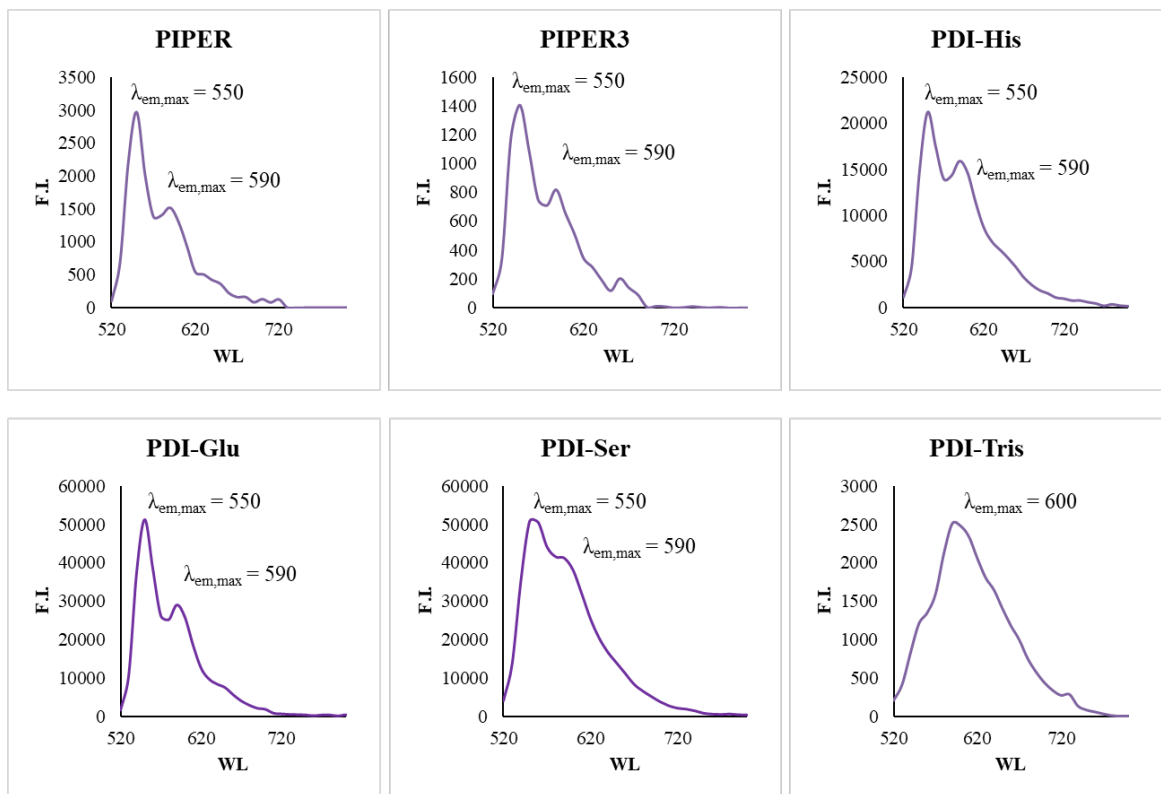
Figure 4.16: Fluorescence spectra of perylene diimide derivatives (PDIs). All compounds were measured at the concentration of 8 μM using microplate reader (Synergy H4) using the λE_{xci} at 488 nm.
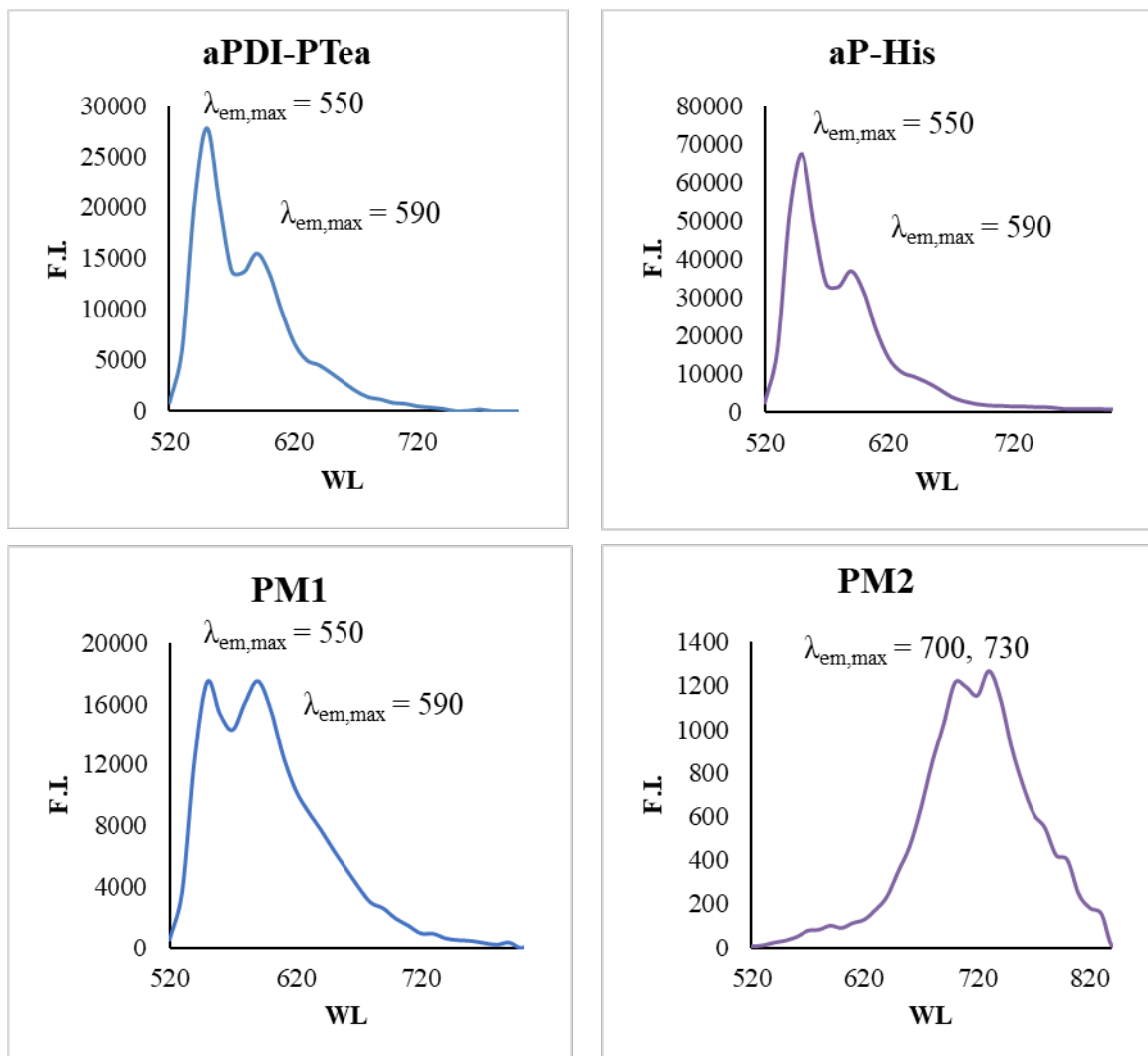
Figure 4.17: Fluorescence spectra of asymmetric perylene diimide derivatives (aPDIs) and asymmetric perylene monoimide derivatives (aPMIs). All compounds were measured at the concentration of 8 μM using microplate reader (Synergy H4) using the λE_{xci} at 488 nm.

4.4 Solubility profile of some perylene derivatives

Perylene derivatives (50 µM) were dispersed in 100 mM of Tris-HCl buffer (pH 7.0-9.0) or potassium phosphate buffer (pH 6.0-8.0) and left at room temperature for 2 days.
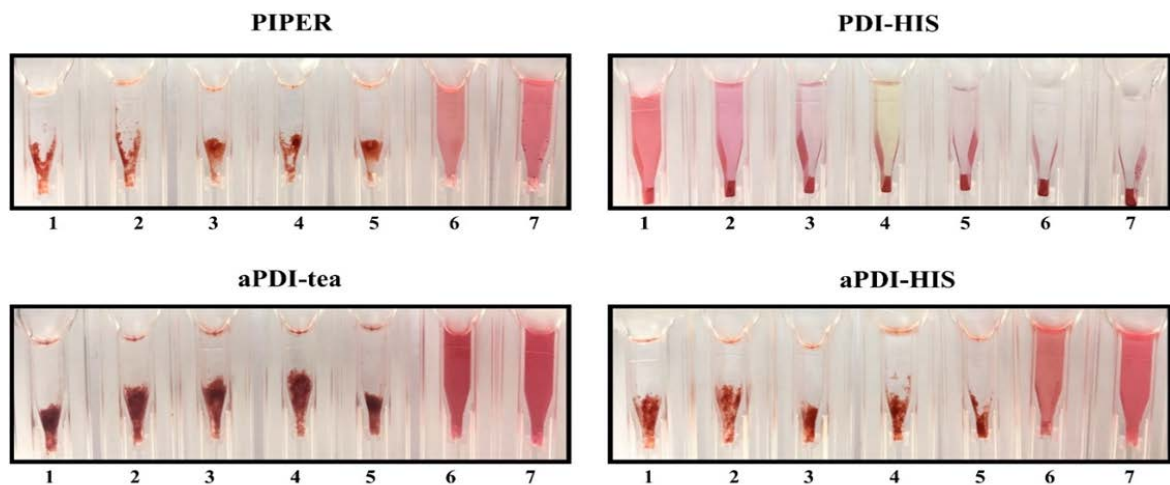

Figure 4.18: Solubility of some perylene derivatives

Table 4.5: Solybility profile of some perylene derivatives

Perylene Derivative	Tris pH 9.0	Tris pH 8.0	Tris pH 7.0	Phos pH 8.0	Phos pH 7.0	Phos pH 6.0	Acet pH 5.2
PIPER	ppt	ppt	ppt	ppt	ppt	sol	sol
PDI-HIS	sol	sol	psol	psol	psol	ppt	ppt
aPDI-tea	ppt	ppt	ppt	ppt	ppt	sol	sol
aPDI-HIS	ppt	ppt	ppt	ppt	ppt	sol	sol

* ppt = precipitation; psol = partial soluble; sol = soluble

4.5   Perylene-DNA binding studies by spectrophotometry

We determined the binding specificity of four perylene derivatives with various preformed DNA structures by spectrophotometry to determine whether these compounds had any preference against G-quadruplex from various biological relevance G-quadruplex motif.   PIPER and PDI-His are symmetrical PDIs, while aPDI-PTea and aPDI-PHis are asymmetrical PDIs.   Each perylene derivative (40 μM) was incubated with each preformed DNA structure (20 μM) in a designated buffer containing 100 mM KCl for 0, 8, and 24 h, and absorption spectra between 400 and 700 nm were recorded (Fig. 3).   The sequences of all oligonucleotides used in this study are shown in Table 4.6.

Table 4.6: DNA sequences of oligonucleotides used for spectrophotometric studies

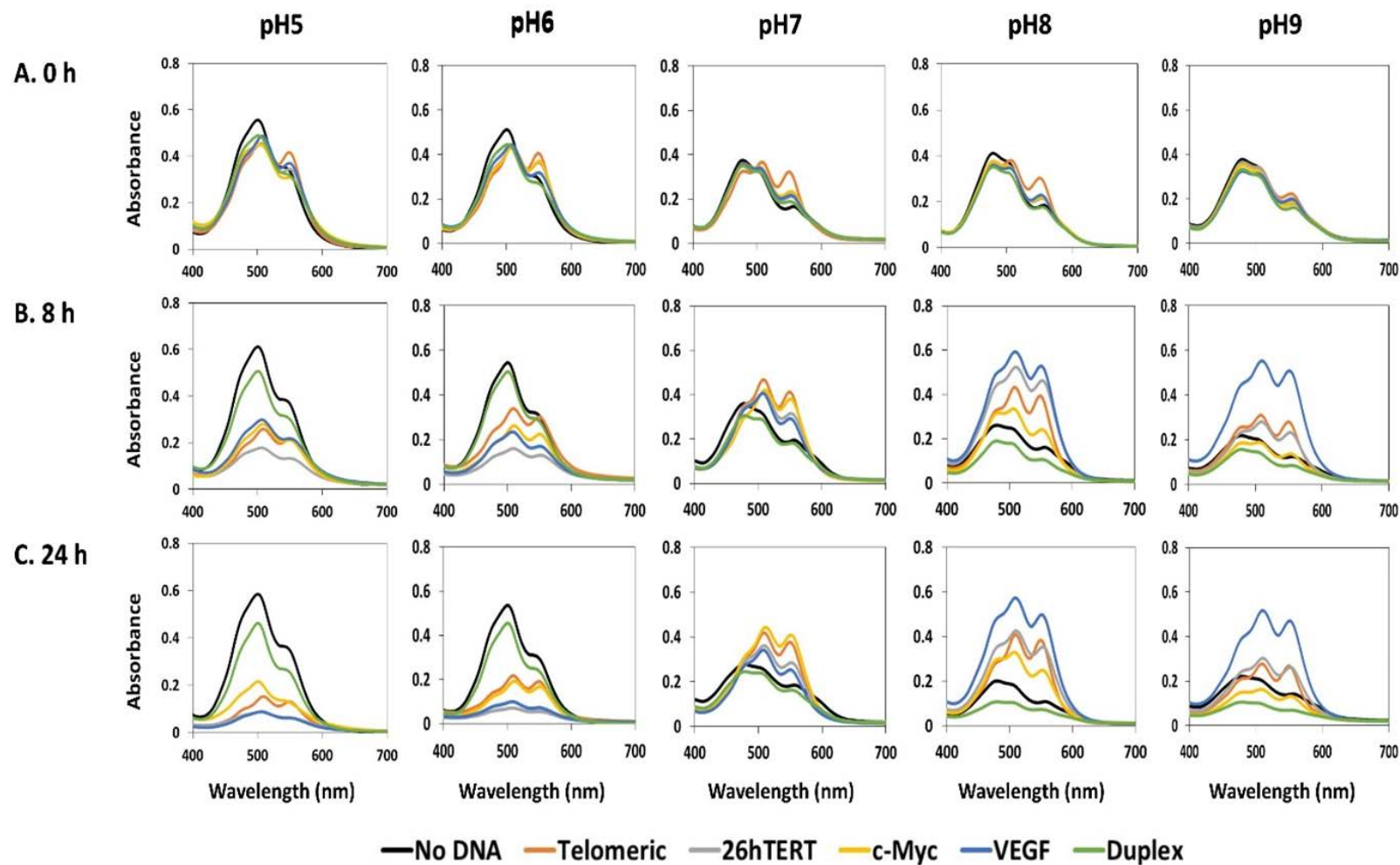| Name	Sequences
Telomeric	5'-AGATAGTTAGGGTTAGGGTTAGGGTTAGGGTT-3'
26hTERT	5'-AAGGGGAGGGGCTGGGAGGGCCCGGA-3'
c-Myc	5'-TGGGGAGGGTGGGGAGGGTGGGGAAGG-3'
VEGF	5'-AGTATAGGGGCGGGCCGGGGGCGGGGTTAGTA-3'
Duplex	5'- CGCGAATTCGCG-3'

Figure 4.19: Visible absorbance spectra of PIPER in the presence of the preformed G-quadruplex DNA structure from various sequences or duplex DNA at various pH after 0, 8, and 24 h of incubation.
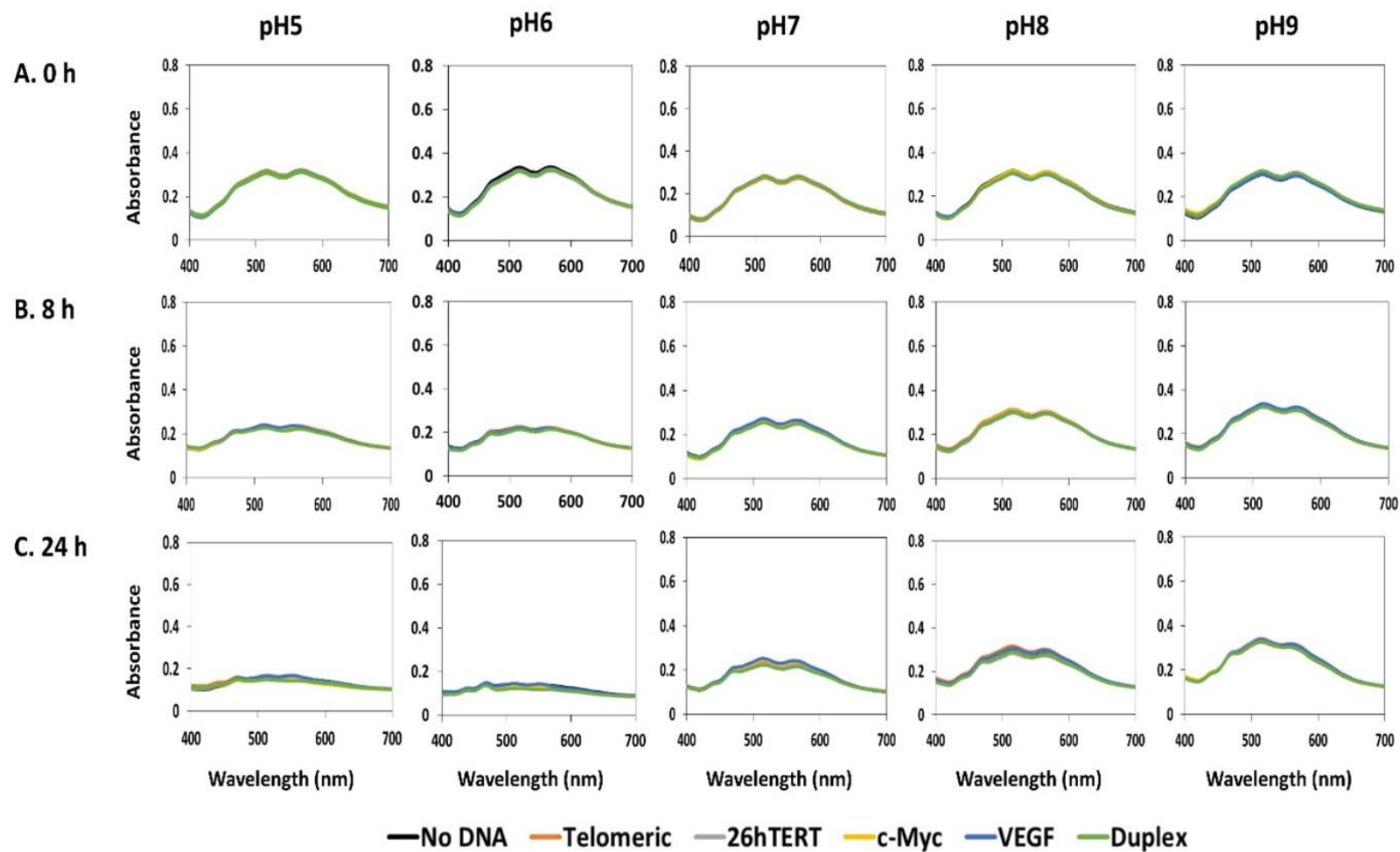
125

Figure 4.20: Visible absorbance spectra of PDI-His in the presence of the preformed G-quadruplex DNA structure from various sequences or duplex DNA at various pH after 0, 8, and 24 h of incubation.

126

Figure 4.21: Visible absorbance spectra of aPDI-PTea in the presence of the preformed G-quadruplex DNA structure from various sequences or duplex DNA at various pH after 0, 8, and 24 h of incubation.

Figure 4.22: Visible absorbance spectra of aPDI-PHis in the presence of the preformed G-quadruplex DNA structure from various sequences or duplex DNA at various pH after 0, 8, and 24 h of incubation.
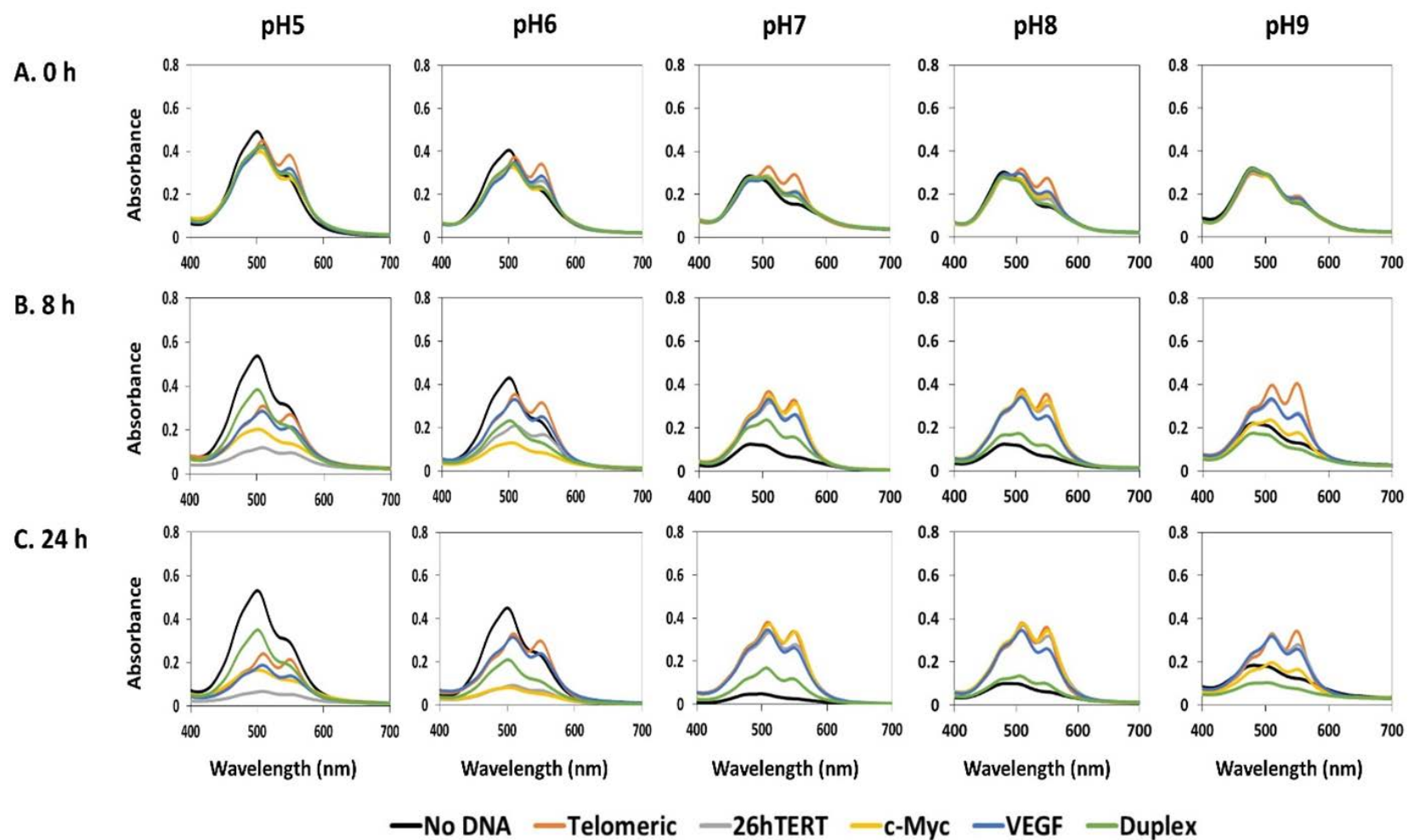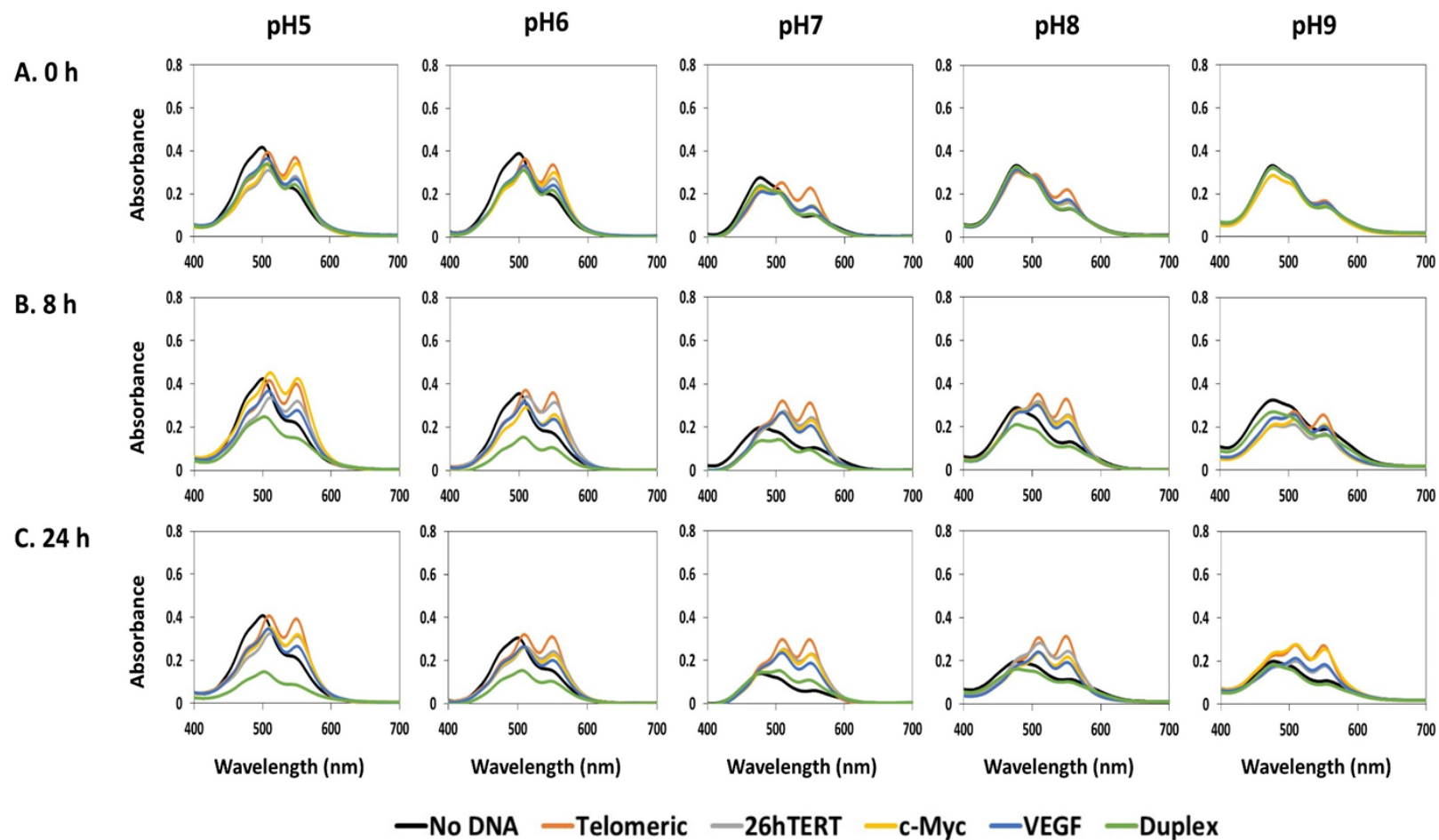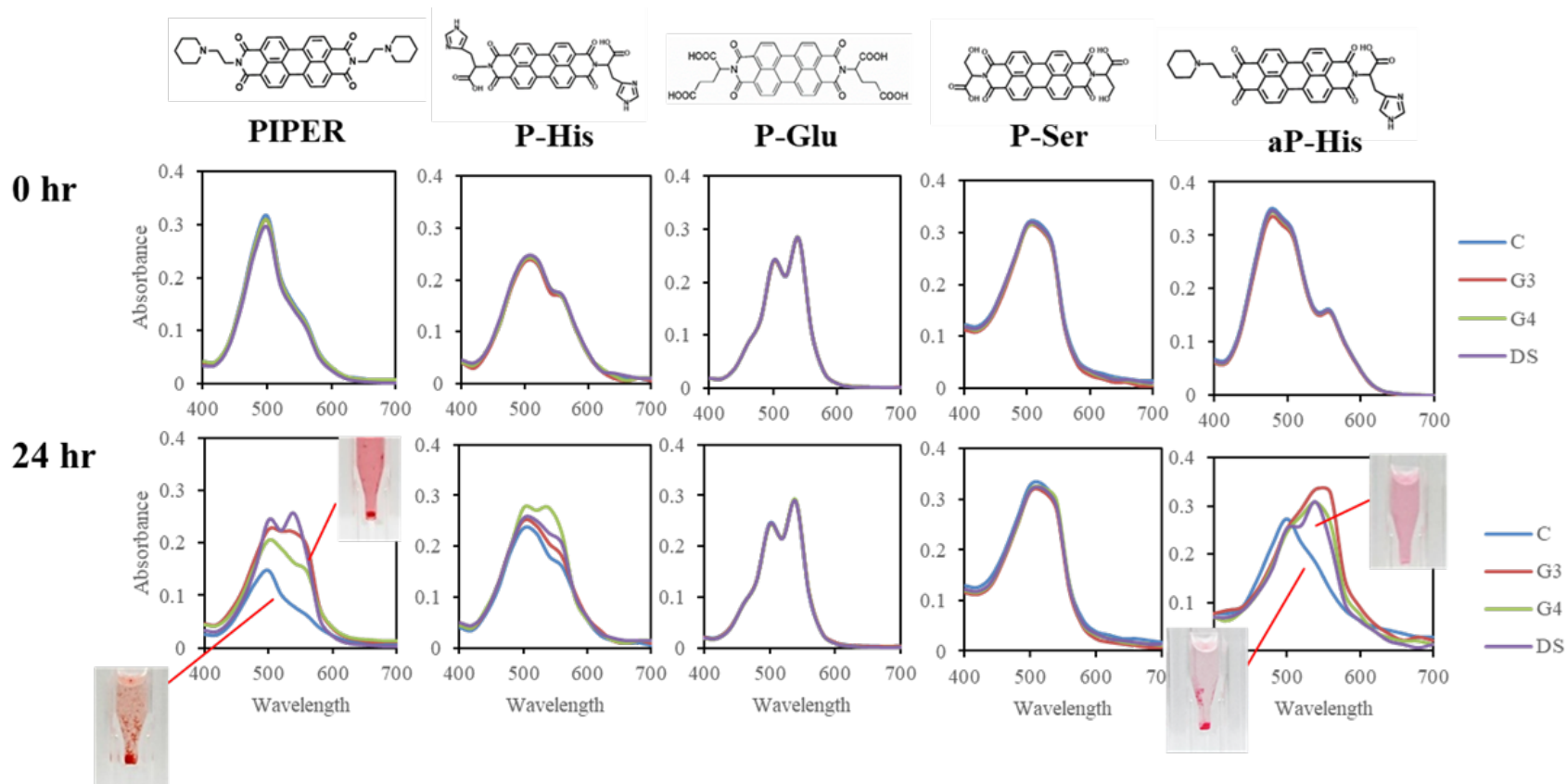
Figure 4.23: Visible absorbance spectra of perylene derivatives in the presence of the preformed G-quadruplex DNA structures G3 and G4, dsDNA (DS), and no DNA (C) in 10 mM Tris-HCl pH 7.4 after 0 and 24 h incubation.

4.6   Binding selectivity study by G4-FID (G-quadruplex fluorescent intercalator displacement)

G4-FID is a simple and fast method that allows the binding affinity and selectivity of a compound to a G-quadruplex DNA or duplex DNA to be evaluated. This assay is based on the loss of thiazole orange (TO) fluorescence intensity upon competitive displacement by a putative ligand from a DNA target under steady-state conditions.

Each experiment was performed in a 96-well plate. The master mixture of 0.25 μM preformed G-quadruplex DNA target and 0.75 μM thiazole orange in a buffer containing 10 mM Tris-HCl buffer pH 7.4 and 100 mM KCl was first prepared and the 200 μL of the mixture was dispensed into each well. A test compound was aliquoted into each well by an additional step from approximately 0.5 to 10 equivalents. At each step, the mixture was allowed to equilibrate for 3 min prior to the fluorescence recording (λ_{exc} = 490 nm, λ_{emi} = 501 nm). Because perylene derivatives have fluorescence spectra from 520-820 nm depending on each derivative, we calculate percentage of displacement based on the fluorescent intensity (FI) at 501 nm using the formula: percentage of TO displacement = 100 - [(FI/FI$_0$) × 100], where is the fluorescence intensity of TO-bound DNA without ligand and FI is the fluorescence intensity in the presence of the ligand. FID curves were obtained by plotting TO displacement percentage versus concentration of ligand. The oligonucleotides used in this assay are summarized in Table 4.7.

Table 4.7: DNA sequences of oligonucleotides used for G4-FID

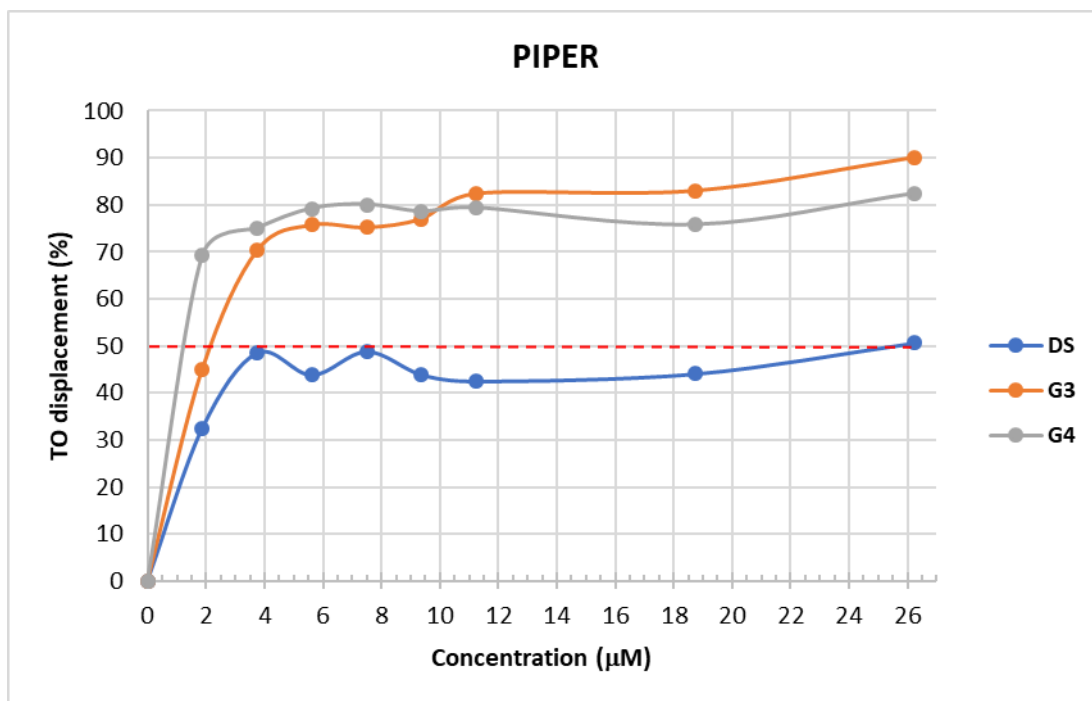| Name	Sequences
DS	CGC GAA TTC GCG
G3	TTA GGG TTA GGG TTA GGG TTA GGG
G4	TTG GGG TTG GGG TTG GGG TTG GGG

Figure 4.24: Percentage of TO displacement by PIPER using various DNA structures
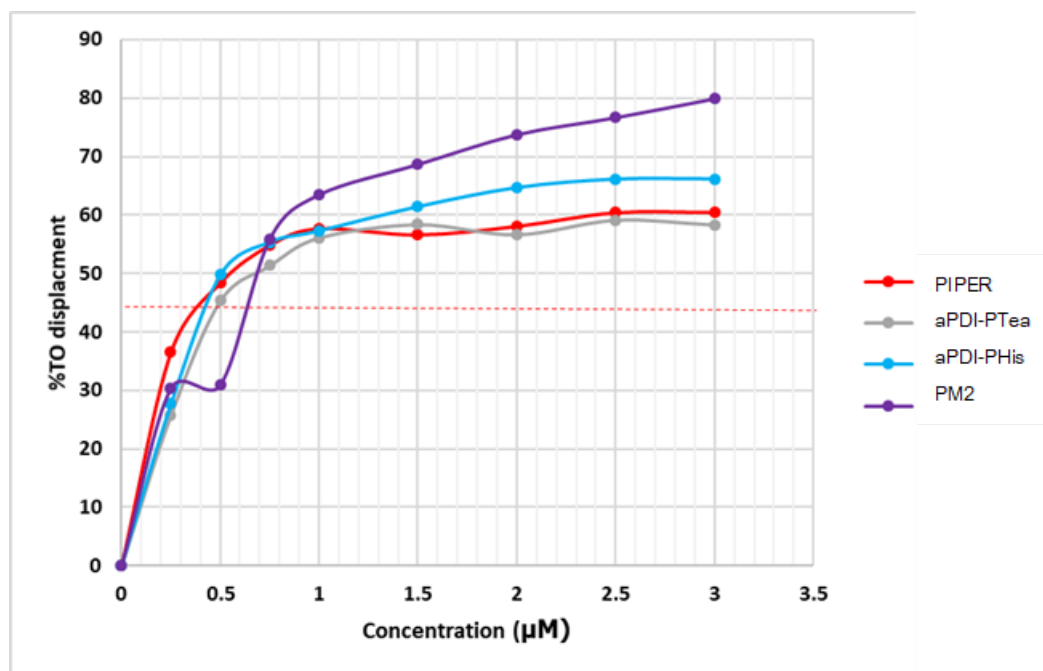

Figure 4.25: Percentage of TO displacement by perylenederivatives using G3 DNA

4.7 G-quadruplex binding selectivity of the perylene derivatives by duplex-quadruplex competition assay

Non-denaturing gel electrophoresis can be used to identify G-quadruplex ligands by its ability to induce G-quadruplex DNA formation from the G-rich strand of a duplex DNA containing a G-quadruplex motif. This assay also reveals the binding selectivity between duplex and G-quadruplex. If the test compound preferentially binds to duplex DNA, such as TmPyP4, the G-quadruplex band will not be seen, and the duplex band will be thicker with the increasing concentration of test compound.

The G-quadruplex motif strand, as indicated, was first mixed with its complementary strand and various concentrations of a test compound in 10 mM buffer containing 100 mM KCl. The mixture was heated to 95 °C for 5 minutes and then incubated at 55 °C for 10 hours in a thermocycler before cooling to 4 °C. The samples were then separated by electrophoresis at 4 °C in a 16% non-denaturing polyacrylamide gel containing 50 mM KCl, with TBE buffer supplemented with 50 mM KCl as electrophoresis buffer. Bands were identified as monomeric G-quadruplex (M), tetramolecular G-quadruplex DNA (T), and duplex (DS).
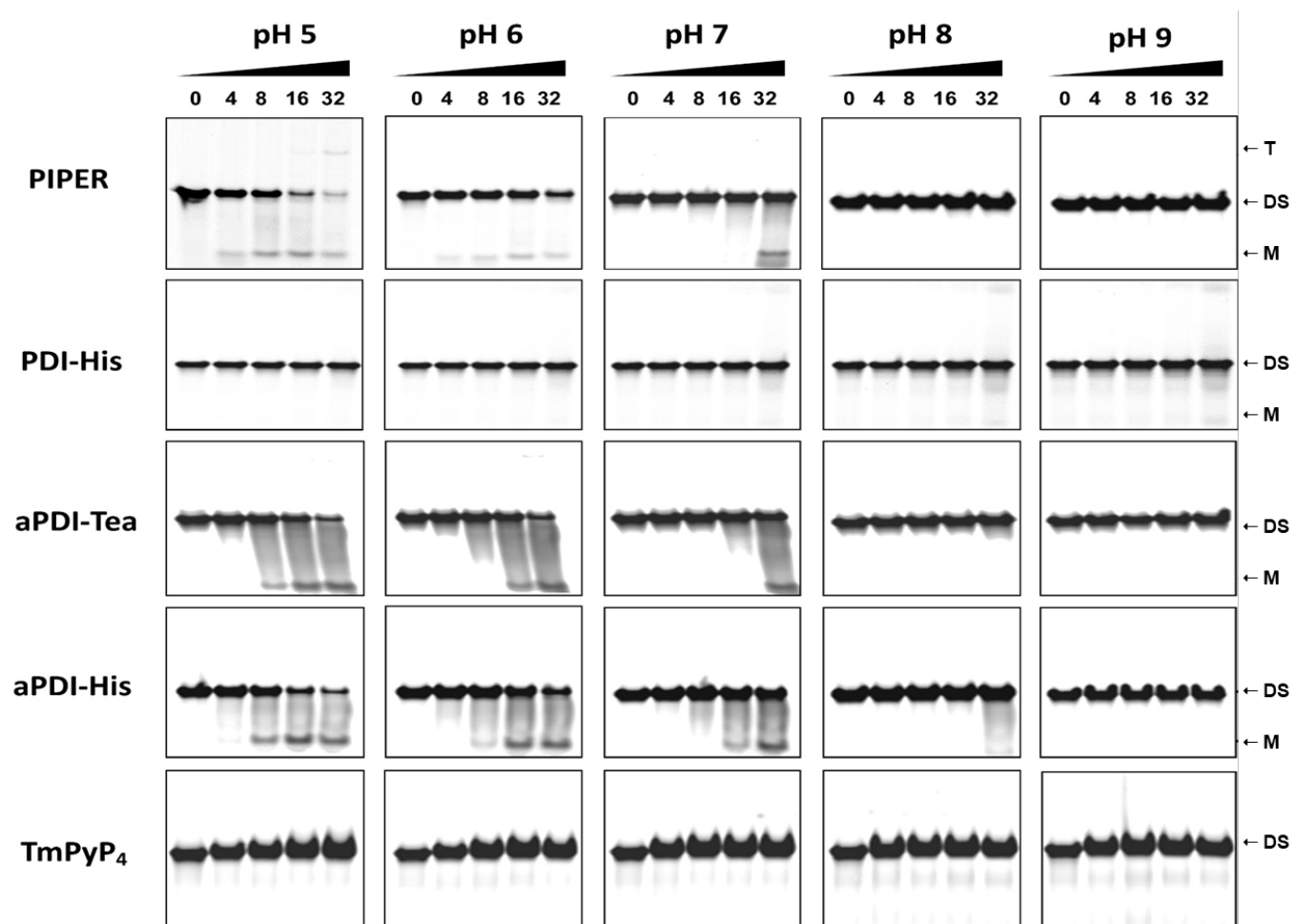
Figure 4.26: Duplex-Quadruplex competition assay with the telomeric sequence. The indicated perylene derivatives were incubated with duplex containing one strand of G-rich telomeric sequence for 10 h in buffer pH 7.4 containing 100 mM KCl. Bands were identified as monomeric G-quadruplex (M), tetramolecular G-quadruplex DNA (T), and duplex (DS).
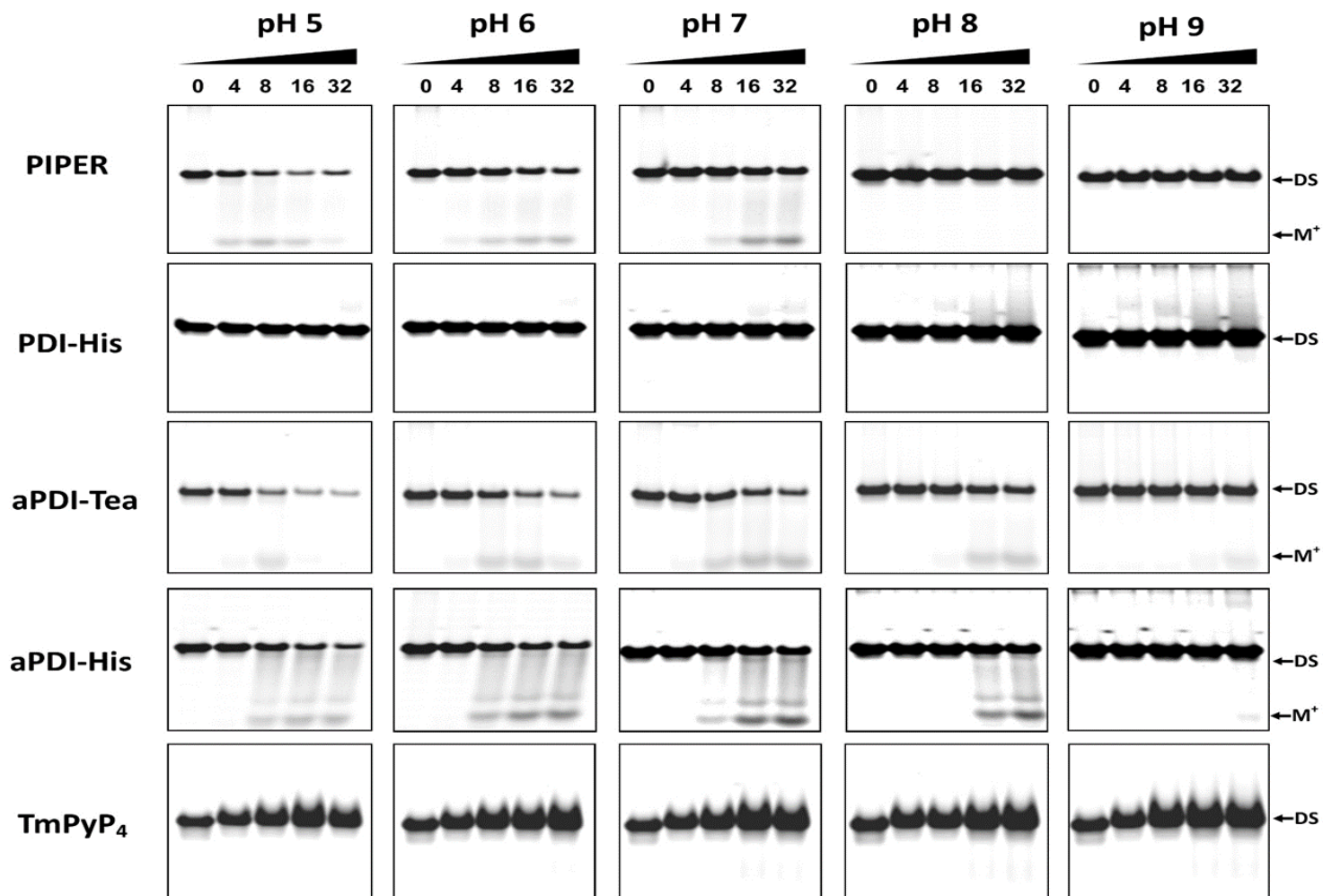
Figure 4.27: Duplex-Quadruplex competition assay with the hTERT promoter sequence. The indicated perylene derivatives were incubated with duplex containing one strand of G-rich hTERT promoter sequence for 10 h in buffer pH 7.4 containing 100 mM KCl. Bands were identified as monomeric G-quadruplex (M), tetramolecular G-quadruplex DNA (T), and duplex (DS).

Figure 4.28: Duplex-Quadruplex competition assay with the VEGF promoter sequence. The indicated perylene derivatives were incubated with duplex containing one strand of G-rich VEGF promoter sequence for 10 h in buffer pH 7.4 containing 100 mM KCl. Bands were identified as monomeric G-quadruplex (M), tetramolecular G-quadruplex DNA (T), and duplex (DS).
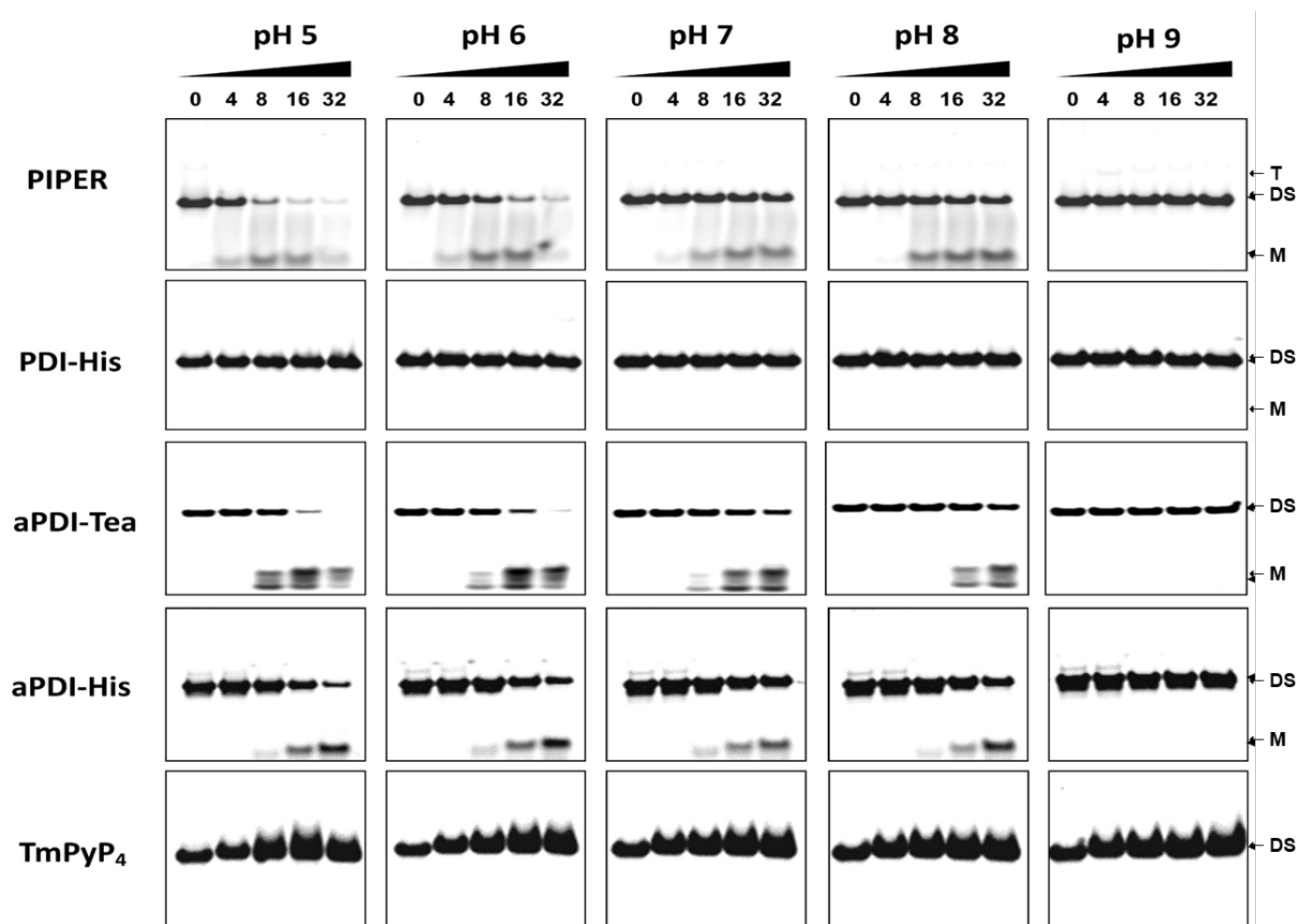
From the various binding studies above, it was difficult to digest and compare many perylene derivatives at once. We are in the process of grouping and discussing a few selected perylene derivatives for their physical properties and G-quadruplex binding specificity. For example, we are comparing PIPER, PDI-His, and aPDI-PHis together to see whether asymmetric perylene derivative may have any advantages over the usual perylene diimide derivatives.
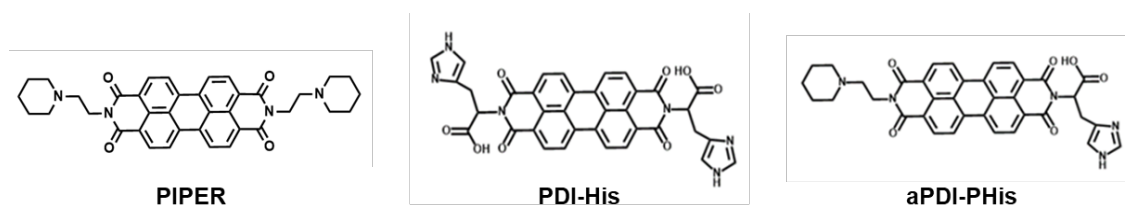

Figure 4.29: Structures of PIPER, PDI-His, and aPDI-PHis

From the solubility study (summarized in Table 4.5), we found that PIPER, with the piperidine rings on both sidechains, precipitated at higher pH (pH 7-9) and soluble at lower pH (pH 5-6) due to protonation of the piperidine sidechains. PDI-His, on the other hand, soluble at higher pH (pH 8-9) due to the ionization of the carboxylic group but precipitated at lower pH (pH 5-6) because of the neutralization of the negatively charged carboxylic group by the protonated imidazole ring. The aPDI-PHis, with one piperidine sidechain and one histidine sidechain, behaved more like PIPER than PDI-His.

Using molecular modeling program Autodock VINA to predict telomeric G-quadruplex binding, as summarized in Table 4.3, the binding affinity of PIPER, PDI-His, and aPDI-PHis was -7.7, -9.1, and -9.7 kcal/mol, respectively.

From DNA binding study using spectrophotometry (Figure 4.30), we found that PIPER and aPDI-PHis preferentially bound to the telomeric G-quadruplex DNA than duplex DNA at all the pH tested (pH 6-8), while PDI-His also preferentially bound to the G-quadruplex at pH 6.0 at a lesser extent, and bound very little to any DNA at pH 7.0 and 8.0. Between PIPER and aPDI-PHis, aPDI-PHis appears to bind G-quadruplex and duplex DNA better than PIPER at higher pH, probably due to its better solubility at these pHs.

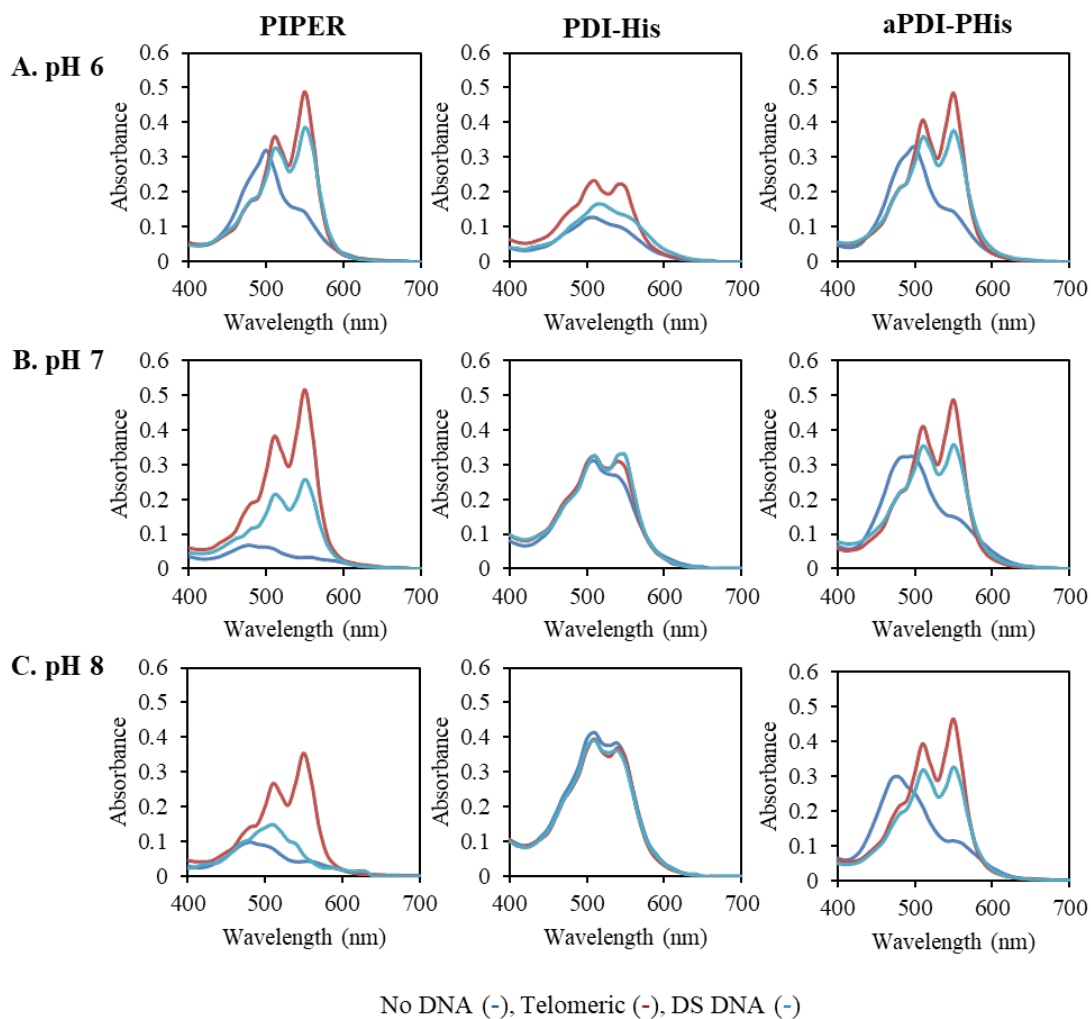No DNA (-), Telomeric (-), DS DNA (-)

Figure 4.30: DNA binding spectra by spectrophotometry. The indicated perylene derivative (40 μM) was incubated with or without a preformed telomeric G-quadruplex (20 μM) or duplex DNA (20 μM) in a 10 mM potassium phosphate and 100 mM KCl at indicated pH for 24 h before the visible absorbance spectra between 400-700 nm were recorded.

The DNA binding study by fluorescent intercalator displacement (FID) assay also revealed that PIPER and aPDI-His preferentially bound to G-quadruplex DNA over duplex DNA at pH 7.4, while PDI-His bound G-quadruplex DNA the least among the three compounds.
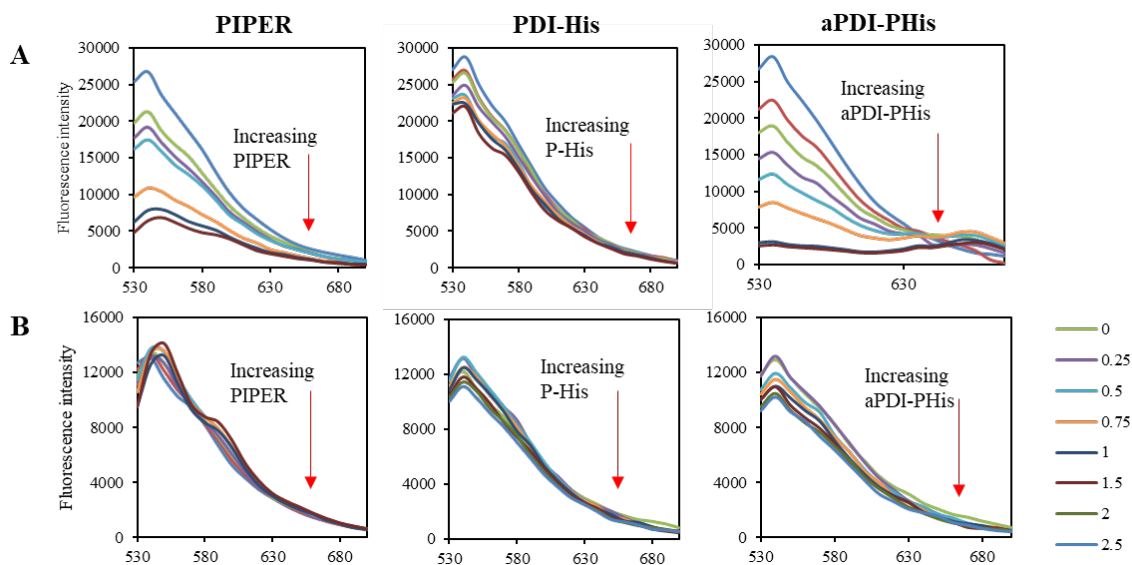
Figure 4.31: DNA binding study by fluorescent intercalator displacement (FID) assay. The 0.25 μM of preformed telomeric G-quadruplex DNA (A) or duplex DNA (B) was first incubated with 0.75 μM thiazole orange in a buffer containing 10 mM Tris-HCl buffer pH 7.4 and 100 mM KCl. The indicated test compound was then aliquoted into the mixture and was allowed to equilibrate for 3 min prior to the fluorescence recording (λ_{exc} = 490 nm, λ_{emi} = 530-700 nm).

4.8   The direct effect on telomerase activity in a cell-free system by modified fluorescent TRAP assay

The Telomeric Repeat Amplification Protocol (TRAP) assay was employed to test whether these three compounds could inhibit telomerase activity through G-quadruplex formation. The test compound at various concentrations was first incubated with a TSG4 primer at 37 °C for 2 h before the telomerase extension mixture (40 ng of crude telomerase extract, 20 mM Tris HCl, pH 8.3, 1.5 mM MgCl$_2$, 63 mM KCl, 1 mM EGTA, 0.1 mg/ml bovine serum albumin, 0.005% Tween 20, 200 μM dNTPs, and 15 pmol MTS primer) was added and the reaction was allowed to proceed at 30 °C for 30 min. After the extension reaction, the perylene was extracted from the reaction mixture by phenol/chloroform, and the telomerase products were precipitated with ethanol. The telomerase-extended products are then amplified by adding amplification reaction mixture (2.5 units Taq DNA polymerase, 15 pmol RP-FAM primer, 0.25 pmol RPc3g, 0.01 pmol IC, and 7.5 pmol NT), and PCR is performed in a thermocycler with the following condition: 3x (94 °C for 30 s; 58 °C for 60 s; and 72 °C for 90 s) and 25x (94 °C for 30 s; 65 °C for 30 s; and 72 °C for 30 s). The amplification products are electrophoretically separated in 8% non-denaturing acrylamide gel and visualized with a phosphoimaging system (Typhoon; Molecular Dynamics). The oligonucleotides used in this assay are shown in Table 4.8.

Table 4.8: Oligonucleotides Used in the Modified Fluorescent TRAP Assay

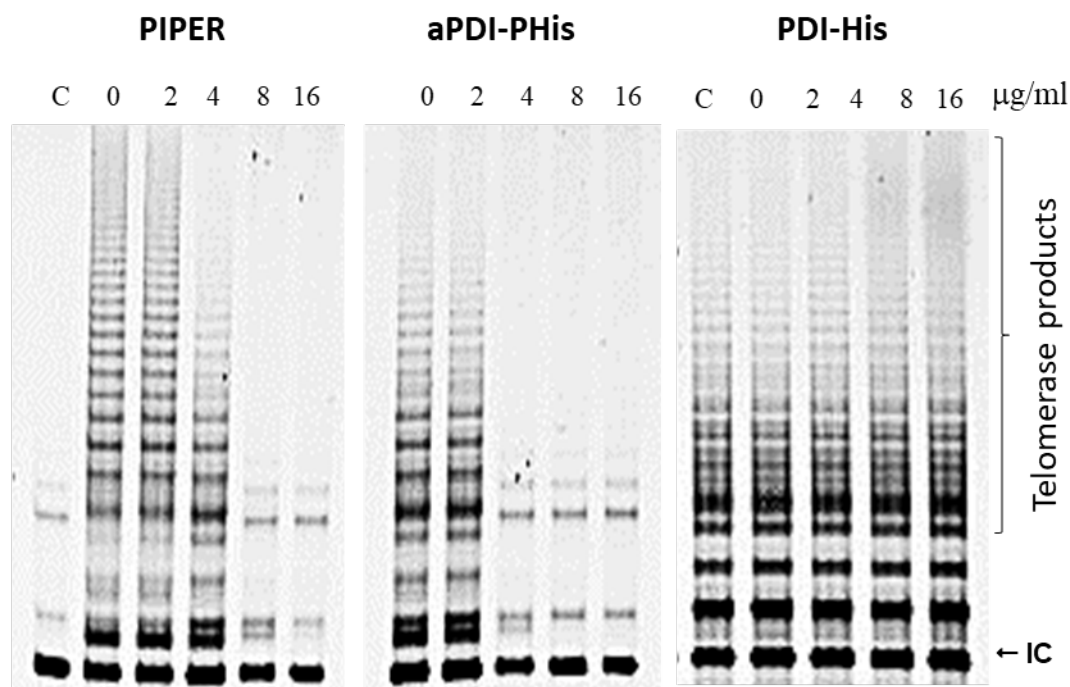| Name	Sequence
MSG4	5'-GGGATTGGGATTGGGATTGGGTT-3'
RPc3g	5′-TAGAGCACAGCCTGTCCGTG(CTAACC)$_3$GG-3′
RP-FAM	FAM-5′-TAGAGCACAGCCTGTCCGTG-3′
IC	5'-TAGAGCACAGCCTGTCCGTGAAAAGGCCGAGAAGCGATCG-3'
NT	5'-CGATCGCTTCTCGGCCTTTT-3'

Figure 4.32: The effect of PIPER, aPDI-PHis, and PDI-His on telomerase activity. The test compound at various concentrations was first incubated with a TSG4 primer at 37 °C for 2 h before the telomerase extension mixture was added. After the extension reaction, the perylene was extracted from the reaction mixture by phenol/chloroform, and the telomerase products were precipitated with ethanol. The telomerase-extended products were then amplified by PCR, and separated by non-denaturing polyacrylamide gel electrophoresis. The data were collected by a phosphoimager. IC represents the internal control.

As shown in Figure 4.32, PIPER and aPDI-PHis inhibited telomerase in a concentration-dependent manner, while PDI-His did not inhibit telomerase at all the concentrations tested. This result suggests that PIPER and aPDI-PHis inhibit telomerase through G-quadruplex formation because PDI-His, which binds very little to G-quadruplex, does not inhibit telomerase. The aPDI-PHis also shows a slightly better in telomerase inhibition than PIPER, supporting the slightly better G-quadruplex binding affinity of aPDI-PHis.

PIPER, the prototypic perylene-based G-quadruplex ligand, has been known to stack on the outer G-tetrad of a G-quadruplex DNA through π-π interaction of the perylene core, and electrostatic interaction with the positive piperidine ring and phosphate backbone. It

seems like one piperidine sidechain is enough to bind G-quadruplex DNA preferentially, as shown by the aPDI-PHis, which has one piperidine sidechain and one histidine sidechain. However, aPDI-PHis is more soluble than PIPER at higher pH and less soluble than PIPER at lower pH. This seems to help aPDI-PHis to bind G-quadruplex at the broader range of pH. These results suggest that asymmetrical perylene derivatives may provide additional qualities to a G-quadruplex ligand, which could potentially be a better anticancer drug based on selectively bind to a particular G-quadruplex DNA.

SUPPLEMENTARY MATERIALS

Output จากโครงการวิจัยที่ได้รับทุนจาก สกว.

1. **ผลงานตีพิมพ์ในวารสารวิชาการนานาชาติ**

   - Kaewtunjai N, Wongpoomchai R, Imsumran A, Pompimon W, Athipornchai A, Suksamrarn A, Lee TR, Tuntiwechapikul W. Ginger Extract Promotes Telomere Shortening and Cellular Senescence in A549 Lung Cancer Cells. *ACS Omega* 2018 3 (12), 18572-18581. DOI: 10.1021/acsomega.8b02853

   - Kaewtunjai N, Summart R, Wongnoppavich A, Lojanapiwat B, Lee TR, Tuntiwechapikul W. Telomerase Inhibition, Telomere Shortening, and Cellular Uptake of the Perylene Derivatives PM2 and PIPER in Prostate Cancer Cells. Biol Pharm Bull. (Accepted on 2019.03.06)

   - Summart A, Supan J, Meepowpan P, Lee TR, Tuntiwechapikul W. G-quadruplex binding selectivity and telomerase inhibition of a new asymmetrical perylene diimide derivative. (manuscript is being written)

2. **การนำผลงานวิจัยไปใช้ประโยชน์**

   - มีการผลิตนักศึกษาระดับปริญญาเอก 2 คน และนักศึกษาปริญญาโท 1 คน

[CPB-BPB] Your Submission MS18-00860R1

From: Bulletins of the Pharmaceutical Society of Japan (em@editorialmanager.com)

To: wirotetunti@yahoo.com

Date: Wednesday, 6 March 2019, 5:19 pm GMT+7

Ref.: Ms. No. MS18-00860R1
BPB-Regular Article

Telomerase Inhibition, Telomere Shortening, and Cellular Uptake of the Perylene Derivatives PM2 and PIPER in Prostate Cancer Cells

Dear Dr. Tuntiwechapikul,

I am pleased to tell you that your work has now been accepted for publication.
It was accepted on 2019.03.06

Comments from the Editor and Reviewers can be found below.
Thank you for submitting your work to this journal.

With kind regards

Bulletins of the Pharmaceutical Society of Japan
Editor
Hidehiko Nakagawa, Ph.D.

Comments from the Editors and Reviewers:

Reviewer #1: This manuscript by Kaewtunjai et al. has been revised precisely. Thus, the reviewer recommends acceptance of this revised manuscript for publication in Biological and Pharmaceutical Bulletin as Regular Article.

Reviewer #2: According to the reviewers' comments, the authors have made the needed changes to the initial manuscript. The revised manuscript now meets the high standard of Bulletins of the Pharmaceutical Society of Japan and thus should be suitable for publication.

_____
In compliance with data protection regulations, please contact the publication office if you would like to have your personal information removed from the database.

Ginger Extract Promotes Telomere Shortening and Cellular Senescence in A549 Lung Cancer Cells

Navakoon Kaewtunjai,[†] Rawiwan Wongpoomchai,[†] Arisa Imsumran,[†] Wilart Pompimon,[‡] Anan Athipornchai,[§] Apichart Suksamrarn,[∥] T. Randall Lee,[⊥] and Wirote Tuntiwechapikul*,[†]

[†]Department of Biochemistry, Faculty of Medicine, Chiang Mai University, Chiang Mai 50200, Thailand

[‡]Laboratory of Natural Products, Department of Chemistry, Faculty of Science and Center of Innovation in Chemistry, Lampang Rajabhat University, Lampang 52100, Thailand

[§]Department of Chemistry, Center of Excellence for Innovation in Chemistry, Burapha University, Chon Buri 20131, Thailand

[∥]Department of Chemistry and Center of Excellence for Innovation in Chemistry, Faculty of Science, Ramkhamhaeng University, Bangkok 10240, Thailand

[⊥]Department of Chemistry and the Texas Center for Superconductivity, University of Houston, Houston, Texas 77204-5003, United States

S *Supporting Information*

ABSTRACT: Replicative senescence, which is caused by telomere shortening from the end replication problem, is considered one of the tumor-suppressor mechanisms in eukaryotes. However, most cancers escape this replicative senescence by reactivating telomerase, an enzyme that extends the 3′-ends of the telomeres. Previously, we reported the telomerase inhibitory effect of a crude *Zingiber officinale* extract (ZOE), which suppressed *hTERT* expression, leading to a reduction in hTERT protein and telomerase activity in A549 lung cancer cells. In the present study, we found that ZOE-induced telomere shortening and cellular senescence during the period of 60 days when these A549 cells were treated with subcytotoxic doses of ZOE. Using assay-guided fractionation and gas chromatography/mass spectrometry analysis, we found that the major compounds in the active subfractions were paradols and shogaols of various chain lengths. The results from studies of pure 6-paradol and 6-shogaol confirmed that these two compounds could suppress *hTERT* expression as well as telomerase activity in A549 cells. These results suggest that these paradols and shogaols are likely the active compounds in ZOE that suppress *hTERT* expression and telomerase activity in these cells. Furthermore, ZOE was found to be nontoxic and had an anticlastogenic effect against diethylnitrosamine-induced liver micronucleus formation in rats. These findings suggest that ginger extract can potentially be useful in dietary cancer prevention.
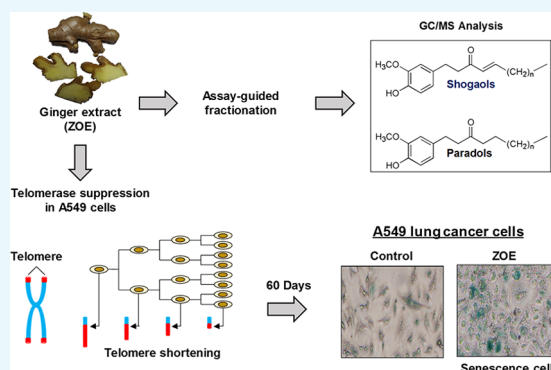
INTRODUCTION

Telomeres are specialized nucleoprotein structures found at the ends of all eukaryotic chromosomes. Telomeres maintain chromosome stability by preventing nucleolytic degradation and end-to-end fusion[1] as well as facilitating chromosome segregation during meiosis.[2] The long repetitive telomeric DNA sequence and the specific telomeric protein complex called shelterin allow the telomere to form a loop structure called T-loop, which differentiates telomeric DNA from other double-stranded DNA breaks.[3] Telomeric DNA is shortened 50−200 base pairs during each round of DNA replication because of the end replication problem.[4] The long telomeric DNA allows somatic cells to replicate for a number of cell divisions until one of the cell's telomeric DNAs is shortened to a critical length when it triggers the irreversible cell cycle arrest called "replicative senescence".[5,6]

Replicative senescence is generally considered a tumor-suppressor mechanism.[7] To escape replicative senescence, the majority of human cancers maintain their telomere length by reactivating telomerase, an enzyme that normally adds telomeric DNA to the 3′-ends of chromosomes in germline cells.[8,9] The isolated active human telomerase consists of two sets of human telomerase reverse transcriptase (hTERT), human telomeric RNA (hTR), and dyskerin.[10] Although both hTERT and hTR are necessary for telomerase activity, the transcriptional regulation of *hTERT* expression is the principal mechanism for controlling the telomerase activity.[9,11]

Dietary phytochemicals have attracted considerable interest for cancer prevention because of at least three factors: (1)

potential therapeutic effects, (2) low cost, and (3) good bioavailability.[12,13] However, applying plant chemicals for cancer prevention requires an in-depth knowledge of their mechanisms of action and their biosafety. One of the attractive targets for cancer prevention is telomerase because telomerase-specific inhibition causes cancer cells and cancer-initiating cells to enter replicative senescence and apoptosis without any significant effect on normal somatic cells.[14,15] A literature search for plant-derived telomerase inhibitors found a few natural phytochemicals that inhibited telomerase in cancer cells; these include curcumin, epigallocatechin-3-gallate (EGCG), resveratrol, genistein, sulforaphane, silibinin, and pristimerin, among others.[16] However, only a few reports show the long-term effects of these phytochemicals on telomere shortening and cellular senescence because the cancer cells must grow and normally divide for several generations in a nontoxic dose in order to attain a discernible telomere shortening. This aspect is crucially important because the viability of using dietary phytochemicals for cancer prevention depends on these agents being effective at nontoxic doses.

For millennia, the ginger (*Zingiber officinale* Roscoe) rhizome has been traditionally used for various ailments, including many gastrointestinal disorders such as nausea, vomiting, and abdominal spasm, as well as rheumatic disorders, arthritis, and muscular discomfort.[17,18] In recent years, scientists have revealed that various chemicals found in ginger rhizome—most notably gingerols, paradols, and shogaols—possess anticancer properties as shown in many experimental models.[19−22] Previously, we reported the telomerase inhibitory effect of the crude ethyl acetate fraction of *Z. officinale* extract (ZOE), which suppressed *hTERT* expression, leading to a reduction in the hTERT protein and telomerase activity in A549 lung cancer cells.[23] However, there were two remaining important questions that we wanted to address; these are as follows: (1) would telomerase suppression by the ginger extract lead to telomere shortening and cellular senescence at subcytotoxic doses? (2) What are the active compounds in the ginger extract that suppress hTERT expression? In this report, we demonstrated that ZOE induced telomere shortening and cellular senescence during long-term treatment when these A549 cells were treated with subcytotoxic doses of ZOE. We then identified the telomerase suppressors in the crude ginger extract using assay-guided fractionation and gas chromatography/mass spectrometry (GC/MS) analysis. Furthermore, we evaluated the safety, clastogenicity, and anticlastogenicity of this extract in rats.

■ RESULTS

We previously reported that ZOE suppressed *hTERT* expression in A549 lung cancer cells, leading to the decrement of the hTERT protein and telomerase activity.[23] In the present study, ZOE was extracted in the same manner, and the thin-layer chromatography (TLC) fingerprint of ZOE was similar to what we previously reported (Supporting Information, Figure S1). The IC$_{50}$ growth inhibitory effect of ZOE in A549 cells was 58 ± 2 μg/mL, compared to 50 ± 4 μg/mL as previously reported.[23]

ZOE Suppressed *hTERT* Expression and Telomerase Activity in A549 Lung Cancer Cells. We retested the new batch of ZOE for the suppression of *hTERT* expression and telomerase activity in A549 lung cancer cells. For the gene expression assay, we incubated the A549 cells with the indicated concentrations of ZOE for 24 h, before their RNAs

were extracted and assayed by semiquantitative reverse transcription polymerase chain reaction (RT-PCR) analysis. For each gene expression assay, we carefully chose the PCR cycle so that the detected amplified product could represent the initial amount of each cDNA in the reaction (Supporting Information, Figure S2). As shown in Figure 1A, the *hTERT*
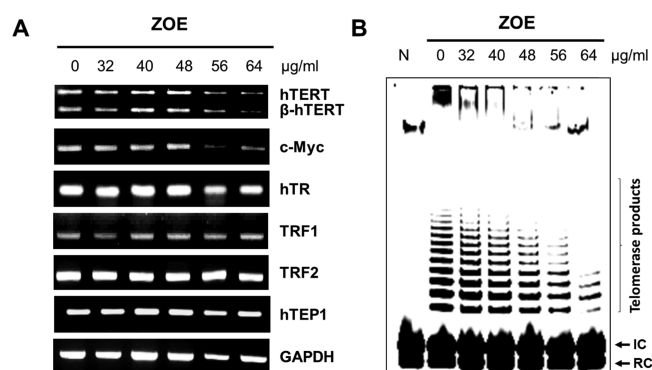

Figure 1. Short-term treatment of ZOE inhibits *hTERT* expression (A) and reduces telomerase activity in A549 lung cancer cells (B). (A) To assay for gene expression, the A549 cells were incubated with the indicated concentrations of ZOE for 24 h before their RNAs were extracted and assayed by semiquantitative RT-PCR analysis. (B) To assay the effect on telomerase activity, the A549 cells were incubated with the indicated concentrations of ZOE for 48 h before the crude protein extract was used as the source of telomerase in a modified TRAP assay. Lane N represents the negative control experiment when telomerase was heat-denatured. IC and RC represent the internal control and recovery control.

and *c-Myc* mRNA expressions were suppressed after the A549 cells were treated with ZOE for 24 h in a concentration-dependent manner. On the other hand, the housekeeping gene *GAPDH* and other telomerase-related genes (*hTR*, *TRF1*, *TRF2*, and *hTEP1*) were not affected. For the telomerase activity assay, we incubated the A549 cells with the indicated concentrations of ZOE for 48 h. The crude protein was then extracted and used as the telomerase source in a modified telomeric repeat amplification protocol (TRAP) assay. Figure 1B demonstrates that the telomerase activity of the A549 cells treated with ZOE for 48 h was also suppressed in a concentration-dependent manner. These results confirmed our initial contention that our new batch of ZOE could suppress *hTERT* expression and telomerase activity in A549 cells.

Long-Term Treatment with ZOE Led to Telomere Shortening in A549 Cells. Most cancers treated with a telomerase suppressor should exhibit telomere shortening after successive rounds of cell replication, just like normal somatic cells. In order for this to happen and be observed, the dose of the agent must allow the cancer cells to proliferate normally for several passages. In this long-term treatment study, we treated the A549 cells with two subcytotoxic doses of ZOE (5 and 10 μg/mL) added in the culture media, with the changing of fresh media every 3 days and subculturing every 6 days for up to 60 days. Cells were collected and counted with each 6 day passage. We then plotted a graph between the cumulative number of population doublings and time (Figure 2A), which shows that the A549 cells in all three sets were steadily proliferating during the course of the 60 day experiment, although the population doublings in the experimental sets
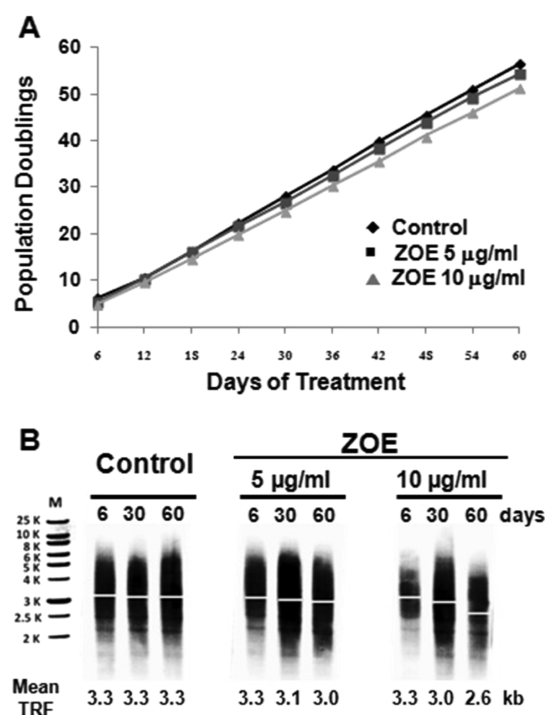
Figure 2. Population doublings (A) and telomere shortening (B) in long-term treatment of A549 cells with subcytotoxic doses of ZOE. A549 cells were incubated with or without (control) the indicated concentration of ZOE supplemented in the culture media, with a change of fresh media every 3 days and subculturing of the cells every 6 days, up to 60 days. (A) Cells from each passage were counted, and the growth curves between the cumulative numbers of population doublings were plotted against time. (B) A549 cells collected on days 6, 30, and 60 were subjected to the telomere length assay. The genomic DNA was extracted, and the mean TRFs were analyzed using the *TeloTAGGG* Telomere Length Assay kit. M represents a molecular weight marker.

with ZOE (5 and 10 μg/mL) were a little less than those in the control set.

A number of A549 cells collected in days 6, 30, and 60 were subjected to the telomere length assay. We first digested the extracted genomic DNA with *Hinf* I and *Rsa* I, before the telomere restriction fragments (TRFs) were analyzed by Southern blotting using a *TeloTAGGG* Telomere Length Assay kit. As shown in Figure 2B, the mean TRF lengths of the experimental sets (cells treated with ZOE) were less than that of the control set in a time- and concentration-dependent manner during the period of the 60 day study. In the control set, the mean TRF length remained relatively stable at 3.3 kb. However, it decreased from 3.3 to 3.1 kb on day 30 and then to 3.0 kb on day 60 in the cells treated with 5 μg/mL ZOE. With the treatment of 10 μg/mL ZOE, the decrease was much more noticeable, in which the mean TRF length decreased from 3.3 to 3.0 kb on day 30 and to 2.6 kb on day 60. On the basis of these results, we conclude that ZOE induces telomere shortening through the suppression of *hTERT* expression and telomerase activity in these cells.

Effect on Cell Senescence after Long-Term Treatment with ZOE. One of the major causes of cellular senescence is telomere shortening. One or a few critically short telomeres can trigger DNA damage response pathways that eventually lead to cellular senescence.[7,24] From the experiments above, treating A549 cells with subcytotoxic

doses of ZOE led to telomere shortening. On the basis of this finding, we further investigated whether this telomere shortening would accompany with the manifestation of cellular senescence. We conducted a senescence-associated β-galactosidase activity assay on the A549 cells collected from the long-term treatment study mentioned above. The A549 cells collected on days 30 and 60 were recultured in a six-well plate and allowed to grow for 24 h, before they were fixed, stained with X-gal solution, and photographed under a phase-contrast microscope. The blue-stained cells indicated the β-galactosidase positive cells, which are often accompanied with morphological changes. As shown in Figure 3A, there are more
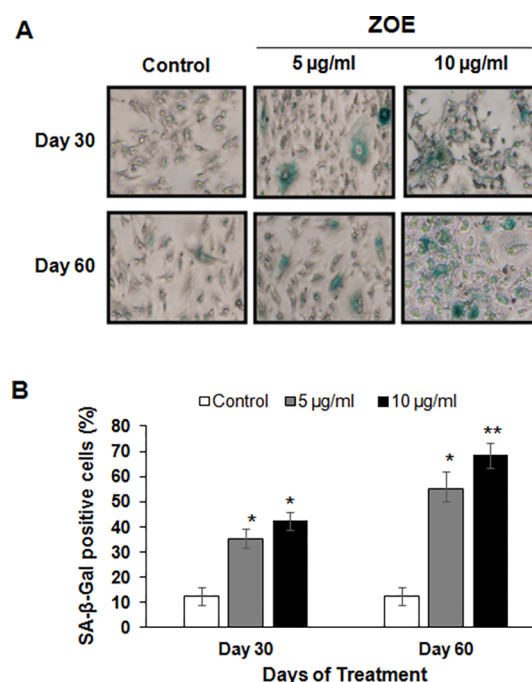

Figure 3. Senescence-associated β-galactosidase positive cells (A) and percentage of these cells (B) after long-term treatment with subcytotoxic doses of ZOE. The A549 cells from the long-term treatment with the subcytotoxic dose experiment, collected on the indicated days, were subjected to the senescence-associated β-galactosidase activity assay. The A549 cells (1 × 10⁵ cells) were recultured in a six-well plate and allowed to grow for 24 h. The cells were fixed, stained with X-gal solution, and photographed under a phase-contrast microscope. (A) Morphological changes and β-galactosidase positive cells (blue-stained cells) are indicators of cell senescence. (B) Cells in each set were counted, and the percentage of the β-galactosidase positive cells was plotted against time. Differences are considered statistically significant when *$p < 0.05$ or **$p < 0.01$, compared to the control group.

blue-stained cells in the experimental sets in which A549 cells were treated with ZOE than those found in the control set. The cells in each set were counted, and a graph between the percentage of the β-galactosidase positive cells and time was plotted (Figure 3B). In the control set, the percentage of the β-galactosidase positive cells remained around 10−15% of the cells collected on days 30 and 60. However, after the A549 cells were treated with 5 μg/mL ZOE, the percentage of the β-galactosidase positive cells increased to 35% on day 30 and then to 55% on day 60, respectively. The percentage of the β-galactosidase positive cells was more profound after the A549 cells were treated with 10 μg/mL ZOE, with the percentage of

the β-galactosidase positive cells rising to 43% on day 30 and then to 69% on day 60.

Effect on Clonogenicity after Long-Term Treatment with ZOE. Cellular senescence is the state by which mitotic cells irreversibly stop dividing. This inability to divide can be tested using a simple colony-forming assay in which individual cells are spread on a tissue culture plate and allowed to form colonies. To evaluate the effect on the clonogenicity of A549 cells after long-term treatment with ZOE, the A549 cells collected on days 30 and 60 from the long-term treatment study were seeded at a low density (2×10^3 cells) in a 10 cm tissue culture dish and allowed to form colonies for a period of 14 days. The colonies were then stained with crystal violet and digitally scanned. The number of colonies was determined using the ImageQuant TL software. Figure 4A shows the
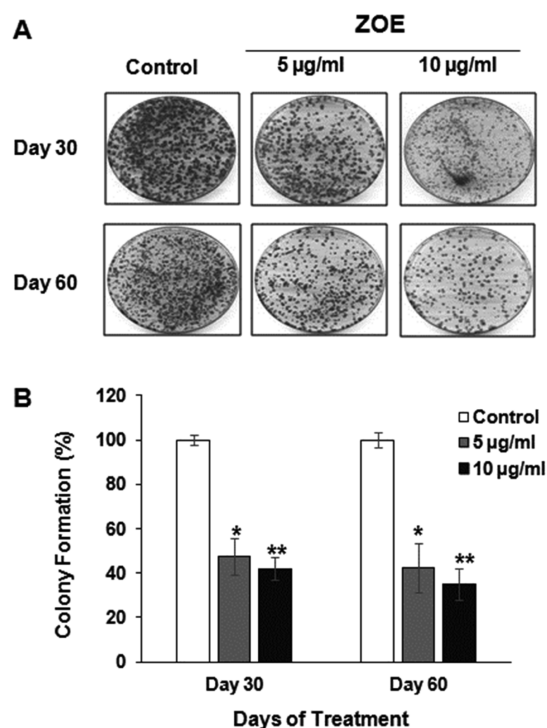

Figure 4. Clonogenicity of A549 cells (A) and percentage of colony formation (B) after long-term treatment with subcytotoxic doses of ZOE. The A549 cells collected on the indicated days were subjected to the colony formation assay. The low number of cells (2×10^3 cells) was recultured on a Petri dish. The cells were allowed to form colonies for 14 days and stained with crystal violet. Each plate was then scanned by a phosphoimager, and the colonies were counted using ImageQuant TL software. The percent colony formation was then plotted against time. Differences are considered statistically significant when *$p < 0.05$ or **$p < 0.01$, compared to the control group.

pictures of the colony formation of the A549 cells collected from the untreated control set and the treated experimental sets (with 5 and 10 μg/mL of ZOE) on days 30 and 60, respectively. The colonies from the untreated control set are densely populated, whereas the colonies from the treated experimental sets are less populous in a time- and concentration-dependent manner. The numbers of colonies were quantified, and the percentage of colony formations was compared to the control and plotted against time. The graph in Figure 4B shows that after the A549 cells were treated with 5

μg/mL ZOE, the percentage of colony formation decreased to 48% on day 30 and to 42% on day 60. After the A549 cells were treated with 10 μg/mL of ZOE, the percentage of colony formation decreased to 42% on day 30 and to 35% on day 60. From all of the experiments presented above, we conclude that ZOE suppresses *hTERT* expression and telomerase activity in A549 cells. The long-term treatment with subcytotoxic doses of ZOE in this cancer cell line leads to a gradual loss of telomere length, an induction of cellular senescence, and a reduction in clonogenicity.

Identification of Telomerase Suppressors in ZOE. We employed assay-guided fractionation and GC/MS analysis to identify the active compounds in ZOE that suppress telomerase expression and activity in A549 cells. ZOE was purified by column chromatography to obtain four fractions: E1–E4. The ZOE and its fractions were fingerprinted by TLC and high performance liquid chromatography (HPLC; Supporting Information, Figures S1, S3, and S4). The amount of 6-gingerol in these fractions was also quantified by HPLC. The E1 and E2 fractions contained an undetectable amount of 6-gingerol, whereas the E3 and E4 fractions contained about 30 and 40% of 6-gingerol, respectively. The semiquantitative RT-PCR analysis found that only the E2 fraction significantly suppressed *hTERT* expression in a dose-dependent manner, whereas the E3 and E4 fractions, which contained a large amount of 6-gingerol, were not found to suppress *hTERT* expression (Supporting Information, Figure S5A). These results confirm our previously published finding that 6-gingerol does not suppress *hTERT* expression.[23]

We further fractionated the E2 fraction by column chromatography into four more subfractions: E2.1–E2.4. The results from RT-PCR studies showed that all of these subfractions could suppress the expression of *hTERT* in A549 cells (Supporting Information, Figure S5B). These subfractions were then subjected to the same telomerase activity assay as previously described. All four subfractions were found to suppress the telomerase activity in a concentration-dependent manner (Supporting Information, Figure S6).

We then employed GC/MS to identify the compounds within these subfractions. The GC chromatograms, GC data, and selected GC/MS spectra are shown in the Supporting Information (Figures S7–S10). By using the fragment analysis of the ginger compounds reported by Tao et al.,[25] and Jolad et al.,[26] we found that these active subfractions contained mostly paradols and shogaols of varying chain lengths (Table 1). Therefore, we conclude that paradols and shogaols are likely to be the active compounds in ZOE that are responsible for the suppression of *hTERT* expression and telomerase activity. Although there are concerns about the thermal degradation and dehydration of compounds containing a β-hydroxyketone group such as gingerols to aliphatic aldehyde, zingerone, and

Table 1. Major Compounds in the E2 Subfractions by GC/MS Analysis[a]

E2.1	E2.2	E2.3	E2.4
11-paradol (75%)	11-paradol (26%)	7-paradol (42%)	6-shogaol (68%)
13-paradol (9%)	7-paradol (22%)	10-shogaol (33%)	8-shogaol (8%)
Bisabolene (7%)	6-paradol (22%)	11-paradol (9%)	10-shogaol (6%)
	9-paradol (16%)	6-paradol (6%)	7-paradol (5%)

[a](%) represents percentage of the peak area in GC chromatogram.

the corresponding shogaols under GC condition,[26] we do not believe the paradols and shogaols we found in the E2.1−E2.4 subfractions were the products of thermal degradation or dehydration because gingerols were absent in the active E2 fraction and were found only in E3 and E4 fractions.

Although the data and results above suggest that paradols and shogaols are likely the active compounds in ZOE and responsible for the suppression of *hTERT* expression and telomerase activity, we cannot rule out the possibility that some minor ingredients in the extract are responsible for the observed effects. To verify whether the activities arose specifically from paradols and shogaols, we obtained pure 6-paradol and pure 6-shogaol as representative compounds and also pure 6-gingerol as a negative control. The same gene expression analysis by semiquantitative RT-PCR and telomerase activity assay were performed. The results are shown in the Supporting Information (Figure S11). The results showed that 6-paradol and 6-shogaol significantly suppressed *hTERT* expression in a dose-dependent manner, whereas 6-gingerol only slightly suppressed the *hTERT* expression at a higher concentration. Telomerase activity in the cells treated with 6-paradol and 6-shogaol, but not 6-gingerol, was also suppressed in a concentration-dependent manner. These results confirmed that the suppression of *hTERT* expression and telomerase activity found in ZOE arose from the paradols and shogaols rather than the gingerols.

The chemical structures of gingerols, shogaols, and paradols (Figure 5) are similar in that they all contain the 4-hydroxy-3-
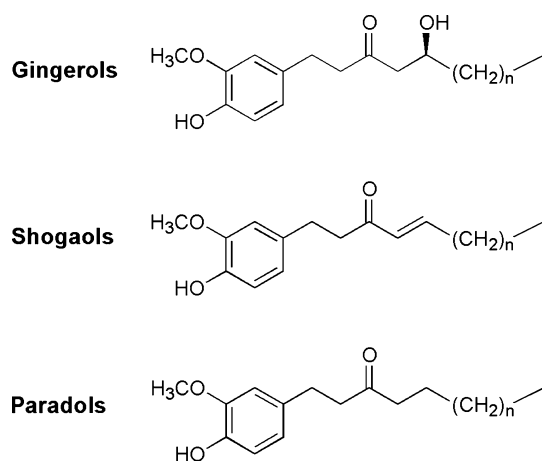

Figure 5. Chemical structures of gingerols, shogaols, and paradols.

methoxyphenyl nucleus linked to different side chains of various lengths at position 1. Gingerols contain a β-hydroxy ketone side chain, whereas shogaols contain an α,β-unsaturated ketone side chain and paradols contain only one ketone group in their alkyl side chain. In terms of chemistry, shogaols are the dehydrated form of gingerols and paradols are the hydrogenated form of shogaols. The loss of activity to suppress *hTERT* expression and telomerase activity in gingerols might be due to the presence of the β-hydroxy group in the hydrocarbon side chain. The length of the side chain in paradols and shogaols might not affect the activity because all four subfractions (E2.1−E2.4), which have different compositions of paradols and shogaols (Table 1), had the capacity to suppress *hTERT* expression and telomerase activity.

Influence of ZOE on Acute Toxicity and DEN-Induced Clastogenicity in Rats. To evaluate the biosafety of our

ZOE, the same ZOE used in the above experiments was assayed for acute toxicity, clastogenicity, and anticlastogenicity in rats. The results from the acute toxicity test showed that rats did not show any signs of toxicity or mortality after treating with the single maximum dose of 5000 mg/kg bw of ZOE for 14 days. Their body weight, food and water intake, and relative organ weight were also similar to those from the control group (Supporting Information, Tables S1 and S2). These results suggest that ZOE is safe in rats, which is in agreement with the ranking of ginger in the generally recognized as safe (GRAS) list by the Food and Drug Administration.[27]

We then employed the liver micronucleus assay to investigate the clastogenicity and anticlastogenicity of ZOE in rats. The treatment scheme is illustrated in Figure 6. Male
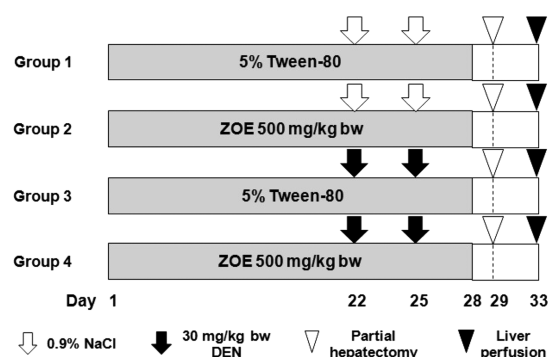

Figure 6. Protocol for clastogenicity and anticlastogenicity determination of ZOE in rats. Male Wistar rats were divided into four groups. Group 1 is a negative control group, whereas group 3 is a positive control group. Group 2 is the experiment group to determine the clastogenic effect of ZOE, whereas group 4 is the experiment group to determine the anticlastogenic effect of ZOE. The liver micronucleus was used as the end-point marker.

Wistar rats were divided into four groups: I and II were used to evaluate the clastogenicity effect, whereas III and IV were used to evaluate the anticlastogenicity effect. The results from group II, rats treated with 500 mg/kg bw of ZOE for 28 days, indicate that ZOE had no clastogenic effects on rat liver because their final body weight, liver micronucleus formation, and mitotic index were not significantly different from those found in the control group (group I). However, the results from groups III and IV suggest that ZOE had an anticlastogenic effect against diethylnitrosamine (DEN)-induced liver micronucleus formation in rats. When rats in group III were injected with two doses of 30 mg/kg bw of DEN on days 22 and 25, their average final body weight reduced significantly (−10.7%), and there was a significant increase in liver micronucleus formation (+525.3%), with no significant change in the mitotic index. On the contrary, the group IV rats that were treated with 500 mg/kg bw of ZOE for 28 days, along with two doses of 30 mg/kg bw of DEN on days 22 and 25, were found to have less reduction in their average final body weight (−6.7%), and the number of micronucleated hepatocytes significantly decreased (−49.8%) compared to the positive control group (group III). The data from these clastogenicity and anticlastogenicity experiments are summarized in Table 2. Our results here are in agreement with previously published articles, which found that the ginger extract had a protective effect against DEN-induced liver carcinogenesis in a rat model,[28] and it had anticancer and anti-inflammatory effects through the reduction of NF-κB and TNF-α in ethionine-induced hepatoma rats.[29]

Table 2. Influence of ZOE on DEN-Induced Clastogenicity in Rats[a]

test group	rat body weight (g)		MNH (per 1000 HEP)	mitotic index
	initial	final		
negative control (5% Tween 80)	113 ± 3	289 ± 14	1.62 ± 0.85	3.36 ± 0.45
ZOE (500 mg/kg bw)	112 ± 7	284 ± 5	1.79 ± 0.45	3.13 ± 0.36
positive control (DEN + 5% Tween 80)	110 ± 6	258 ± 11*	8.51 ± 1.82*	3.25 ± 0.33
DEN + ZOE (DEN + 500 mg/kg bw)	110 ± 6	265 ± 4*	4.24 ± 1.02**	3.39 ± 0.52

[a]Values expressed as mean ± SD; MNH: micronucleated hepatocytes; HEP: hepatocytes; DEN; diethylnitrosamine; (*) indicates statistical significance at $p < 0.05$ compared to the negative control group; (**) indicates statistical significance at $p < 0.05$ compared to the positive control group.

■ DISCUSSION

Replicative senescence is a basic feature of normal somatic cells and is widely considered as a cancer prevention mechanism.[7] However, 85−90% of cancers escape this phenomenon by reactivating telomerase, which adds telomeric repeats to the 3′-end of telomeres.[8] Telomerase-specific inhibition should, therefore, not affect normal somatic cells. It would render cancer cells entering replicative senescence naturally, with the manifestation of telomere erosion occurring with each round of cell division similar to that of normal somatic cells. With this safe mode of action, telomerase-specific inhibition is an attractive strategy for cancer chemoprevention.

Dietary phytochemicals have attracted considerable interest for cancer prevention for some time because of their potential therapeutic effects and safety. In search of telomerase inhibitors from plants, a few natural phytochemicals were found to inhibit telomerase in cancer cells; these include curcumin, EGCG, resveratrol, genistein, sulforaphane, silibinin, and pristimerin, among others.[30] However, it is worth noting that only a few reports show the long-term effect of these phytochemicals on telomere shortening and cellular senescence after successive rounds of cell divisions using a nontoxic dose. This is probably due to their broad mechanism of actions and cytotoxicity. Among these few reports, EGCG is the only example that was found to induce telomere shortening and cellular senescence (in U937 leukemic cells and HT29 colon adenocarcinoma cells) with its nontoxic dose up to 55−60 population doublings.[31] Curcumin was also found to induce telomere shortening in several brain tumor cell lines after treating these cells with half the concentration of their IC$_{50}$ for 15 days.[32] Similar to curcumin, thymoquinone (a compound from *Nigella sativa*) was found to induce telomere shortening in glioblastoma cell line M059K after treating these cells with approximately half the concentration of their IC$_{50}$ for 15 days.[33] The *Inula viscosa* extracts, and its purified sesquiterpene lactone, tomentosin, were claimed to induce telomere shortening in cervical cancer cells.[34,35] However, these two reports only measured the length of the 3′ G-rich telomeric overhang after the cells were treated with the test sample for 72 h.

In the present study, we add *ZOE* to this short list of plant-originated telomerase inhibitors that induce telomere shortening and cellular senescence in cancer cells using subcytotoxic doses. We first demonstrated that ZOE could suppress *hTERT* expression and telomerase activity in A549 lung cancer cells. The cells treated with subcytotoxic doses of ZOE proliferated normally but were soon found to manifest telomere shortening and cellular senescence. Using assay-guided fractionation and GC/MS analysis, we found several paradols and/or shogaols as the major compounds in the active subfractions. The results

from pure 6-paradol and 6-shogaol showed that these two compounds could suppress *hTERT* expression and telomerase activity in the A549 cells, although 6-gingerol could not. We have concluded that the active compounds in ZOE that are responsible for the suppression of *hTERT* expression and telomerase activity in A549 lung cancer cells are paradols and shogaols. Last, we also found that ZOE did not induce acute toxicity in rats and showed the anticlastogenic effect against liver micronucleus formation in rats.

Nowadays, much attention has been focused on products derived from food sources that provide extra health benefits. Cancer chemoprevention by dietary phytochemicals is of considerable interest because of their potential therapeutic effects and safety. Many dietary phytochemicals were found to possess chemopreventive properties in various epidemiological and preclinical studies.[36] Recently, clinical trials have added to the evidence supporting the efficacy of some selected compounds.[37,38] Ginger (*Z. officinale Roscoe*), an already established nutraceutical product, has been reputed to have anticancer properties in various experimental models. Experiments in A549 lung cancer cells reveal that gingerol, shogaol, and zerumbone exhibit anticancer activity through various mechanisms.[39−43] For example, gingerol was found to sensitize human lung cancer cells apoptosis.[39] 6-Shogaol was found to induce autophagy through the AKT/mTOR pathway and inhibit cancer via microsomal prostaglandin E2 synthase 1 (mPGES-1), β-catenin, and glycogen synthase kinase 3β (GSK-3β) pathways.[40,41] Moreover, 6-shogaol and its cysteine-conjugated metabolite induce lung cancer cell apoptosis through a p53 pathway in both in vitro and in vivo experiments.[42] Zerumbone was also found to suppress cell invasion through inhibiting the FAK/AKT/ROCK pathway.[43] Our present study shows that paradols and shogaols in the ginger extract (ZOE) suppressed telomerase, which led to telomere shortening and cellular senescence, with a significant reduction in the clonogenicity of the A549 lung cancer, using only subcytotoxic doses. The extract was also found to be safe in rats, with an additional chemoprotective effect against DEN-induced liver micronucleus formation. These results lead us to believe that the ginger extract could potentially be a valuable tool in dietary cancer prevention against lung cancer.

■ METHODS

Chemicals. We purchased all materials from commercial suppliers. All oligonucleotides were supplied by Ward Medic (Thailand). Sulforhodamine B, 6-gingerol, and DEN were purchased from Sigma-Aldrich. Taq DNA polymerase was purchased from Vivantis. The collagenase type IV was purchased from Invitrogen (USA). Standard 6-shogaol and 6-paradol were provided by Prof. Apichart Suksamrarn (details

of extraction, purification, and identification are shown in Supporting Information, S1).

Plant Collection and Extraction. Ginger rhizome was collected in March 2012 from Lampang Province, Thailand, and was identified as *Z. officinale Roscoe*. A voucher specimen (BKF no. 118527) was deposited in the Forest Herbarium, Ministry of Natural Resources and Environment, Bangkok, Thailand. For the assay-guided fractionation study, ginger rhizomes (4.0 kg) were air-dried and finely pulverized. The ginger powder was then extracted into hexane, ethyl acetate, acetone, and methanol sequentially. After drying the solvents, we afforded 371.5, 235.8, 276.1, and 189.6 g of residues, respectively. The crude ethyl acetate extract (235.8 g) was purified by column chromatography using silica gel (Merck no. 7734, Mesh 70−230 ASTM) as the stationary phase. The first mobile phase was a gradient mixture of hexane (1 L) and ethyl acetate (1 L), followed by a gradient mixture of ethyl acetate (1 L) and methanol (1 L). The eluent was collected in a series of fractions, and the composition was visualized by TLC, before the fractions with similar composition were collected into four main fractions, E1−E4. After evaporation, dry powders of E1 (85.7 g), E2 (16.5 g), E3 (23.1 g), and E4 (46.2 g) were obtained. The E2 fraction was found to suppress *hTERT* mRNA expression and telomerase activity, and 10 g of the E2 fraction was further purified by the same chromatography. The first mobile phase was a gradient mixture of hexane (100 mL) and ethyl acetate (100 mL), followed by a gradient mixture of ethyl acetate (100 mL) and methanol (100 mL). After evaporation, dry powders of E2.1 (2.2 g), E2.2 (1.7 g), E2.3 (3.1 g), and E2.4 (2.8 g) were obtained. These fractions and subfractions were dissolved in dimethyl sulfoxide (DMSO) and stored at 4 °C. Prior to use, the stock solutions were diluted with distilled deionized water to working solutions with the same concentration of DMSO. The final concentration of DMSO was the same in all samples and was between 0.16 and 0.64% in the short-term cell culture experiments. For the long-term treatment of A549 cells, the crude ethyl acetate fraction of *Z. officinale* (ZOE) was obtained in a similar manner. The final concentration of DMSO in both experimental set and control set was 0.05%.

TLC Analysis. ZOE and its fractions and subfractions were TLC fingerprinted using silica gel GF254 (Fluka) as the stationary phase, and a mixture of hexane and ethyl acetate was used as the mobile phase. The TLC plate was then dipped in *p*-anisaldehyde/sulfuric acid reagent before color developing by heating at 100 °C.

HPLC Analysis. We performed the HPLC analyses using an HPLC system (Agilent 1200 infinity series, Agilent, USA) and a C18 reverse phase column (4.6 mm × 150 mm, ZORBAX Eclipse Plus) as the stationary phase. A 50 µL sample of ZOE and its fractions (E1−E4) (10 mg/ml) were separated using a mixture of acetonitrile (A) and water (B) as the mobile phase at a flow rate of 2.0 mL/min. Within the total run time of 10 min, the solvent mixture profile of the mobile phase was as follows: 0−0.5 min, 35A:65B; 0.5−5 min, gradient mixture from 35A:65B to 95A:5B; and 5−10 min, 95A:5B. The compounds were detected using a UV−visible detector (Spec Monitor 3200) at 280 nm. A mixture of standard 6-gingerol (0.4 mg/mL), 6-shogaol (0.2 mg/mL), and 6-paradol (0.2 mg/mL) was run separately using the same conditions.

Cell Culture. The A549 human lung carcinoma cell line was obtained from American Type Culture Collection (Rockville, MD) and grown in RPMI 1640 culture media with 10% fetal bovine serum and 1% antibiotics (50 µg/mL streptomycin, 50 units/mL penicillin) at 37 °C in a humidified incubator with 5% CO_2.

In Vitro Growth Inhibition Assays. We determined the growth inhibition of A549 cells by the ginger extract and selected ginger compounds using the sulforhodamine B (SRB) assay according to a published protocol.[44] The A549 cells (1.0 × 10^4 cells) were incubated with various concentrations of the indicated ginger fraction or the pure compound at 37 °C for 72 h in a humidified incubator with 5% CO_2. The graphs between the concentration of the test sample and the percentage of cell viability, from three independent experiments, were plotted, and the 50% growth inhibitory concentrations (IC_{50}) were determined. The IC_{50} growth inhibitory concentrations of A549 lung cancer cells by ZOE, its subfractions, and some pure compounds are summarized in the Supporting Information (Table S3).

Semiquantitative RT-PCR Analysis. We grew A549 cells (5.0 × 10^5 cells) on a six-well tissue culture plate for 24 h at 37 °C before they were treated with the indicated concentration of the test sample for another 24 h. The total RNA was collected, and the mRNA was converted into cDNA using RevertAid reverse transcriptase (Thermo Scientific). PCR amplification for each gene was carried out with the gene-specific primers. The primer sequences, annealing temperatures, and PCR cycles are summarized in the Supporting Information (Table S4).

Modified TRAP Assay. We performed the TRAP assay according to a published protocol and our previous publication.[23,45] Briefly, the A549 cells (5.0 × 10^5 cells) were seeded on a six-well tissue culture plate for 24 h before the test sample at the indicated concentration was added to the culture media. The cells were incubated for another 48 h before they were lysed with 200 µL of CHAPS lysis buffer. The 10 µg of the crude cell extract was then used as the telomerase source in the telomerase reaction mixture, in which it extends a primer at 30 °C for 30 min. The DNA amplification mixture was added, and the telomerase-extended products were amplified by PCR. The amplified products were separated by nondenaturing acrylamide gel electrophoresis, and results were recorded using a phosphoimaging system (Typhoon; Molecular Dynamics). The oligonucleotides used in this assay are summarized in the Supporting Information (Table S5).

Long-Term Proliferation Assay. We compared three sets of A549 cell cultures for the long-term proliferation assay: the control group and the two experimental groups with the subcytotoxic doses (5 and 10 µg/mL) of ZOE added in the culture media. We subcultured A549 cells (1.5 × 10^5 cells) onto a 75 cm² tissue culture flask, with or without the indicated concentration of ZOE, in RPMI 1640 medium supplemented with 10% fetal bovine serum. We changed the culture media after 3 days, and on day 6, we trypsinized, collected, and counted the cells. Then, the process was repeated up to 60 days. The equation: $n = (\log P_n - \log P_0)/\log 2$, where P_n is the number of cells after n doublings and P_0 is the initial seeding density, was then used to calculate the number of population doublings. The graph between the cumulative number of population doublings and time was then plotted.

Telomere Length Assay. We performed a telomere length analysis using the *TeloTAGGG* Telomere Length Assay kit (Roche Applied Science) according to the manufacturer's instruction and our published protocol.[46] The formula $\sum(OD_i)/\sum(OD_i/L_i)$, where OD_i indicates the signal at the

position i and L_i is the molecular weight marker at the same position, was used to calculate the mean TRF length.

Senescence-Associated β-Galactosidase Activity Assay. We performed a β-galactosidase activity assay according to our published protocol.[46] We first grew the A549 cells (1×10^5 cells) collected from the long-term proliferation study in a six-well plate for 24 h before they were fixed with 2% formaldehyde and 0.2% glutaraldehyde solution. After that, the cells were washed and incubated in the 5-bromo-4-chloro-3-indolyl-β-D-galactopyranoside (X-gal) solution overnight at room temperature. Cells with β-galactosidase activity cleave X-gal and produce a blue stain. The β-galactosidase positive cells were monitored under a phase contrast microscope with a blue stain, usually accompanied by cell morphological changes. In each experiment, the blue-stained cells were counted in the field with more than 400 cells for at least 10 fields. The graph between the percentage of β-galactosidase positive cells and time was then plotted.

Colony-Forming Assays. We performed a colony-forming assay according to our published protocol.[46] We first seeded the A549 cells collected from the long-term proliferation assay in a 10 cm dish at a low density (2×10^3 cells) and allowed the colonies to form for 2 weeks, with the change of fresh growth media every 3 days. Crystal violet was then used to stain the colonies. The number of colonies was obtained using the ImageQuant TL software (Nonlinear Dynamics).

Gas Chromatography/Mass Spectrometry. GC/MS data were collected with a GC7890 instrument from Agilent Technologies, with a DB-5MS column (30 m × 0.25 mm ID × 0.25 μm film thickness). The temperature programming was as follows: 50 °C, 5 min; to 200 °C at 10 °C/min; to 250 °C at 5 °C/min; and 250 °C, 35 min, and the ionizing voltage was 70 eV, with 1 μL split injection (split ratio 25:1). The flow rate of helium gas was 1.5 mL/min. The identification of compounds was obtained using the Agilent Enhanced Chemstation MSD Data Analysis Tool with the W8N08 mass spectrum library (John Wiley & Sons, Inc., USA).

Animals. Wistar rats were fed with the CP082 diet (Perfect Companion Group) and tap water ad libitum under constant conditions of 12 h light/dark cycle and 50−60% humidity at 25 °C. The Animal Ethics Committee of the Faculty of Medicine, Chiang Mai University, approved our experimental protocols.

Acute Toxicity Test. The acute toxicity of ZOE was evaluated according to OECD Guideline 425.[47] The 6 weeks old (190−200 g) female Wistar rats were divided into two groups of five rats. The vehicle control group received 5 mL/kg of 5% Tween 80, whereas the experimental group received a single dose of 5000 mg/kg bw of ZOE by oral gavage. The body weight, behaviors, signs of toxicity, and mortality were observed and recorded every day for 14 days. The gross pathological observation of the tissues and organs was performed after the rats were sacrificed at the end of the study.

Liver Micronucleus Assay. We performed a liver micronucleus assay according to our published protocol.[48] The 4 weeks old (110−120 g) male Wistar rats were divided into four groups of six rats. Group 1 was a negative control group in which the rats were supplemented with 5% Tween 80 for 28 days, whereas group 3 was a positive control group in which the rats were treated in the same way as group 1 but with an injection of 30 mg/kg bw of DEN on day 22 and day 25 to induce micronucleated hepatocytes. Group 2 was the experimental group to determine the clastogenic effects of

ZOE, in which 500 mg/kg bw of ZOE was administered to rats by oral gavage for 28 days. Group 4 was the experimental group to determine the anticlastogenic effects of ZOE, in which 500 mg/kg bw of ZOE was administered to rats by oral gavage for 28 days, and rats were injected with 30 mg/kg bw of DEN on day 22 and day 25. On day 29, partial hepatectomy was performed, and single hepatocytes were isolated by the two-step collagenase perfusion method. The liver cell suspension was stained with the 4′,6-diamidino-2-phenylindole solution, and the incidence of micronucleated hepatocytes was analyzed under a fluorescent microscope on day 33, 4 days after partial hepatectomy. The initial body weight, final body weight, and mitotic index were also recorded.

Statistical Analysis. For assays in cell culture, data were taken from triplicate samples of three independent experiments. Statistical significance between treatments and controls was analyzed using Student's t-test analysis. For assays in rats, data of each variable for each group are reported as means ± SD. The significance of differences between groups was analyzed using one-way analysis of variance with the least significant difference for post hoc tests. Values of $p < 0.05$ (*) were considered to be significant.

■ ASSOCIATED CONTENT

Ⓢ Supporting Information

The Supporting Information is available free of charge on the ACS Publications website at DOI: 10.1021/acsomega.8b02853.

> TLC fingerprinting and HPLC chromatograms of the crude ethyl acetate extract of *Z. officinale* (ZOE) and its fractions; effects of some ZOE fractions on *hTERT* expression and telomerase activity; GC chromatogram and selected GC/MS spectra of ginger extract subfractions (E2.1−E2.4); effects of 6-gingerol, 6-paradol, and 6-shogaol on gene expression and telomerase activity in A549 lung cancer cells; effects of ZOE on body weight, food and water intake and relative organ weights from acute cytotoxicity tests in rats; extraction, purification, and identification of 6-paradol and 6-shogaol; IC_{50} of ZOE, its subfractions, and selected pure compounds; primer sequences and conditions used in semiquantitative RT-PCR; and oligonucleotides used in the modified fluorescent TRAP assay (PDF)

■ AUTHOR INFORMATION

Corresponding Author

*E-mail: wirotetunti@yahoo.com. Phone: +66-53-945323, +66-53-934-438. Fax: +66-53-894031 (W.T.).

ORCID Ⓘ

T. Randall Lee: 0000-0001-9584-8861
Wirote Tuntiwechapikul: 0000-0003-1365-476X

Notes

The authors declare no competing financial interest.

■ REFERENCES

(1) Meena, J.; Rudolph, K. L.; Günes, C. Telomere dysfunction, chromosomal instability and cancer. *Recent Results Cancer Res.* **2015**, *200*, 61−79.

(2) Tomita, K.; Cooper, J. P. The telomere bouquet controls the meiotic spindle. *Cell* **2007**, *130*, 113−126.

(3) Martínez, P.; Blasco, M. A. Role of shelterin in cancer and aging. *Aging Cell* **2010**, *9*, 653−666.

(4) Shay, J. W.; Wright, W. E. Hayflick, his limit and cellular ageing. *Nat. Rev. Mol. Cell Biol.* **2000**, *1*, 72−76.

(5) Victorelli, S.; Passos, J. F. Telomeres and cell senescence - Size matters not. *EBioMedicine* **2017**, *21*, 14−20.

(6) Benarroch-Popivker, D.; Pisano, S.; Mendez-Bermudez, A.; Lototska, L.; Kaur, P.; Bauwens, S.; Djerbi, N.; Latrick, C. M.; Fraisier, V.; Pei, B.; Gay, A.; Jaune, E.; Foucher, K.; Cherfils-Vicini, J.; Aeby, E.; Miron, S.; Londoño-Vallejo, A.; Ye, J.; Le Du, M.-H.; Wang, H.; Gilson, E.; Giraud-Panis, M.-J. TRF2-mediated control of telomere DNA topology as a mechanism for chromosome-end protection. *Mol. Cell* **2016**, *61*, 274−286.

(7) Ohtani, N.; Mann, D. J.; Hara, E. Cellular senescence: Its role in tumor suppression and aging. *Cancer Sci.* **2009**, *100*, 792−797.

(8) Kim, N.; Piatyszek, M.; Prowse, K.; Harley, C.; West, M.; Ho, P.; Coviello, G.; Wright, W.; Weinrich, S.; Shay, J. Specific association of human telomerase activity with immortal cells and cancer. *Science* **1994**, *266*, 2011−2015.

(9) Kumar, M.; Lechel, A.; Güneş, Ç. Telomerase: The Devil Inside. *Genes* **2016**, *7*, No. E43.

(10) Cohen, S. B.; Graham, M. E.; Lovrecz, G. O.; Bache, N.; Robinson, P. J.; Reddel, R. R. Protein composition of catalytically active human telomerase from immortal cells. *Science* **2007**, *315*, 1850−1853.

(11) Ramlee, M. K.; Wang, J.; Toh, W. X.; Li, S. Transcription regulation of the human telomerase reverse transcriptase (hTERT) gene. *Genes* **2016**, *7*, No. E50.

(12) Scalbert, A.; Andres-Lacueva, C.; Arita, M.; Kroon, P.; Manach, C.; Urpi-Sarda, M.; Wishart, D. Databases on food phytochemicals and their health-promoting effects. *J. Agric. Food Chem.* **2011**, *59*, 4331−4348.

(13) Gullett, N. P.; Ruhul Amin, A. R. M.; Bayraktar, S.; Pezzuto, J. M.; Shin, D. M.; Khuri, F. R.; Aggarwal, B. B.; Surh, Y.-J.; Kucuk, O. Cancer prevention with natural compounds. *Semin. Oncol.* **2010**, *37*, 258−281.

(14) Gomez, D. L. M.; Armando, R. G.; Cerrudo, C. S.; Ghiringhelli, P. D.; Gomez, D. E. Telomerase as a Cancer Target. Development of New Molecules. *Curr. Top. Med. Chem.* **2016**, *16*, 2432−2440.

(15) Shay, J. W.; Keith, W. N. Targeting telomerase for cancer therapeutics. *Br. J. Cancer* **2008**, *98*, 677−683.

(16) Alibakhshi, A.; Ranjbari, J.; Pilehvar-Soltanahmadi, Y.; Nasiri, M.; Mollazade, M.; Zarghami, N. An update on phytochemicals in molecular target therapy of cancer: Potential inhibitory effect on telomerase activity. *Curr. Med. Chem.* **2016**, *23*, 2380−2393.

(17) Kundu, J. K.; Na, H.-K.; Surh, Y.-J. Ginger-derived phenolic substances with cancer preventive and therapeutic potential. *Forum. Nutr.* **2009**, *61*, 182−192.

(18) Nigam, N.; George, J.; Shukla, Y. Ginger (6-gingerol). In *Molecular Targets and Therapeutic Uses of Spices: Modern Uses for Ancient Medicine*; Aggarwal, B. B., Kunnumakkara, A. B., Eds.; World Scientific Publishing Co. Inc.: Hackensack, NJ, 2009; pp 225−256.

(19) Kaur, I. P.; Deol, P. K.; Kondepudi, K. K.; Bishnoi, M. Anticancer potential of ginger: Mechanistic and pharmaceutical aspects. *Curr. Pharm. Des.* **2016**, *22*, 4160−4172.

(20) Wang, C.-Z.; Qi, L.-W.; Yuan, C.-S. Cancer chemoprevention effects of ginger and its active constituents: Potential for new drug discovery. *Am. J. Chin. Med.* **2015**, *43*, 1351−1363.

(21) Zhang, F.; Thakur, K.; Hu, F.; Zhang, J.-G.; Wei, Z.-J. 10-Gingerol, a Phytochemical Derivative from "Tongling White Ginger", Inhibits Cervical Cancer: Insights into the Molecular Mechanism and Inhibitory Targets. *J. Agric. Food Chem.* **2017**, *65*, 2089−2099.

(22) Hsu, Y.-L.; Hung, J.-Y.; Tsai, Y.-M.; Tsai, E.-M.; Huang, M.-S.; Hou, M.-F.; Kuo, P.-L. 6-shogaol, an active constituent of dietary ginger, impairs cancer development and lung metastasis by inhibiting the secretion of CC-chemokine ligand 2 (CCL2) in tumor-associated dendritic cells. *J. Agric. Food Chem.* **2015**, *63*, 1730−1738.

(23) Tuntiwechapikul, W.; Taka, T.; Songsomboon, C.; Kaewtunjai, N.; Imsumran, A.; Makonkawkeyoon, L.; Pompimon, W.; Lee, T. R. Ginger extract inhibits human telomerase reverse transcriptase and c-Myc expression in A549 lung cancer cells. *J. Med. Food* **2010**, *13*, 1347−1354.

(24) Hemann, M. T.; Strong, M. A.; Hao, L.-Y.; Greider, C. W. The shortest telomere, not average telomere length, is critical for cell viability and chromosome stability. *Cell* **2001**, *107*, 67−77.

(25) Tao, Y.; Li, W.; Liang, W.; Van Breemen, R. B. Identification and Quantification of Gingerols and Related Compounds in Ginger Dietary Supplements Using High-Performance Liquid Chromatography−Tandem Mass Spectrometry. *J. Agric. Food Chem.* **2009**, *57*, 10014−10021.

(26) Jolad, S. D.; Lantz, R. C.; Solyom, A. M.; Chen, G. J.; Bates, R. B.; Timmermann, B. N. Fresh organically grown ginger (*Zingiber officinale*): Composition and effects on LPS-induced PGE2 production. *Phytochemistry* **2004**, *65*, 1937−1954.

(27) Moghaddasi, M. S.; Kashani, H. H. Ginger (*Zingiber officinale*): a review. *J. Med. Plants Res.* **2012**, *6*, 4255−4258.

(28) Mansour, M. A.; Bekheet, S. A.; Al-Rejaie, S. S.; Al-Shabanah, O. A.; Al-Howiriny, T. A.; Al-Rikabi, A. C.; Abdo, A. A. Ginger ingredients inhibit the development of diethylnitrosoamine induced premalignant phenotype in rat chemical hepatocarcinogenesis model. *Biofactors* **2010**, *36*, 483−490.

(29) Habib, S. H.; Makpol, S.; Abdul Hamid, N. A.; Das, S.; Ngah, W. Z.; Yusof, Y. A. Ginger extract (*Zingiber officinale*) has anti-cancer and anti-inflammatory effects on ethionine-induced hepatoma rats. *Clinics* **2008**, *63*, 807−813.

(30) Alibakhshi, A.; Ranjbari, J.; Pilehvar-Soltanahmadi, Y.; Nasiri, M.; Mollazade, M.; Zarghami, N. An update on phytochemicals in molecular target therapy of cancer: Potential inhibitory effect on telomerase activity. *Curr. Med. Chem.* **2016**, *23*, 2380−2393.

(31) Naasani, I.; Seimiya, H.; Tsuruo, T. Telomerase inhibition, telomere shortening, and senescence of cancer cells by tea catechins. *Biochem. Biophys. Res. Commun.* **1998**, *249*, 391−396.

(32) Khaw, A. K.; Hande, M. P.; Kalthur, G.; Hande, M. P. Curcumin inhibits telomerase and induces telomere shortening and apoptosis in brain tumour cells. *J. Cell. Biochem.* **2013**, *114*, 1257−1270.

(33) Gurung, R. L.; Lim, S. N.; Khaw, A. K.; Soon, J. F. F.; Shenoy, K.; Mohamed Ali, S.; Jayapal, M.; Sethu, S.; Baskar, R.; Hande, M. P. Thymoquinone induces telomere shortening, DNA damage and apoptosis in human glioblastoma cells. *PLoS One* **2010**, *5*, No. e12124.

(34) Merghoub, N.; El Btaouri, H.; Benbacer, L.; Gmouh, S.; Trentesaux, C.; Brassart, B.; Terryn, C.; Attaleb, M.; Madoulet, C.; Benjouad, A.; Amzazi, S.; El Mzibri, M.; Morjani, H. Inula ViscosaExtracts Induces Telomere Shortening and Apoptosis in Cancer Cells and Overcome Drug Resistance. *Nutr. Cancer* **2016**, *68*, 131−143.

(35) Merghoub, N.; El Btaouri, H.; Benbacer, L.; Gmouh, S.; Trentesaux, C.; Brassart, B.; Attaleb, M.; Madoulet, C.; Wenner, T.; Amzazi, S.; Morjani, H.; El Mzibri, M. Tomentosin Induces Telomere Shortening and Caspase-Dependant Apoptosis in Cervical Cancer Cells. *J. Cell. Biochem.* **2016**, *118*, 1689−1698.

(36) Surh, Y.-J. Cancer chemoprevention with dietary phytochemicals. *Nature Rev. Cancer* **2013**, *3*, 768−780.

(37) Kotecha, R.; Takami, A.; Espinoza, J. L. Dietary phytochemicals and cancer chemoprevention: a review of the clinical evidence. *Oncotarget* **2016**, *7*, 52517−52529.

(38) Baena Ruiz, R.; Salinas Hernández, P. Cancer chemoprevention by dietary phytochemicals: Epidemiological evidence. *Maturitas* **2016**, *94*, 13−19.

(39) Nazim, U.; Jeong, J.-K.; Seol, J.-W.; Hur, J.; Eo, S.-K.; Lee, J.-H.; Park, S.-Y. Inhibition of the autophagy flux by gingerol enhances TRAIL-induced tumor cell death. *Oncol. Rep.* **2015**, *33*, 2331−2336.

(40) Hung, J.-Y.; Hsu, Y.-L.; Li, C.-T.; Ko, Y.-C.; Ni, W.-C.; Huang, M.-S.; Kuo, P.-L. 6-Shogaol, an active constituent of dietary ginger, induces autophagy by inhibiting the AKT/mTOR pathway in human non-small cell lung cancer A549 cells. *J. Agric. Food Chem.* **2009**, *57*, 9809−9816.

(41) Eren, D.; Betul, Y. M. Revealing the effect of 6-gingerol, 6-shogaol and curcumin on mPGES-1, GSK-3β and β-catenin pathway in A549 cell line. *Chem. Biol. Interact.* **2016**, *258*, 257−265.

(42) Warin, R. F.; Chen, H.; Soroka, D. N.; Zhu, Y.; Sang, S. Induction of lung cancer cell apoptosis through a p53 pathway by [6]-shogaol and its cysteine-conjugated metabolite M2. *J. Agric. Food Chem.* **2014**, *62*, 1352−1362.

(43) Kang, C. G.; Lee, H.-J.; Kim, S.-H.; Lee, E.-O. Zerumbone suppresses osteopontin-induced cell invasion through inhibiting the FAK/AKT/ROCK pathway in human non-small cell lung cancer A549 cells. *J. Nat. Prod.* **2015**, *79*, 156−160.

(44) Vichai, V.; Kirtikara, K. Sulforhodamine B colorimetric assay for cytotoxicity screening. *Nat. Protoc.* **2006**, *1*, 1112−1116.

(45) Szatmari, I.; Aradi, J. Telomeric repeat amplification, without shortening or lengthening of the telomerase products: a method to analyze the processivity of telomerase enzyme. *Nucleic Acids Res.* **2001**, *29*, No. E3.

(46) Taka, T.; Huang, L.; Wongnoppavich, A.; Tam-Chang, S.-W.; Lee, T. R.; Tuntiwechapikul, W. Telomere shortening and cell senescence induced by perylene derivatives in A549 human lung cancer cells. *Bioorg. Med. Chem.* **2013**, *21*, 883−890.

(47) *OECD Guidelines for the Testing of Chemicals. No. 425: Acute Oral Toxicity-Fixed Dose Procedure*, 2008.

(48) Punvittayagul, C.; Sankam, P.; Taya, S.; Wongpoomchai, R. Anticlastogenicity and anticarcinogenicity of purple rice extract in rats. *Nutr. Cancer* **2016**, *68*, 646−653.

SUPPORTING INFORMATION

Ginger Extract Promotes Telomere Shortening and Cellular Senescence in A549 Lung Cancer Cells

Navakoon Kaewtunjai,[a] Rawiwan Wongpoomchai,[a] Arisa Imsumran,[a] Wilart Pompimon,[b] Anan Athipornchai,[c] Apichart Suksamrarn,[d] T. Randall Lee,[e] and Wirote Tuntiwechapikul[a,*]

[a]Department of Biochemistry, Faculty of Medicine, Chiang Mai University, Chiang Mai 50200, Thailand.
[b]Laboratory of Natural Products, Department of Chemistry, Faculty of Science and Center of Innovation in Chemistry, Lampang Rajabhat University, Lampang 52100, Thailand.
[c]Department of Chemistry, Center of Excellence for Innovation in Chemistry, Burapha University, Chon Buri 20131, Thailand.
[d]Department of Chemistry and Center of Excellence for Innovation in Chemistry, Faculty of Science, Ramkhamhaeng University, Bangkok 10240, Thailand.
[e]Department of Chemistry and the Texas Center for Superconductivity, University of Houston, Houston, TX 77204-5003, USA.

* Corresponding author.
110 Intavaroros Rd., Muang, Chiang Mai 50200, Thailand.
Tel: +66-53-945323; Fax: +66-53-894031
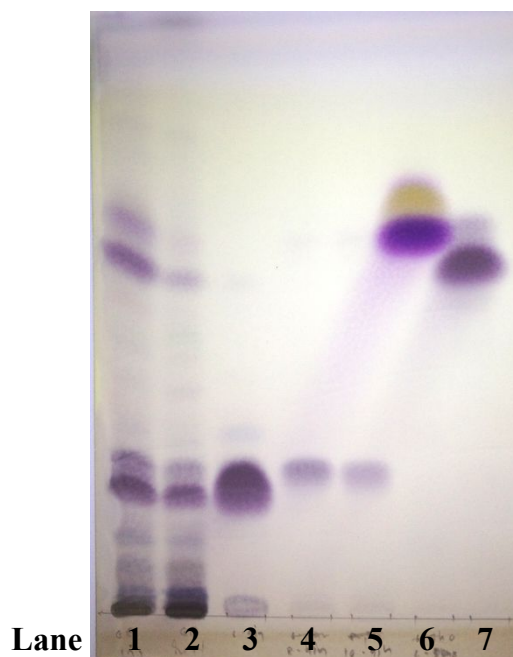E-mail address: wirotetunti@yahoo.com

Figure S1: Chemical fingerprinting of ZOE by TLC. The ethyl acetate fraction of *Z. officinale* extract (ZOE Lot #1 and #2), along with standard chemicals, were separated on a silica gel GF254 TLC plate using hexane and ethyl acetate (3:1) as the mobile phase. The TLC plate was then dipped in *p*-anisaldehyde/sulfuric acid reagent before color developing by heating at 100 °C. Lane 1 and 2 = ethyl acetate fraction of *Z. officinale* extract (Lot #1 and #2); Lane 3 = 6-gingerol; Lane 4 = 8-gingerol; Lane 5 = 10-gingerol; Lane 6 = 6-paradol; Lane 7 = 6-shogaol.
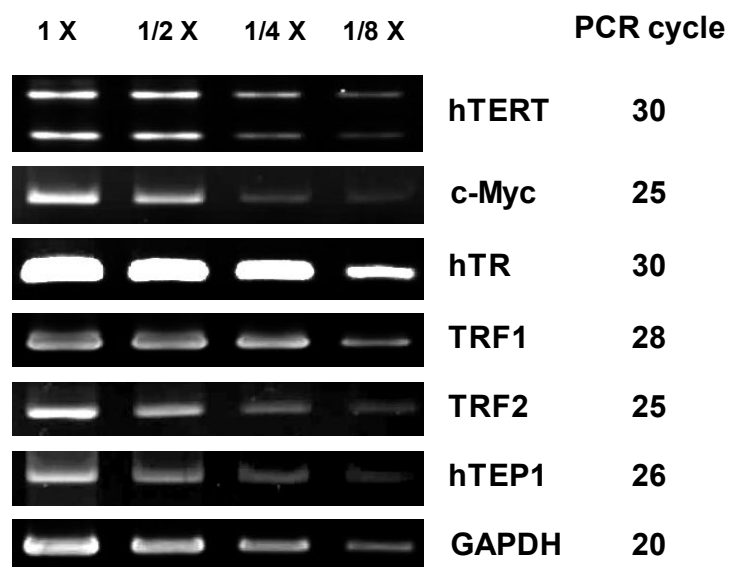
Figure S2: The chosen PCR cycle for semiquantitative RT-PCR analysis. The PCR cycle for each gene (right column) was carefully chosen so that it represents the amount of the cDNA in the sample. The cDNA from A549 cells was diluted two-fold serially and was amplified using gene-specific primers.
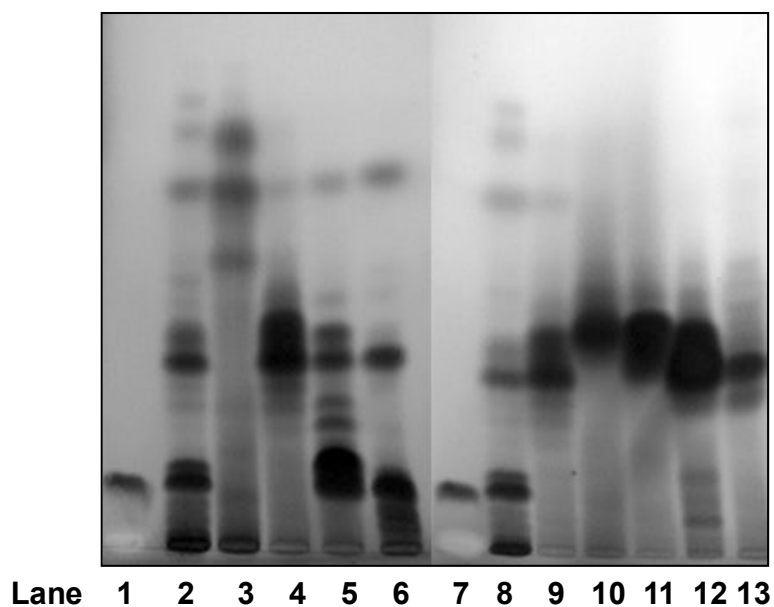
Figure S3: TLC fingerprinting of the *Z. officinale* extracts (E1-E4 fractions and E2.1-E2.4 subfractions). TLC fingerprinting of the *Z. officinale* extracts was performed using silica gel GF254 (Fluka) as the stationary phase and the solvent mixture of hexane and ethyl acetate (3:1) as the mobile phase. The TLC plate was then dipped in *p*-anisaldehyde/sulfuric acid reagent before color developing by heating at 100 °C. Lane 1, 7 = standard 6-gingerol; Lane 2, 8 = crude ethyl acetate extract; Lane 3-6 = E1-E4 fractions; Lane 9 = E2 fraction; Lane 10-13 = E2.1-E2.4 subfractions.
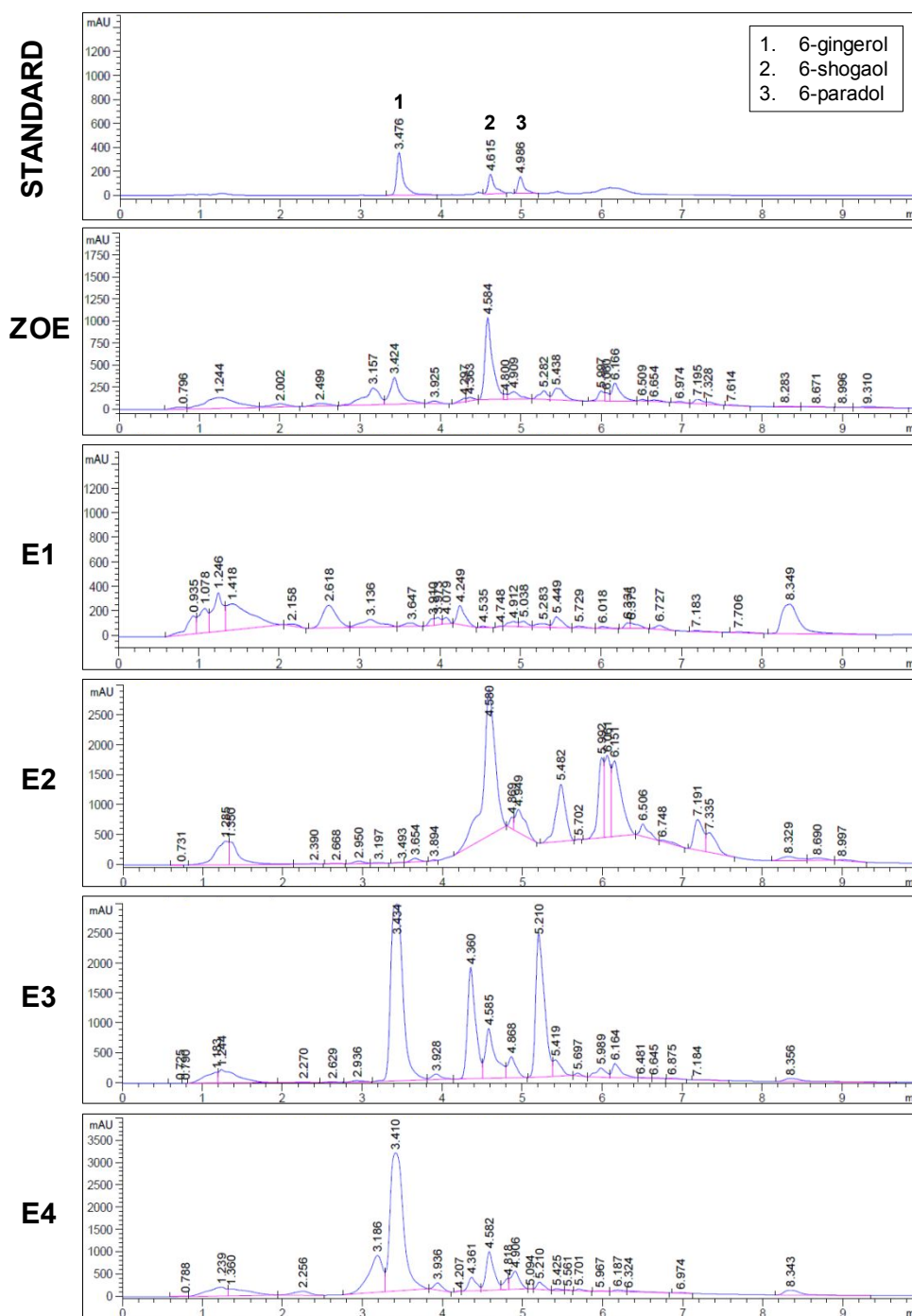
Figure S4: The HPLC chromatograms of the crude ethyl acetate extract of *Z. officinale* (ZOE) and its fractions (E1-E4). A 50 µL aliquot of each sample (10 mg/ml) was separated by HPLC (Agilent 1200 infinity series, Agilent, USA) using a C18 reverse phase column (4.6 mm x 150 mm, ZORBAX Eclipse Plus) as the stationary phase and a mixture of acetonitrile (A) and water (B) as the mobile phase at a flow rate of 2.0 mL/min. Within the total run time of 10 minutes, the solvent mixture profile of the mobile phase was as follows: 0-0.5 min, 35A:65B; 0.5-5 min, gradient mixture from 35A:65B to 95A:5B; and 5-10 min, 95A:5B. The compounds were detected using a UV-visible detector (Spec Monitor® 3200) at 280 nm. The mixture of standard 6-gingerol (0.4 mg/ml), 6-shogaol (0.2 mg/ml), and 6-paradol (0.2 mg/ml) was run separately using the same conditions.

Figure S5: Effects of ZOE fractions on *hTERT* expression by semiquantitative RT-PCR: (A) E1-E4 fractions and (B) E2.1-E2.4 subfractions. A549 cells (5.0 x 10^5 cells) were treated with various concentrations of each fraction for 24 h before the mRNAs were extracted from the cell lysate, converted to cDNAs, and amplified by PCR using gene-specific primers. The 457-bp RT-PCR products represent the full-length hTERT mRNA, and the 275-bp RT-PCR products represent the β-hTERT mRNA. The 450-bp RT-PCR products represent the GAPDH mRNA as the internal control gene.

Figure S6: Effects of ZOE subfractions (E2.1-E2.4) on telomerase activity by modified TRAP assay. A549 cells (5.0 x 10^5 cells) were incubated with the indicated concentrations of each subfraction for 48 h before the crude protein extract was used as the source of telomerase in a modified TRAP assay. IC and RC represent internal control and recovery control, respectively.

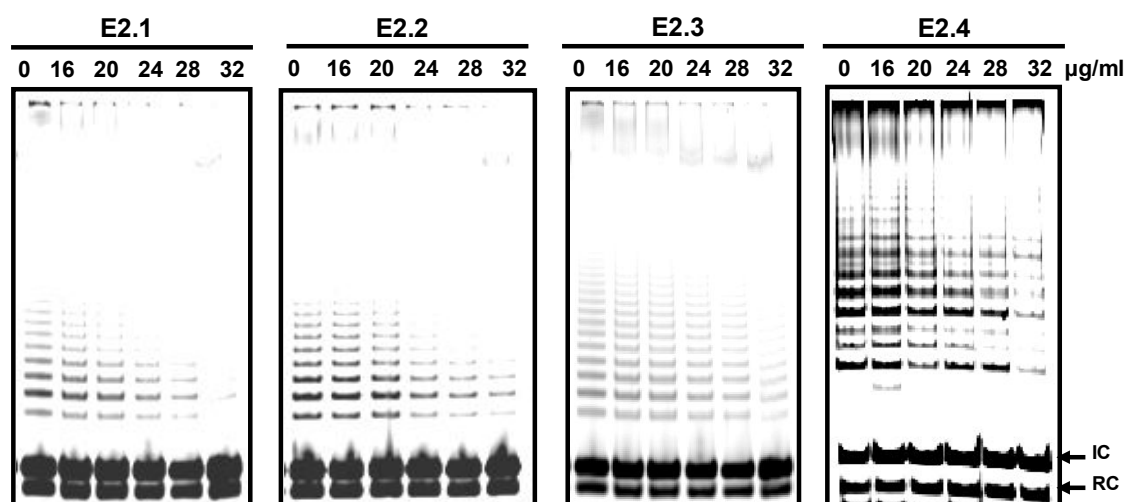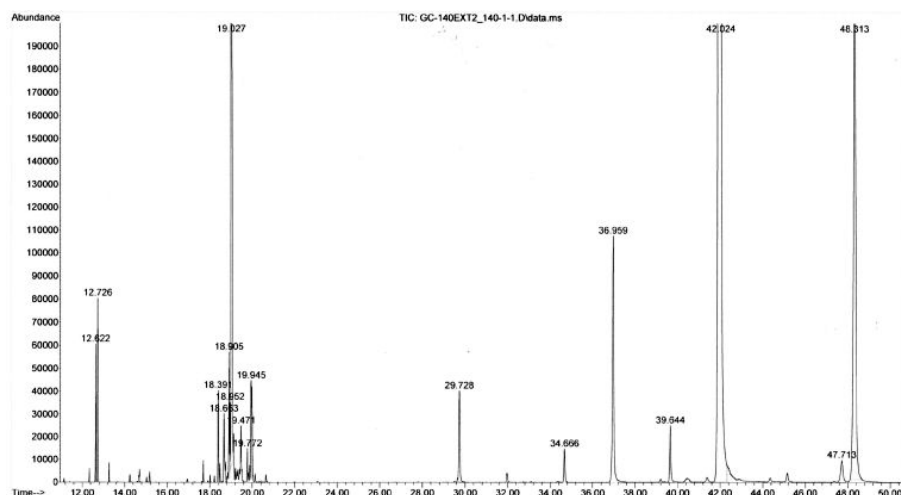**Figure S7.1: GC chromatogram of E2.1 subfraction.** GC data were recorded with a GC 7890A from Agilent Technologies and MSD 5975 (EI). The gas chromatograph was fitted with a HP5-MS column (30 m × 0.25 mm ID × 0.25 μm film thickness) and obtained using the following temperature programming (50 °C, 5 min; to 180 °C at 10 °C/min; to 250 °C at 3 °C/min; and 250 °C, 10 min), ionizing voltage 70 eV, and 1 μL split injection (split ratio 25:1). Helium was used as the carrier gas at a flow rate of 1.5 mL/min.

```
peak   R.T.  first  max  last   PK    peak      corr.     corr.    % of
 #     min   scan  scan scan    TY   height     area     % max.   total
---   -----  ----- ---- ----   ---   -------   -------   ------   -------
 1    12.622  1645 1651 1658   rBB    60610      77913    0.57%    0.430%
 2    12.726  1662 1669 1679   rBB    80543     124995    0.92%    0.690%
 3    18.391  2643 2650 2659   rBV    40587      61016    0.45%    0.337%
 4    18.663  2691 2697 2707   rBV4   30315      65470    0.48%    0.361%
 5    18.905  2734 2739 2744   rBV    55393      94425    0.69%    0.521%

 6    18.952  2744 2747 2751   rVV2   30042      44328    0.32%    0.245%
 7    19.027  2751 2760 2772   rVV5  421725    1286824    9.42%    7.105%
 8    19.471  2833 2837 2843   rVB2   20554      35974    0.26%    0.199%
 9    19.772  2877 2889 2893   rBV3   14959      28399    0.21%    0.157%
10    19.945  2912 2919 2922   rBV3   43551      92403    0.68%    0.510%

11    29.728  4602 4613 4639   rVB    40114     134049    0.98%    0.740%
12    34.666  5454 5468 5485   rBV2   14851      54743    0.40%    0.302%
13    36.959  5833 5865 5905   rBV2  107608     524641    3.84%    2.897%
14    39.644  6314 6330 6361   rBV3   25032     110005    0.81%    0.607%
15    42.024  6689 6742 6793   rBV   2063746  13656660  100.00%   75.406%

16    47.713  7694 7727 7761   rBV2    9729      79745    0.58%    0.440%
17    48.313  7796 7831 7881   rBV2  220021    1639317   12.00%    9.052%


             Sum of corrected areas:     18110907

GC-140EXT2.M Mon May 17 16:07:33 2010
```
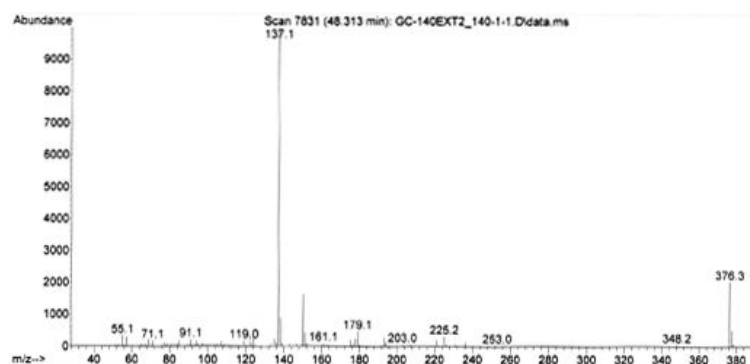
Figure S7.2: GC chromatogram data from E2.1 subfraction.
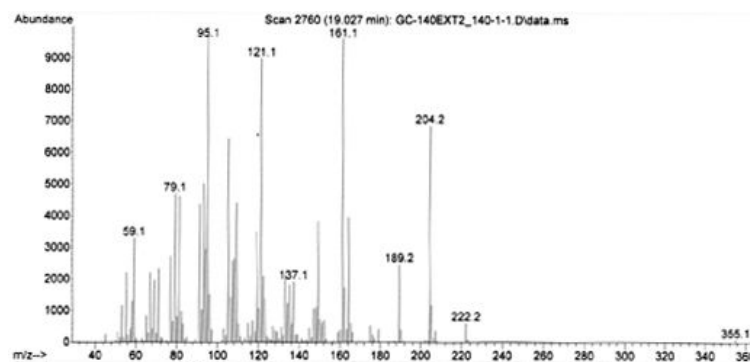
A.
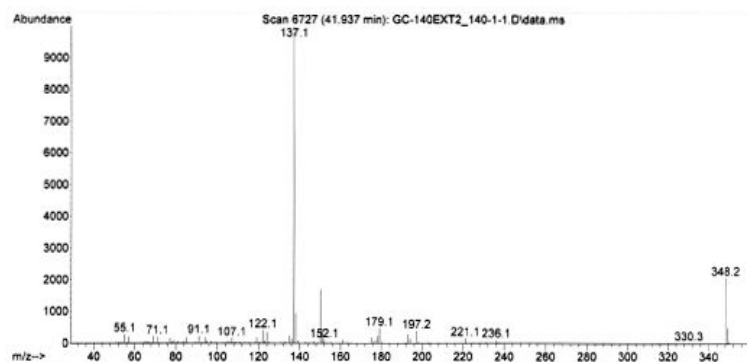
B.

C.

Figure S7.3: Selected GC/MS spectra from E2.1 subfraction. The spectra are from the three most abundant peaks: A) Peak #15 (75%), B) Peak #17 (9%), and C) Peak #7 (7%). The compounds were identified as 11-paradol, 13-paradol, and β-bisabolene, respectively.
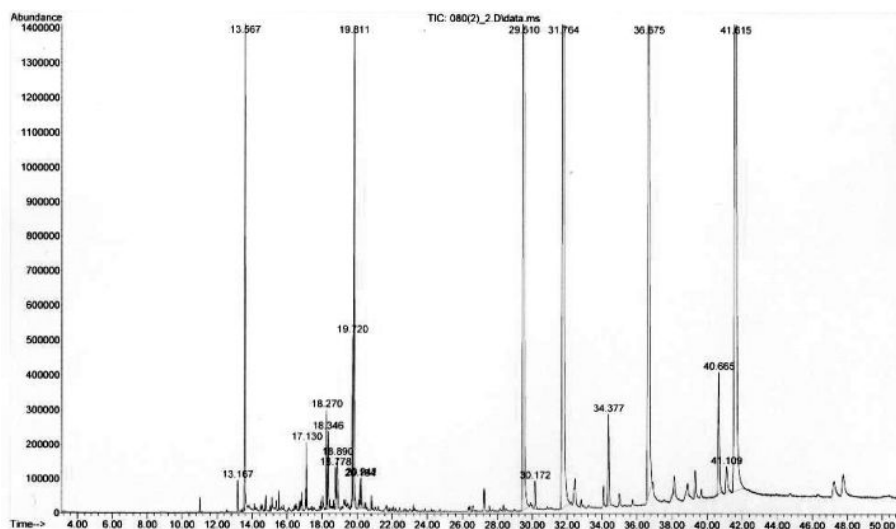
Figure S8.1: GC/MS chromatogram of E2.2 subfraction. GC data were recorded with a GC 7890A from Agilent Technologies and MSD 5975 (EI). The gas chromatograph was fitted with a HP5-MS column (30 m × 0.25 mm ID × 0.25 μm film thickness) and was obtained using the following temperature programming (50 °C, 5 min; to 180 °C at 10 °C/min; to 250 °C at 3 °C/min; and 250 °C, 10 min), ionizing voltage 70 eV, and 1 μL split injection (split ratio 25:1). Helium was used as the carrier gas at a flow rate of 1.5 mL/min.

peak #	R.T. min	first scan	max scan	last scan	PK TY	peak height	corr. area	corr. % max.	% of total
1	13.167	1706	1714	1725	BB	91844	1471508	0.64%	0.167%
2	13.567	1766	1782	1810	BB	1675895	25247765	10.97%	2.869%
3	17.130	2383	2388	2396	VV	187873	2849011	1.24%	0.324%
4	18.270	2561	2581	2588	PV	283285	4895902	2.13%	0.556%
5	18.346	2588	2594	2610	VV 3	223400	4595450	2.00%	0.522%
6	18.778	2657	2668	2674	PV 4	120740	2678803	1.16%	0.304%
7	18.890	2674	2687	2702	VV 9	150218	5905791	2.57%	0.671%
8	19.720	2815	2828	2835	PV	490715	9532364	4.14%	1.083%
9	19.811	2835	2843	2853	VV	1349816	24980402	10.85%	2.838%
10	20.164	2898	2903	2911	VV 2	85413	1991588	0.87%	0.226%
11	20.242	2911	2917	2933	VB 2	86910	2019875	0.88%	0.229%
12	29.510	4470	4492	4549	BB	5031797	192394913	83.60%	21.860%
13	30.172	4586	4605	4629	BB 2	82435	3217681	1.40%	0.366%
14	31.764	4847	4875	4944	BV 3	2825624	197241771	85.70%	22.410%
15	34.377	5289	5320	5352	VB	269431	11217088	4.87%	1.274%
16	36.675	5681	5710	5744	BV	2254444	139532635	60.63%	15.854%
17	40.665	6346	6389	6416	BV 2	349818	15481843	6.73%	1.759%
18	41.109	6447	6464	6491	BV 2	76182	4732959	2.06%	0.538%
19	41.615	6513	6550	6634	BV 2	3370277	230148009	100.00%	26.149%

Sum of corrected areas: 880135358

Figure S8.2: GC chromatogram data from E2.2 subfraction.

Figure S8.3: Selected GC/MS spectra from E2.2 subfraction. The spectra are from the four most abundant peaks: A) Peak #19 (26%), B) Peak #14 (22%), C) Peak #12 (22%), and D) Peak #7 (7%). The compounds were identified as 11-paradol, 7-paradol, 6-paradol, and 9-paradol, respectively.

Figure S9.1: GC chromatogram of E2.3 subfraction. GC data were recorded with a GC 7890A from Agilent Technologies and MSD 5975 (EI). The gas chromatograph was fitted with a HP5-MS column (30 m × 0.25 mm ID × 0.25 μm film thickness) and was obtained using the following temperature programming (50 °C, 5 min; to 180 °C at 10 °C/min; to 250 °C at 3 °C/min; and 250 °C, 10 min), ionizing voltage 70 eV, and 1 μL split injection (split ratio 25:1). Helium was used as the carrier gas at a flow rate of 1.5 mL/min.

peak #	R.T. min	first scan	max scan	last scan	PK TY	peak height	corr. area	corr. % max.	% of total
1	13.667	1826	1832	1840	rBB	12099	14938	0.26%	0.108%
2	14.574	1983	1989	2001	rBV	6193	16777	0.29%	0.121%
3	18.166	2605	2611	2620	rBB	44738	62682	1.08%	0.452%
4	18.443	2654	2659	2665	rBB	23628	31504	0.54%	0.227%
5	29.734	4592	4614	4651	rBV	246093	773445	13.34%	5.580%
6	30.450	4726	4738	4751	rBB2	4568	14913	0.26%	0.108%
7	31.114	4842	4853	4877	rBB2	5282	18576	0.32%	0.134%
8	32.061	4979	5017	5078	rBV	1090380	5799982	100.00%	41.842%
9	36.052	5690	5708	5739	rBV	159505	560858	9.67%	4.046%
10	36.947	5830	5863	5905	rBV2	91749	528546	9.11%	3.813%
11	39.026	6207	6223	6238	rBV	25301	98033	1.69%	0.707%
12	39.200	6240	6253	6273	rVV	33974	137299	2.37%	0.991%
13	39.379	6277	6284	6310	rVB3	2890	12273	0.21%	0.089%
14	41.019	6543	6568	6619	rBV	1048066	4546273	78.38%	32.798%
15	41.891	6694	6719	6772	rBV	218509	1185027	20.43%	8.549%
16	46.788	7547	7567	7592	rBV4	5384	32223	0.56%	0.232%
17	48.250	7799	7820	7822	rBV2	6842	28205	0.49%	0.203%

Sum of corrected areas: 13861554

Figure S9.2: GC chromatogram data from E2.3 subfraction.

S-13

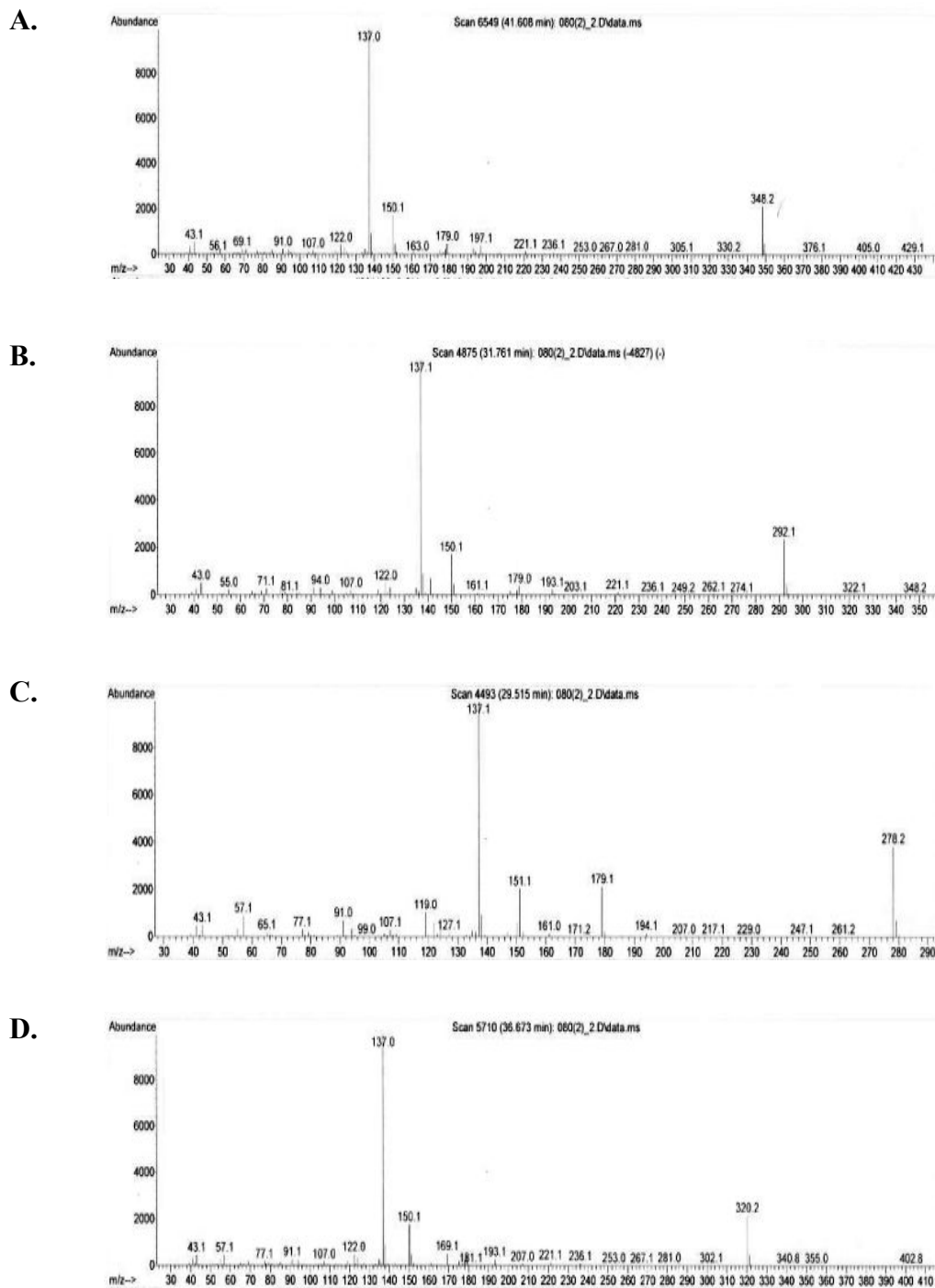**A.**

B.
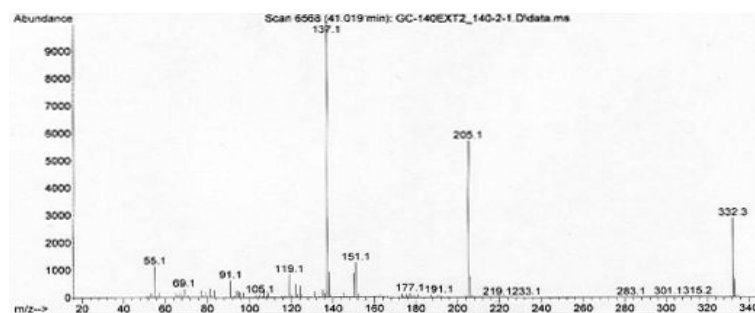
C.

D.

Figure S9.3: Selected GC/MS spectra from E2.3 subfraction. The spectra are from the four most abundant peaks: A) Peak #8 (42%), B) Peak #14 (33%), C) Peak #14 (9%), and D) Peak #5 (6%). The compounds were identified as 7-paradol, 10-shogaol, 11-paradol, and 6-paradol, respectively.
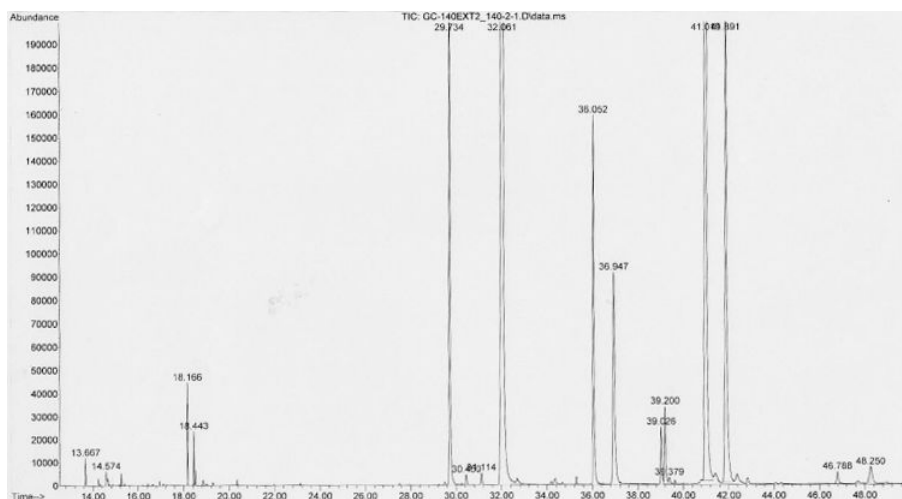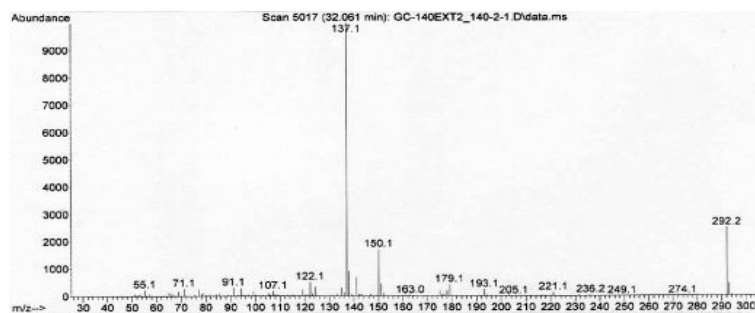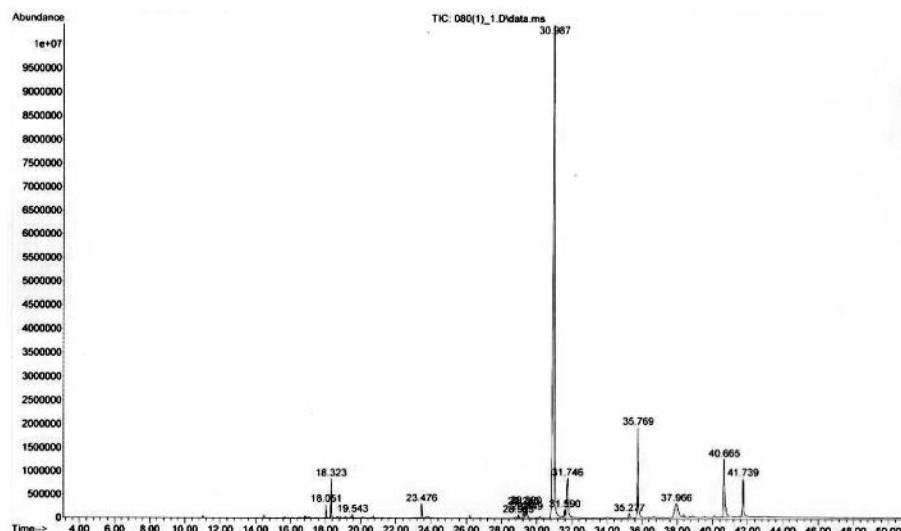
Figure S10.1: GC chromatogram of E2.4 subfraction. GC data were recorded with a GC 7890A from Agilent Technologies and MSD 5975 (EI). The gas chromatograph was fitted with a HP5-MS column (30 m × 0.25 mm ID × 0.25 μm film thickness) and was obtained using the following temperature programming (50 °C, 5 min; to 180 °C at 10 °C/min; to 250 °C at 3 °C/min; and 250 °C, 10 min), ionizing voltage 70 eV, and 1 μL split injection (split ratio 25:1). Helium was used as the carrier gas at a flow rate of 1.5 mL/min.

peak #	R.T. min	first scan	max scan	last scan	PK TY	peak height	corr. area	corr. % max.	% of total
1	18.051	2538	2544	2568	BB	289899	5047687	0.74%	0.499%
2	18.323	2583	2590	2599	BV	798587	12171687	1.77%	1.202%
3	19.543	2787	2798	2807	VV 2	77903	1598943	0.23%	0.158%
4	23.476	3455	3466	3493	BB 2	303623	8520575	1.24%	0.842%
5	28.953	4385	4398	4412	VB 6	73554	2752700	0.40%	0.272%
6	29.240	4428	4446	4460	BV	239367	9575232	1.40%	0.946%
7	29.390	4460	4472	4481	VV 3	258165	10431958	1.52%	1.030%
8	29.449	4481	4482	4506	VB 2	129938	3603593	0.53%	0.356%
9	30.987	4700	4743	4812	BV 2	10427091	686384915	100.00%	67.792%
10	31.590	4832	4846	4855	VV 2	171700	6518286	0.95%	0.644%
11	31.746	4855	4872	4924	VB 2	845012	52893015	7.71%	5.224%
12	35.277	5457	5473	5502	BB 5	96631	4915157	0.72%	0.485%
13	35.769	5531	5556	5611	BV	1923597	78944616	11.50%	7.797%
14	37.966	5869	5930	5935	BBA5	301109	29472886	4.29%	2.911%
15	40.665	6366	6389	6459	BV 2	1231251	62524742	9.11%	6.175%
16	41.739	6513	6571	6618	BV	820395	37132481	5.41%	3.667%

Sum of corrected areas: 1012488476

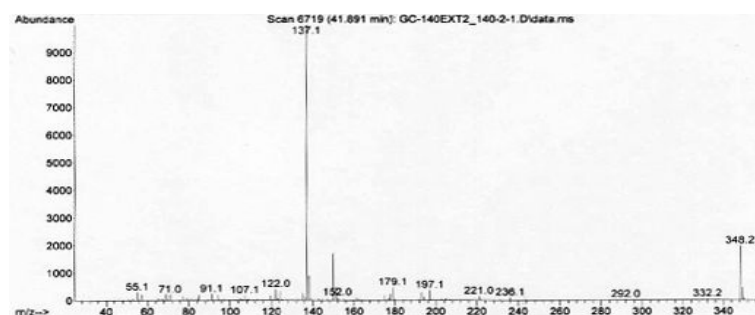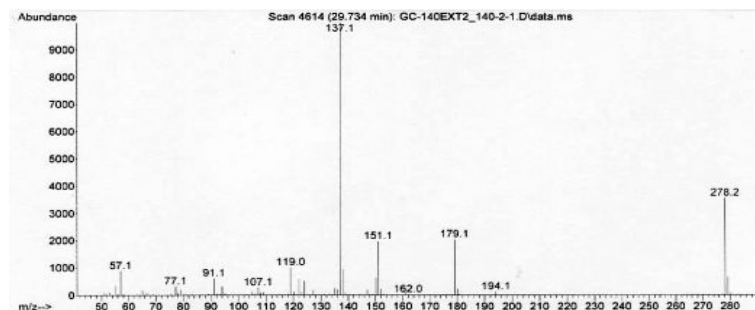**Figure S10.2: GC chromatogram data from E2.4 subfraction.**

S-15
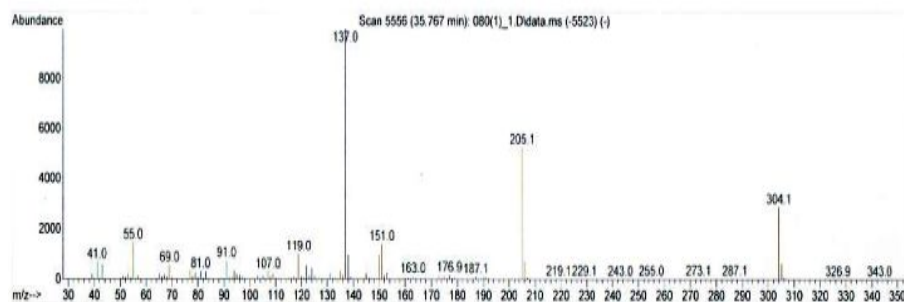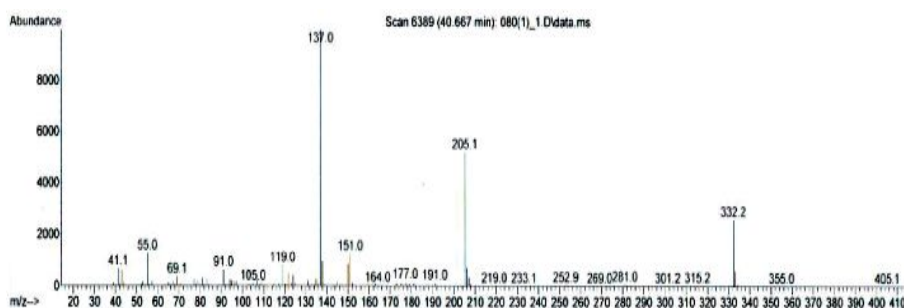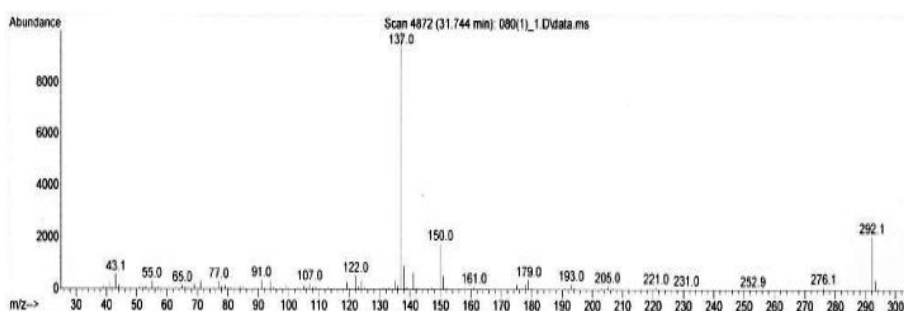
Figure S10.3: Selected GC/MS spectra from E2.4 subfraction. The spectra are from the four most abundant peaks: A) Peak #9 (68%), B) Peak #13 (8%), C) Peak #15 (6%), and D) Peak #11 (5%). The compounds were identified as 6-shogaol, 10-shogaol, 8-shogaol and 7-paradol, respectively.
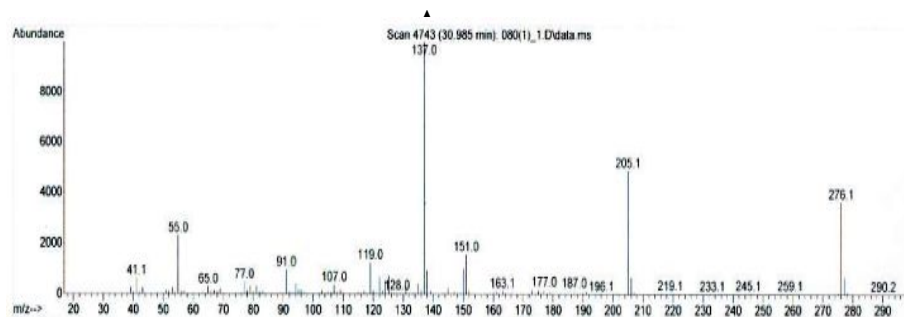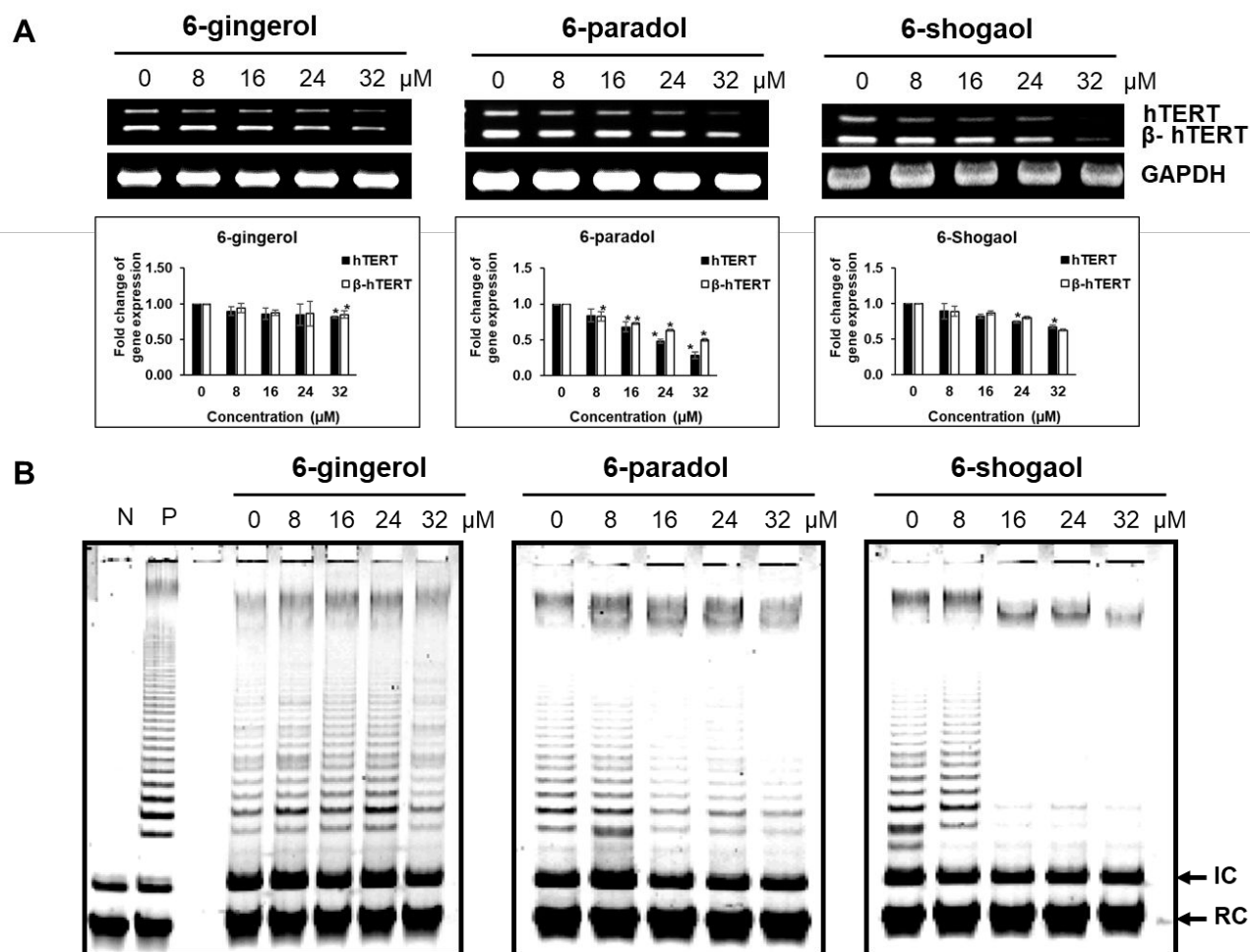
Figure S11. Effects of 6-gingerol, 6-paradol, and 6-shogaol on gene expression and telomerase activity in A549 lung cancer cells. (A) To assay for gene expression, the A549 cells were incubated with the indicated concentrations of the compound for 24 h before their RNAs were extracted and assayed by semiquantitative RT-PCR analysis. The hTERT and β-hTERT bands were quantified and normalized with those of GAPDH, and the graphs were plotted between fold change of gene expression and concentration. Differences are considered statistically significant when * $p < 0.05$ or ** $p < 0.01$. (B) To assay the effect on telomerase activity, the A549 cells were incubated with the indicated concentrations of the compound for 48 h before the crude protein extract was used as the source of telomerase in a modified TRAP assay. Lane N represents the negative control experiment when telomerase was heat-denatured. Lane P represents the positive control.

Table S1: Effects of the *Z. officinale* Extract on Body Weight and Food and Water Intake from Acute Cytotoxicity Tests in Rats

Parameters	Control	*Z. officinale* extract
Initial body weight (g)	188.0 ± 7.6	188.0 ± 7.6
Finial body weight (g)	217.0 ± 21.1	206.0 ± 11.9
Body weight change (%)	15.3 ± 8.1	9.5 ± 3.4
Average water intake (ml/rat/day)	23.0 ± 4.6	24.6 ± 2.1
Average food intake (ml/rat/day)	15.5 ± 0.4	13.1 ± 1.5

Table S2: Effects of the *Z. officinale* Extract on Relative Organ Weights from Acute Cytotoxicity Tests in Rats

Organs	Relative organ weight	
	Control	*Z. officinale* extract
Lung	0.53 ± 0.04	0.49 ± 0.04
Liver	3.23 ± 0.35	3.17 ± 0.04
Spleen	0.24 ± 0.04	0.25 ± 0.03
Heart	0.34 ± 0.02	0.35 ± 0.05
Kidney	0.67 ± 0.09	0.66 ± 0.04
Adrenal gland	0.05 ± 0.01	0.05 ± 0.01
Pancreas	0.29 ± 0.07	0.43 ± 0.09
Thymus gland	0.18 ± 0.03	0.17 ± 0.04
Stomach	0.60 ± 0.04	0.52 ± 0.05
Ovary	0.08 ± 0.01	0.08 ± 0.01
Fallopian tube	0.23 ± 0.03	0.25 ± 0.07

S1: Extraction, purification, and identification of 6-paradol and 6-shogaol

Plant material. The rhizomes of *Zingiber officinale* were collected from Phetchabun province, Thailand, in May, 2009. A voucher specimen (Apichart Suksamrarn, No. 052) is deposited at the Faculty of Science, Ramkhamhaeng University.

Extraction and isolation. The ground air-dried rhizomes of *Zingiber officinale* (11.0 kg) were pulverized and extracted successively with *n*-hexane, ethyl acetate and methanol at ambient temperature. After evaporation under reduced pressure, the hexane extract (dark brownish oil, 576.9 g), ethyl acetate extract (dark brownish oil, 425.0 g) and methanol extract (dark brownish oil, 1180.4 g) were obtained. Separation of the constituents of the hexane (576.9 g) and ethyl acetate (208.4 g) extracts were carried out by column chromatography (CC) using hexane and ethyl acetate in a polarity gradient manner and repeated column chromatography on Sephadex LH-20 (MeOH) and silica gel (hexane-CH_2Cl_2, 1:5) to afford [6]-paradol (38.2 mg) and [6]-shogaol (4.5 g).

Identification.

General. IR spectra were recorded in ATR on a Perkin-Elmer FT-IR Spectrum 400 spectrometer. ^1H and ^{13}C NMR spectra were recorded on a Bruker AVANCE 400 FT-NMR spectrometer operating at 400 and 100 MHz, respectively. Mass spectra were obtained using a Finnigan LC-Q mass spectrometer. Unless indicated otherwise, column chromatography and TLC were carried out using Merck silica gel 60 (finer than 0.063 mm) and precoated silica gel 60 F254 plates, respectively. Spots on TLC were detected under UV light and by spraying with anisaldehyde-H_2SO_4 reagent followed by heating.
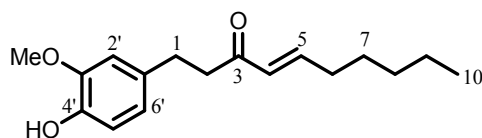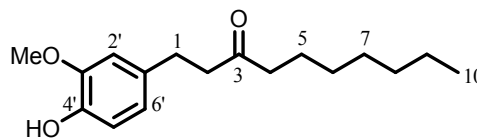
[6]-Shogaol   [6]-Paradol

[6]-Shogaol. Pale yellow oil; IR ν_{max}: 3420, 2928, 2857, 1666, 1626, 1515, 1464, 1452, 1431, 1365, 1268, 1234, 1205, 1151, 1121, 1034, 982, 814, 795 cm^{-1}; ^1H NMR (400 MHz, CDCl$_3$) δ 6.80 (d, J = 8.0 Hz, 1H, H5), 6.79 (m, J = 15.9, 6.9 Hz, 1H, H5), 6.69 (d, J = 1.8 Hz, 1H, H2), 6.66 (dd, J = 8.0, 1.8 Hz, 1H, H6), 6.07 (d, J = 15.9 Hz, 1H, H4), 5.47 (br s, 1H, 4′-OH), 3.85 (s, 3H, 3′-CH_3O), 2.83 (m, 4H, H1 and H2), 2.17 (m, 2H, H6), 1.42 (m, 2H, H7), 1.26 (m, 4H, H8 and H9), 0.87 (t, J = 7.0 Hz, 3H, H10); ^{13}C NMR (100 MHz, CDCl$_3$) δ 199.8 (C3), 147.9 (C5), 146.4 (C3), 143.9 (C4), 133.2 (C1), 130.3 (C4), 120.8 (C6), 114.3 (C5), 111.1 (C2), 55.9 (CH_3O), 42.0 (C2), 32.4 (C6), 31.3 (C8), 29.9 (C1), 27.8 (C7), 22.4 (C9), 13.9 (C10); ESMS (+ve) *m/z* (% rel. abund.), 575.2 [2M + Na]$^+$ (100).

[6]-Paradol. Pale yellow oil; IR ν_{max}: 3439, 2926, 2855, 1709, 1604, 1515, 1463, 1453, 1431, 1367, 1268, 1234, 1205, 1151, 1121, 1034, 814, 791 cm^{-1}; ^1H NMR (400 MHz, CDCl$_3$) δ 6.80 (d, J = 8.0 Hz, 1H, H5), 6.66 (br s, 1H, H2), 6.64 (d, J = 8.0 Hz, 1H, H6), 5.49 (br s, 1H, 4′-OH), 3.85 (s, 3H, 3′-CH_3O), 2.80 (t, J = 7.4 Hz, 2H, H1), 2.67 (t, J = 7.4 Hz, 2H, H2), 2.34 (t, J = 7.4 Hz, 2H, H4), 1.52 (m, 2H, H5), 1.23 (m, 8H, H6, H7, H8 and H9), 0.85 (t, J = 7.2 Hz, 3H, H10); ^{13}C NMR (100 MHz, CDCl$_3$) δ 210.5 (C4), 146.3 (C3), 143.8 (C4), 133.1 (C1), 120.7 (C6), 114.3 (C5), 111.0 (C2), 55.8 (CH_3O), 44.5 (C2), 43.1 (C4), 31.6 (C8), 29.5 (C1), 29.1 (C6), 29.0 (C7), 23.8 (C5), 22.5 (C9), 14.0 (C10); ESMS (+ve) *m/z* (% rel. abund.), 277.1 [M − H]$^-$ (100).

Table S3: The IC$_{50}$ Growth Inhibitory Concentration of A549 Lung Cancer Cells by ZOE, Its Subfractions, and Selected Pure Compounds

Z. officinale Extracts	IC$_{50}$ (µg/ml)
ZOE	58.2 ± 2.1
E1	54.9 ± 3.5
E2	21.1 ± 1.6
E3	38.9 ± 0.7
E4	25.6 ± 4.3
E2.1	43.2 ± 4.5
E2.2	26.5 ± 1.6
E2.3	23.6 ± 1.2
E2.4	17.4 ± 3.9
6-gingerol	11.3 ± 0.8
	(38.6 ± 2.8 µM)
6-paradol	10.1 ± 0.2
	(36.2 ± 0.7 µM)
6-shogaol	8.0 ± 0.3
	(28.9 ± 1.3 µM)

Table S4: Primer Sequences and Conditions Used in Semiquantitative RT-PCR

Name	Primer Sequence	Product Size (bp)	Annealing Temp. (°C)	PCR Cycle
GAPDH (F)	CCACAGTCCATGCCATCAC	450	60	20
GAPDH (R)	CCACCACCCTGTTGCTGTA			
c-Myc (F)	TAATTCCAGCGAGAGGCAGA	290	60	25
c-Myc (R)	GTCCCCAAATGGGCAGAATA			
hTEP1 (F)	TCAAGCCAAACCTGAATCTGAG	264	60	26
hTEP1 (R)	CCCCGAGTGAATCTTTCTACGC			
hTERT (F)	GCCTGAGCTGTACTTTGTCAA	275, 457	62	30
hTERT (R)	CGCAAACAGCTTGTTCTCCATGTC			
hTR (F)	GAAGGGCGTAGGCGCCGTGCTTTTGC	111	62	30
hTR (R)	GTTTGCTCTAGAATGAACGGTGGAAGG			
TRF1 (F)	TGTGCGGATGGTAGGGATGC	421	62	28
TRF1 (R)	GGGCTGATTCCAAGGGTGTA			
TRF2 (F)	AGTCAATCGCTGGGTGCTCA	636	62	25
TRF2 (R)	CCTGGTGCTGGCTGTTTATC			

* F = Forward primer, R = Reverse primer

Table S5: Oligonucleotides Used in the Modified Fluorescent TRAP Assay

Name	Sequence
MTS	5'-AGCATCCGTCGAGCAGAGTT-3'
RPc3g	5′-TAGAGCACAGCCTGTCCGTG(CTAACC)$_3$GG-3′
RP-FAM	FAM-5′-TAGAGCACAGCCTGTCCGTG-3′
IC	5'-TAGAGCACAGCCTGTCCGTGAAAAGGCCGAGAAGCGATCG-3'
NT	5'-CGATCGCTTCTCGGCCTTTT-3'

Development of a fluorescent intercalator displacement assay (G4-FID) for establishing quadruplex-DNA affinity and selectivity of putative ligands

David Monchaud, Clémence Allain and Marie-Paule Teulade-Fichou*

Laboratoire de Chimie des Interactions Moléculaires, Collège de France, CNRS UPR285, 75005 Paris, France

Abstract—A fluorescent intercalator displacement assay (G4-FID) has been designed based on the displacement of thiazole orange (TO) positioned onto a quadruplex-forming oligonucleotide by putative ligands. This technique was validated by the use of a set of representative and fully characterized G-quadruplex binders (ranging from pyridodicarboxamide to macrocyclic ligands). To further extend its applicability, a comparative version has been developed which allows a rapid and viable determination of quadruplex-over duplex-selectivity.
© 2006 Elsevier Ltd. All rights reserved.

A wide variety of techniques are currently available to establish the DNA binding properties of small molecules, but their application to other DNA structures than duplex-DNA is sometimes difficult. Concerning the G-quadruplex DNA (noted hereafter G4-DNA), which is currently the focus point of much attention,[1] only a limited number of methods are employed. Among these, FRET-melting assay,[2] SPR (biacore) technique[3] and fluorimetric titrations[4] are the most widely used. However, the two former are somewhat technically challenging and/or require specialized equipment whereas the latter is limited to fluorescent ligands. Consequently, the development of easy-to-use methods is still needed. The FID (fluorescent intercalator displacement)[5] is a well-known assay based on the loss of fluorescence of a DNA-bound intercalator (ethidium bromide, thiazole orange (TO, Fig. 1)) or minor-groove binder (Hoechst 33258) upon displacement by a DNA-binding molecule. FID has been recently used on DNA hairpins to establish binding affinity and sequence selectivity of small molecules, proteins and triplex forming oligonucleotides.[6]

In this context, we have been interested in the development of an alternative FID assay (G4-FID) based on

the displacement of TO from the human telomeric derived quadruplex-DNA, which requires neither modified oligonucleotides nor specific equipments.

Preliminary studies have demonstrated that TO binds the quadruplex-forming oligonucleotide 22AG (Fig. 1) in a single-site manner, with high affinity ($K_a = 3 \times 10^6$ M^{-1});[7] this recognition efficiency explains our preference for TO over ethidium bromide (known to weakly bind quadruplex)[8] and ensures probing of a high affinity site in G4-DNA. More importantly, TO is highly fluorescent upon interaction with G4-DNA (~500- to 3000-fold exaltation) whereas totally quenched when free in solution (quantum yield (ϕ) = 2×10^{-4}); consequently, the displacement ability of a given ligand can be easily monitored by the decrease of TO fluorescence ($\lambda_{max} = 539$ nm) upon selective excitation at 501 nm.[9] This test has been designed to be performed with inexpensive material (22AG and thiazole orange) in a non-demanding manner (0.75, 1.5 and 7.5 nmol/test
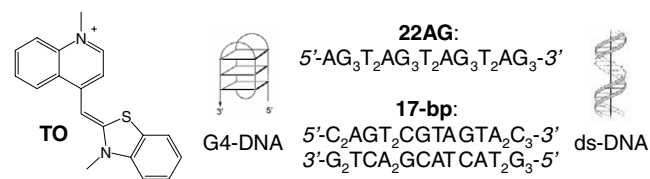
Figure 1. Structure of thiazole orange and oligonucleotides 22AG and 17-bp ds-DNA (counter-ion is p-CH$_3$(C$_6$H$_4$)SO$_3^-$ for TO).

22AG:
5'-AG$_3$T$_2$AG$_3$T$_2$AG$_3$T$_2$AG$_3$-3'

17-bp:
5'-C$_2$AGT$_2$CGTA GTA$_2$C$_3$-3'
3'-G$_2$TCA$_2$GCAT CAT$_2$G$_3$-5'

for 22AG, TO and tested ligand, respectively) with a standard spectrofluorimeter. Additionally, it is neither technically demanding nor time consuming (~40 min/ sample).

In the course of our long-time program of developing new G-quadruplex ligands, we have designed and obtained a family of quinacridine ligands (Fig. 2).[4,10] Full investigations (syntheses, biochemical evaluations and NMR studies) will be reported elsewhere.[11] These compounds have been initially evaluated for their ability to bind G-quadruplex DNA by the FRET melting assay recently developed by Mergny and Maurizot.[2] This test is based on the monitoring of melting profile of a quadruplex-forming oligonucleotide labelled with FRET fluorophores, and allows to sort ligands with respect to their quadruplex-stabilization ability (ΔT_m). Up to now it has been successfully applied to a wide panel of ligands, including the high-affinity G4-binders telomestatine,[12] pyridodicarboxamide[13] or bisquinacridine.[10] Eight of the most representative quinacridines (Fig. 2) have been used to validate the FID assay, ranging from polyammonium (1–4) to N-methylated quinacridines (5–7) as well as macrocyclic bisquinacridine (BOQ$_1$).

The test is designed as follows: onto a mixture of prefolded 22AG-quadruplex (0.25 μM) and TO (0.50 μM), in a 10 mM sodium cacodylate, pH 7.3, 100 mM K$^+$ buffer, addition of increasing amount of ligand (from 0.5 to 10 equiv) is followed by a 3 min equilibration period before the fluorescence spectrum is recorded. The fluorescence area (FA, 510–750 nm), converted in percentage displacement (PD, with PD = 100 − [(FA/ FA$_0$) × 100], FA$_0$ being FA before addition of ligand), is then plotted versus the concentration of added ligand.

Figure 3. FID results onto 22AG for quinacridines 1 (□), 2 (△), 3 (○), 4 (◇), N-methylated quinacridines 5 (●), 6 (■), 7 (▲), BOQ1 (■), 360A (●) and TMPyP4 (▲).

FID curves are presented in Figure 3. In order to precisely quantify the ligand-induced TO displacement, and in turn to sort ligands with respect to this ability, a $^{G4}DC_{50}$ value was designed as the required concentration to displace 50% TO from 22AG. Values are reported in Table 1.

Remarkably, in most cases FID results are in good agreement with the FRET data. Indeed, in a same series (e.g., polyammonium quinacridines, white motif), the TO displacement ability of quinacridines 1–4 parallels their thermal stabilization capacity (Table 1).

Ligand 1 appears poorly efficient which indicates that the FID test displays a high-level of selection for ligands due to the high affinity of the TO probe. In turn, ligands

Figure 2. Structure of quinacridine-based ligands (1–7), macrocyclic bisquinacridine BOQ$_1$, pyridodicarboxamide 360A and TMPyP4 (counter-ions are CF$_3$SO$_3$$^-$ for 5–7, I$^-$ for 360A and p-CH$_3$(C$_6$H$_4$)SO$_3$$^-$ for TMPyP4).

Table 1. FID (DC$_{50}$ and selectivity) and FRET (ΔT_m) characterisations of compounds **1–7**, **BOQ1**, **360A** and **TMPyP4**
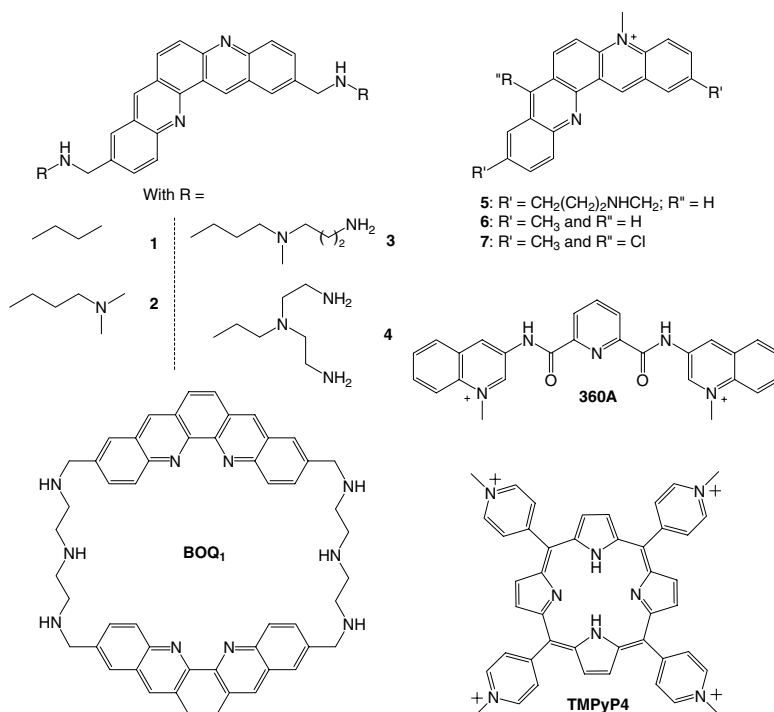
Ligand	$^{G4}DC_{50}$[a] (μM)	ΔT_m[b] (°C)	$^{ds}DC_{50}$[a] (μM)	Sel.[d]	Est. Sel.[e]
1	>2.5	12	n.d.[c]	n.d.[c]	—
2	1.185	19	0.667	0.6	—
3	0.611	21	0.497	0.8	—
4	0.480	32	0.392	0.8	—
BOQ$_1$	0.475	28	1.862	3.9	—
360A	0.320	26	>2.5	>6.4	43.5
5	0.162	21	0.400	2.5	—
6	0.217	10	0.925	4.3	—
7	0.096	16	>2.5	>25.9	31.7
TMPyP4	0.106	22	0.190	1.8	—

[a] $^{G4}DC_{50}$ and $^{ds}DC_{50}$ stand for the concentration required for 50% displacement of TO onto quadruplex (G4-DNA) and duplex-DNA (ds-DNA) respectively (experimental errors estimated at ±5 %).

[b] $\Delta T_m = T_m(\text{DNA} + \text{ligand}) - T_m(\text{DNA})$; determined by standard FRET measurements.

[c] n.d. for not determined.

[d] Sel. for selectivity G4- versus ds-DNA, established with: Sel. = $^{ds}DC_{50}/^{G4}DC_{50}$.

[e] Est. Sel. for estimated selectivity, see text for explanation.

2–4 whose affinity was not possible to measure by fluorimetric titration due to their high cationic charge[11] can be evaluated through the present FID assay. Altogether, this means that this test is devoted to the detection of ligands with K_d in the sub-micromolar range. In order to further validate the assay with ligands of various structures, the macrocyclic bisquinacridine **BOQ$_1$** and the high affinity quadruplex binder **360A** (Fig. 2)[13] have been tested. In both cases, high FID levels are observed ($^{G4}DC_{50} < 0.5\ \mu$M, Table 1). These results confirmed the overall generality of the assay since both ligands are characterized by a high ΔT_m response (>25 °C, Table 1). Interestingly, N-methylated quinacridines **5–7** appear to be more potent TO displacers than the polyammonium ligands **2–4** (grey motif, $^{G4}DC_{50} < 0.3\ \mu$M) whereas they exhibit lower thermal stabilizations (Table 1). A striking example is ligand **6** which exhibit a $^{G4}DC_{50}$ as low as 0.217 μM and a ΔT_m of only 10 °C. The discrepancy between the two groups of ligands comes obviously from different binding modes and/or sites. Indeed, whereas N-methylated quinacridines are likely to stack on one tetrad (as do pentacyclic acridinium ligands),[14] polyammonium quinacridines, **BOQ1** and **360A** are susceptible to establish additional interactions with the loops and/or the grooves. Hence in the former case a strict competition occurs with the probe whereas in the latter case TO displacement might result from both direct and indirect competition (i.e., fixation to nearby sites). Furthermore, in the N-methylated series, the observation that the electronically poorer the quinacridine (**7** > **5** > **6**) the more efficient the TO displacement also suggest that this displacement highly depends on the quinacridine/quadruplex stacking relationship. Additionally, the well-documented **TMPyP4** (Fig. 2),[15] known to interact via π-stacking, has been tested.[16] Its high TO displacement ability ($^{G4}DC_{50} = 0.106\ \mu$M, Table 1), in the same range as that of N-methylated quinacridines, supports our hypothesis. In that sense, this G4-FID test might complement the use of the

FRET assay since the relative weights of the π-stacking and the electrostatic contributions seem to differ for the two methods. Nevertheless, care should be taken when interpreting the data, which should be considered in the context of the experiment.

To further extend the usability of this FID assay, a comparative version has been developed, which allows the estimation of preference for quadruplex- over duplex-DNA, if any. The 'comparative G4-FID' is based on the comparison of results obtained with 22AG and a 17-bp duplex-DNA (or ds-DNA, Fig. 1)[17] under strictly the same conditions (22AG or 17 bp (0.25 μM), TO (0.50 μM), in a 100 mM K$^+$ buffer, upon addition of increasing amount of ligand (from 0.5 to 10 equiv)). This comparison is feasible since TO has the same level of affinity for duplex- and quadruplex-DNA, and is known to exhibit a poor sequence-specificity.[6] However, considering that the duplex-binding stoichiometry of TO is higher than that of quadruplex (i.e., 3/1 for a 17 bp duplex),[6] it is worth noting that the comparative G4-FID gives the same results when conducted with a higher TO/oligonucleotide ratio (4/1 instead of 2/1). Upon interaction with ds-DNA, a $^{ds}DC_{50}$ is determined, and the ratio between the two DC$_{50}$ (ds vs G4) allows to estimate the ligand selectivity for quadruplex-DNA (Sel., Table 1). Nevertheless, in some cases (**7**, **360A**) we were unable to determine a $^{ds}DC_{50}$ due to the low affinity of these ligands for ds-DNA. In these cases, the selectivity is calculated on the basis of the level of displacement (in %) obtained with 2.5 μM of ligand onto the 17-bp duplex; the concentration required with 22AG to reach the same level (^{G4}C) allows then to determine the estimated selectivity (Est. Sel., Table 1) via the equation: Est. Sel. = 2.5/^{G4}C. Results are shown in Figure 4 and summarized in Table 1.

BOQ$_1$ and **360A** are known to be quadruplex-selective, and this preference has been quantified by various techniques: for **BOQ$_1$**, a 10- and 3.3-fold selectivity have been determined by SPR and dialysis equilibrium,
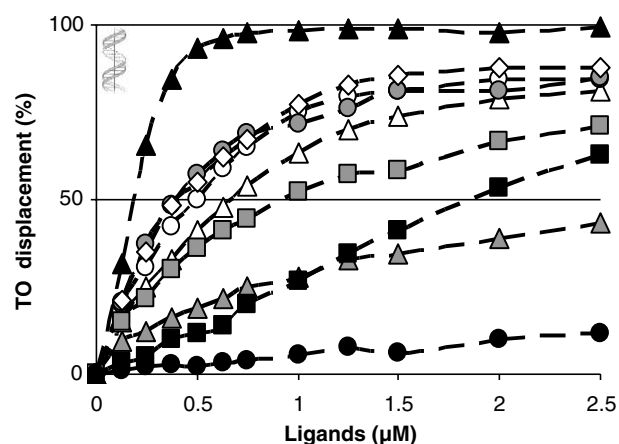
Figure 4. FID results onto 17-bp duplex-DNA for quinacridines **2** ($\triangle$), **3** ($\bigcirc$), **4** ($\diamondsuit$), N-methylated quinacridines **5** (grey $\bullet$), **6** ($\blacksquare$), **7** (grey $\blacktriangle$), **BOQ1** ($\blacksquare$), **360A** ($\bullet$) and **TMPyP4** ($\blacktriangle$).

respectively, while a selectivity higher than 50-fold has been measured for **360A** via AlphaScreen test.[13] Herein, a 3.9- and 43.5-fold selectivity is obtained for **BOQ**$_1$ and **360A**, respectively. On the opposite, **TMPyP4** is known to be poorly selective.[18] The low selectivity factor evaluated here (Sel. = 1.8, Table 1) confirms the validity of the test. Concerning the quinacridines, while polyammonium ligands appear not selective (Sel. 0.6–0.8 for **2**–**4**), N-methylated quinacridines show a clear preference for the quadruplex-DNA (especially **7** with a 31-fold selectivity). This class of compounds is currently studied, and results will be reported soon.

In conclusion, we have developed a simple G4-FID assay, based on the displacement of TO positioned on a quadruplex-forming oligonucleotide mimicking the human telomeric DNA. The validation of the assay using a set of known and fully characterized quadruplex-ligands was fully satisfactory and indicates that the test ensures a high level of quality for the detected G4-ligands. Additionally, a 'comparative G4-FID' has also been developed, and results obtained are in good agreement with the reported data based on various methods. The structural diversity of tested ligands (from bisquinolinium to 42-membered macrocyclic ligand and condensed heteroaromatic ones) testifies to the wide applicability of the present technique. Indeed, in spite of shortcomings due to direct versus indirect displacement of the probe, the G4-FID method is suitable for rapid examination of putative G4-binders. Consequently, this very 'easy-to-use' test can be of great help in the drug-discovery process. Finally, this FID assay represents a unique opportunity to evaluate ligand affinity for other quadruplex-structures (e.g., bi- or tetra-molecular ones), the protocol being easily adaptable to these nucleic acid structures. These results will be also reported in due time.

Acknowledgments

References and notes

1. Neidle, S.; Parkinson, G. *Nat. Rev. Drug Disc.* **2002**, *1*, 383; Hurley, L. H. *Nat. Rev. Cancer* **2002**, *2*, 188.

2. Mergny, J. L.; Maurizot, J. C. *ChemBioChem* **2001**, *2*, 124.

3. Rezler, E. M.; Seenisamy, J.; Bashyam, S.; Kim, M. Y.; White, E.; Wilson, W. D.; Hurley, L. H. *J. Am. Chem. Soc.* **2005**, *127*, 9439; Seenisamy, J.; Bashyam, S.; Gokhale, V.; Vankayalapati, H.; Sun, D.; Siddiqui-Jain, A.; Streiner, N.; Shin-ya, K.; White, E.; Wilson, W. D.; Hurley, L. H. *J. Am. Chem. Soc.* **2005**, *127*, 2944; Read, M.; Harrison, R. J.; Romagnoli, B.; Tanious, F. A.; Gowan, S. H.; Reszka, A. P.; Wilson, W. D.; Kelland, L. R.; Neidle, S. *Proc. Natl. Acad. Sci. U.S.A.* **2001**, *98*, 4844.

4. Mergny, J. L.; Lacroix, L.; Teulade-Fichou, M. P.; Hounsou, C.; Guittat, L.; Hoarau, M.; Arimondo, P. B.; Vigneron, J. P.; Lehn, J. M.; Riou, J. F.; Garestier, T.; Helene, C. *Proc. Natl. Acad. Sci. U.S.A.* **2001**, *98*, 3062.

5. Boger, D. L.; Fink, B. E.; Hedrick, M. P. *J. Am. Chem. Soc.* **2000**, *122*, 6382; Morgan, A. R.; Lee, J. S.; Pulleyblank, D. E.; Murray, N. L.; Evans, D. H. *Nucleic Acids Res.* **1979**, *7*, 547; Baguley, B. C.; Falkenhaug, E.-M. *Nucleic Acids Res.* **1978**, *5*, 161; Browne, K. A.; He, G.-X.; Bruice, T. C. *J. Am. Chem. Soc.* **1993**, *115*, 7072.

6. Boger, D. L.; Fink, B. E.; Brunette, S. R.; Tse, W. C.; Hedrick, M. P. *J. Am. Chem. Soc.* **2001**, *123*, 5878; Ham, Y. W.; Tse, W. C.; Boger, D. L. *Bioorg. Med. Chem. Lett.* **2003**, *13*, 3805; Yeung, B. K. S.; Tse, W. C.; Boger, D. L. *Bioorg. Med. Chem. Lett.* **2003**, *13*, 3801; Tse, W. C.; Boger, D. L. *Acc. Chem. Res.* **2004**, *37*, 61.

7. Allain, C.; Monchaud, D.; Teulade-Fichou, M. P., submitted for publication.

8. Koeppel, F.; Riou, J. F.; Laoui, A.; Mailliet, P.; Arimondo, P. B.; Labit, D.; Petitgenet, O.; Helene, C.; Mergny, J. L. *Nucleic Acids Res.* **2001**, *29*, 1087.

9. Nygren, J.; Svanvik, N.; Kubista, M. *Biopolymers* **1998**, *46*, 39.

10. Teulade-Fichou, M. P.; Carrasco, C.; Guittat, L.; Bailly, C.; Alberti, P.; Mergny, J. L.; David, A.; Lehn, J. M.; Wilson, W. D. *J. Am. Chem. Soc.* **2003**, *125*, 4732.

11. Teulade-Fichou, M. P.; Hounsou, C., unpublished results.

12. Gomez, D.; Paterski, R.; Lemarteleur, T.; Shin-ya, K.; Mergny, J. L.; Riou, J. F. *J. Biol. Chem.* **2004**, *279*, 41487.

13. Pennarun, G.; Granotier, C.; Gauthier, L. R.; Gomez, D.; Hoffshir, F.; Mandine, E.; Riou, J. F.; Mergny, J. L.; Mailliet, P.; Boussin, F. D. *Oncogene* **2005**, *24*, 2917; Granotier, C.; Pennarun, G.; Riou, L.; Hoffschir, F.; Gauthier, L. R.; De Cian, A.; Gomez, D.; Mandine, E.; Riou, J. F.; Mergny, J. L.; Mailliet, P.; Dutrillaux, B.; Boussin, F. D. *Nucleic Acids Res.* **2005**, *33*, 4182.

14. Gavathiotis, E.; Heald, R. A.; Stevens, M. F. G.; Searle, M. S. *Angew. Chem., Int. Ed.* **2001**, *40*, 4749.

15. Shi, D. F.; Wheelhouse, R. T.; Sun, D.; Hurley, L. H. *J. Med. Chem.* **2001**, *44*, 4509; Phan, A. T.; Kuryavyi, V.; Gaw, H. Y.; Patel, D. J. *Nat. Chem. Biol.* **2005**, *1*, 167.

16. In this case, a TO fluorescence attenuation effect is due to a minor absorbance of the porphyrin at the excitation wavelength (501 nm). An attenuation factor has been calculated < 10% for a **TMPyP4** concentration of 2.5 μM (10 equiv). Consequently, DC$_{50}$ evaluation is not affected since it is obtained at ligand concentration <0.25 μM (Figs. 3 and 4).

17. The 17 bp duplex-DNA is a biological sequence, used as control in previous studies (Ref. 10).

18. Ren, J.; Chaires, J. B. *Biochemistry* **1999**, *38*, 16067.

Research paper

Fluorescence intercalator displacement assay for screening G4 ligands towards a variety of G-quadruplex structures

Phong Lan Thao Tran [a,b,c], Eric Largy [d], Florian Hamon [d], Marie-Paule Teulade-Fichou [d], Jean-Louis Mergny [a,b,*]

[a] University of Bordeaux, ARNA laboratory, F-33000 Bordeaux, France
[b] INSERM, U869, Laboratoire ARNA, IECB, F-33600 Pessac, France
[c] INSERM, U565, Acides nucléiques: dynamique, ciblage et fonctions biologiques, Muséum National d'Histoire Naturelle (MNHN) USM503, CNRS, UMR7196, F-75231 Paris, France
[d] Institut Curie, Section Recherche, CNRS UMR176, Centre Universitaire Paris XI, Bât. 110, F-91405 Orsay, France

ARTICLE INFO

ABSTRACT

The potential formation of G-quadruplexes in many regions of the genome makes them an attractive target for drug design. A large number of small molecules synthesized in recent years display an ability to selectively target and stabilize G-quadruplexes. To screen for G4 ligands, we modified a G4-FID (G-quadruplex Fluorescent Intercalator Displacement) assay. This test is based on the displacement of an "on/off" fluorescence probe, Thiazole Orange (TO), from quadruplex or duplex DNA matrices by increasing amounts of a putative ligand. Selectivity measurements can easily be achieved by comparing the ability of the ligand to displace TO from various quadruplex and duplex structures. G4-FID requires neither modified oligonucleotides nor specific equipment and is an isothermal experiment. This test was adapted for high throughput screening onto 96-well plates allowing the comparison of more than twenty different structures. Fifteen different known G4 ligands belonging to different families were tested. Most compounds showed a good G4 vs duplex selectivity but exhibited little, if any, specificity for one quadruplex sequence over the others. The quest for the "perfect" specific G4 ligand is not over yet!

© 2011 Elsevier Masson SAS. All rights reserved.

1. Introduction

G-quadruplexes are a polymorphic class of secondary DNA structures in which the structural unit is formed by a planar arrangement of four guanines, known as G-quartets or G-tetrads [1,2]. A vertical stacking of several G-quartets are stabilized by the presence of monovalent cations. These DNA structures can be formed by one, two or four G-rich strands. Tetramolecular quadruplexes generally adopt a well-defined structure, in which all guanines are in the anti-glycosidic conformation and all strands are parallel, and might be useful for biotechnology applications. Intramolecular G-quadruplexes formed by single DNA strand have attracted much interest because of their putative biological regulatory function at telomeres, oncogene promoters and other relevant regions of the genome [3–5]. In contrast to tetramolecular quadruplexes, intramolecular structures form faster and are more complex, showing great conformational diversity [3]. Different sequences can adopt distinct topologies, but a given sequence can also fold into various different conformations, which may coexist. One of the best illustrations of this complexity are human telomere sequences, in particular in potassium conditions [6].

The potential formation of G-quadruplexes in many regions of the genome makes them an attractive target for drug design ever since quadruplex ligands were found to inhibit telomerase [7], to induce rapid apoptosis owing to the displacement of telomere-binding proteins and to regulate transcription or translation of genes, especially oncogenes [8–12]. A large number of small molecules synthesized in recent years display an ability to target and stabilize selectively G-quadruplexes [13,14]. Nowadays, the challenge is to develop small molecules capable of selective binding to one quadruplex type over another. To be effective, screening for selectivity has to be performed at the early stage of development and ideally this should be rapid and easy to implement. Several methods are currently used, such as the FRET-melting assays [15], SPR techniques [16], ITC experiments [17], ESI-MS analyses [18], multifluorescent probes assays [19] or equilibrium microdialysis [20]. Although these methods are reliable and powerful, they require specific equipment or buffer conditions, modified or immobilized oligonucleotides, and/or specific ligand properties (e.g. fluorescence).

* Corresponding author. INSERM, U869, Laboratoire ARNA, IECB, F-33600 Pessac, France. Tel.: +33 0 540 003 022; fax: +33 0 557 571 015.
E-mail address: jean-louis.mergny@inserm.fr (J.-L. Mergny).

In this context, we decided to use a simple alternative assay developed by Teulade-Fichou's team since 2006, G4-FID (G-quadruplex Fluorescent Intercalator Displacement) [21–24]. The principle of G4-FID assay is schematically presented in Fig. 1. This assay is based on the displacement of an "on/of" fluorescence probe, Thiazole Orange (TO), from quadruplex or duplex DNA matrices by increasing amounts of a putative ligand. TO being virtually non-fluorescent when free in solution but strongly fluorescent when bound to DNA, the ligand-induced displacement leads to a decrease of the fluorescence which is monitored as function of the ligand concentration. Therefore, the quadruplex-affinity of a candidate compound can be evaluated through its ability to displace TO from quadruplex DNA. Moreover, selectivity measurements can easily be achieved by comparing the ability of the ligand to displace TO from various quadruplex and duplex structures. Moreover, G4-FID requires neither modified oligonucleotides nor specific equipment and is an isothermal experiment. Initially, this assay was performed in a high total volume (3 mL), using quartz cells (referred hereafter as *standard G4-FID assay*). In this work, we developed a low-cost G4-FID assay for high throughput screening onto 96-well plates (which may be easily transposed into 384-well plates) where the total volume does not exceed 25 μL. Notably, we decided to use a qPCR apparatus for all fluorescent measurements. Although it displays a relatively moderate fluorescence sensibility compared to dedicated fluorimeters or microplate readers, it is a widely spread device among research laboratories, already used for FRET-melting measurements.

In order to get more insight into the structure selectivity of the studied molecules, we have used a large number of oligonucleotides displaying various structures (quadruplexes, duplexes and single-strands). Thus, we have exhaustively characterized the structure and stability of 30 DNA and RNA sequences, by absorbance thermal difference spectra (TDS), circular dichroism (CD), UV melting and PAGE. We have determined which sequences could be reliably used in function of the fluorescence enhancement of bound TO. Finally, we have assayed 15 compounds, displaying different binding properties, using our screening method. All these ligands have already been tested by FRET-melting assay and/or standard G4-FID assay enabling a comparison of the results.

2. Experimental conditions

2.1. Relevant oligonucleotides and ligands

2.1.1. Oligonucleotides

Oligonucleotides were purchased from Eurogentec (Seraing, Belgium), dissolved in bi-distilled water and stored at −20 °C. Concentrations of all oligonucleotides were determined by UV-absorption using the extinction coefficients provided by the manufacturer. Sequences are given in the 5′ to 3′ direction (Table S1). For spectroscopic measurements, Reverse-Phase Cartridge•Gold™ (RPC) purified oligonucleotides were used without further purification.

2.1.2. Ligands

TrisK3-NH, TrisQ [25], 360A, 832A, 307A, iPDC [26], Phen-DC3, Phen-DC6, Bipy-DC3, Bipy-DC6 [27], and the metallo-organic complex Cu-ttpy [28] have been synthesized and supplied by Teulade-Fichou's team (Fig. 2). BRACO-19 [29] and 12459 [30] were a kind gift from Dr. P. Mailliet (Sanofi). Piper [31] and BSU1051 [7] are commercially available. Stock solutions of these ligands (1–10 mM in DMSO) were used for G4-FID assay and are stored at −20 °C. TO was purchased from Sigma–Aldrich and used without further purification.

2.2. Preparation of oligonucleotides

Oligonucleotides (intramolecular quadruplexes, duplexes and single-strands) were prepared by heating the corresponding oligonucleotides at 90 °C for 5 min in a 10 mM lithium cacodylate buffer pH 7.2, 100 mM KCl then slowly cooling to room temperature for 2 h. Oligonucleotide structures were formed at 50 μM strand concentration. Tetramolecular quadruplexes from TG_4T, TG_5T and UG_5U were pre-folded at high strand concentration (200 μM), at 4 °C for 48 h, in the same buffer.

2.3. Fluorescence enhancement measurements

Experiments were performed with 96-well microplates from Stratagene. Each condition was tested at least in duplicate, in a volume of 25 μL for each sample. Measurements were performed at 25 °C, all G-quadruplex sequences being folded in KCl at this temperature. Two equivalents of TO (2 μM) were added in a solution of 1 μM oligonucleotide. Samples were incubated in 10 mM lithium cacodylate buffer pH 7.2, 100 mM KCl. Fluorescence emission was collected at 516 nm with 8-fold gain after excitation at 492 nm in a real-time quantitative PCR (Stratagene Mx3005P instrument).

2.4. G4-FID protocol: isothermal assay

All experiments were performed with 96-well microplates. Each condition was tested in duplicate and at least 3 times, in a volume of 25 μL for each sample. Samples were incubated in 10 mM lithium cacodylate buffer pH 7.2, 100 mM KCl. Pre-folded DNA target (0.5 μM strand concentration for intramolecular G4, 2 μM strand concentration for tetramolecular G4 and 1 μM strand concentration for duplexes) was mixed with 1 μM of Thiazole Orange. Five equivalents of each ligand (2.5 μM) were added for each structure. The fluorescence of samples was measured at 25 °C in a qPCR (Stratagene Mx3005P) instrument. The temperature was kept constant with a thermostat cell holder (Peltier). The Thiazole Orange was excited at 492 nm (±5 nm) and the emission was collected at 516 nm (±5 nm) with 8-fold gain.
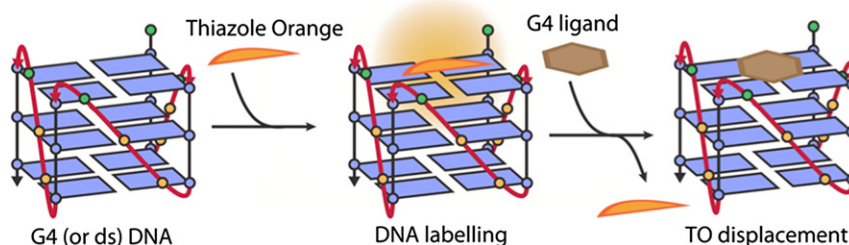
Fig. 1. Schematic representation of the two main steps of the G4-FID assay, *i.e.,* (a) labelling of the DNA matrices (quadruplex or duplex DNA) by Thiazole Orange (TO) and (b) displacing the fluorescent probe from the DNA matrices by a small molecule candidate.
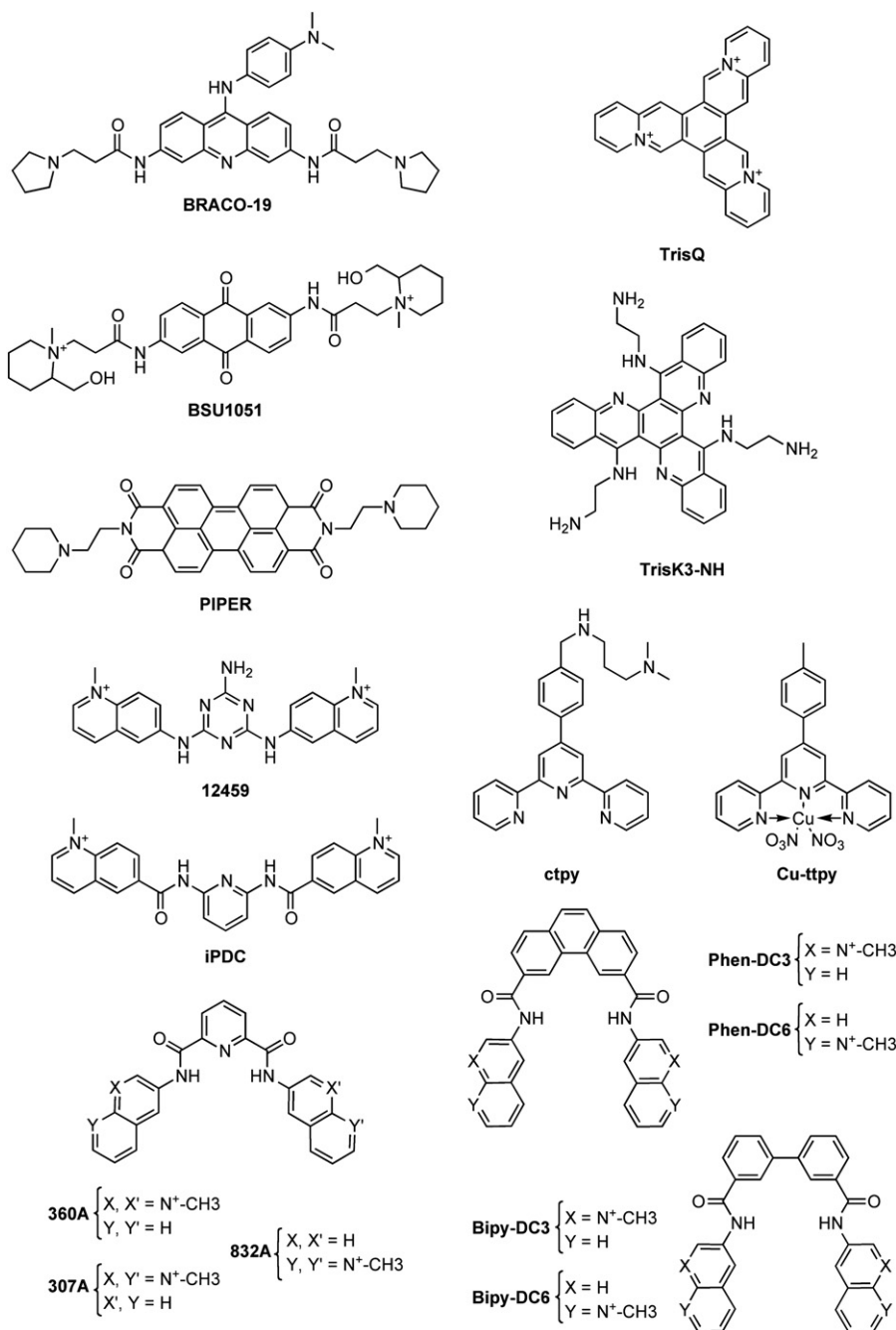
Fig. 2. Selected G-quadruplex ligands used in the G4-FID assay.

3. Analysis and interpretation of FID results

3.1. Choice of the oligonucleotides for FID test

3.1.1. Absorbance, circular dichroism measurement and PAGE of G-rich sequences

Initial experiments (UV−visible absorption, circular dichroism measurement and gel electrophoresis) were performed to confirm that all selected G-rich sequences could adopt a quadruplex structure. Except the trinucleotide CGG12, all the studied G-rich sequences displayed TDS (Thermal Difference Spectra) signatures characteristic of G-quadruplex structure in KCl (Fig. 3A) [32]. The trinucleotide CGG12 changed the conformation in presence of

ligand. In particular, the G4 formation of sequence CGG12 induced by 360A (Fig. S2).

Circular dichroism spectra recorded at 4 °C confirmed TDS results (Fig. 3B). Most of them exhibited a negative peak around 240 nm and a positive peak around 260 nm (a "Type I" signature) in 10 mM lithium cacodylate and 100 mM KCl (Fig. 3B, left). However, the thrombin binding aptamer (TBA), Bombyx (Bom17), Ascaris (Asc20) and mutant of human telomeric motifs (21CTA) [33] showed two maxima at 245 and 290 nm (a "Type II" signature) (Fig. 3B, right). The short (22Ag) and long (45Ag) human telomeric motif, Plasmodium (PlasC24), Oxytricha (Oxy 3.5) and promoter AKT1 displayed a positive peak around 290 nm and a positive peak or shoulder in the 260−270 nm region (Fig. 3B, right) in KCl
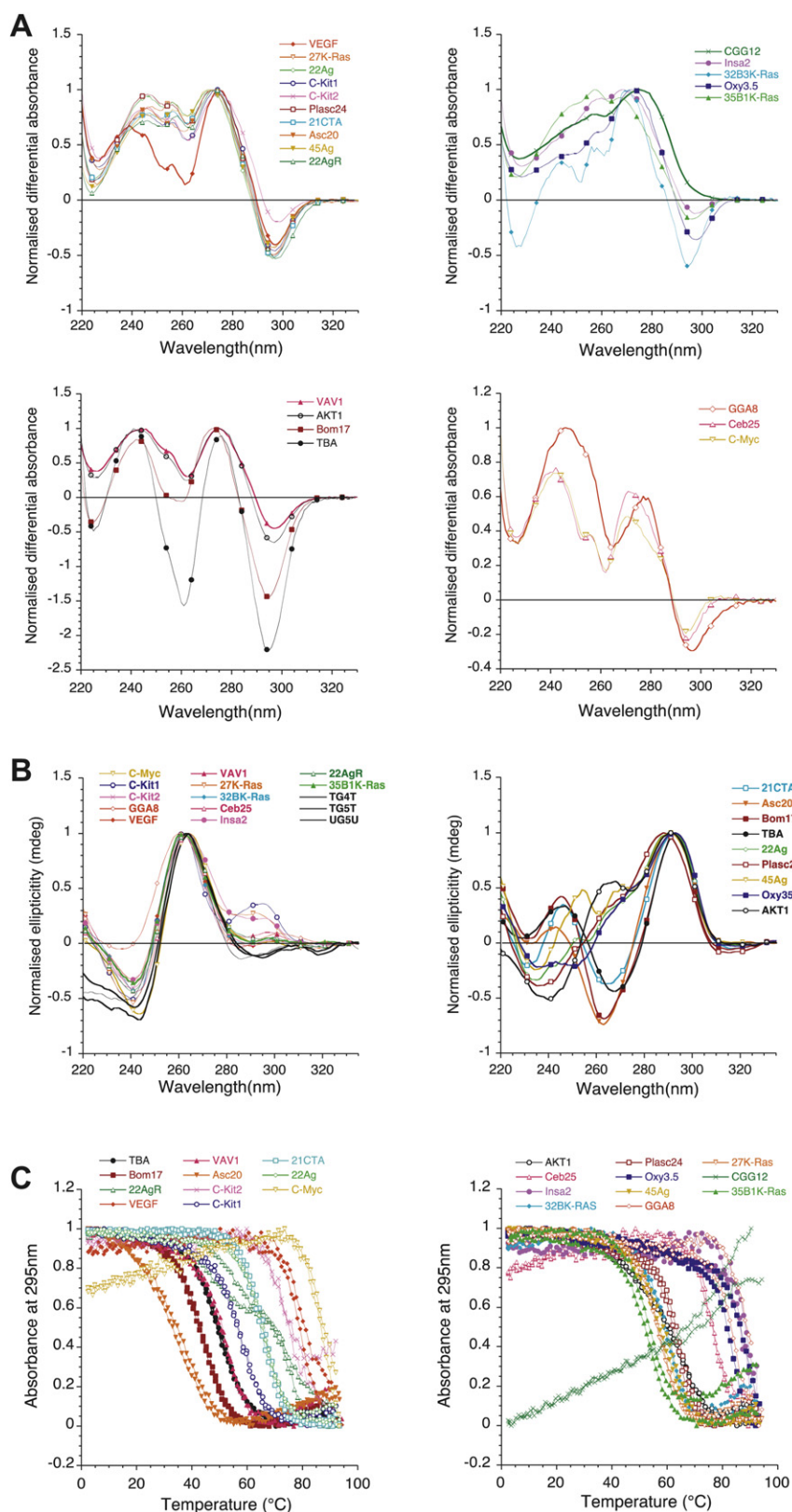
Fig. 3. UV melting curves, thermal difference spectra (TDS) and circular dichroism (CD). (**A**) Thermal difference spectra resulting from the difference between the absorbance recorded at high and low temperature in 100 mM KCl containing 10 mM lithium cacodylate at pH 7.2. (**B**) CD spectra recorded at 4 °C (in the same buffer). Data were normalized (TDS$_{norm}$ = TDS/max(TDS) or CD$_{norm}$ = CD/max(CD)) over the 220–335 nm wavelength range. (**C**) Normalized UV melting curves (cooling and heating) at 295 nm in 100 mM KCl containing 10 mM lithium cacodylate (1 cm optical path length). Oligonucleotides were prepared at 5 μM strand concentration.
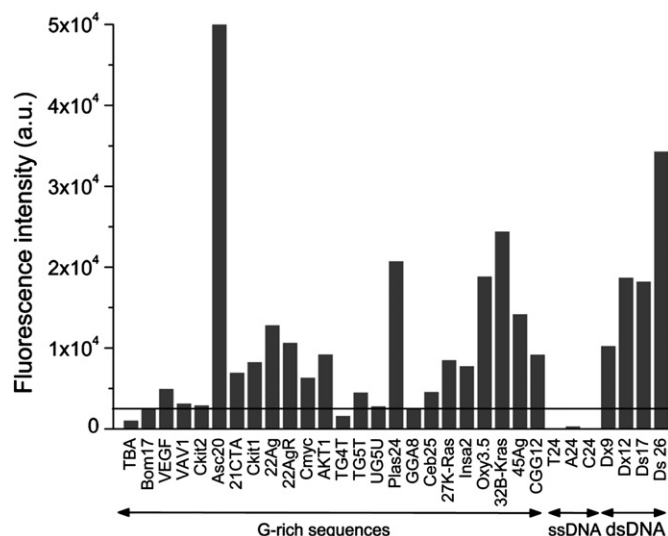
Fig. 4. Bar graph of fluorescence enhancement with 1 μM of oligonucleotides and 2 μM of TO. ssDNA: single-stranded DNA (C_{24}, A_{24} or T_{24}). dsDNA: double-stranded DNA (9–26 bp-long).

condition. The CD spectra showed the diversity of G-quadruplex structures formed by selected sequences.

The stability of the quadruplexes was measured by UV melting experiments, recording absorbance at 295 nm [34]. Melting temperature of all G-quadruplex folding sequences were determined graphically [35]: T_m ranged from 37 °C to > 70 °C in KCl (Fig. 3C & Table S1). The formation of tetramolecular quadruplexes (TG_4T, TG_5T, UG_5U) was not studied by UV melting because of their high stability (>90 °C) and their slow association kinetics [36]. Consequently, in order to demonstrate the formation of tetramolecular quadruplex structures, we used non-denaturing polyacrylamide gel (PAGE) (Fig. S1). Non-denaturing gel electrophoresis allows separation of single-stranded oligonucleotides (indicated by "−") from tetramolecular G-quadruplex structures (indicated by "+").

UV melting, TDS, CD spectra and PAGE confirmed that all selected G-rich sequences form stable quadruplexes. All of them melt at temperatures higher than 35 °C thereby enabling us to fix the temperature of FID experiments at 25 °C.

3.1.2. Fluorescence enhancement

Fluorescence enhancement of TO in presence of all the oligonucleotides was monitored in order to determine which sequences could be used in the G4-FID assay with a qPCR device. It is worth noting that the choice of wavelengths available with this experimental setting does not correspond to the maximum excitation and emission wavelengths of TO (501/534 nm), but to commonly available fluorescein filters (492/516). However, this is not detrimental to the measurements given that the bandwidths (±5 nm) allow a good excitation and recovery of the emission.

We have measured fluorescence enhancement using 2 equivalents of TO *vs* DNA as it is the preferential stoichiometry for the G4-FID assay [23]. Results are gathered in Fig. 4. These measurements led us to eliminate oligonucleotides for which fluorescence intensity was not sufficient (<2500) to be reliably detected by a qPCR device, making the observation of TO displacement more difficult. Then from all previous experiments, the thrombin binding aptamer (TBA), *Bombyx* (Bom17), trinucleotide $(GGA)_8$, two tetramolecular quadruplexes ($TG4T$ and $UG5U$), two double-strands (dx9 and ds17) and all single-strands (dT_{24}, dA_{24} and dC_{24}) were eliminated for further studies. The sequences of the twenty remaining G4 oligonucleotides and of the two control duplex oligonucleotides (dx12, ds26) are shown in Table 1.

3.2. Analysis of FID results examplified with 360A, a quadruplex ligand used as a benchmark

The G4-FID assay involves the following elements (Fig. 5A):

i. A number of wells are dedicated to controls and calibration, such as:
   1. *buffer only* (background level = F_b; tested in 10 mM lithium cacodylate + 100 mM KCl),

Table 1
Selected oligonucleotides used in the G4-FID assay.

Name		Sequence (from 5′ to 3′)	T_m[a]	Maxima CD	TO FI(2:1)[b]
VEGF	Promoter	$G_3AG_3TTG_4TG_3$	>70	(+) 260 nm	5×10^3
VAV1	Promoter	$G_3CAG_3AG_3AACTG_3$	51	(+) 260 nm	3×10^3
C-Kit2	Promoter	$G_3CG_3CGCGAG_3AGG_3$	>70	(+) 260 nm	3×10^3
Asc20	*Ascaris* telomere	$G_2CTTAG_2CTTAG_2CTTAG_2$	37	(+) 290 nm	50×10^3
				(+) 245 nm	
21CTA	Telomere	$G_3CTAG_3CTAG_3CTAG_3$	67	(+) 290 nm	7×10^3
				(+) 245 nm	
C-Kit1	Promoter	$G_3AG_3CGCTG_3AGGAG_3$	57.5	(+) 260 nm	8×10^3
22Ag	Human DNA-telomere	$AG_3TTAG_3TTAG_3TTAG_3$	66	(+) 290 nm	13×10^3
22AgR	Human RNA-telomere	$AG_3UUAG_3UUAG_3UUAG_3$	>70	(+) 260 nm	10×10^3
C-Myc	Promoter	$TGAG_3TG_3TAG_3TG_3TAA$	>70	(+) 260 nm	6×10^3
AKT1	Promoter	$G_3CG_3CGGCTCCG_3CGCG_3$	62	(+) 290 nm	9×10^3
TG5T	DNA-G4 tetramolecular	TG_5T	>90	(+) 260 nm	4.5×10^3
PlasC24	*Plasmodium* telomere	$G_3TTCAG_3TTCAG_3TTCAG_3$	64	(+) 290 nm	20×10^3
Ceb25	Minisatellites	$AG_3TG_3TGTAAGTGTG_3TG_3T$	>70	(+) 260 nm	4.5×10^3
27KRas	Promoter	$G_3CGGTGTG_3AAGA\ G_3AAGAGG_3$	52	(+) 260 nm	8.5×10^3
Insuline a2	Promoter	$ACAG_4TGTG_4ACAG_4TGTG_4$	>70	(+) 260 nm	8×10^3
Oxy3.5	*Oxytricha* telomere	$G_4TTTTG_4TTTTG_4TTTTG_4$	>70	(+) 290 nm	19×10^3
32B3 (K-Ras)	Promoter	$AG_3CGGTGTG_3AAGAG_3AAGAG_5AGG$	60	(+) 260 nm	25×10^3
35B1 (K-Ras)	Promoter	$AG_3CGGTGTG_3AAGAG_3AAGAG_5AGGCAG$	54	(+) 260 nm	19×10^3
45Ag	Human DNA-telomere	$G_3TTAG_3TTAG_3TTAG_3TTAG_3TTAG_3TTAG_3$	59	(+) 290 nm	14×10^3
CGG12	Trinucleotide	$(CGG)_{12}$	no G4	no G4	9×10^3
dx12	Duplex	(a)GCGTGAGTTCGG(b)CCGAACTCACGC	ND[c]	ND[c]	18×10^3
ds26	Duplex	CAATCGGATCGAATTCGATCCGATTG	ND[c]	ND[c]	34×10^3

[a] T_m (in °C) determined by UV melting experiments using absorbance at 295 nm, in 100 mM KCl with 10 mM lithium cacodylate.
[b] Fluorescence of TO with 1 oligo for 2 TO.
[c] T_m no determined.

Fig. 5. G4-FID assay and the percentage displacement of TO. (**A**) Representation of a 96-well plate and disposition of wells. (**B**) Percentage displacement of TO for 360A.

2. *buffer + TO* should exhibit very low fluorescence, close to F_b, as no DNA is present and emission of free TO is very weak.
3. *buffer + ligand* should also exhibit very low fluorescence, close to F_b, except if the ligand is naturally fluorescent.
4. *buffer + TO + ligand* should also be close to F_b, except if the ligand interacts with TO.

ii. The truly informative wells correspond to samples containing nucleic acids. Pre-folded DNA target (0.5 μM of strand concentration for intramolecular G4, 2 μM of strand concentration for tetramolecular G4 and 1 μM of strand concentration for duplexes) is mixed with 1 μM of Thiazole Orange. The fluorescence of TO bound to DNA is called FI_0.

iii. Five equivalents of each ligand (2.5 μM) were added for each oligonucleotide. The fluorescence of TO after adding ligand is called FI.

The initial fluorescence (FI and FI_0) is subtracted by the background fluorescence ($FA = FI - F_b$ or $FA_0 = FI_0 - F_b$). We can then calculate the percentage of TO displacement by the formula as previously described:

$$\text{TO Displacement } (\%) = 100 - ((FA/FA_0) \times 100)$$

We can see that 360A strongly binds to G-quadruplex structures (Fig. 5B), all the TO displacement percentages for G4 structures being superior or equal to 40. However, it does not bind to duplex-forming sequences as the TO displacement in those cases is close to 0. Consequently, the compound 360A can be considered as a potent and selective G-quadruplex binder, which is in full agreement with both FRET-melting and standard G4-FID results [23].

The use of 5 equivalents of ligands allows to screen the displacement of most compounds, including weakly binding compounds but,
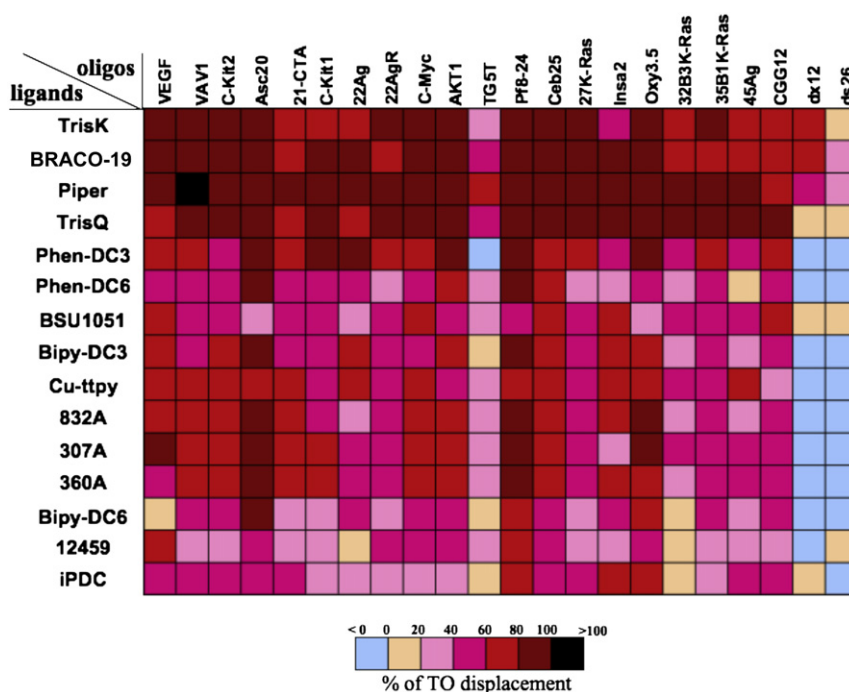
Fig. 6. Screening results are shown for the set of 22 oligonucleotides (20 quadruplexes + two duplexes on the rightmost columns) and all selected ligands. The colour chart representation is used to allow for visual comparison of the percentage of TO displacement obtained with different test molecules (colour code indicated below). (For interpretation of the references to colour in this figure legend, the reader is referred to the web version of this article.)

as a drawback, does not allow to sort finely potent binders. Thus, the best compounds should be re-assayed at a lower concentration. Also, the use of a higher TO/oligonucleotide ratio as compared to the standard G4-FID assay (0.5 vs 0.25 μM in DNA) enables to use less sensitive fluorescence reader. Nevertheless, care should be taken not to use too high concentrations of TO since it could result in non-specific binding of the probe (by electrostatic interactions notably, unpublished results).

3.3. G4-FID screening results

The results are presented in Fig. 6 with blue indicating a "negative percentage" of TO displacement and hot colours, from light to dark, standing for 0–100% of TO displacement. The colour chart mode of presentation allows a direct and easy visual comparison of the results.

First of all, we verified that results obtained herein are in accordance with previously published results obtained by standard G4-FID assay and FRET-melting experiments. Well-known potent G4-DNA binders (Phen-DC compounds, BRACO-19, PIPER, etc.) were found to be very effective on most G4-DNA structures. Conversely, iPDC, which features an inverted connectivity of the two amide bondings as compared to 360A, exhibited the weakest TO displacement in comparison with most of the other tested compounds and remarkably as compared with 360A. This is fully consistent with results obtained both with the standard G4-FID assay (unpublished data) and by FRET-melting experiments [37].

Selective and non-selective compounds can also be easily distinguished. The four compounds TrisK, BRACO-19, Piper and TrisQ tend to bind quite well to duplex structures (although one should note that the fluorescence of BRACO-19 may interfere with the assay). Interestingly, we found that TrisQ is slightly more selective than TrisK3-NH as recently published [25]. As previously outlined, the use of 5 equivalents of ligands vs DNA may be detrimental for sorting highly potent binders and the use of a lower amount of compound may allow to better measure selectivity in this specific case. In that situation, it is thus recommended to re-assay the best compounds at a lower concentration, or to perform standard G4-FID assay to generate a displacement curve over a range of ligand concentration. The other compounds exhibit good to very good selectivity for G-quadruplex structures in comparison with the duplex structure.

Overall, we observed a weak affinity of compounds for TG_5T, which is not surprising since tetramolecular quadruplexes can accommodate more TO molecules than intramolecular structures [23]. Conversely, high TO-displacements were found for Ascaris 20, Plasmodium 24 and Oxytricha 3.5 which may be explained either by a weaker affinity of TO for those DNA matrices (and thus an easier displacement) or a higher affinity of the compounds for these structures.

Disappointingly, we were unable to identify any compound capable of discriminating one conformation of G-quadruplex in particular. However, these results were expected since, to the best of our knowledge, no compound able to selectively target one particular quadruplex structure has ever been reported.

4. Discussion and conclusion

The method presented here allows the screening of an important number of unmodified nucleic acids structures with widespread equipment i.e., a qPCR device. Nevertheless, the use of a moderately sensitive fluorescence reader does not allow to use all the 32 DNA structures of the initial panel since some of them lead to a weak increase in TO emission, which prevents an accurate determination of the displacement efficiency. The lower fluorescent enhancement

of the probe observed in certain cases may be the result of a non-planar conformation of TO upon interaction (especially with single-strands) and/or of a non sufficient isolation from the aqueous environment. Thus, out of the 30 sequences tested, we had to discard 8 motifs – including all single-strands – and we finally kept 22 sequences (20 quadruplexes and 2 duplexes). Also, the working concentration ratio in TO/oligonucleotide should be higher (>2) than in the standard G4-FID assay to circumvent the detection limits of the apparatus.

Additionally, we found that the screening results presented in Fig. 6 illustrate a general property of reported G4 binders: most of them do discriminate between duplexes and quadruplexes (the two rightmost columns exhibit a low competition level); on the other hand, none of the tested ligands have a clear selectivity for one quadruplex over the others as they efficiently displace TO from most of the G4 structures. A relative exception may be found for TG_5T: TO is notably harder to displace from this structure than from other quadruplexes. The absence of loops and therefore of potential additional hydrogen bonds or van der Waals interactions may explain these results. Also, flanking thymine nucleotides could render the external G-quartets accessibility more difficult than expected. In the same line, the remarkably low fluorescence of TO bound to this tetramolecular matrix might indicate a binding mode different from the classical stacking on G-quartets. For instance groove binding of the probe can be hypothesized thereby resulting in indirect competition with the ligands.

The total number of structures tested for each ligand, including oncogenes sequences, dimers and RNA, is within the same order as competition dialysis [38] and the duplex–quadruplex test we recently developed [39], and superior to what is commonly performed with FRET-melting [15] or surface plasmon resonance [40,41]. Moreover, virtually any sequence can be used provided that TO fluorescence enhancement is sufficient. Furthermore, this test is simple to implement, as it involves unmodified DNA/RNA sequences and an inexpensive dye, Thiazole Orange. Finally, widespread qPCR apparatus may be used to perform these measurements.

This test nevertheless has some limitations: i) compounds that are naturally fluorescent with excitation and emission maxima overlapping TO may interfere with the measurements. This is why it is necessary to evaluate prior to screening TO and compounds to be tested in absence of DNA, and compound + DNA with TO. Alternative fluorescent dyes are currently developed to circumvent this problem [43] ii) TO does not equally bind to all structures (different Kd) and has different quantum yields when bound (see above) iii) One cannot formally exclude that simultaneous binding of a compound and of TO is not formally exclusive: if a ternary complex is formed, then the test will underestimate the affinity of the dye to the structure as no decrease in TO fluorescence will be obtained despite binding. However, from the results shown in Fig. 6 and our unpublished results, this seems to be a relatively rare case. Even if TO and the tested compound have different binding modes, the quadruplex structure is a relatively small object, and simultaneous binding appears disfavoured iv) the "<0%" or ">100%" displacement values found for certain targets cannot easily be explained. One may propose a direct interaction between the dye and TO leading to total quenching (for >100%) or that the rigidification/conformational change of a nucleic acid structure induced by a ligand may alter TO properties.

To obtain an independent validation of this method, we performed binding studies by spectroscopic titrations with one of the compounds tested here. Such experiments are indeed possible for ligands that undergo a significant change of absorbance or fluorescence upon binding to nucleic acids. For sensitivity purposes, we performed such titrations using the fluorescence signal of a pyridine dicarboxamide derivative, 360A. Its weak emission is almost

completely quenched upon binding to DNA. This allowed us to compare fluorescence intensity as a function of DNA concentration. This titration is presented as Supplementary Fig. S3. These experiments qualitatively confirm the results obtained by FID: such G4 ligand has a much weaker affinity for duplexes than for quadruplexes. Unpublished surface plasmon resonance data on other G4 ligands also confirmed that ligands that easily displace TO from quadruplex structures exhibit a high affinity (Kd in the nM range) for this conformation (data not shown).

To conclude, we have determined user-friendly experimental conditions in which a large number of DNA/RNA sequences, displaying various well-characterized structures (intra/tetramolecular quadruplexes, dimeric quadruplexes and duplexes), can be used in G4-FID screenings, employing widespread materials. The set of structures presented here is obviously biased towards G4 structures, but can be easily modified to accommodate other structures such triplexes, Z-DNA, i-motifs, trinucleotide repeats…provided that TO be sufficiently fluorescent when bound to these motifs [42]. Additional work enabling to perform full TO displacement titration curves in microplates in the standard assay conditions [43], as well as an example of screening of a chemical library will be presented elsewhere.

Acknowledgements

Appendix. Supplementary material

Supplementary material associated with this article can be found, in the online version, at doi:10.1016/j.biochi.2011.05.011.

References

[1] S. Neidle, S. Balasubramanian, Quadruplex Nucleic Acids. RSC Biomolecular Sciences, Cambridge, 2006, pp. 301.

[2] D. Sen, W. Gilbert, Formation of parallel four-stranded complexes by guanine-rich motifs in DNA and its applications for meiosis, Nature 334 (1988) 364−366.

[3] D.J. Patel, A.T. Phan, V. Kuryavyi, Human telomere, oncogenic promoter and 5′-UTR G-quadruplexes: diverse higher order DNA and RNA targets for cancer therapeutics, Nucleic Acids Res. 35 (2007) 7429−7455.

[4] Y. Qin, L.H. Hurley, Structures, folding patterns, and functions of intramolecular DNA G-quadruplexes found in eukaryotic promoter regions, Biochimie 90 (2008) 1149−1171.

[5] B.S. Herbert, J.L. Huppert, F.B. Johnson, A.N. Lane, A.T. Phan, Meeting report: second international meeting on quadruplex DNA, Biochimie 91 (2009) 1059−1065.

[6] A.T. Phan, Human telomeric G-quadruplex: structures of DNA and RNA sequences, FEBS J. 277 (2010) 1107−1117.

[7] D. Sun, B. Thompson, B.E. Cathers, M. Salazar, S.M. Kerwin, J.O. Trent, T.C. Jenkins, S. Neidle, L.H. Hurley, Inhibition of human telomerase by a G-quadruplex-interactive compound, J. Med. Chem. 40 (1997) 2113−2116.

[8] T.A. Brooks, S. Kendrick, L. Hurley, Making sense of G-quadruplex and i-motif functions in oncogene promoters, FEBS J. 277 (2010) 3459−3469.

[9] J.L. Huppert, Structure, location and interactions of G-quadruplexes, FEBS J. 277 (2010) 3452−3458.

[10] H.J. Lipps, D. Rhodes, G-quadruplex structures: in vivo evidence and function, Trends Cell Biol. 19 (2009) 414−422.

[11] P. Wang, C.-H. Leung, D.-L. Ma, S.-C. Yan, C.-M. Che, Structure-based design of platinum(II) complexes as c-myc oncogene down-regulators and luminescent probes for G-quadruplex DNA, Chem. Eur. J. 16 (2010) 6900−6911.

[12] Z.A.E. Waller, S.A. Sewitz, S.-T.D. Hsu, S. Balasubramanian, A small molecule that disrupts G-quadruplex DNA structure and enhances gene expression, J. Am. Chem. Soc. (2009).

[13] D. Monchaud, M.P. Teulade-Fichou, A hitchhiker's guide to G-quadruplex ligands, Org. Biomol. Chem. 6 (2008) 627−636.

[14] A. De Cian, J.L. Mergny, Quadruplex ligands may act as molecular chaperones for tetramolecular quadruplex formation, Nucleic Acids Res. 35 (2007) 2483−2493.

[15] A. De Cian, L. Guittat, M. Kaiser, B. Saccà, S. Amrane, A. Bourdoncle, P. Alberti, M.P. Teulade-Fichou, L. Lacroix, J.L. Mergny, Fluorescence-based melting assays for studying quadruplex ligands, Methods 42 (2007) 183−195.

[16] E.W. White, F. Tanious, M.A. Ismail, A.P. Reszka, S. Neidle, D.W. Boykin, W.D. Wilson, Structure-specific recognition of quadruplex DNA by organic cations: influence of shape, substituents and charge, Biophys. Chem. 126 (2007) 140−153.

[17] B. Pagano, C.A. Mattia, C. Giancola, Applications of isothermal titration calorimetry in biophysical studies of G-quadruplexes, Int. J. Mol. Sci. 10 (2009) 2935−2957.

[18] F. Rosu, E. De Pauw, V. Gabelica, Electrospray mass spectrometry to study drug−nucleic acids interactions, Biochimie 90 (2008) 1074−1087.

[19] S. Paramasivan, P.H. Bolton, Mix and measure fluorescence screening for selective quadruplex binders, Nucleic Acids Res. 36 (2008) e106.

[20] P. Ragazzon, J.B. Chaires, Use of competition dialysis in the discovery of G-quadruplex selective ligands, Methods 43 (2007) 313−323.

[21] D. Monchaud, C. Allain, M.-P. Teulade-Fichou, Development of a fluorescent intercalator displacement assay (G4-FID) for establishing quadruplex-DNA affinity and selectivity of putative ligands, Bioorg. Med. Chem. Lett. 16 (2006) 4842−4845.

[22] D. Monchaud, C. Allain, M.P. Teulade-Fichou, Thiazole orange: a useful probe for fluorescence sensing of G-quadruplex-ligand interactions, Nucleosides, Nucleotides Nucleic Acids 26 (2007) 1585−1588.

[23] D. Monchaud, C. Allain, H. Bertrand, N. Smargiasso, F. Rosu, V. Gabelica, A. De Cian, J.L. Mergny, M.P. Teulade-Fichou, Ligands playing musical chairs with G-quadruplex DNA: a rapid and simple displacement assay for identifying selective G-quadruplex binders, Biochimie 90 (2008) 1207−1223.

[24] D. Monchaud, M.-P. Teulade-Fichou, G4-FID: a fluorescent DNA probe displacement assay for rapid evaluation of quadruplex ligands. in: P. Baumann (Ed.), G-quadruplex DNA. Springer, Kansas City, 2010, pp. 257−271.

[25] H. Bertrand, A. Granzhan, D. Monchaud, N. Saettel, R. Guillot, S. Clifford, A. Guédin, J.-L. Mergny, M.-P. Teulade-Fichou, Recognition of G-quadruplex DNA by triangular star-shaped compounds: with or without side chains? Chem. Eur. J. 17 (2011) 4529−4539.

[26] A. Hittinger, T. Caulfied, P. Mailliet, H. Bouchard, E. Mandine, J.-L. Mergny, L. Guittat, J.-F. Riou, D. Gomez, C. Belmokhtar, Chemical Derivatives Binding Very Specifically with G-quadruplex DNA Structures and Use Thereof as a Specific Anti-cancer Agent. (2004), Patent WO2004072027.

[27] A. De Cian, E. DeLemos, J.-L. Mergny, M.-P. Teulade-Fichou, D. Monchaud, Highly efficient G-quadruplex recognition by bisquinolinium compounds, J. Am. Chem. Soc. 129 (2007) 1856−1857.

[28] H. Bertrand, D. Monchaud, A.D. Cian, R. Guillot, J.-L. Mergny, M.-P. Teulade-Fichou, The importance of metal geometry in the recognition of G-quadruplex-DNA by metal-terpyridine complexes, Org. Biomol. Chem. 5 (2007) 2555−2559.

[29] M. Read, R.J. Harrison, B. Romagnoli, F.A. Tanious, S.H. Gowan, A.P. Reszka, W.D. Wilson, L.R. Kelland, S. Neidle, Structure-based design of selective and potent G quadruplex-mediated telomerase inhibitors, Proc. Natl. Acad. Sci. U. S. A. 98 (2001) 4844−4849.

[30] J.F. Riou, L. Guittat, P. Mailliet, A. Laoui, E. Renou, O. Petitgenet, F. Mégnin-Chanet, C. Hélène, J.L. Mergny, Cell senescence and telomere shortening induced by a new series of specific G-quadruplex ligands, Proc. Natl. Acad. Sci. U. S. A. 99 (2002) 2672−2677.

[31] O.Y. Fedoroff, M. Salazar, H. Han, V.V. Chemeris, S.M. Kerwin, L.H. Hurley, NMR-based model of a telomerase-inhibiting compound bound to G-quadruplex DNA, Biochemistry 37 (1998) 12367−12374.

[32] J.L. Mergny, J. Li, L. Lacroix, S. Amrane, J.B. Chaires, Thermal difference spectra: a specific signature for nucleic acid structures, Nucleic Acids Res. 33 (2005) e138.

[33] K.W. Lim, P. Alberti, A. Guédin, L. Lacroix, J.F. Riou, N. Royle, J.L. Mergny, A.T. Phan, Sequence variant (CTAGGG)n in the human telomere favors a G-quadruplex structure containing a G•C•G•C tetrad, Nucleic Acids Res. 37 (2009) 6239−6248.

[34] J.L. Mergny, A.T. Phan, L. Lacroix, Following G-quartet formation by UV-spectroscopy, FEBS Lett. 435 (1998) 74−78.

[35] J.L. Mergny, L. Lacroix, UV melting of G-quadruplexes, Curr. Protoc. Nucleic Acid Chem. 17 (2009) 17.11.11-17.11.15.

[36] J.L. Mergny, A. De Cian, A. Ghelab, B. Saccà, L. Lacroix, Kinetics of tetramolecular quadruplexes, Nucleic Acids Res. 33 (2005) 81−94.

[37] C. Granotier, G. Pennarun, L. Riou, F. Hoffschir, L.R. Gauthier, A. De Cian, D. Gomez, E. Mandine, J.F. Riou, J.L. Mergny, P. Mailliet, B. Dutrillaux, F.D. Boussin, Preferential binding of a G-quadruplex ligand to human chromosome ends, Nucleic Acids Res. 33 (2005) 4182−4190.

[38] J.S. Ren, J.B. Chaires, Rapid screening of structurally selective ligand binding to nucleic acids. in: J.B. Chaires, M.J. Waring (Eds.), Drug Nucleic Acid Interaction.

Academic Press Inc, 525 B Street, Suite 1900, San Diego, CA 92101-4495, USA, 2001, pp. 99−108.

[39] L. Lacroix, A. Séosse, J.L. Mergny, Fluorescence-based duplex−quadruplex competition test to screen for telomerase RNA quadruplex ligands, Nucleic Acids Res. 39 (2011) e21.

[40] C. Carrasco, F. Rosu, V. Gabelica, C. Houssier, E. De Pauw, C. Garbay-Jaureguiberry, B. Roques, W.D. Wilson, J.B. Chaires, M.J. Waring, C. Bailly, Tight binding of the antitumor drug ditercalinium to quadruplex DNA, Chembiochem 3 (2002) 1235−1241.

[41] M.P. Teulade-Fichou, C. Carrasco, L. Guittat, C. Bailly, P. Alberti, J.L. Mergny, A. David, J.M. Lehn, W.D. Wilson, Selective recognition of G-quadruplex telomeric DNA by a bis(quinacridine) macrocycle, J. Am. Chem. Soc. 125 (2003) 4732−4740.

[42] D.P. Arya, New approaches toward recognition of nucleic acid triple helices, Account. Chem. Res. 44 (2011) 134−146.

[43] E. Largy, F. Hamon, M.-P. Teulade-Fichou, Development of a high-throughput G4-FID assay for screening and evaluation of small molecules binding quadruplex nucleic acid structures, Anal. Bioanal. Chem. (2011), doi:10.1007/s00216-00011-05018-z.

CrossMark
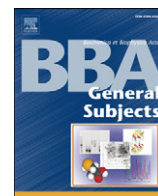
Phenanthroline-bis-oxazole ligands for binding and stabilization of G-quadruplexes☆

João Medeiros-Silva [a,b], Aurore Guédin [c,d], Gilmar F. Salgado [c,d], Jean-Louis Mergny [c,d], João A. Queiroz [a], Eurico J. Cabrita [b], Carla Cruz [a,*]

[a] CICS-UBI - Centro de Investigação em Ciências da Saúde, Universidade da Beira Interior, Av. Infante D. Henrique, 6200-506 Covilhã, Portugal
[b] UCIBIO, REQUIMTE, Departamento de Química, Faculdade de Ciências e Tecnologia, Universidade Nova de Lisboa, 2829-516 Caparica, Portugal
[c] INSERM, U1212, CNRS, UMR 5320, IECB, F-33600 Pessac, France
[d] Univ. Bordeaux, ARNA laboratory, F-33000 Bordeaux, France

ARTICLE INFO

ABSTRACT

Background: G-quadruplexes (G4) are found at important genome regions such as telomere ends and oncogene promoters. One prominent strategy to explore the therapeutic potential of G4 is stabilized it with specific ligands.
Methods: We report the synthesis of new phenanthroline, phenyl and quinoline acyclic bisoxazole compounds in order to explore and evaluate the targeting to c-myc and human telomeric repeat 22AG G4 using FRET-melting, CD-melting, NMR, fluorescence titrations and FID assays.
Results: The design strategy has led to potent compounds (Phen-1 and Phen-2) that discriminate different G4 structures (human telomeric sequences and c-myc promoter) and selectively stabilize G4 over duplex DNA. CD studies show that Phen-2 binds and induces antiparallel topologies in 22AG quadruplex and also binds c-myc promotor, increasing their T_m in about 12 °C and 30 °C respectively. In contrast, Phen-1 induces parallel topologies in 22AG and c-myc, with a moderate stabilization of 4 °C for both sequences. Consistent with a CD melting study, Phen-2 binds strongly ($K = 10^6$ to 10^7 M^{-1}) to c-myc and 22AG quadruplexes.
Conclusions: Phen-1 and Phen-2 discriminated among various quadruplex topologies and exhibited high selectivity for quadruplexes over duplexes. Phen-2 retains antiparallel topologies for quadruplex 22AG and does not induce conformational changes on the parallel c-myc quadruplex although Phen-1 favors the parallel topology. NMR studies also showed that the Phen-2 binds to the c-myc quadruplex via end stacking.
General significance: Overall, the results suggest the importance of Phen-2 as a scaffold for the fine-tuning with substituents in order to enhance binding and stabilization to G4 structures. This article is part of a Special Issue entitled "G-quadruplex" Guest Editor: Dr. Concetta Giancola and Dr. Daniela Montesarchio.

1. Introduction

Structurally, nucleic acids are very versatile molecules and as a consequence DNA may adopt different conformations [1,2]. Particularly relevant are guanine-rich single-stranded DNA stretches that exhibit a propensity to spontaneously dissociate from their complementary strands and fold into various G-quadruplex (G4) structures in which guanine bases associate into plain hydrogen bonded arrangements termed G-quartets, which are further stabilized by cations such as Na$^+$ and K$^+$ [1–5].

The particular interest in G4 relies on the fact that G4 forming sequences are widely distributed in functional regions of the human genome, such as telomeres, ribosomal DNA (rDNA), transcription start sites, promoter regions (*c-myc*, *c-kit*, *KRas* and *HIF-1α*) and untranslated regions of mRNA, suggesting that G-quadruplex structures may play an important role in the control of a variety of cellular processes. Due to this fact G4 are viewed as valid therapeutic targets in human cancer diseases [6,7].

Promoting the G4 motif in these sequences may induce telomere uncapping and/or stop telomere elongation by inhibiting telomerase, ultimately leading to cellular apoptosis [8–10]. In addition, the G4 motif could block the binding of transcriptions factors and RNA-polymerase, consequently repressing the expression of key oncogenes [11, 12]. Apart from the telomere ends, G-quadruplex formation requires local unfolding of the double-helix. This process, which may be kinetically and/or thermodynamically disfavoured depending on sequence, supercoiling, crowding conditions and other factors, can be modulated by the presence of G-quadruplex ligands.

Small molecules are being exploited to specifically target G4 and have proven to be a new class of anticancer agents [13,14]. Indeed,

heterocycles are an important source of G-quadruplex ligands and have significant bioactivities in anticancer therapy [15,16]. The demand of G4 binders that combine specificity, affinity, biocompatibility and drug-like properties is a current challenge.

Notably, phenanthroline-derived compounds have been investigated for the targeting of a specific G4 conformation. Phenanthroline provides a basic aromatic system for π-π stacking interactions that can fit the G-tetrad, as demonstrated in recent studies with Phen-DC$_3$ and other similars [17–19], which enhanced G4 thermal stability and selectivity for G4 over duplexes [19–33]. Non-charged compounds and oxazole-derived compounds have also revealed potential to bind and stabilize G4 [34–36] while displaying biocompatibility such as the natural compound telomestatin [37], L$_2$H$_2$-6OTD [38] and TOxaPy [39].

In this context we report the synthesis of new phenanthroline derivatives (Phen) combined with bisoxazole (PhenBisOx) groups (Fig. 1) and characterization of their interactions with G4. Different aromatic scaffolds such as phenyl (Iso and Ter) and quinoline (Quin) derivatives were also investigated in order to explore and compare the efficiency of the PhenBisOx scaffold to target G4 structures. Several biophysical techniques were employed to study the interaction of ligands with G4 sequences, such as fluorescence intercalator displacement (FID) assay, Circular Dichroism (CD) and fluorescence titrations, CD melting and FRET-melting.

2. Materials and methods

All solvents were purchased from Fluka and employed without further purification.

All reactions were monitored by thin-layer chromatography on 0.2 mm E. Merck silica gel plates (60F-254) and monitored with UV light at 224 nm and 334 nm. Compounds were purified with a 50 cm chromatography column stacked with 60–200 μm silica gel.

^{1}H and ^{13}C NMR spectra were acquired in a 400 MHz spectrometer with a TXI probe. The pulse programs applied were based on the corresponding templates provided by Bruker. Isotope labeled solvents were purchased from Cambridge Isotopes. Compound spectra are presented in Figs. S9–S18 of Supporting Information.

Mass spectrometry (ES-MS) were performed by the microanalysis service on a QSTAR XL instrument.

Fluorescence spectra were acquired with a Perkin Elmer Precisely Luminescence Spectrometer, model LS 45, and the UV–Vis spectral data with a Thermo Scientific Evolution 201/220 UV–Vis, at 25 °C.

High-throughput G4-FID assay was performed in a Bio-Rad CFX RT-PCR fluorimeter. Thiazole Orange was calibrated as indicated by the manufacturer.

2.1. Ligand synthesis

General procedure for allylic reduction with selenium dioxide. Selenium dioxide (CAS# 7446-08-4, Acros Organics) were dissolved in 100 mL of dioxane. In order to aid its dissolution, a minimum amount of water (about 400 μL) was added. Substrate reagents were dissolved in 60 mL of dioxane and added drop-wise to the refluxed solution. The reaction was carried out for 6 h. The selenium by-products were removed by filtration in hot conditions and the filtrate's solvent was evaporated in a vacuum assisted system. The residue was resuspended in CHCl$_3$ and any insoluble particles were filtered off. Chloroform was evaporated to afford the product.

Note: Fresh batches of selenium dioxide were employed, otherwise the selenium should be purified by sublimation.

2.1.1. 1,10-phenantroline-2,9-dicarbaldehyde (Phen-0)

4 g of SeO$_2$ (4.0 eq) and 2 g of neocuproine were applied in the reaction. Phen-0 was obtained as a white solid, with an approximate 60% yield. ^{1}H-NMR: (25 °C, 400 MHz, CDCl$_3$) δ = {10.49 (s,2H); 8.44 (d,2H), ^{3}J = 8.6 Hz; 8.31 (d,2H), ^{3}J = 8.6 Hz; 7.98 (s,2H)}; ^{13}C-NMR: (25 °C, 100 MHz, CDCl$_3$) δ = {192.32, 2CH; 151.65, 2C; 144.91, 2C; 136.91, 2CH; 130.60, 2C; 128.02, 2CH}.

2.1.2. 6-methylquinoline-2-carbaldehyde (Quin-0)

5.9 g of SeO$_2$ (4.0 eq) and 2 g of 2,6-dimethylquinoline were applied in the reaction. Quin-0 was obtained as a brown solid, with an approximate 87% yield. ^{1}H-NMR: (25 °C, 400 MHz, CDCl$_3$) δ = {9.13 (s,1H); 8.12 (d,1H), ^{3}J = 8.62 Hz; 8.05 (d,1H), ^{3}J = 8.62 Hz; 7.92 (s,1H); 7.89 (d,1H), ^{3}J = 8.62 Hz; 7.58 (m,2H); 2.5 (s,9H)}; ^{13}C–NMR: (25 °C, 100 MHz, CDCl$_3$) δ = {192.50, 1CH; 150.91, 1C; 145.46, 1C; 138.72, 1C; 135.51, 1CH; 131.88, 1CH; 129.11, 1C; 128.93, 1CH; 125.70, 1CH; 116.23, 1CH; 20.85, 1CH$_3$}.

2.1.3. General procedure for oxazole formation through van Leusen reaction

In a 100 mL round-bottomed flask, potassium carbonate (CAS# 584-08-7, anhydrous, Chem Lab) and p-(tolylsulfonyl)methylisocyanide (TosMIC, CAS# 366635-61-7, Acros Organics) were suspended in 80 mL of methanol and stirred for 20 min at room temperature. Aldehyde reactants were stirred in 15 mL of methanol and added drop-
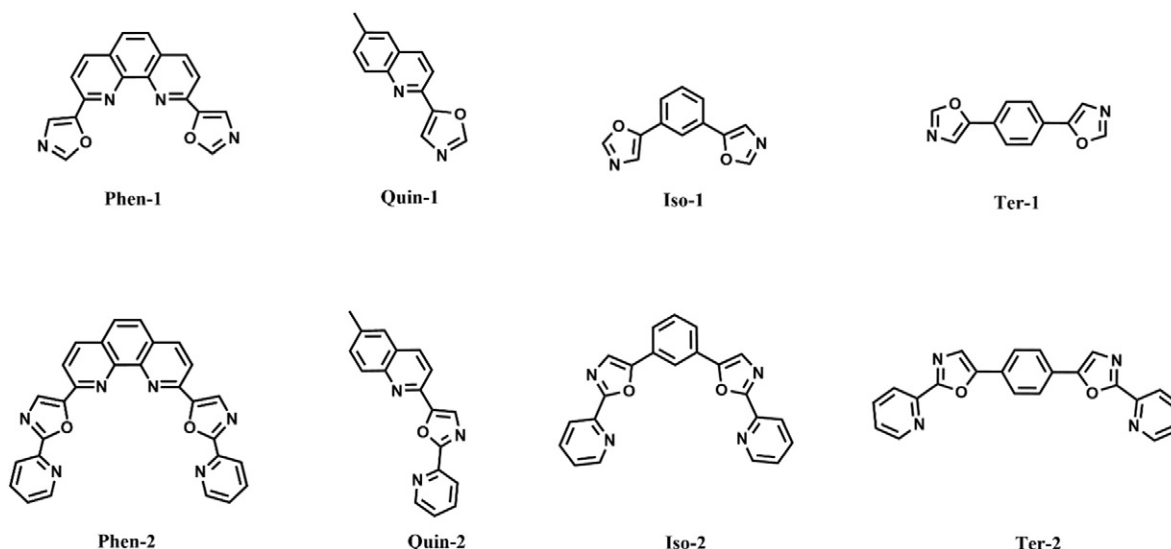

Fig. 1. Chemical structures of the ligands used in the study.

wise to the solution in the flask. The solution was stirred for 3 h at approximately 20 °C and other 4 h at the reflux temperature, by this necessary order. A change of color should occur upon heating. The solvent was evaporated assisted by a low pressure system to obtain a solid residue.

2.1.4. 2,9-bis(oxazole-5-yl)-1,10-phenantroline (Phen-1)

2.43 g of K_2CO_3 (4 eq), 1.64 g of TosMIC (2 eq) and 1.0 g of Phen-0 were applied in the reaction. The compound was purified by washing the residue with water and methanol. The compound was extracted with boiling dioxane and the non-soluble impurities were removed by filtration. Dioxane was then evaporated affording Phen-1 as an orange solid (50%). ^{1}H-NMR: (25 °C, 400 MHz, DMSO-d_6) δ = {8.46 (s,2H); 8.40 (d,2H), [3]J = 8.25 Hz; 7.97 (d,2H), [3]J = 8.25 Hz, 7.97 (s,2H); 7.80 (s,2H)}; ^{13}C-NMR: (25 °C, 100 MHz, DMSO-d_6) δ = {153.77, 2CH; 151.22, 2C; 146.70, 2C; 145.50, 2C; 138.24, 2CH; 128.78, 2C; 128.78, 2CH; 127.23, 2CH; 120.04, 2CH}. ESI-MS m/z: 315.09 [M + H]$^+$.

2.1.5. 1,3-bis(oxazol-5-yl)benzene (Iso-1)

4.12 g of K_2CO_3 (4 eq), 2.9 g of TosMIC and 1 g of isophtaldehyde (Acros Organics) were applied in the reaction. The compound was purified by a 5 × 30 mL extraction with diethyl ether. Organic phases were filtered, combined and evaporated in vacuum. The obtained residue was washed with a minimum amount of methanol and Iso-1 was collected by filtration as a pale-yellow pure solid (65%).^{1}H-NMR: (25 °C, 400 MHz, CDCl$_3$) δ = {8.09 (s,2H); 7.96 (s,1H); 7.65 (d,2H), [3]J = 7.69 Hz; 7.52 (t, 1H), [3]J = 7.71 Hz; 7.45 (s, 2H)}; ^{13}C-NMR: (25 °C, 100 MHz, CDCl$_3$) = {150.95, 2C; 150.86, 2CH; 129.66, 1CH; 127.36, 2C; 124.55, 2CH; 121.87, 1CH; 120.15, 1CH}. ESI-MS m/z: 213.07 [M + H]$^+$.

2.1.6. 1,4-bis(oxazol-5-yl)benzene (Ter-1)

4.12 g of K_2CO_3 (4 eq), 2.90 g of TosMIC and 1.0 g of terephtaldehyde (Acros Organics) were applied in the reaction. The compound was purified by a 5 × 30 mL extraction with diethyl ether. Organic phases were filtered, combined and evaporated in vacuum. The obtained residue was washed with a minimum amount of methanol and Ter-1 was collected by filtration as a pale-yellow pure solid (85%).^{1}H-NMR: (25 °C, 400 MHz, CDCl$_3$) δ = {7.86 (s,2H); 7.63 (s,4H); 7.33 (s,2H)}; ^{13}C-NMR: (25 °C, 100 MHz, CDCl$_3$) δ = {149.89, 2C; 149.89, 2CH; 126.75, 2C, 123.84, 4CH; 121.11, 2CH}. ESI-MS m/z: 289.06 [M + Na]$^+$.

2.1.7. 6-methyl-(2-oxazol-5-yl)quinoline (Quin-1)

1.65 g of K_2CO_3 (2 eq), 1.17 g of TosMIC (1 eq) and 1.17 g of Quin-0 were applied in the reaction. The compound was purified by a 5 × 30 mL extraction with diethyl ether. Organic phases were filtered, combined and evaporated in vacuum affording Quin-1 as a dark orange residue (85%).^{1}H-NMR: (25 °C, 400 MHz, CDCl$_3$) δ = {8.56 (d, 1H), [3]J = 8.06 Hz; 7.96 (s, 1H); 7.95 (d, 1H), [3]J = 8.62 Hz; 7.75, (s, 1H); 7.66 (d, 1H), [3]J = 8.62 Hz; 7.49 + 7.48, (m, 2H); 2.45, (s, 3H); 2.45 (s, 9H)}; ^{13}C–NMR: (25 °C, 100 MHz, CDCl$_3$) δ = {151.55, 1CH; 151.35, 1C; 146.59, 1C; 145.93, 1C; 137.10, 1C; 136.46, 1CH; 132.62, 1CH; 129.10, 1CH; 127.58, 1C; 126.57, 1CH; 125.74, 1CH; 117.63, 1CH; 21.63, 3CH$_3$}. ESI-MS m/z: 211.09 [M + H]$^+$.

2.1.8. General procedure for direct cross coupling with heteroaryl halides

Oxazole substrate, tricyclohexylphosphetetrafluoroborate (CAS# 58656-04-5, Acros Organics), copper iodate (CAS# 7681.65.4, Fluka) and palladium(II)-acetate (CAS# 3375-31-3, Acros Organics) were suspended in 5 mL of dioxane in a 50 mL argon flushed round bottomed flask. Cesium carbonate (CAS# 534-17-8, Acros Organics) was added and the mixture was heated, then 1,6-bromopyridine (CAS# 109-04-6, Aldrich) was added and the mixture was refluxed at 125 °C for 24 h in an argon atmosphere. The solvent was evaporated and the black mixture was suspended in a minimum amount of water, followed by 5 × 50 mL extraction with chloroform.

2.1.9. 2,9-bis(2-(pyridine-2-yl)oxazole-5-yl)-1,10-phenantroline (Phen-2)

100 mg of Phen-1, 24.2 mg of PCy$_3$ HBF$_4$ (0.2 eq), 186.2 mg of CuI (3.0 eq), 30 mg of Pd(OAc)$_2$ (0.4 eq), 504.4 mg of Cs$_2$CO$_3$ (4.4 eq) and 121 μL of 1.6-bromopyridine (4 eq) were applied in the reaction. After chloroform extraction, the organic phases were discarded and the blue aqueous phase was filtered. The filter containing the non-soluble residue was collected and boiled at 80 °C in dioxane for a few minutes. While still hot, the solution was once again filtered, the black residue was discarded and the filtrate was evaporated affording a yellow residue. A final extraction with chloroform was applied in order to remove trace impurities affording pure Phen-2 (20%). ^{1}H-NMR: (25 °C, 400 MHz, DMSO-d_6) δ = {8.44 (d,2H), [3]J = 8.50 Hz; 8.85 (d,2H), [3]J = 4.08 Hz; 8.25 (s,2H); 8.13 (d,2H), [3]J = 7.90 Hz; 8.80 (d,2H), [3]J = 8.50 Hz; 8.06 (t,2H), [3]J = 7.73 Hz; 7.89 (s,2H); 7.53 (dd,2H), [3]J = 5.16 Hz, 1.80 Hz)}; ^{13}C-NMR: (25 °C, 100 MHz, DMSO-d_6) δ = {161.10, 2C; 151.45, 2C; 149.90, 2CH; 145.73, 2C; 145.17, 2C; 144.80, 2C; 138.25, 4CH; 130.17, 2CH; 128.66, 2C; 127.35, 2CH; 126.17, 2CH; 123.21, 2CH; 120.60, 2CH}. ESI-MS m/z: 469.14 [M + H]$^+$.

2.1.10. 1,3-bis(2-(pyridine-2-yl)oxazol-5-yl)benzene (Iso-2)

200 mg of Iso-1, 71.6 mg of PCy$_3$ HBF$_4$ (0.2 eq), 407.2 mg of CuI (2.2 eq), 91 mg of Pd(OAc)$_2$ (0.4 eq), 1.47 g of Cs$_2$CO$_3$ (4.4 eq) and 296 μL of 1,6-bromopyridine (3.3 eq) were applied in the reaction. Chloroform was evaporated and the residue was resuspended in ethyl acetate. Insoluble particles were filtered and discarded, and the solvent was evaporated affording a brown oil. Compound was isolated by partition liquid chromatography Et$_2$O/propan-2-ol 90:10 affording Iso-2 as an orange residue (Rf ≈ 0.20, 20% yield). Mono-substituted Iso-1.5 was also isolated as an orange residue (Rf ≈ 0.12, 8% yield). ^{1}H-NMR: (25 °C, 400 MHz, CDCl$_3$) δ = {8.72 (d,2H), [3]J = 4.75 Hz; 8.15 (d,2H), [3]J = 7.84 Hz; 8.10 (s,1H); 7.79 (t,2H), [3]J = 7.61 Hz; 7.72 (d,2H), [3]J = 7.76 Hz; 7.57 (s,2H) [3]J = 7.46 (t,1H) [3]J = 7.71 Hz; 7.33 (dd,2H) [3]J = 5.16 Hz, 0.80 Hz}; ^{13}C-NMR: (25 °C, 100 MHz, CDCl$_3$) δ = {159.26, 2C; 150.84, 2C; 149.06, 2CH; 144.98, 2C; 136.02, 2CH; 128.58, 1CH; 127.44, 2C; 123.96, 2CH; 123.71 + 123.69, 3CH; 121.26, 2CH; 119.58, 2CH}. ESI-MS m/z: 290.09 [M + H]$^+$.

2.1.11. 1,4-bis(2-(pyridine-2-yl)oxazol-5-yl)benzene (Ter-2)

100 mg of Ter-1, 35.4 mg of PCy$_3$ HBF$_4$ (0.2 eq), 202 mg of CuI (2.2 eq), 45 mg of Pd(OAc)$_2$ (0.4 eq), 741 mg of Cs$_2$CO$_3$ (4.4 eq) and 150 μL of 1,6-bromopyridine (3.3 eq) were applied in the reaction. Chloroform was evaporated and the residue was resuspended in ethyl acetate. Insoluble particles were filtered and discarded, and the solvent was evaporated affording a brown oil. The compound was isolated by partition liquid chromatography Et$_2$O/propan-2-ol 90:10 affording Ter-2 as an orange residue (Rf ≈ 0.23, 35% yield). ^{1}H-NMR: (25 °C, 400 MHz, CDCl$_3$) δ = {8.72 (d,2H), [3]J = 4.75 Hz; 8.13 (d,2H), [3]J = 7.33 Hz; 7.80 (s,4H); 7.78 (t,2H), [3]J = 7.54 Hz; 7.52 (s,2H); 7.32 (d,2H), [3]J = 5.56 Hz}; ^{13}C-NMR: (25 °C, 100 MHz, CDCl$_3$) δ = {159.23, 2C; 150.90, 2C; 149.11, 2CH; 144.99, 2C; 135.99, 4CH; 126.73, 2C; 124.06 2CH; 123.67 2CH; 123.52, 2CH; 121.23, 2CH}. ESI-MS m/z: 367.12 [M + H]$^+$.

2.1.12. 1,4-bis(2-(pyridine-2-yl)oxazol-5-yl)benzene (Quin-2)

150 mg of Quin-1, 34.9 mg of PCy$_3$ •HBF$_4$ (0.2 eq), 200 mg of CuI (2.2 eq), 44.6 mg of Pd(OAc)$_2$ (0.4 eq), 746 mg of Cs$_2$CO$_3$ (4.4 eq) and 75 μL of 1,6-bromopyridine (1.5 eq) were applied in the reaction. Chloroform was evaporated and the residue was resuspended in ethyl acetate. Insoluble particles were filtered and discarded, and the solvent was evaporated affording a brown oil. The compound was isolated by partition liquid chromatography Et$_2$O/propan-2-ol 90:10 affording Quin-2 as an orange residue (Rf ≈ 0.25, 45% yield). ^{1}H-NMR: (25 °C, 400 MHz, CDCl$_3$) δ = {8.80 (d,1H), [3]J = 4.05 Hz; 8.22 (d,2H), [3]J = 7.87 Hz; 8.12 (d,1H) [3]J = 8.60 Hz; 8.02 (s,1H); 8.00 (s,1H); 7.92 (d,2H), [3]J = 8.56 Hz; 7.84 (t,1H) [3]J = 6.91 Hz; 7.56 + 7.54, (t + s,2H); 7.39, (dd,1H), [3]J = 5.30, 1.8 Hz; 2.52 (s,9H)}; ^{13}C-NMR:

(25 °C, 100 MHz, CDCl$_3$) δ = {160.83, 1C; 152.34, 1C; 150.11, 1CH; 146.72, 1C; 145.99, 1C; 145.92, 1C; 136.96, 1CH, 163.93, 1C; 136.25, 1CH; 132.48, 1CH; 129.06, 1CH; 127.78, 1CH; 127.64, 1C; 126.53, 1CH; 124.83, 1CH, 122.48, 1CH, 117.84, 1CH, 21.62, 3CH$_3$)}. ESI-MS *m/z*: 288.11 [M + H]$^+$.

2.2. Oligonucleotides

The following oligonucleotides sequences were used in this work: human telomeric DNA sequence 22AG: 5′-AGGGTTAGGGTTAGGGTT AGGG-3′; mutated promoter DNA sequence c-myc: 5′-TGAGGGTGGG TAGGGTGGGTAA-3′ and double-stranded ds26: 5′-CAATCGGATCG AATTCGATCCGATTG-3′. Stock solutions of approximately 0.5 mM strand concentration were prepared with Milli-Q water and were stored at −20 °C. Oligonucleotides were dissolved in 30 mM phosphate buffer; the salt content is specified along the manuscript. Oligonucleotides were purchased from STAB VIDA laboratories.

2.3. G4-FID

Stock solutions of thiazole orange (CAS# 107091-89-4, Aldrich) were prepared in DMSO at a 1 mM concentration, and kept in 4 °C at a maximum period of 3 weeks.

A temperature of 20 °C was constant with thermostated cell holders. Experiments were performed in conventional hard-shell 96-well PCR plate, in 30 mM phosphate buffer pH 7.2 with 50 mM KCl or 100 mM NaCl depending on the experiments, in a total volume of 25 μL. The G4-FID assay is designed as follows: 0.25 mM pre-folded DNA target is mixed with thiazole orange (0.5 mM, 2 molar equiv) and each ligand addition step (from 0.2 to 10 equiv) is followed by a 3-min equilibration period after which the fluorescence spectrum is recorded λ$_{exc}$ = 490 nm, λ$_{emi}$ = 501 nm. The percentage of displacement is calculated by: *TO Displacement* (%) = 100 − ((*FA/FA$_0$*) × 100), where FA$_0$ is the fluorescence area of DNA-TO complex without ligand and FA is the fluorescence area in the presence of the ligand. FID curves were obtained by plotting TO displacement percentage versus concentration of ligand used.

2.4. Fluorescence resonance energy transfer (FRET) melting assay

A Stratagene Mx3005P instrument was used to carry out the FRET melting experiments in 96-well plates as previously described [40]. The fluorescently labelled oligonucleotides used were F21T (5′-FAM-GGGTTAGGGTTAGGGTTAGGG-TAMRA-3′), c-myc (5′-FAM-TTGAGGGTGGGTAGGGTGGGTAA-TAMRA-3′) and FdxT (5′-FAM-TATAGCTATA-hexa ethyleneglycol-TATAGCTATA-TAMRA-3′), where FAM and TAMRA are fluorescein and rhodamine, respectively. The excitation and detection wavelengths were 492 nm and 516 nm, respectively. After an initial incubation at 25 °C for 5 min, the temperature was increased by 1 °C every minute until 95 °C was reached. The experiments were performed with samples containing 0.2 μM oligonucleotide, 10 mM lithium cacodylate (pH 7.2), and indicated concentrations of KCl, NaCl and LiCl (for a total salt concentration of 100 mM). For measurements in the presence of a ligand, the concentration of ligand was 5 and 10 μM. Each experimental condition was tested in duplicate on at least three separate plates. The melting temperature was determined from normalized curves.

2.5. Circular dichroism

Circular dichroism spectra were acquired on a Jasco J-815 spectropolarizer equipped with a Peltier CDF-426S temperature controller. Readings were performed in a 1 mm light-path quartz cell. CD spectra were recorded with 1 nm bandwidth at a speed of 50 nm/min and averaged over 3 recordings per scan, with a 1 s DIT response. Buffer spectra was subtracted to all spectra. CD melting studies were

performed by monitoring the correspondent wavelength ranging temperatures from 25 to 110 °C with 1.0 ± 0.1 nm data pitch, ramp rate 4 °C/min and with a 4 s temperature stabilization.

2.6. Fluorescence measurements

Titrations were performed with successive additions of concentrated oligonucleotide solution to a ligand solution. Measurements were performed after a 2–3 min equilibration time. The signal areas were plotted against the DNA concentration and fitted according to their appropriate models. Assuming that the fluorescent signal is the contribution of free ligand and bound DNA-ligand complex, it can be defined by

$$F = (1 - \alpha_b)F_0 + \alpha_b F_b$$

where *F* is the value of the experimental variable at each titrant concentration, F_0 and F_b are the values of the variable at the initial and final states of titration, and α$_b$ is the mole fraction of ligand in bound form.

Considering a 1:1 binding stoichiometry and no intermediate states for the equilibria $L + G4 \overset{K_a}{\leftrightarrow} [G4-L]$, results

$$[L_0] - \alpha_b^2 - \left([L_0] + \mathrm{n}[G4] + \frac{1}{K_a}\right)\alpha_b + [G4] = 0$$

where K_a is the binding constant, $[L_0]$ is the total ligand concentration, n the number of binding sites and [G4] is the added DNA concentration. From combination of previous equation and considering

$$\alpha_b = \frac{F - F_0}{F_b - F_0}$$

it can be shown that:

$$\Delta F = \left(\frac{\Delta F_{max}}{[L_0]}\right)\frac{\left\{\left([L_0] + n[G4] + \frac{1}{K_a}\right) - \sqrt{\left([L_0] + n[G4] + \frac{1}{K_a}\right)^2 - 4([L_0]n[G4])}\right\}}{2}$$

where $\Delta F = \mathrm{F} - F_0$ and $\Delta F_{max} = F_{min} - F_0$. F_{min} is the minimum value obtained for the quenching process.

Following the same strategy and considering a 1:2 binding stoichiometry for the equilibria $L + G4 \overset{K_{a1}}{\leftrightarrow} [G4-L] + L \overset{K_{a2}}{\leftrightarrow} [G4-L_2]$, results

$$\Delta F = \left(\frac{\Delta F_{\max([G4-L])}[L_0]K_{a1}[G4] + \Delta F_{\max([G4-L_2])}[L_0]K_{a1}K_{a2}[G4]^2}{1 + K_{a1}[G4] + K_{a1}K_{a2}[G4]^2}\right)$$

2.6.1. Job plots by fluorescence method

Stock solutions of Phen-2 and 22AG/c-myc both at 5 μM were prepared in potassium phosphate buffer. The fluorescence intensity in each case with different Phen-2:c-myc or 22AG ratios but equal in volume (500 μL) was recorded. Job plots were drawn by plotting ΔI (I-I$_0$) versus mole fraction of Phen-2 for each case.

2.7. NMR spectroscopy

NMR experiments were performed on a 600 MHz Bruker Avance III spectrometer with QCI cryoprobe operating at proton frequency of 600 MHz. One dimensional ^{1}H NMR spectra were obtained with a 20 ppm spectral width, 32 k data points, a 2 s relaxation delay, 64 transients and a maximum excitation centered at 12.0 ppm was used for water suppression. The titrations were done with compound Phen-2 and quadruplex c-myc in a 90% H$_2$O/10%D$_2$O solution containing 150 mM KCl and 25 mM KH$_2$PO$_4$ (pH 7.2).

3. Results and discussion

3.1. Design and synthesis

The phenanthroline derivatives (Phen) were synthesized following the procedure depicted in Scheme 1. The phenyl (Iso and Ter) and quinolyl (Quin) scaffolds were also employed in order to explore the importance of the phenanthroline scaffold on G4 recognition.

Briefly, 1,10-phenanthroline-2,9-dicarbaldehyde and 6-methyl-quinoline-2-carbaldehyde were obtained through allylic oxidation of 2,9-dimethyl-1,10-phenanthroline and 2,6-dimethylquinoline, respectively, with selenium dioxide as reported previously [41,42]. After that, the dicarbaldehydes were submitted to Van Leusen reaction through direct cross-coupling of activated C-H with heteroarene halides [39,43] (Scheme 1 and Table S1 of Supporting Information).

Compounds R$_{(I–IV)}$-0 were submitted to the van Leusen reaction conditions in order to form the 4,5-disubstituted oxazole rings. Van Leusen reaction with TosMIC (p-toluenesulfonylmethyl isocyanide) is well described concerning monoaldehyde and recently with dialdehydes [39]. Following the established procedure, Iso-1 and Quin-1 were obtained in good-to-high yield (50 and 80%, respectively). However, with 10-phenanthroline-2,9-dicarbaldehyde and terephthalaldehyde only trace amounts of Phen-1 and Ter-1 were obtained. This led us to modify the reported procedure. The mechanism for the synthesis of TosMIC oxazole from aldehydes occurs in two steps; the first is the formation of a 4-tosyloxazoline intermediate and the second is the 1,2-elimination of the tosyl leaving group upon heating [44]. Accordingly, and in order to accomplish the complete substitution of bis-4-tosyloxazoline, the temperature of the reactions was first kept around 10–20 °C for a few hours. Oxazole formation was then achieved by increasing the reaction temperature until reflux. This modification enabled formation of Phen-1 (50%) and Ter-1 (85%), increased the yield of Iso-1 (65%) but had no effect for Quin-1 yield (85%).

Coupling reaction of 2-bromopyridine with (R$_{I–IV}$) provided the oligoheteroaryle form of the ligands. Quin-2 was obtained in satisfactory yield (45%). However, Phen-2, Iso-2 and Ter-2 were obtained with low reaction yields 20, 21 and 35%, respectively.

All compounds were characterized by 1D and 2D NMR and mass spectrometry.

3.2. Ligands binding and stabilization of G-quadruplexes
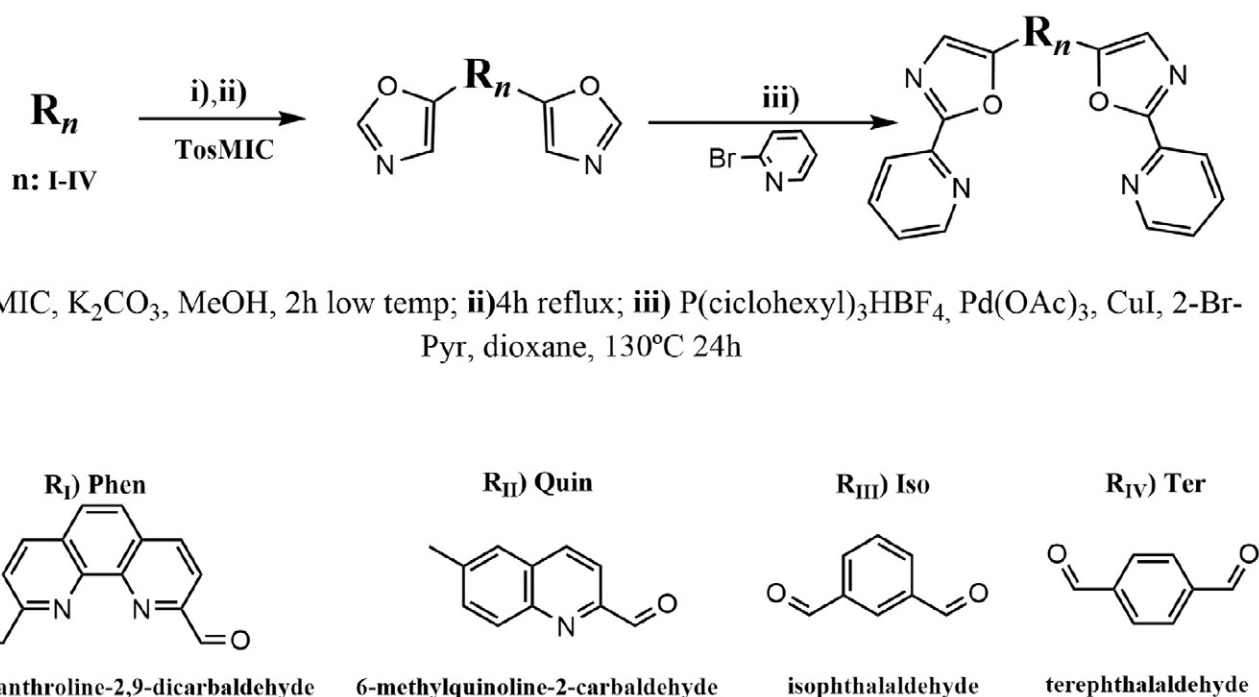
3.2.1. FRET-melting assays

All compounds were first evaluated for their ability to stabilize two reference intramolecular quadruplexes, the human telomeric motif (F21T) and c-myc. The selectivity of these ligands for G-quadruplexes relative to double-stranded DNA FdxT was also evaluated. All compounds were evaluated at 5 μM and 10 μM concentrations. The melting data obtained for the different G4 and double-stranded DNA in the presence of the ligands is reported in Table 1.

According to the ΔT_m values presented in Table 1 for FdxT none of the compounds stabilize duplex DNA ($\Delta T_m \approx 0$ °C). Concerning the G4 sequences, the most effective binder for F21T and c-myc is Phen-2, with ΔT_m values of 8.6 °C and 11.3 °C, respectively, at 5 μM, a much higher value than that obtained with the precursor compound Phen-1 ($\Delta T_m = 4.5$ °C for F21T and 2.4 °C for c-myc at 5 μM). It appears that the extension of the π system of Phen-1 by coupling with 2-bromo-6-(1,3-dioxolan-2-yl)pyridine to afford Phen-2, leads to an increase in G-quadruplex stabilization. F21T stabilization was then monitored in the presence of increasing concentrations (10 μM and 50 μM) of double-stranded FdxT. The thermal stabilization induced by Phen-1 and Phen-2 on the telomeric G-quadruplex was not significantly affected by excess of ds26 (see Table S2 of Supporting Information). This finding suggests that the recognition of 22AG and c-myc by Phen-1 and Phen-2 ligands is a selective process.

The phenyl and quinolyl scaffolds present no G4 binding ability ($\Delta T_m \approx 0$ °C). Particularly relevant is the fact that Iso-1 and Iso-2 show no stabilization, thus enhancing the importance of the central phenanthroline scaffold of Phen-1 and Phen-2, that would have the shape to position the oxazole and pyridine moieties in a relevant arrangement for interaction with the G4. Iso-2 is actually very close to the BOxaPy compound described in Ref. [39], which was also inactive.

The FRET-melting results indicated that only Phen-1 and Phen-2 increased the stabilization to G4 sequences with selective over duplex DNA.

i) TosMIC, K$_2$CO$_3$, MeOH, 2h low temp; ii) 4h reflux; iii) P(ciclohexyl)$_3$HBF$_4$, Pd(OAc)$_3$, CuI, 2-Br-Pyr, dioxane, 130°C 24h

R$_I$) Phen

1,10-phenanthroline-2,9-dicarbaldehyde

R$_{II}$) Quin

6-methylquinoline-2-carbaldehyde

R$_{III}$) Iso

isophthalaldehyde

R$_{IV}$) Ter

terephthalaldehyde

Scheme 1. Synthesis of the compounds employed in this study with four different main scaffolds (R$_{I–IV}$, see lower part of the figure).

Table 1
Thermal stabilization of F21T, c-myc and FdxT oligonucleotides by the different ligands measured by FRET-melting.

	ΔT_m at 5 µM ligand concentration (°C)			ΔT_m at 10 µM ligand concentration (°C)		
Ligand	F21T	Fc-MYCT	FdxT	F21T	Fc-MYCT	FdxT
Phen-1	4.5 ± 0.2	2.4 ± 0.1	0.5 ± 0.1	5.6 ± 0.2	3.1 ± 0.1	−0.4 ± 0.0
Phen-2	8.6 ± 0.2	11.3 ± 0.1	0.5 ± 0.1	11.2 ± 0.2	9.0 ± 0.2	−0.7 ± 0.2
Iso-1	−0.3 ± 0.2	0.5 ± 0.1	0.3 ± 0.0	0.5 ± 0.5	0.8 ± 0.2	−0.4 ± 0.0
Iso-2	−0.1 ± 0.8	0.6 ± 0.1	0.5 ± 0.0	0.2 ± 0.6	1.3 ± 02	0.0 ± 0.2
Ter-1	0.2 ± 0.0	0.5 ± 0.2	0.4 ± 0.5	0.3 ± 0.0	2.2 ± 1.5	−0.3 ± 0.0
Ter-2	0.4 ± 0.3	1.0 ± 0.2	0.6 ± 0.4	0.2 ± 0.3	0.2 ± 0.2	−0.2 ± 0.1
Quin-1	0.4 ± 0.0	0.6 ± 0.1	0.7 ± 0.2	−0.2 ± 0.1	0.8 ± 0.1	−0.2 ± 0.4
Quin-2	−0.1 ± 0.2	0.5 ± 0.1	0.7 ± 0.1	1.0 ± 0.4	−0.4 ± 0.0	−0.4 ± 0.0

0.2 µM of F21T, Fc-MYCT and FdxT in 10 mM KCl, 90 mM LiCl and 10 mM lithium cacodylate at pH 7.2 and 8 studied ligands at concentrations 5 µM and 10 µM.
F21T (5′-FAM-GGGTTAGGGTTAGGGTTAGGG-TAMRA-3′), Fc-MYCT (5′-FAM-TTGAGGGTGGGTAGGGTGGGTAA-TAMRA-3′) and FdxT (5′-FAM-TATAGCTATA-hexa ethyleneglycol-TATAGCTATA-TAMRA-3′).

3.2.2. CD experiments

CD was performed to explore the potential of new ligands to induce G4 formation and further conformational changes, including thermal denaturation studies (CD-melting). Following the FRET-melting results only Phen-1 and Phen-2 were selected for assessing the G4 stabilization and induced conformational changes.

Stock solutions of Phen-1 and Phen-2 were prepared in DMSO and diluted in the required buffer prior to use. No major alterations on the CD profile of the G4 topologies were verified due to addition of DMSO (see Fig. S1 of Supporting Information).

The mutated oncogene promoter c-myc and human telomeric 22AG sequences were selected for the CD studies. These G4 structures, especially the telomeric 22AG, are sensible to the concentration and type of salt applied. For example, in Na⁺, 22AG adopts an antiparallel topology in contrast to a mixture of parallel or hybrid antiparallel topologies formed in K⁺ solution [45–47]. On the other hand, the mutated c-myc adopts a well-defined parallel topology, which was studied in a Li⁺ solution in order to displace its melting temperature to practical values [40,48,49]. The DNA-stabilizing properties of Phen-1 and Phen-2 were evaluated by measuring the ligand-induced variation in the melting temperature (ΔT_m) of 22AG and c-myc, as well as duplex-forming sequences with CD melting experiments. These thermal denaturation experiments were monitored at the wavelengths of maximum CD intensity.

In 100 mM K⁺ solution, 22AG adopts a hybrid telomeric quadruplex with a strong positive peak at 290 nm with shoulder at 265 nm, a smaller positive peak at 250 nm and a small negative peak at 235 nm (Fig. 2A).
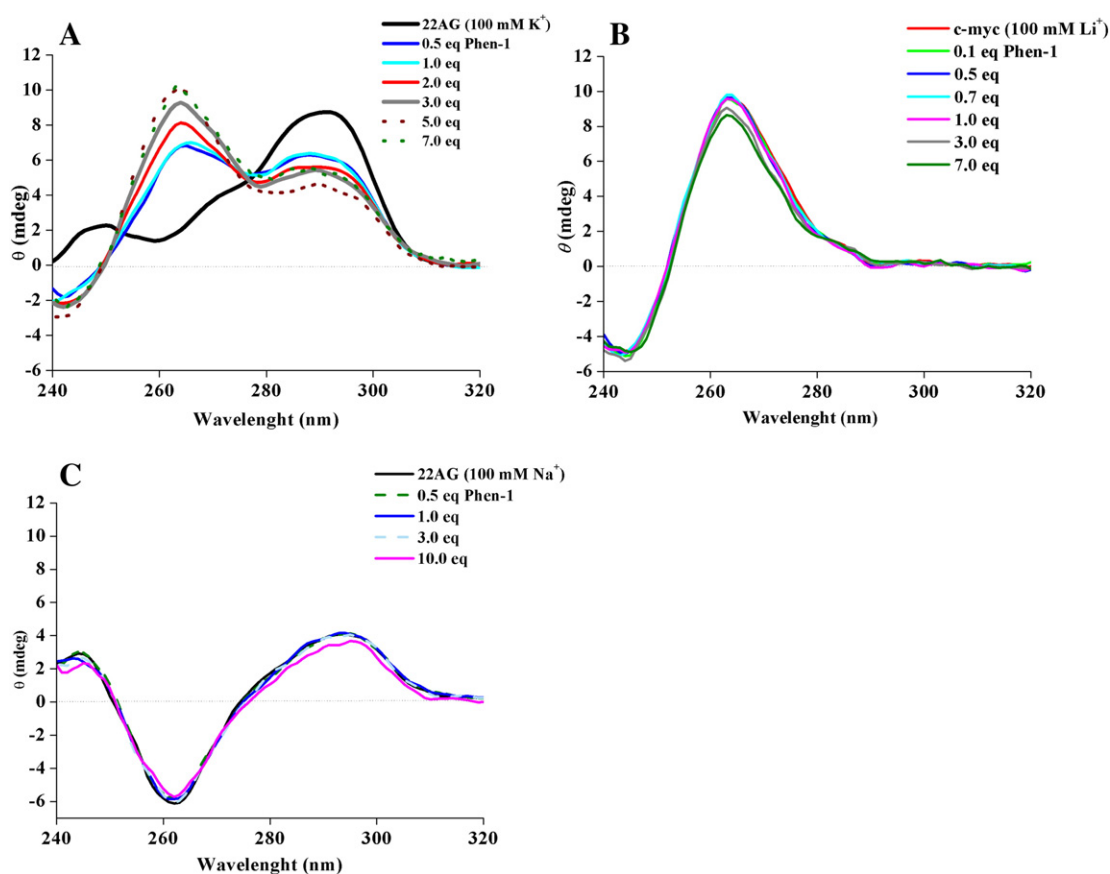

Fig. 2. (A) CD titration spectra of Phen-1 (0–7 molar equiv) to quadruplex 22AG (10 µM) in the presence of K⁺ (100 mM). (B) CD titration spectra of Phen-1 (0–7 molar equiv) to quadruplex c-myc (5 µM) in Li⁺ (100 mM). (C) 22AG in the presence of Na⁺ (100 mM) and upon addition of Phen-1 (0.5–10 equiv). All DNA samples were suspended in phosphate buffer (30 mM, pH 7.2).

Upon addition of 0.5–1.25 equiv of Phen-1, the positive peak at 250 nm disappeared while a positive peak at 265 nm appeared accompanied by a weak negative band around 240 nm. These data are consistent with a mixed hybrid quadruplex folding topology.

After addition of an excess of Phen-1 (5 equiv), the CD spectrum showed a change of conformation towards a parallel structure, with a characteristic positive peak centered around 260 nm and a negative peak at 240 nm (Fig. 2A). This profile is also similar to the transition that occurs naturally upon heating at approximately 70 °C (Fig. S2 of Supporting Information) in ligand-free 100 mM K^+ media, a transition that is described for this type of topology. Phen-1 enhanced the stability of the parallel telomeric by 4.1 °C at 7 equiv (Fig. S3 of Supporting Information) and the Phen-1 concentration-stabilization profile is consistent with a 1:1 stoichiometry.

Titration of antiparallel 22AG with Phen-1 in 100 mM Na^+ showed no relevant variations on DNA ellipticity, suggesting an overall conservation of the unimolecular antiparallel quadruplex topology (Fig. 2B). Even after increasing the Phen-1 concentration 10-fold, only a slight increase (up to 2.5 °C) on the thermal stability was observed.

The mutated c-myc quadruplex adopts a parallel topology, which was retained after Phen-1 was added to the solution (Fig. 2B); nevertheless, the parallel c-myc structure was further stabilized by 4.3 °C after 7 molar equiv were added.

Duplex DNA was also monitored by CD and CD melting studies to examine the interaction and the stabilization effect of the ligands towards these structures. The CD spectra of duplex sequence in the absence and in presence of excess Phen-1 in 10 mM K^+ solution (10 equiv) were almost superimposable (Fig. S4 of Supporting Information) and no change

in melting temperature was observed, thus suggesting that Phen-1 did not interact with the duplex.

These results show that Phen-1 favours parallel quadruplex topologies and selectively stabilize quadruplex over duplex DNA structures, which agrees with the FRET-melting data.

Phen-2 is the most effective binder to the G-quadruplex sequences studied.

The effect of Phen-2 on 22AG was studied in low salt conditions (the only salt contributions were those of the phosphate buffer), and shows a positive peak around 290 nm with a small shoulder peak at 270 nm, a negative peak at 260 nm and a small positive peak at 250 nm (Fig. 3A).

Upon addition of Phen-2 the positive peak at 290 nm was retained and appeared a positive peak at 262 nm characteristic of hybrid-type structure (Fig. 3A). An increase in thermal stability (up to 12.8 °C) was obtained under those conditions, after addition of 10 equiv of Phen-2. These results highlight the fact that Phen-2 has a thermal stabilization effect for 22AG even under low K^+ concentrations.

In 10 mM K^+ solution, 22AG also exhibits a mixture of hybrid-type quadruplex, which have a characteristic positive peak at 290 nm with a shoulder peak at 270 nm and a small positive peak at 252 nm. Upon addition of 1.0 and 2 molar equiv of Phen-2, a positive peak appeared at 260 nm and the positive peak at 290 nm was retained, suggesting that hybrid-type mixed structure was maintained (Fig. 3B). Phen-2 led to an increase in thermal stability of 22AG (13 °C and 15 °C at 1 equiv and 10 equiv, respectively).

Likewise, we tested the influence of Na^+ on the observed topological switching and thermal stability. In the presence of Na^+ (10 mM or 100 mM), 22AG exists in an antiparallel conformation. Upon addition
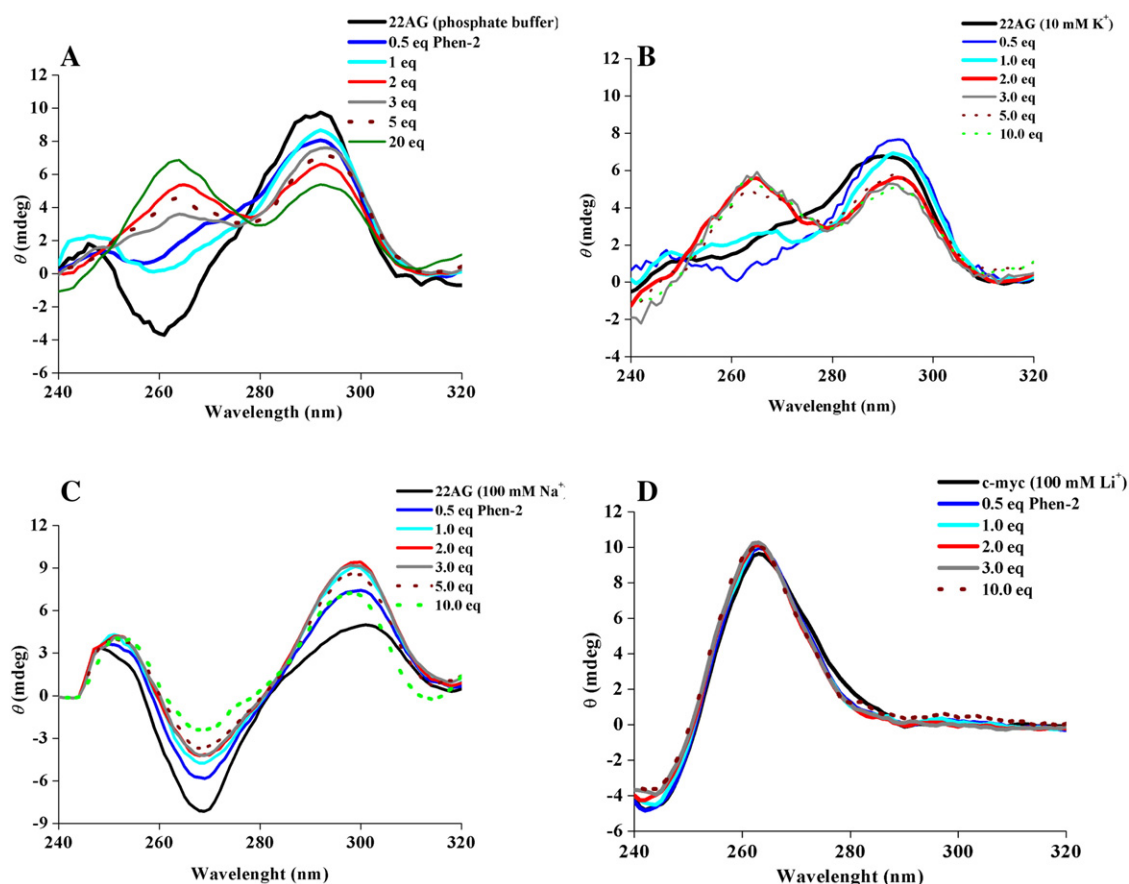

Fig. 3. (A) CD titration spectra of Phen-2 (0–10 molar equiv) to quadruplex 22AG (10 μM) at low salt content, only contribution from the phosphate buffer (0.2 mM K^+). (B) CD titration spectra of Phen-2 (0–20 molar equiv) to quadruplex 22AG (10 μM) in the presence of K^+ (10 mM) and phosphate buffer (30 mM, pH 7.2). (C) CD titration spectra of Phen-2 (0–10 equiv) to 22AG (10 μM) in the presence of Na^+ (100 mM) and phosphate buffer (30 mM, pH 7.2). (D) CD titration spectra of Phen-2 (0–25 molar equiv) to quadruplex c-myc (5 μM) in Li^+ (100 mM) and phosphate buffer (30 mM, pH 7.2).

Table 2
Thermal stabilization of several G4 by Phen-1 and Phen-2 (10 equiv) measured by CD melting.

Ligands	ΔT_m (°C)[a]			
	ds26	c-myc	22AG[b]	22AG[c]
Phen-1	0.3 ± 1.5	4.3 ± 0.6[d]	4.1 ± 0.1[d]	2.5 ± 0.4
Phen-2	-2.8 ± 1.6	31.1 ± 0.3	15.1 ± 0.2	12.7 ± 0.3

[a] ΔT_m represents difference in melting temperature [$\Delta T_m = T_m$ (DNA + 10 molar eq ligand) $- T_m$ (DNA)]. The buffer used was 30 mM phosphate buffer, pH 7.2; Measured T_m for G-quadruplexes in absence of ligand: 50.1 ± 0.1 °C [c-myc (5 μM) in 100 mM LiCl]; 60.9 ± 0.2 °C [hybrid type telomeric DNA (10 μM) in 10 mM KCl]; 61.1 ± 0.1 °C [antiparallel telomeric DNA (10 μM) in 100 mM NaCl]. All experiments were done in triplicate, and the values reported are average of 3 measurements with the estimated standard deviation.
[b] Hybrid type parallel-antiparallel topology of 22AG in 10 mM K$^+$ buffer.
[c] Antiparallel topology of 22AG in 100 mM Na$^+$ buffer.
[d] 7 molar equiv

of Phen-2, this antiparallel structure was retained (Fig. S5 of Supporting Information and Fig. 3C). Phen-2 stabilizes the antiparallel topology of 22AG in 100 mM of Na$^+$ by 12.7 °C.

Adding an excess of Phen-2 (10 equiv) to c-myc in 100 mM Li$^+$ did not induce any change in c-myc ellipticity, suggesting that c-myc retains the parallel topology (Fig. 3D). Interestingly, Phen-2 enhanced the stability of c-myc quadruplex by 31 °C upon addition of 10 equiv. The ΔT_m values of Phen-1 and Phen-2 are listed in Table 2.

These results are somewhat unexpected given that Phen-2 induced hybrid antiparallel topologies but also greatly stabilizes parallel conformation. Moreover, these results show that Phen-2 potentially stabilizes the c-myc promoter quadruplex much better than the human telomeric quadruplex.

Effects of Phen-2 were also investigated on duplex (Fig. S4 of Supporting Information) and, as expected, no major modifications on the CD profile and no significant change in the thermal stability of the double helix were observed, in agreement with FRET-melting studies.

Fig. 4 plots the calculated ΔT_m of the sequences in the conditions mentioned above *versus* concentration (in molar equiv) of Phen-2. Surprisingly, the concentration dependency is very different for the two G4 investigated. In the case of 22AG, the melting temperature increases linearly with the concentration of Phen-2 until a plateau is reached at approximately 2.0 molar equiv of Phen-2. In contrast, c-myc's melting temperature continuously increased with Phen-2 concentration.

Altogether, these results suggest distinct binding modes for Phen-2 depending on quadruplex topology.

The nature of the cation does not seem to have a major impact on the binding event although, as expected, a larger stabilization was observed in K$^+$ solution when compared to Na$^+$. This underscores the importance of the PhenBisOx moiety on the recognition of different quadruplex topology.

In summary, for 22AG in K$^+$ or low salt conditions, Phen-2 led to an increase in thermal stability with retention of the 22AG hybrid-type mixed structures. In contrast, for 22AG in Na$^+$ solution Phen-2 stabilized the antiparallel topology with an increase of the antiparallel profile ellipticity. For c-myc, the stabilization by Phen-2 is much higher than that observed for 22AG, but the parallel topology is retained.

3.2.3. Fluorescence intercalator displacement (FID) assay

Phen-1 and Phen-2 affinities toward 22AG and c-myc quadruplexes and duplex sequence were also determined by the FID assay using thiazole orange (TO). This assay is based on the loss of the fluorescence intensity of TO due to its displacement from the quadruplex structure upon titration with the ligands [50]. This assay was performed with c-myc, 22AG and duplex in potassium and sodium phosphate buffers.

The intrinsic fluorescence of Phen-1 and Phen-2 was prior evaluated in absence of DNA, and ligands + DNA with TO. The excitation and emission maxima did not overlap TO's (Fig. S6 of Supporting Information).

In the presence of a large (10 equiv) excess of Phen-1 and Phen-2, partial displacement of TO was detected; however, the 50% threshold was not reached (Fig. 5). Noteworthy, no TO-displacement was verified for the duplex sequence.

This partial displacement is somewhat surprising given the relatively high stabilizations found for 22AG with Phen-1 and Phen-2, since TO should be easier to displace by an end-stacking ligand; however, groove or loop binders may also displace TO [50].

3.2.4. Fluorescence spectroscopic studies

Since the phenanthroline moiety is fluorescent, the interaction of Phen-1 and Phen-2 with G4 was also evaluated by monitoring the spectroscopic properties of these molecules in the presence or absence of G4 [51].

It was verified that Phen-1 and Phen-2 exhibit an emission band centered at 388 nm (λ_{exc} = 311 nm) and 415 nm (λ_{exc} = 352 nm) respectively, as shown in the emission spectra in Fig. S5 of Supporting Information. Addition of 22AG to Phen-2 in K$^+$ (Fig. 6A) led to a strong quenching effect (60% at 1 equiv, >90% at 7 equiv) and concentration-dependent decrease in fluorescence intensity while in Na$^+$ (Fig. 6B) it also resulted in a strong but less pronounced quenching effect (50% at 1 equiv, 75% at 12 equiv). Titration with c-myc (Fig. 6C) also revealed a very strong quenching of the Phen-2 total signal (70% at 1 equiv, >95% at 10 equiv).

A milder quenching effect was observed for Phen-1 with both sequences. Titration of Phen-1 with 22AG and c-myc resulted in a signal quenching effect although less pronounced (Fig. S7A and B of Supporting Information). However, it was verified that the quenching efficiency was not the same before and after annealing of 22AG and c-myc quadruplexes (in contrast to Phen-2, which exhibited the exact
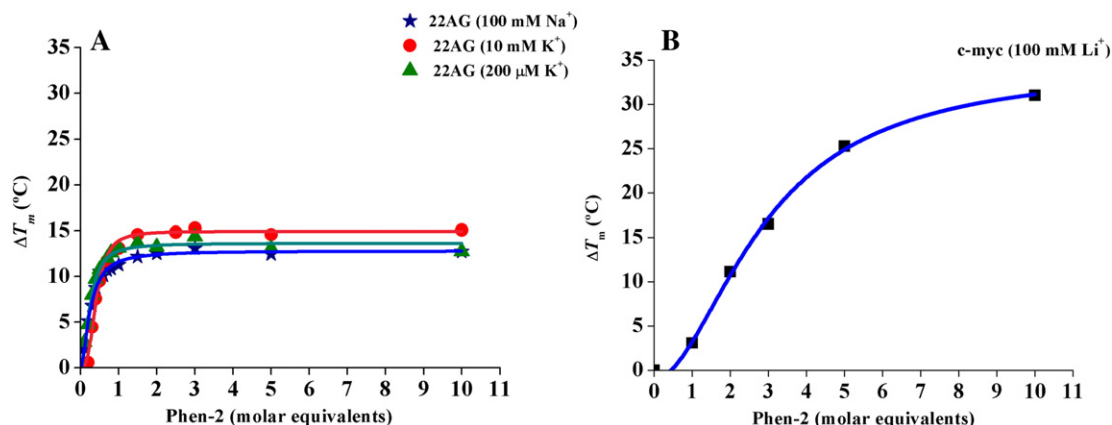

Fig. 4. Effect of Phen-2 on melting temperature increase determined by CD of (A) 22AG quadruplex in 10 mM K$^+$, 200 μM K$^+$ and 100 mM Na$^+$ and (B) c-myc in 100 mM Li$^+$.
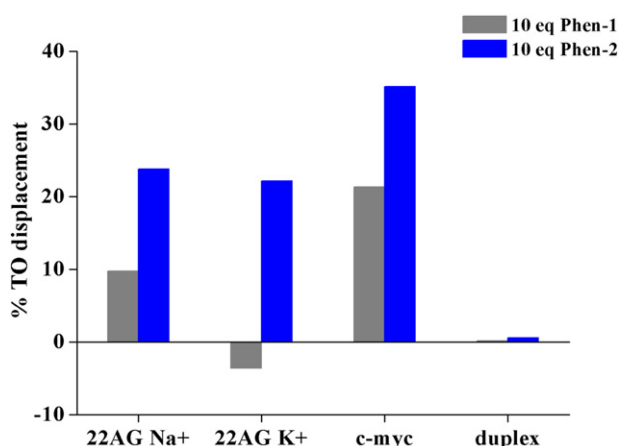
Fig. 5. Diagrammatic bar representation of G4-FID for Phen-1 and Phen-2 performed with 22AG in Na$^+$ (100 mM) and K$^+$ (50 mM), c-myc in K$^+$ (50 mM) and duplex in K$^+$ (50 mM).

same data values). Thus, for Phen-1 the accuracy of K_a is questionable. No significant quenching was observed (10% at 37 equiv) after addition of duplex to Phen-1 (Fig. S7C of Supporting Information).

While these results indicate that Phen-1 and Phen-2 cannot be used as G4 fluorescent light-up probes, they also reveal a strong and specific affinity for their targets. The fitting of Phen-2 quenching curves yielded affinity constants of $(3.2 \pm 0.4) \times 10^7$ M^{-1} and $(1.2 \pm 0.2) \times 10^7$ M^{-1} for 22AG in K$^+$ and Na$^+$, respectively (Fig. 6A and B). The curves were fitted admitting a 1:1 binding stoichiometry, which was confirmed by a Job plot (Fig. S8 of Supporting Information). As for c-myc, the Job

plot experiment indicated a 1:2 (G4:ligand) stoichiometry and the fitting of the fluorescence data resulted in the affinity constants of $(3.8 \pm 0.3) \times 10^7$ M^{-1} and $(4.3 \pm 1.5) \times 10^6$ M^{-1} (Fig. 6C).

Titration of Phen-2 with a duplex sequence emphasized the lack of affinity towards this conformation. In contrast to G4 sequences, addition of 50 equiv of duplex resulted in 10% signal quenching (Fig. 6D).

3.2.5. NMR spectroscopy

The ^{1}H NMR spectrum of c-myc in 30 mM of phosphate buffer and 50 mM KCl at pH 7.0 is presented in Fig. 7A and showed 12 well-resolved distinct peaks in the imino region corresponding to 12 guanines of three G-tetrad planes indicating an intramolecular propeller-type parallel-stranded G-quadruplex as reported previously [52].

Addition of 0.5 molar equiv of Phen-2 to the c-myc solution clearly altered the signature profile of the G4 imino proton peaks with a general signal broadening effect. And while some of these signals suffered a shift, other signals indicate a new chemical environment (Fig. 7B, indicated with arrows), hence suggesting the formation of Phen-2 — quadruplex complex. This indicates slow exchange on the NMR time scale between free and bound states, which is usually interpreted as an indication of tight and specific binding. Interestingly, upon addition of 1 molar equiv of Phen-2 the imino region became considerably broader and the upfield shifted imino protons of the complex quadruplex-Phen-2 become dominant (Fig. 7C). Continuous titration to a 1:2 c-myc-Phen-2 stoichiometry accentuated the broadening of the imino proton resonances (Fig. 7D) and the complete disappearance of the free c-myc resonances. This is in accordance with the Job plot, in which Phen-2 stoichiometry is 1:2 (c-myc-Phen-2).
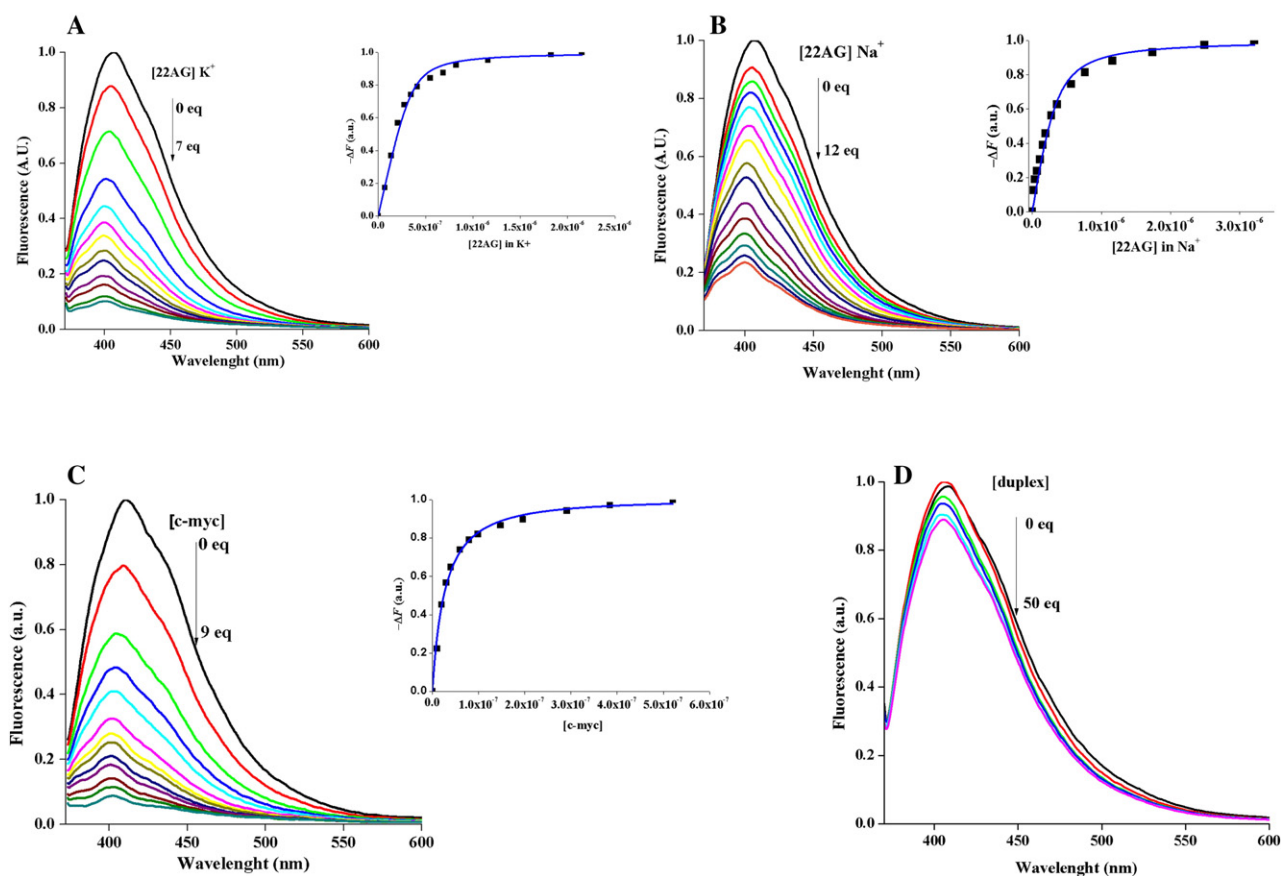

Fig. 6. Fluorescence emission spectra of Phen-2 ($\lambda_{exc} = 352$ nm) with successive addition of (A) 22AG in 30 mM of potassium phosphate buffer; (B) 22AG in 30 mM sodium phosphate buffer; (C) c-myc in 30 mM potassium phosphate buffer and (D) duplex in 30 mM potassium phosphate buffer. The inset is the variation of the signal fluorescent area ($-\Delta F$) vs the concentration of Phen-2. The data was plotted as minus ($-$)ΔF for convenience and was fitted according the appropriate stoichiometry model suggested by the job plot experiments.
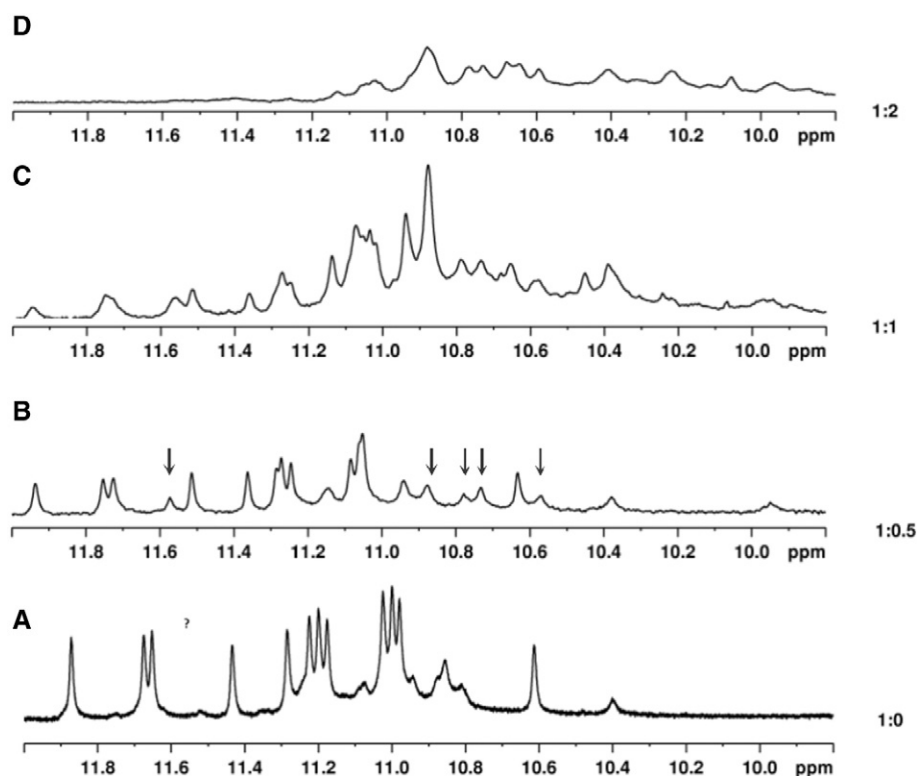
Fig. 7. 1D ^{1}H NMR spectra of the imino proton peaks of (A) free c-myc G4 and c-myc G4/Phen-2 complexes at 1:0.5 (B) 1:1 (C) and 1:2 (D) molar ratio, respectively. The c-myc concentration was 500 μM in 50 mM KCl and 30 mM potassium phosphate buffer at pH 7.0 and the concentration of Phen-2 stock solution was 5 mM in DMSO_d_6. The spectra were recorded with 10% of D_2O at 25 °C. The percentage of DMSO_d_6 in the NMR tube was <5% and did not interfere with the structure of the complex.

Regardless of the detriment of imino signal resolution, the effects observed in this region indicates that the interaction of Phen-2 is with the c-myc terminal G-tetrads, most probably though G-tetrad end-stacking binding, as the intermediate G-tetrads are physically hindered by the loops [52]. The induced upfield-shift of the imino protons is in line with recently reported NMR studies of quadruplex–ligand complexes where quindoline and phenanthroline-bisquinolinium (Phen-DC3) compounds induce an upfield shift of all imino-protons as they bind onto the terminal quartet of the c-myc quadruplex [18].

Overall, these studies demonstrated the potential of acyclic phenanthroline-heterocyclic compounds to act as potential G4 ligands. The PhenBisOx moiety conferred very high selectivity between strong G-quadruplex and duplex DNA structures.

The functionalization of PhenBisOx sharply increased its affinity towards telomeric and c-myc G-quadruplexes as indicated by FRET assay in which Phen-2 stabilizes quadruplexes human telomeric and c-myc by 8.6 °C and 11.3 °C, respectively. Also CD melting studies showed that Phen-2 led to thermal stability of 15 °C for 22AG and 31 °C for c-myc.

The binding affinity and stoichiometry of the Phen-2 to quadruplexes has been evaluated with more detail by fluorescence titrations and showed high affinity with both sequences (10^7 M^{-1}).

These results are comparable to other phenanthroline related ligands reported such as Phen-DC3 and TOxaPy [18,39]. Altogether, these data reflect a very high level of quadruplex stabilization for Phen-2 and represent a significant improvement as compared to the pyridine series [39].

The NMR studies of c-myc quadruplex indicated that Phen-2 can also stack both ends of the quadruplex because the imino-proton peaks of all G-quartets get shielded. This is reported for ligands that bind to the quadruplex by the end-stacking mode [52].

Overall, this study underscores the importance of the PhenBisOx moiety in the ligands, which should be taken into consideration for the design of structure-specific quadruplex stabilizing agents.

4. Conclusions

New phenanthroline, phenyl and quinoline acyclic bisoxazole ligands were synthesized and characterized. Concerning their synthesis, we proposed an optimized step on bisoxazole coupling through van Leusen reaction. CD-melting, FRET-melting and FID assays 22AG showed that Phen-1 and Phen-2 discriminated among various quadruplex topologies and exhibited high selectivity for quadruplexes over duplexes. Furthermore, CD melting studies indicated that Phen-2 stabilizes G-quadruplexes up to 30 °C and 10 °C for c-myc and 22AG, respectively.

CD titration studies revealed that Phen-2 retains antiparallel topologies for quadruplex 22AG and does not induce conformational changes on the parallel c-myc quadruplex. NMR studies also showed that the Phen-2 possibly binds to the c-myc quadruplex via end stacking. In contrast, Phen-1 favours the parallel topology but barely stabilized the G-quadruplex motif.

Fluorescence titrations studies reflected the strong interactions between the Phen-2 and quadruplexes 22AG and c-myc (K ~ 10^6 and 10^7 M^{-1}).

This study underscores the importance of the central aromatic scaffold phenanthroline that can be further fine-tuned with substituents in order to enhance binding and stabilization to G-quadruplex structures, as occurred with Phen-2.

Transparency document

The Transparency document associated with this article can be found, in the online version.

Acknowledgments

Appendix A. Supplementary data

Additional experimental data from G4-FID assays, CD and fluorescence titrations are available. Supplementary data to this article can be found online at http://dx.doi.org/10.1016/j.bbagen.2016.11.024.

References

[1] S. Burge, G.N. Parkinson, P. Hazel, A.K. Todd, S. Neidle, Quadruplex DNA: sequence, topology and structure, Nucleic Acids Res. 34 (19) (2006) 5402–5415.

[2] P. Schultze, N.V. Hud, F.W. Smith, J. Feigon, The effect of sodium, potassium and ammonium ions on the conformation of the dimeric quadruplex formed by the oxytricha nova telomere repeat oligonucleotide d(G(4)T(4)G(4)), Nucleic Acids Res. 27 (15) (1999) 3018–3028.

[3] W. Li, P. Wu, T. Ohmichi, N. Sugimoto, Characterization and thermodynamic properties of quadruplex/duplex competition, FEBS Lett. 526 (1–3) (2002) 77–81.

[4] A.T. Phan, J.-L. Mergny, Human telomeric DNA: G-quadruplex, I-Motif and Watson-Crick double helix, Nucleic Acids Res. 30 (21) (2002) 4618–4625.

[5] S.E. Pierce, J. Wang, J. Jayawickramarajah, A.D. Hamilton, J.S. Brodbelt, Examination of the effect of the annealing cation on higher order structures containing guanine or isoguanine repeats, Chem. Eur. J. 15 (42) (2009) 11244–11255.

[6] S. Neidle, M.A. Read, G-quadruplexes as therapeutic targets, Biopolymers 56 (3) (2001) 195–208.

[7] S. Balasubramanian, L.H. Hurley, S. Neidle, Targeting G-quadruplexes in gene promoters: a novel anticancer strategy? Nat. Rev. Drug Discov. 10 (4) (2011) 261–275.

[8] N.W. Kim, M.A. Piatyszek, K.R. Prowse, C.B. Harley, M.D. West, P.L. Ho, G.M. Coviello, W.E. Wright, S.L. Weinrich, J.W. Shay, Specific association of human telomerase activity with immortal cells and cancer, Science 266 (5193) (1994) 2011–2015.

[9] A.M. Zahler, J.R. Williamson, T.R. Cech, D.M. Prescott, Inhibition of telomerase by G-quartet DNA structures, Nature 350 (6320) (1991) 718–720.

[10] H. Fernando, R. Rodriguez, S. Balasubramanian, Selective recognition of a DNA G-quadruplex by an engineered antibody, Biochemistry 47 (36) (2008) 9365–9371.

[11] T.S. Dexheimer, D. Sun, L.H. Hurley, Deconvoluting the structural and drug-recognition complexity of the G-quadruplex-forming region upstream of the Bcl-2 P1 promoter, J. Am. Chem. Soc. 128 (16) (2006) 5404–5415.

[12] T.A. Brooks, S. Kendrick, L. Hurley, Making sense of G-quadruplex and I-Motif functions in oncogene promoters, FEBS J. 277 (17) (2010) 3459–3469.

[13] T. Ou, Y. Lu, J. Tan, Z. Huang, K. Wong, L. Gu, G-quadruplexes: targets in anticancer drug design, ChemMedChem 3 (5) (2008) 690–713.

[14] D. Monchaud, M.-P. Teulade-Fichou, A hitchhiker's guide to G-quadruplex ligands, Org. Biomol. Chem. 6 (4) (2008) 627–636.

[15] D. Sun, B. Thompson, B.E. Cathers, M. Salazar, S.M. Kerwin, J.O. Trent, T.C. Jenkins, S. Neidle, L.H. Hurley, Inhibition of human telomerase by a G-quadruplex-interactive compound, J. Med. Chem. 40 (14) (1997) 2113–2116.

[16] D. Drygin, A. Siddiqui-Jain, S. O'Brien, M. Schwaebe, A. Lin, J. Bliesath, C.B. Ho, C. Proffitt, K. Trent, J.P. Whitten, et al., Anticancer activity of CX-3543: a direct inhibitor of rRNA biogenesis, Cancer Res. 69 (19) (2009) 7653–7661.

[17] A. De Cian, E. Delemos, J.-L. Mergny, M.-P. Teulade-Fichou, D. Monchaud, Highly efficient G-quadruplex recognition by bisquinolinium compounds, J. Am. Chem. Soc. 129 (7) (2007) 1856–1857.

[18] W.J. Chung, B. Heddi, F. Hamon, M.-P. Teulade-Fichou, A.T. Phan, Solution structure of a G-quadruplex bound to the bisquinolinium compound Phen-DC(3), Angew. Chem. Int. Ed. Engl. 53 (4) (2014) 999–1002.

[19] J. Amato, N. Iaccarino, B. Pagano, R. Morigi, A. Locatelli, A. Leoni, M. Rambaldi, P. Zizza, A. Biroccio, E. Novellino, et al., Bis-indole derivatives with antitumor activity turn out to be specific ligands of human telomeric G-quadruplex, Front. Chem. 54 (2) (2014) 1–8.

[20] M.C. Nielsen, A.F. Larsen, F.H. Abdikadir, T. Ulven, Phenanthroline-2,9-Bistriazoles as selective G-quadruplex ligands, Eur. J. Med. Chem. 72 (2014) 119–126.

[21] C.-Y. Wei, J.-H. Wang, Y. Wen, J. Liu, L.-H. Wang, 4-(1H-imidazo[4,5-F]-1,10-Phenanthrolin-2-Yl)phenol-based G-quadruplex DNA binding agents: telomerase inhibition, cytotoxicity and DNA-binding studies, Bioorg. Med. Chem. 21 (11) (2013) 3379–3387.

[22] L. Wang, Y. Wu, T. Chen, C. Wei, The interactions of phenanthroline compounds with DNAs: preferential binding to telomeric quadruplex over duplex, Int. J. Biol. Macromol. 52 (2013) 1–8.

[23] M. Nakano, H. Tateishi-Karimata, S. Tanaka, N. Sugimoto, Choline ion interactions with DNA atoms explain unique stabilization of A-T base pairs in DNA duplexes: a microscopic view, J. Phys. Chem. B 118 (2) (2014) 379–389.

[24] J.E. Reed, S. Neidle, R. Vilar, Stabilisation of human telomeric quadruplex DNA and inhibition of telomerase by a platinum-phenanthroline complex, Chem. Commun. (Camb.) 42 (2007) 4366–4368.

[25] A.F. Larsen, M.C. Nielsen, T. Ulven, Tetrasubstituted phenanthrolines as highly potent, water-soluble, and selective G-quadruplex ligands, Chemistry 18 (35) (2012) 10892–10902.

[26] M.C. Nielsen, J. Borch, T. Ulven, Design, synthesis and evaluation of 4,7-Diamino-1,10-phenanthroline G-quadruplex ligands, Bioorg. Med. Chem. 17 (24) (2009) 8241–8246.

[27] C. Wei, Y. Wang, M. Zhang, Synthesis and binding studies of novel di-substituted phenanthroline compounds with genomic promoter and human telomeric DNA G-quadruplexes, Org. Biomol. Chem. 11 (14) (2013) 2355–2364.

[28] S. Shi, J. Liu, T. Yao, X. Geng, L. Jiang, Q. Yang, L. Cheng, L. Ji, Promoting the formation and stabilization of G-quadruplex by Dinuclear RuII complex Ru2(obip)L4, Inorg. Chem. 47 (8) (2008) 2910–2912.

[29] M. Kaiser, A. De Cian, M. Sainlos, C. Renner, J.-L. Mergny, M.-P. Teulade-Fichou, Neo-mycin-capped aromatic platforms: quadruplex DNA recognition and telomerase inhibition, Org. Biomol. Chem. 4 (6) (2006) 1049–1057.

[30] S. Bianco, C. Musetti, A. Waldeck, S. Sparapani, J.D. Seitz, A.P. Krapcho, M. Palumbo, C. Sissi, Bis-phenanthroline derivatives as suitable scaffolds for effective G-quadruplex recognition, Dalton Trans. 39 (25) (2010) 5833–5841.

[31] C. Musetti, L. Lucatello, S. Bianco, A.P. Krapcho, S.A. Cadamuro, M. Palumbo, C. Sissi, Metal ion-mediated assembly of effective phenanthroline-based G-quadruplex ligands, Dalton Trans. 19 (2009) 3657–3660.

[32] L. Wang, Y. Wen, J. Liu, J. Zhou, C. Li, C. Wei, Promoting the formation and stabilization of human telomeric G-quadruplex DNA, inhibition of telomerase and cytotoxicity by phenanthroline derivatives, Org. Biomol. Chem. 9 (8) (2011) 2648–2653.

[33] D. Sun, Y. Liu, D. Liu, R. Zhang, X. Yang, J. Liu, Stabilization of G-quadruplex DNA, inhibition of telomerase activity and live cell imaging studies of chiral ruthenium(II) complexes, Chemistry 18 (14) (2012) 4285–4295.

[34] S.G. Rzuczek, D.S. Pilch, A. Liu, L. Liu, E.J. LaVoie, J.E. Rice, Macrocyclic pyridyl polyoxazoles: selective RNA and DNA G-quadruplex ligands as antitumor agents, J. Med. Chem. 53 (9) (2010) 3632–3644.

[35] G.S. Minhas, D.S. Pilch, J.E. Kerrigan, E.J. LaVoie, J.E. Rice, Synthesis and G-quadruplex stabilizing properties of a series of oxazole-containing macrocycles, Bioorg. Med. Chem. Lett. 16 (15) (2006) 3891–3895.

[36] S.A. Ohnmacht, E. Varavipour, R. Nanjunda, I. Pazitna, G. Di Vita, M. Gunaratnam, A. Kumar, M.A. Ismail, D.W. Boykin, W.D. Wilson, et al., Discovery of new G-quadruplex binding chemotypes, Chem. Commun. 50 (8) (2014) 960–963.

[37] M.-Y. Kim, H. Vankayalapati, K. Shin-ya, K. Wierzba, L.H. Hurley, Telomestatin, a potent telomerase inhibitor that interacts quite specifically with the human telomeric intramolecular G-quadruplex, J. Am. Chem. Soc. 124 (10) (2002) 2098–2099.

[38] M. Tera, H. Ishizuka, M. Takagi, M. Suganuma, K. Shin-ya, K. Nagasawa, Macrocyclic hexaoxazoles as sequence- and mode-selective G-quadruplex binders, Angew. Chem. Int. Ed. Engl. 47 (30) (2008) 5557–5560.

[39] F. Hamon, E. Largy, A. Guédin-Beaurepaire, M. Rouchon-Dagois, A. Sidibe, D. Monchaud, J.-L. Mergny, J.-F. Riou, C.-H. Nguyen, M.-P. Teulade-Fichou, An acyclic oligoheteroaryle that discriminates strongly between diverse G-quadruplex topologies, Angew. Chem. Int. Ed. Engl. 50 (37) (2011) 8745–8749.

[40] A. De Cian, L. Guittat, M. Kaiser, B. Saccà, S. Amrane, A. Bourdoncle, P. Alberti, M.-P. Teulade-Fichou, L. Lacroix, J.-L. Mergny, Fluorescence-based melting assays for studying quadruplex ligands, Methods 42 (2) (2007) 183–195.

[41] T. Sakamoto, T. Sakasai, H. Yamanaka, Studies on pyrimidine derivatives. XXII. site-selective oxidation of di-methylpyrimidines with selenium dioxide to pyrimidine-monoaldehydes, Chem. Pharm. Bull. 29 (9) (1981) 2485–2490.

[42] C.J. Chandler, L.W. Deady, J.A. Reiss, Synthesis of some 2,9-disubstituted-1,10-phenanthrolines, J. Heterocycl. Chem. 18 (3) (1981) 599–601.

[43] F. Besselièvre, F. Mahuteau-Betzer, D.S. Grierson, S. Piguel, Ligandless microwave-assisted Pd/Cu-catalyzed direct arylation of oxazoles, J. Org. Chem. 73 (8) (2008) 3278–3280.

[44] D.V. Leusen, A.M.V. Leusen, Synthetic uses of tosylmethyl isocyanide (TosMIC), in: L.E. Overman (Ed.), Organic Reactions, John Wiley & Sons, Inc., Hoboken, NJ, USA 2004, pp. 420–432.

[45] Z. Zhang, J. Dai, E. Veliath, R.A. Jones, D. Yang, Structure of a two-G-tetrad intramolecular G-quadruplex formed by a variant human telomeric sequence in K⁺ solution: insights into the interconversion of human telomeric G-quadruplex structures, Nucleic Acids Res. 38 (3) (2010) 1009–1021.

[46] G. Sattin, A. Artese, M. Nadai, G. Costa, L. Parrotta, S. Alcaro, M. Palumbo, S.N. Richter, Conformation and stability of intramolecular telomeric G-quadruplexes: sequence effects in the loops, PLoS One 8 (12) (2013) e84113.

[47] G.N. Parkinson, M.P.H. Lee, S. Neidle, Crystal structure of parallel quadruplexes from human telomeric DNA, Nature 417 (6891) (2002) 876–880.

[48] A.T. Phan, Y.S. Modi, D.J. Patel, Propeller-type parallel-stranded G-quadruplexes in the human c-myc promoter, J. Am. Chem. Soc. 126 (28) (2004) 8710–8716.

[49] R.I. Mathad, E. Hatzakis, J. Dai, D. Yang, c-myc promoter G-quadruplex formed at the 5′-end of NHE III1 element: insights into biological relevance and parallel-stranded G-quadruplex stability, Nucleic Acids Res. 39 (20) (2011) 9023–9033.

[50] P.L.T. Tran, E. Largy, F. Hamon, M.-P. Teulade-Fichou, J.-L. Mergny, Fluorescence intercalator displacement assay for screening G4 ligands towards a variety of G-quadruplex structures, Biochimie 93 (8) (2011) 1288–1296.

[51] V. Dhamodharan, S. Harikrishna, A.C. Bhasikuttan, P.I. Pradeepkumar, Topology specific stabilization of promoter over telomeric G-quadruplex DNAs by bisbenzimidazole carboxamide derivatives, ACS Chem. Biol. 10 (3) (2015) 821–833.

[52] A. Ambrus, D. Chen, J. Dai, R.A. Jones, D. Yang, Solution structure of the biologically relevant G-quadruplex element in the human c-myc promoter. implications for G-quadruplex stabilization, Biochemistry 44 (6) (2005) 2048–2058.